



Michigan Technological University
Create the Future Digital Commons @ Michigan Tech

Dissertations, Master's Theses and Master's
Reports - Open

Dissertations, Master's Theses and Master's
Reports

2012

Implementation of a phenomenological evaporation model into a porous network simulation for water management in low temperature fuel cells

David L. Fritz III.
Michigan Technological University

Follow this and additional works at: <https://digitalcommons.mtu.edu/etds>



Part of the [Mechanical Engineering Commons](#)

Copyright 2012 David L. Fritz III.

Recommended Citation

Fritz, David L. III., "Implementation of a phenomenological evaporation model into a porous network simulation for water management in low temperature fuel cells", Dissertation, Michigan Technological University, 2012.

<https://doi.org/10.37099/mtu.dc.etds/360>

Follow this and additional works at: <https://digitalcommons.mtu.edu/etds>



Part of the [Mechanical Engineering Commons](#)

AN IMPLEMENTATION OF A PHENOMENOLOGICAL EVAPORATION MODEL
INTO A POROUS NETWORK SIMULATION FOR WATER MANAGEMENT IN LOW
TEMPERATURE FUEL CELLS

By

DAVID L. FRITZ III

A DISSERTATION

Submitted in partial fulfillment of the requirements for the degree of

DOCTOR OF PHILOSOPHY

(Mechanical Engineering-Engineering Mechanics)

MICHIGAN TECHNOLOGICAL UNIVERSITY

2012

© 2012 DAVID L. FRITZ III

This dissertation, "An Implementation of a Phenomenological Evaporation Model into a Porous Network Simulation For Water Management in Low Temperature Fuel Cells," is hereby approved in partial fulfillment of the requirements for the Degree of DOCTOR OF PHILOSOPHY IN MECHANICAL ENGINEERING-ENGINEERING MECHANICS.

Department of Mechanical Engineering-Engineering Mechanics

Signatures:

Dissertation Advisor _____

Dr. Jeffrey Allen

Committee Member _____

Dr. Amitabh Narain

Committee Member _____

Dr. C. K. Choi

Committee Member _____

Dr. Zhengfu Xu

Department Chair _____

Dr. William Predebon

Date _____

To my very supportive and loving family for being there for me every step of the way, my loving wife Archita Fritz who has given me the drive and motivation necessary to succeed and in the loving memory of my grandparents Joyce Fritz, David Fritz Sr and Fredrick Krueger.

Contents

List of Figures	xi
List of Tables	xxi
Acknowledgments	xxiii
Nomenclature	xxv
Abstract	xxxi
1 Introduction	1
1.1 Modeling Background	8
1.1.1 Zero-Dimensional Models	10
1.1.2 One Dimensional Models	11
1.2 Evaporation in the Multi Dimensional Model	20
1.3 Film Evaporation	27
1.4 Summary	34
2 Transition Film Evaporation Model	37
2.1 Transition Film Model Development	38
2.2 Evaporation Rate Boundary Conditions	51
2.3 Transition Film Evaporation Results	52
2.4 Transition Film Evaporation Validation	59
2.5 Summary	68
3 Modeling Transport in the PTL	71
3.1 The Porous Transport Layer Domain	72
3.2 PTL Water Transport	76
3.3 Thermal Transport	81
3.4 Vapor Transport	87
3.4.1 Diffusive Evaporation Model	89
3.5 Boundary Conditions	91
3.5.1 Liquid-phase Boundary Conditions	92
3.5.2 Saturation Boundary Conditions	95
3.5.3 Thermal Boundary Conditions	96

3.6	Fluid Transport Validation	97
3.7	Summary	99
4	Modeling Results	101
4.1	Diffusive/Transition Film Model Comparison at 60% Relative Humidity and 70°C	103
4.2	Diffusive/Transition Film Model Comparison at 70% Relative Humidity and 75°C	121
4.3	Diffusive/Transition Film Model Comparison at 80% Relative Humidity and 80°C	130
4.4	Diffusive/Transition Film Model Comparison at 80% RH and 75°C With a Microporous Layer	137
4.5	Summary	144
5	Membrane Permeability	147
5.1	Experiment	149
5.1.1	Membrane and fluids tested	149
5.1.2	Testing apparatus	150
5.2	Uncertainty Management	151
5.2.1	Height Correction	152
5.3	Data Processing	154
5.4	Results and Discussion	156
5.4.1	Deionized Water Results	156
5.4.2	3M Fluorinert FC-3283 Results	160
5.5	Summary	163
6	Conclusions and Recommendations	165
6.1	Recommendations	166
	Bibliography	171
	References	171
A	Transition Film Pore Network Model Results	187
A.1	70°C Land Temperature Results	188
A.1.1	Drainage	188
A.1.2	Pressure Distribution	189
A.1.3	Temperature Distribution	190
A.1.4	Vapor Concentration Distribution	191
A.2	75°C Land Temperature Results	192
A.2.1	Drainage	192
A.2.2	Pressure Distribution	193
A.2.3	Temperature Distribution	194

A.2.4	Vapor Concentration Distribution	195
A.3	80°C Land Temperature Results	196
A.3.1	Drainage	196
A.3.2	Pressure Distribution	197
A.3.3	Temperature Distribution	198
A.3.4	Vapor Concentration Distribution	199
B	Diffusive Pore Network Model Results	201
B.1	70°C Land Temperature Results	202
B.1.1	Drainage	202
B.1.2	Pressure Distribution	203
B.1.3	Temperature Distribution	204
B.1.4	Vapor Concentration Distribution	205
B.2	75°C Land Temperature Results	206
B.2.1	Drainage	206
B.2.2	Pressure Distribution	207
B.2.3	Temperature Distribution	208
B.2.4	Vapor Concentration Distribution	209
B.3	80°C Land Temperature Results	210
B.3.1	Drainage	210
B.3.2	Pressure Distribution	211
B.3.3	Temperature Distribution	212
B.3.4	Vapor Concentration Distribution	213
C	Pore Evaporation Subroutine	215

List of Figures

1.1	Fuel cell single cell schematic	4
1.2	Fuel cell polarization curve loss contributions.	7
1.3	Polarization curves with varying inlet humidity.	21
2.1	Schematic of transition film region	39
2.2	Conservation of mass for film evaporation model	43
2.3	Multiple Pore Evaporation Comparison	49
2.4	Transition Film Model Thickness Results.	53
2.5	Transition Film Model Interface Temperature Results.	54
2.6	Transition Film Evaporation at Different Contact Angles	55
2.7	Transition Film Evaporation at Different Contact Angles.	56
2.8	Contact Angle Evaporation	57
	(a) Low contact angle experiment	57
	(b) High contact angle experiment	57
	(c) High and low contact angle images superimposed	57
2.9	Disjoining Pressure	58
2.10	Sessile drop evaporation experimental setup.	60
2.11	Evaporating sessile drop.	61
2.12	Evaporating non-zero contact angle drop mass comparison	62
2.13	Pinning/Depinning of Sessile Drop Evaporation at $57^{\circ}C$	63
2.14	Pinning/Depinning of Sessile Drop Evaporation at $27^{\circ}C$	64
2.15	Non-zero contact angle transition film evaporation validation	68
	(a) $t = 0$	68
	(b) $t = 600s$	68
	(c) $t = 1180s$	68
3.1	Mercury intrusion porosimetry data for PTL	73
3.2	Weibull probability distribution function	74
3.3	2-D porous network domain	75
3.4	Computational domain and network model schematic	76
3.5	Transition Viscosity	78
3.6	Capillary Pressure as Interface Progresses	80
3.7	Conductive transport domain schematic	84
3.8	Conductive thermal resistance circuit	85

3.9	Temperature distribution of PTL	86
3.10	Computational domain and boundary conditions	93
3.11	Constant temperature boundary profile	96
3.12	Liquid Transport Validation	98
(a)	Simulation	98
(b)	Experimental	98
4.1	Tested Pore Distributions	102
4.2	Diffusive and Transition Film Percolation at 60% RH and 70°C for a 9.7 μm mean pore size.	104
(a)	Diffusive model percolation at 60% RH and 70°C with a 9.7 μm mean pore size.	104
(b)	Transition film model percolation at 60% RH and 70°C with a 9.7 μm mean pore size.	104
4.3	Diffusive Saturation at 60% RH and 70°C for a 9.7 μm mean pore size.	106
4.4	Transition Film Saturation at 60% RH and 70°C for a 9.7 μm mean pore size.	107
4.5	Drainage and Vapor Concentration Sequence	108
(a)	90 seconds	108
(b)	90 seconds	108
(c)	94 seconds	108
(d)	94 seconds	108
(e)	98 seconds	108
(f)	98 seconds	108
(g)	102 seconds	108
(h)	102 seconds	108
(i)	106 seconds	108
(j)	106 seconds	108
(k)	110 seconds	108
(l)	110 seconds	108
4.6	Temperature Distribution at 60% RH and 70°C	109
(a)	Diffusive model temperature distribution at 60% RH and 70°C with an 9.7 μm mean pore size.	109
(b)	Transition film model temperature distribution at 60% RH and 70°C with an 9.7 μm mean pore size.	109
4.7	Average Temperature of Domain at 60% RH and 70°C	110
4.8	Saturation Distribution at 60% RH and 70°C	111
(a)	Diffusive model saturation distribution at 60% RH and 70°C with an 9.7 μm mean pore size.	111
(b)	Transition film model saturation distribution at 60% RH and 70°C with an 9.7 μm mean pore size.	111
4.9	Pressure Distribution at 60% RH and 70°C	112
(a)	Diffusive model pressure distribution at 60% RH and 70°C with an 9.7 μm mean pore size.	112

(b)	Transition film model pressure distribution at 60% RH and 70°C with an 9.7 μm mean pore size.	112
4.10	Diffusive and Transition Film Percolation at 60% RH and 70°C for an 8.7 μm mean pore size.	113
(a)	Diffusive model percolation at 60% RH and 70°C with an 8.7 μm mean pore size.	113
(b)	Transition film model percolation at 60% RH and 70°C with an 8.7 μm mean pore size.	113
4.11	Diffusive Saturation at 60% RH and 70°C for an 8.7 μm mean pore size. . .	114
4.12	Transition Film Saturation at 60% RH and 70°C for an 8.7 μm mean pore size.	115
4.13	Temperature Distribution at 60% RH and 70°C	116
(a)	Diffusive model temperature distribution at 60% RH and 70°C with an 8.7 μm mean pore size.	116
(b)	Transition film model temperature distribution at 60% RH and 70°C with an 8.7 μm mean pore size.	116
4.14	Average Temperature of Domain at 60% RH and 70°C	117
4.15	Saturation Distribution at 60 % RH and 70°C	118
(a)	Diffusive model saturation distribution at 60% RH and 70°C with an 8.7 μm mean pore size.	118
(b)	Transition film model saturation distribution at 60% RH and 70°C with an 8.7 μm mean pore size.	118
4.16	Pressure Distribution at 60 % RH and 70°C	119
(a)	Diffusive model pressure distribution at 60% RH and 70°C with an 8.7 μm mean pore size.	119
(b)	Transition film model pressure distribution at 60% RH and 70°C with an 8.7 μm mean pore size.	119
4.17	Injection and Interface Pressure Over 60% RH and 70°C Simulation	120
4.18	Diffusive and Transition Film Percolation at 70% RH and 75°C for a 9.7 μm mean pore size.	121
(a)	Diffusive model percolation at 70% RH and 75°C with a 9.7 μm mean pore size.	121
(b)	Transition film model percolation at 70% RH and 75°C with a 9.7 μm mean pore size.	121
4.19	Diffusive Saturation at 70% RH and 75°C for a 9.7 μm mean pore size. . . .	123
4.20	Transition Film Saturation at 70% RH and 75°C for a 9.7 μm mean pore size. .	124
4.21	Diffusive and Transition Film Percolation at 70% RH and 75°C for an 8.7 μm mean pore size.	125
(a)	Diffusive model percolation at 70% RH and 75°C with an 8.7 μm mean pore size.	125
(b)	Transition film model percolation at 70% RH and 75°C with an 8.7 μm mean pore size.	125

4.22	Diffusive Saturation at 70% RH and 75°C for an 8.7 μ m mean pore size. . .	126
4.23	Transition Film Saturation at 70% RH and 75°C for an 8.7 μ m mean pore size.	127
4.24	Percent Occupied Volume/Percent Front Length at 70% RH and 75°C . . .	129
4.25	Diffusive and Transition Film Percolation at 80% RH and 80°C for a 9.7 μ m mean pore size.	130
(a)	Diffusive model percolation at 80% RH and 80°C with a 9.7 μ m mean pore size.	130
(b)	Transition film model percolation at 80% RH and 80°C with a 9.7 μ m mean pore size.	130
4.26	Diffusive Saturation at 80% RH and 80°C for a 9.7 μ m mean pore size. . . .	131
4.27	Transition Film Saturation at 80% RH and 80°C for a 9.7 μ m mean pore size.	132
4.28	Diffusive and Transition Film Percolation at 80% RH and 80°C for an 8.7 μ m mean pore size.	134
(a)	Diffusive model percolation at 80% RH and 80°C with an 8.7 μ m mean pore size.	134
(b)	Transition film model percolation at 80% RH and 80°C with an 8.7 μ m mean pore size.	134
4.29	Diffusive Saturation at 80% RH and 80°C for an 8.7 μ m mean pore size. . .	135
4.30	Transition Film Saturation at 80% RH and 80°C for an 8.7 μ m mean pore size.	136
4.31	PTL with MPL Pore Size Distribution	138
4.32	Modeling domain with MPL	139
4.33	Diffusive and Transition Film Percolation at 80% RH and 70°C for a 9.7 μ m mean pore size and a MPL.	140
(a)	Transition film model percolation at 80% RH and 70°C with a 9.7 μ m mean pore size and no MPL	140
(b)	Diffusive model percolation at 80% RH and 70°C with a 9.7 μ m mean pore size and a MPL.	140
(c)	Transition film model percolation at 80% RH and 70°C with a 9.7 μ m mean pore size and a MPL.	140
4.34	Diffusive Saturation at 80% RH and 80°C for a 9.7 μ m mean pore size. . . .	141
4.35	Transition Film Saturation at 80% RH and 80°C for a 9.7 μ m mean pore size.	142
4.36	Transition Film Vapor Concentration at 80% RH and 70°C for a 9.7 μ m Mean Pore Size With and Without a MPL.	143
(a)	Transition film model vapor concentration at 80% RH and 70°C with a 9.7 μ m mean pore size and no MPL.	143
(b)	Transition film model vapor concentration at 80% RH and 70°C with a 9.7 μ m mean pore size and a MPL.	143
4.37	Transition Film Pressure Distribution at 80% RH and 70°C for a 9.7 μ m Mean Pore Size With and Without a MPL.	144

(a)	Transition film model pressure distribution at 80% RH and 70°C with a 9.7 μ m mean pore size and no MPL.	144
(b)	Transition film model pressure distribution at 80% RH and 70°C with a 9.7 μ m mean pore size and a MPL.	144
5.1	Schematic of the experimental apparatus used to test membrane permeability	151
5.2	Permeability Experiment Image	155
5.3	Permeability of Nafion NR-211 with 20M $\Omega \cdot$ cm deionized water tested at 69.75°C.	158
5.4	Deionized Water Displacement Through Nafion Membrane at 58°C	159
5.5	Deionized Water Displacement Through Nafion Membrane at 80°C	160
5.6	Permeability of Nafion NR-211 with 3M Fluorinert FC-3283 tested at 61.25°C.	162
6.1	Thermal Contact Resistance	168
A.1	Drainage for transition film model at 70°C.	188
(a)	Transition film model 70°C land temperature and a 60% relative humidity.	188
(b)	Transition film model 70°C land temperature and a 70% relative humidity.	188
(c)	Transition film model 70°C land temperature and a 80% relative humidity.	188
(d)	Transition film model 70°C land temperature and a 90% relative humidity.	188
A.2	Pressure Distribution for Transition Film Model at 70°C.	189
(a)	Transition film model 70°C land temperature and a 60% relative humidity.	189
(b)	Transition film model 70°C land temperature and a 70% relative humidity.	189
(c)	Transition film model 70°C land temperature and a 80% relative humidity.	189
(d)	Transition film model 70°C land temperature and a 90% relative humidity.	189
A.3	Temperature Distribution for Transition Film Model at 70°C.	190
(a)	Transition film model 70°C land temperature and a 60% relative humidity.	190
(b)	Transition film model 70°C land temperature and a 60% relative humidity.	190
(c)	Transition film model 70°C land temperature and a 60% relative humidity.	190
(d)	Transition film model 70°C land temperature and a 60% relative humidity.	190

A.4	Vapor Concentration Distribution for Transition Film Model at 70°C.	191
(a)	Transition film model 70°C land temperature and a 60% relative humidity.	191
(b)	Transition film model 70°C land temperature and a 60% relative humidity.	191
(c)	Transition film model 70°C land temperature and a 60% relative humidity.	191
(d)	Transition film model 70°C land temperature and a 60% relative humidity.	191
A.5	Drainage for transition film model at 75°C.	192
(a)	Transition film model 75°C land temperature and a 60% relative humidity.	192
(b)	Transition film model 75°C land temperature and a 70% relative humidity.	192
(c)	Transition film model 75°C land temperature and a 80% relative humidity.	192
(d)	Transition film model 75°C land temperature and a 90% relative humidity.	192
A.6	Pressure Distribution for Transition Film Model at 75°C.	193
(a)	Transition film model 75°C land temperature and a 60% relative humidity.	193
(b)	Transition film model 75°C land temperature and a 70% relative humidity.	193
(c)	Transition film model 75°C land temperature and a 80% relative humidity.	193
(d)	Transition film model 75°C land temperature and a 90% relative humidity.	193
A.7	Temperature Distribution for Transition Film Model at 75°C.	194
(a)	Transition film model 75°C land temperature and a 60% relative humidity.	194
(b)	Transition film model 75°C land temperature and a 60% relative humidity.	194
(c)	Transition film model 75°C land temperature and a 60% relative humidity.	194
(d)	Transition film model 75°C land temperature and a 60% relative humidity.	194
A.8	Vapor Concentration Distribution for Transition Film Model at 75°C.	195
(a)	Transition film model 75°C land temperature and a 60% relative humidity.	195
(b)	Transition film model 75°C land temperature and a 60% relative humidity.	195

(c)	Transition film model 75°C land temperature and a 60% relative humidity.	195
(d)	Transition film model 75°C land temperature and a 60% relative humidity.	195
A.9	Drainage for transition film model at 80°C.	196
(a)	Transition film model 80°C land temperature and a 60% relative humidity.	196
(b)	Transition film model 80°C land temperature and a 70% relative humidity.	196
(c)	Transition film model 80°C land temperature and a 80% relative humidity.	196
(d)	Transition film model 80°C land temperature and a 90% relative humidity.	196
A.10	Pressure Distribution for Transition Film Model at 80°C.	197
(a)	Transition film model 80°C land temperature and a 60% relative humidity.	197
(b)	Transition film model 80°C land temperature and a 70% relative humidity.	197
(c)	Transition film model 80°C land temperature and a 80% relative humidity.	197
(d)	Transition film model 80°C land temperature and a 90% relative humidity.	197
A.11	Temperature Distribution for Transition Film Model at 80°C.	198
(a)	Transition film model 80°C land temperature and a 60% relative humidity.	198
(b)	Transition film model 80°C land temperature and a 60% relative humidity.	198
(c)	Transition film model 80°C land temperature and a 60% relative humidity.	198
(d)	Transition film model 80°C land temperature and a 60% relative humidity.	198
A.12	Vapor Concentration Distribution for Transition Film Model at 80°C.	199
(a)	Transition film model 80°C land temperature and a 60% relative humidity.	199
(b)	Transition film model 80°C land temperature and a 60% relative humidity.	199
(c)	Transition film model 80°C land temperature and a 60% relative humidity.	199
(d)	Transition film model 80°C land temperature and a 60% relative humidity.	199
B.1	Drainage for diffusive model at 70°C.	202
(a)	Diffusive model 70°C land temperature and a 60% relative humidity.	202

(b)	Diffusive model 70°C land temperature and a 70% relative humidity. .	202
(c)	Diffusive model 70°C land temperature and a 80% relative humidity. .	202
(d)	Diffusive model 70°C land temperature and a 90% relative humidity. .	202
B.2	Pressure Distribution for Transition Film Model at 70°C.	203
(a)	Diffusive model 70°C land temperature and a 60% relative humidity. .	203
(b)	Diffusive model 70°C land temperature and a 70% relative humidity. .	203
(c)	Diffusive model 70°C land temperature and a 80% relative humidity. .	203
(d)	Diffusive model 70°C land temperature and a 90% relative humidity. .	203
B.3	Temperature Distribution for Transition Film Model at 70°C.	204
(a)	Diffusive model 70°C land temperature and a 60% relative humidity. .	204
(b)	Diffusive model 70°C land temperature and a 60% relative humidity. .	204
(c)	Diffusive model 70°C land temperature and a 60% relative humidity. .	204
(d)	Diffusive model 70°C land temperature and a 60% relative humidity. .	204
B.4	Vapor Concentration Distribution for Transition Film Model at 70°C.	205
(a)	Diffusive model 70°C land temperature and a 60% relative humidity. .	205
(b)	Diffusive model 70°C land temperature and a 60% relative humidity. .	205
(c)	Diffusive model 70°C land temperature and a 60% relative humidity. .	205
(d)	Diffusive model 70°C land temperature and a 60% relative humidity. .	205
B.5	Drainage for diffusive model at 75°C.	206
(a)	Diffusive model 75°C land temperature and a 60% relative humidity. .	206
(b)	Diffusive model 75°C land temperature and a 70% relative humidity. .	206
(c)	Diffusive model 75°C land temperature and a 80% relative humidity. .	206
(d)	Diffusive model 75°C land temperature and a 90% relative humidity. .	206
B.6	Pressure Distribution for Transition Film Model at 75°C.	207
(a)	Diffusive model 75°C land temperature and a 60% relative humidity. .	207
(b)	Diffusive model 75°C land temperature and a 70% relative humidity. .	207
(c)	Diffusive model 75°C land temperature and a 80% relative humidity. .	207
(d)	Diffusive model 75°C land temperature and a 90% relative humidity. .	207
B.7	Temperature Distribution for Transition Film Model at 75°C.	208
(a)	Diffusive model 75°C land temperature and a 60% relative humidity. .	208
(b)	Diffusive model 75°C land temperature and a 60% relative humidity. .	208
(c)	Diffusive model 75°C land temperature and a 60% relative humidity. .	208
(d)	Diffusive model 75°C land temperature and a 60% relative humidity. .	208
B.8	Vapor Concentration Distribution for Transition Film Model at 75°C.	209
(a)	Diffusive model 75°C land temperature and a 60% relative humidity. .	209
(b)	Diffusive model 75°C land temperature and a 60% relative humidity. .	209
(c)	Diffusive model 75°C land temperature and a 60% relative humidity. .	209
(d)	Diffusive model 75°C land temperature and a 60% relative humidity. .	209
B.9	Drainage for diffusive model at 80°C.	210
(a)	Diffusive model 80°C land temperature and a 60% relative humidity. .	210
(b)	Diffusive model 80°C land temperature and a 70% relative humidity. .	210
(c)	Diffusive model 80°C land temperature and a 80% relative humidity. .	210

(d)	Diffusive model 80°C land temperature and a 90% relative humidity. .	210
B.10	Pressure Distribution for Transition Film Model at 80°C.	211
(a)	Diffusive model 80°C land temperature and a 60% relative humidity. .	211
(b)	Diffusive model 80°C land temperature and a 70% relative humidity. .	211
(c)	Diffusive model 80°C land temperature and a 80% relative humidity. .	211
(d)	Diffusive model 80°C land temperature and a 90% relative humidity. .	211
B.11	Temperature Distribution for Transition Film Model at 80°C.	212
(a)	Diffusive model 80°C land temperature and a 60% relative humidity. .	212
(b)	Diffusive model 80°C land temperature and a 60% relative humidity. .	212
(c)	Diffusive model 80°C land temperature and a 60% relative humidity. .	212
(d)	Diffusive model 80°C land temperature and a 60% relative humidity. .	212
B.12	Vapor Concentration Distribution for Transition Film Model at 80°C. . . .	213
(a)	Diffusive model 80°C land temperature and a 60% relative humidity. .	213
(b)	Diffusive model 80°C land temperature and a 60% relative humidity. .	213
(c)	Diffusive model 80°C land temperature and a 60% relative humidity. .	213
(d)	Diffusive model 80°C land temperature and a 60% relative humidity. .	213

List of Tables

1.1	Evaporation rate coefficients	27
1.2	Accommodation coefficients	32
1.3	Contact-line Length to Surface Area Ratios.	33
3.1	Pore Network Boundary Conditions	92
4.1	Tested Pore Distributions	101
4.2	Diffusive/Transition Film Model Comparison With a Mean Pore Size of 9.7 μm	108
4.3	Diffusive/Transition Film Model Comparison With a Mean Pore Size of 8.7 μm	113
4.4	Diffusive/Transition Film Model Comparison With a Mean Pore Size of 9.7 μm	122
4.5	Diffusive/Transition Film Model Comparison With a Mean Pore Size of 8.7 μm	128
4.6	Diffusive/Transition Film Model Comparison With a Mean Pore Size of 9.7 μm	133
4.7	Diffusive/Transition Film Model Comparison With a Mean Pore Size of 8.7 μm	137
5.1	Thermal Expansion Coefficients	153
5.2	Permeabilities of Nafion NR-211 for FC-3283 and deionized at various temperatures.	157
5.3	Fluid properties of 3M Fluorinert FC-3283.	161

Acknowledgments

It is a great pleasure to express my gratitude to my advisor, Dr. Jeffrey Allen, for his support, his patience, and the guidance he has given throughout my Ph.D. I would also like to thank my research group, Vinay Konduru, for his help setting up the ADPA apparatus to measure evaporation rates, Aneet Dharmavaram Navenvrananth for his thorough proof reading and a special thanks to Ezequiel Medici for helping to understand parts of his network model, even while on vacation.

I am very grateful for the financial support received throughout my studies and would like to again thank Dr. Jeffrey Allen for all the work he has done to provide funding for his graduate students, the Mechanical Engineering - Engineering Mechanics department for their support as a Graduate Teaching Assistant for the Energy Lab, funds from the John F. and Joan M. Calder professorship that supported conference visits.

I would also like to thank my friends, especially Greg Ehlert, Chris Cooney, Devon Moore, and Phil Menerick for their support and timeless friendships. Much of where I am today I owe to my parents Pamela and David Fritz Jr. and cannot thank them enough for everything they have done for me to make this possible. My sister, Lauren Fritz for her encouragement and always being a solid shoulder to lean on. Finally, I would like to thank my beloved wife Archita Fritz, words can not quantify her positive influence she has had and I would like to

thank her for always being that voice of reason, for all the sacrifices she has made, for all the love she has given me on the good days and the bad, and her inspiring words that have allowed me to pursue and finish my Ph.D. successfully.

Nomenclature

Abbreviations

ADPA Axisymmetric Drop Profile Analysis

MIP Mercury intrusion porosimetry

MPL Microporous layer

PDF Probability Distribution Function

PEM Polymer Electrolyte Membrane

PTFE Polytetrafluoroethylene

PTL Porous transport layer

SEM Scanning Electron Microscope

Variables

A Dispersion constant, *J*

a, b Evaporative mass flux coefficient, eqn. 2.25 and 2.26

A_r Empirical rate of electrochemical reaction, *V*

a_{G,L} Liquid interface area, *m*²

B Material constant, *J*

B_l Empirical mass transfer loss coefficient, *V*

Bo Bond number

C Concentration of vapor

C^{ev} Maximum vapor concentration

C₁, C₂ Integration constants defined in eqn. 2.12 and eqn. 2.13

c_a Non-dimensional capillary constant

c_T Molar density of all species, *mol/m*³

D Diffusion coefficient of water vapor in air, *cm*²/*s*

$D_{i,j}^{\text{eff}}$	Effective diffusivity of species i in j , m^2/s
e_0	Electron Charge, C
E_r	Reversible open circuit voltage, V
F_{1-5}	Constants defined by eqns. 2.16 - 2.20
g	Acceleration due to gravity, $9.81m/s^2$
G_1	Constant defined in eqn. 2.29
h	Film thickness, m
h_{fg}	Enthalpy of formation, kJ/mol
i_0	Exchange current density, A
i_c	Current density, A
i_n	Fuel cross-over equivalent current density, A
K	Curvature of liquid-air interface, $1/m$
k	Weibull function scale factor
k_c	Condensation rate constant, $1/s$
k_e	Evaporation rate constant, $1/(Pa \cdot s)$
k_l	Thermal conductivity, $W/(m \cdot K)$
k_m	Generic evaporation rate coefficient, $1/(Pa \cdot s)$
l	Length of pore, m
L_s	Non-dimensional arc length
l_s	Arc length on sessile drop surface, m
\dot{m}^{ev}	Evaporation rate, kg/s
\dot{m}_{evp}	Evaporative mass flux, $kg/(m \cdot s)$
m, n	Disjoining pressure coefficients, eqn. 2.5
m_{ij}^l	Mass of liquid phase between node i and j
m_l	Empirical mass transfer loss coefficient, V

M_w	Molecular weight of water, $kg/kmol$
N_i, N_j	Superficial flux densities of species i and j , $mol/(cm^2s)$
n_l	Empirical mass transfer loss coefficient
p	Pressure, N/m^2
p_{ij}^c	Capillary pressure in pore connecting i and j , N/m^2
p_v	Partial pressure of water vapor in air, N/m^2
p_v^{sat}	Saturation vapor pressure, Pa
q	Volumetric flow rate, m^3/s
\dot{Q}_{ij}	Rate of heat conduction from node i to j , W/s
r	Wetted radius, m
R_a	Non-dimensional radius of curvature
r_a	Area specific resistance, Ω/m^2
R_g	Gas constant, $J/(kg \cdot K)$
r_a	Radius of curvature at the apex of a sessile drop, m
r_{ij}	Radius of the pore connecting nodes i and j , m
R_{ij}^{tot}	Equivalent Thermal resistance, $K \cdot m/W$
$R_{t,cond}$	Thermal resistance, $K \cdot m/W$
s	Liquid saturation
T_i	Liquid-vapor interface temperature, K
u	Fluid velocity, m/s
V_{trans}	Voltage loss due to mass transfer, V
V_c	Cell voltage, V
V_i	Volume of pores surrounding node i , m^3
V_l	Molar volume, m^3/mol
X	Non-dimensional length

\bar{x}_v	Mass fraction of water vapor
x_v	Molar fraction of water vapor
x_{ij}	Position of the liquid-air interface between node i and j
Z	Non-dimensional drop height
z	Height of sessile droplet, m
V_p	Cell potential, V

Greek Symbols

α	Mass accommodation coefficient
β_{ff}	Van der Waals strength potential, $J \cdot m^4$
Γ	Mass flow rate, kg/s
κ	Ionic conductivity, S/cm
μ	Fluids dynamic viscosity, $N \cdot s/m^2$
μ_{ij}^e	Dynamic transition viscosity, $N \cdot s/m^2$
ω	Humidity ratio
ϕ	Relative humidity
Π	Disjoining pressure, N/m^2
ψ	Weibull function shape factor
ρ	Density of fluid, kg/m^3
σ	Surface tension, N/m
θ	Contact angle, rad
ε	Porosity
$\xi^{lv}(S_r)$	Ratio of liquid/vapor interface area to electrode surface area

Subscripts

f	Property of carbon fibers in PTL
g	Property of the gas phase
i	Property at node i

ij	Property of the pore connecting nodes i and j
j	Property at node j
l	Property of the liquid phase
nw	Non-wetting fluid
s	Property of the solid phase
sat	Property at saturated state
w	Wetting fluid
x	Spatial derivative

Abstract

A phenomenological transition film evaporation model was introduced to a pore network model with the consideration of pore radius, contact angle, non-isothermal interface temperature, microscale fluid flows and heat and mass transfers. This was achieved by modeling the transition film region of the menisci in each pore throughout the porous transport layer of a half-cell polymer electrolyte membrane (PEM) fuel cell. The model presented in this research is compared with the standard diffusive fuel cell modeling approach to evaporation and shown to surpass the conventional modeling approach in terms of predicting the evaporation rates in porous media.

The current diffusive evaporation models used in many fuel cell transport models assumes a constant evaporation rate across the entire liquid-air interface. The transition film model was implemented into the pore network model to address this issue and create a pore size dependency on the evaporation rates. This is accomplished by evaluating the transition film evaporation rates determined by the kinetic model for every pore containing liquid water in the porous transport layer (PTL).

The comparison of a transition film and diffusive evaporation model shows an increase in predicted evaporation rates for smaller pore sizes with the transition film model. This is an important parameter when considering the micro-scaled pore sizes seen in the PTL and

becomes even more substantial when considering transport in fuel cells containing an MPL, or a large variance in pore size.

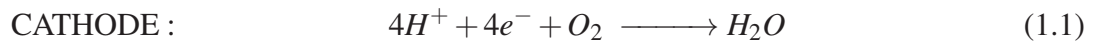
Experimentation was performed to validate the transition film model by monitoring evaporation rates from a non-zero contact angle water droplet on a heated substrate. The substrate was a glass plate with a hydrophobic coating to reduce wettability. The tests were performed at a constant substrate temperature and relative humidity. The transition film model was able to accurately predict the drop volume as time elapsed.

By implementing the transition film model to a pore network model the evaporation rates present in the PTL can be more accurately modeled. This improves the ability of a pore network model to predict the distribution of liquid water and ultimately the level of flooding exhibited in a PTL for various operating conditions.

Chapter 1

Introduction

A fuel cell is an electrochemical device that like a heat engine converts a fuel (namely hydrogen in the PEM fuel cell) into electrical work. While a heat engine converts the fuel into heat then to mechanical work a fuel cell converts the fuel directly to electrical work. The electrochemical reaction in a PEM fuel cell is with reactants hydrogen and oxygen with water as the products. Equation 1.1 demonstrates each half cell reaction for a PEM fuel cell.



When operating with pure oxygen two moles of oxygen are required for every mole of hydrogen however when a fuel cell is supplied with air the amount of oxygen in the air becomes a factor, at standard atmospheric pressure and temperature 21% of the air is oxygen, thus the air flow supply must be greater than that of pure oxygen. For example, with a given power output, P_e and cell voltage, V_c the oxygen supply rates in kg/s would be as follows¹:

$$\begin{aligned}
 O_2 \text{ Usage} &= \frac{M_{O_2} \cdot P_e}{4 \cdot F \cdot V_c} \\
 &= \frac{32 \times 10^{-3} \cdot P_e}{4 \cdot 96485.3 \cdot V_c} \\
 &= 8.29 \times 10^{-8} \cdot \frac{P_e}{V_c}
 \end{aligned}$$

The air usage will change due to the composition of primarily the molecular weight of the mixture (M_{air}) and the percentage of air that is comprised of oxygen thus changing the required air supply for the same power to cell voltage ratio to:

$$\begin{aligned}
 \text{Air Usage} &= \frac{M_{O_2} \cdot P_e}{\frac{m_{O_2}}{m_{air}} \cdot 4 \cdot F \cdot V_c} \\
 &= \frac{28.97 \times 10^{-3} \cdot P_e}{0.21 \cdot 4 \cdot 96485.3 \cdot V_c} \\
 &= 35.7 \times 10^{-8} \cdot \frac{P_e}{V_c}
 \end{aligned}$$

A PEM fuel cell has a simple design, it makes use of a solid polymer membrane which conducts protons, rigid transport layers and has a fairly low platinum content of approximately

0.2 mg/cm^2 as reported by Larminie and Dicks¹. Figure 1.1 illustrates a typical single cell of a PEM fuel cell stack.

The membrane layer of the PEM fuel cell is referred to as the proton exchange membrane and is one of the distinguishing components to a PEM fuel cell. This solid electrolyte is typically comprised of a sulphonated fluoropolymer which is a modified polyethylene chain where the hydrogen groups are replaced with fluorine through a process called perfluorination. When sulphonated the long chain fluoroethylene grows side chains that contain a sulphonic acid (HSO_3) group that are ionically bonded making the actual end group a SO_3^- ion. This is why this component is sometimes referred to as the ionomer¹⁻⁴. The chemical composition of the membrane portion of the PEM fuel cell has a base chain of hydrophobic PTFE (polytetrafluoroethylene) with hydrophilic side chains. These hydrophilic side chains are responsible for the high water absorption found in these membranes. This is a very important property of the polymer electrolyte membranes as it is required for high proton conductivity, low electron conductivity and to insulate the fuel cell from pure diatomic hydrogen crossover. The thickness of this layer varies from $25 \text{ }\mu\text{m}$ to $200 \text{ }\mu\text{m}$ depending on the application. The most common catalyst used for the catalyst layer of the PEM fuel cell is platinum. The catalyst layer as mentioned previously contains very low amounts of platinum, on the order of 0.2 mg/cm^2 . To create the catalyst layer very small particles of platinum are usually adhered to a carbon based powder that is then hot pressed onto the surface of the polymer electrolyte membrane. The method in which the platinum catalyst is installed in the fuel cell can differ from manufacturer to manufacturer.

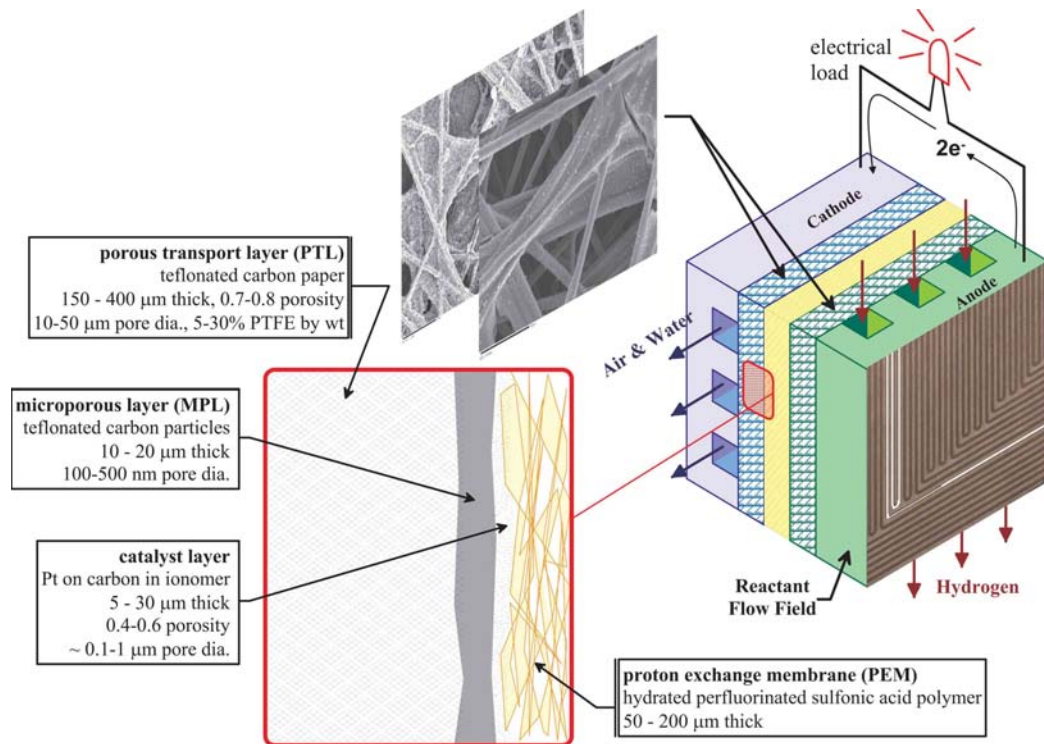


Figure 1.1: A single cell schematic illustrating the individual components of a fuel cell with average pore data, thicknesses and images depicting actual appearance of the anode and cathode PTLs.

The MPL is sandwiched between the cathode PTL and the cathode catalyst layer. The MPL is used to increase the liquid water pressure on the cathode side promoting an increased back-diffusion rate of liquid water to the anode⁵. This back-diffusion is thought to keep the cathode side porous transport layer from flooding thereby reducing the blockage of reaction sites. The MPL also aids in reducing ohmic losses and better utilization of the catalyst sites⁶.

The porous transport layer (PTL) sometimes referred to as a gas diffusion layer, shown in Figure 1.1 serves as a path for electrons to follow to get to the bipolar plates. The PTL also allows for supply of the reactant air (O_2) to the catalyst and for exhaust of the

product water away from the catalyst. This portion of the cell plays a vital role in water management, which is one of the key issues hindering the performance of a PEM fuel cell⁷. If the PTL does not transport the product water away from the catalyst layer the reaction sites will be blocked and the reactions will slow. However, if the PTL removes the water too quickly and the membrane dries out the proton conductivity will be reduced and again the reactions will slow¹.

The last “layer” on the cathode side is the cathode bipolar plate, this component has many variations currently in use. Many of the variations on the bipolar plate consist of either a material or flow field (channel configuration) pattern. The materials range from composites such as injection molded graphite filled polymers to stamped plates such as stainless steel or machined graphite blocks. The available material choices are vast and ever expanding. However material selection of the bipolar plate is beyond the scope of this research so for more information on this subject see the work by Mehta and Cooper⁸. The flow field design is as diverse as the variability of the material selection. The flow fields may be parallel flow paths, serpentine paths, parallel serpentine, grids and interdigitated. Among these configurations the anode and cathode bipolar plates can be offset as well allowing for endless variations on flow path configurations. For more information on the impact of the flow field design to the PEM fuel cells operation see the work by Shimpalee et al.⁹.

The designs for each of these layers listed is typically quite similar from the anode side to the cathode side with the exception of the microporous layer and in some cases the anode

side PTL. The alternative designs to the anode PTL utilize a hydrophilic PTL to help relieve liquid water buildup on the cathode side. This is done with the hopes that the liquid water will have less impact on the reaction rates due to the higher diffusion rates of hydrogen thus allowing more time for the removal of water without slowing the cell reaction rates¹⁰.

Water management in a PEM fuel cell is a delicate balance; the membrane requires full saturation to operate to the best of its ability while the catalyst layer, which resides immediately adjacent to the membrane, needs to be kept dry and free from water to optimize platinum reaction sites. If either of these conditions falls too far below optimal, the fuel cell will become flooded and the oxygen will not be able to reach the reaction sites stopping the reaction, or the membrane will become dehydrated and stop conducting protons and eventually breaking the side chains on the membrane permanently reducing proton conductivity, thus resulting in reduced efficiency¹¹. The reaction of hydrogen ions and oxygen occur in the cathode side which means that the water is generated at the cathode. The excess water can most easily be removed in the gas phase however, in situations where liquid water is present, the fuel cell must rely on the capillary flows, evaporation, inlet humidities and air flow rates to clear the reaction sites of the liquid water. To make the situation worse the proton conduction of the membrane tends to carry water from the anode side to the cathode side by a phenomenon known as electro-osmotic drag. It is because of these complications that understanding how water travels through the cathode layer is of the highest importance in creating a robust design of a PEM fuel cell.

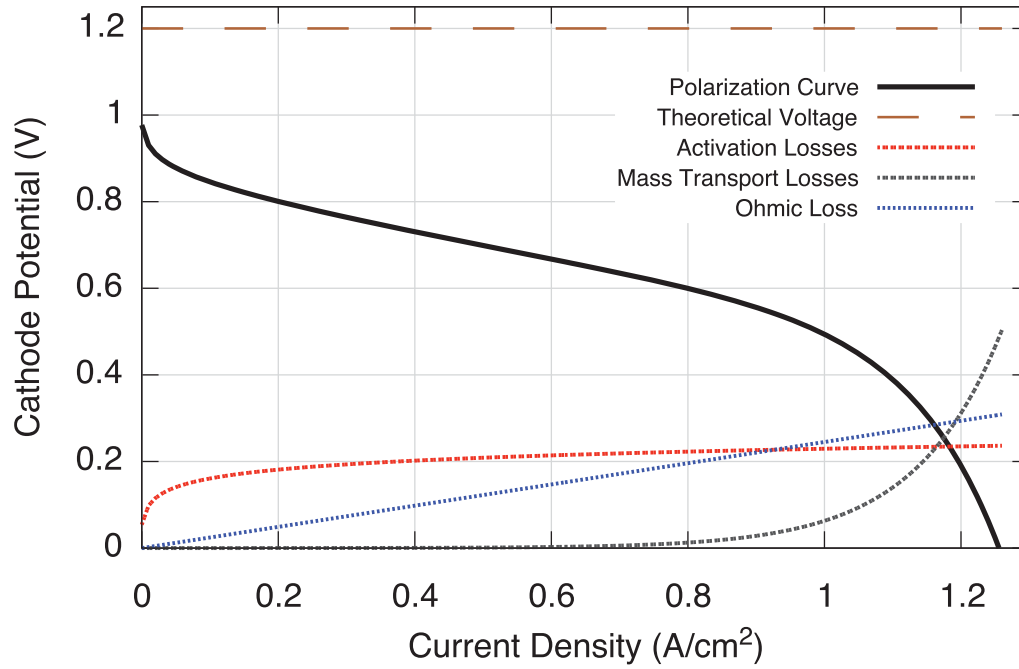


Figure 1.2: Fuel cell polarization curve showing all the losses using a typical zero dimensional modeling approach which can be found in Larminie and Dicks¹.

One of the most commonly reported parameters used to describe how well a PEM fuel cell is operating is called the polarization curve. An example of this curve is illustrated using a zero-dimensional model (see section 1.1.1). The polarization curve is a plot of the voltage a PEM fuel cell will output at various current densities. Figure 1.2 illustrates a polarization curve along with an estimate of where the losses associated with the operation of a fuel cell effect the overall output.

The losses observed in a PEM fuel cell can be categorized into three primary sources, the activation losses, the ohmic losses and the mass transport losses. The activation losses are

affected by the catalyst material selection, amount of catalyst used, and the temperature at which the reaction is taking place. Activation losses are primarily due to the energy required to start the chemical reaction. Figure 1.2 illustrates how at low current densities the energy consumed to sustain the reaction grows quickly but as the current density increases the energy losses become relatively constant. The losses due to fuel crossover, or the hydrogen that leaks through the membrane from the anode side to the cathode side, are sometimes added to the activation losses. The ohmic losses are linearly dependent of the current density, this is because these losses are a function of the electrode resistivity which will remain constant for all operating parameters. Finally there are the mass transport losses, these losses include reduction in diffusivities due to the use of air over pure oxygen, reduction in oxygen transport to the catalyst sites due to the higher humidities found inside the cell and the blockage of pores and catalyst sites by the presence of liquid water.

1.1 Modeling Background

One of the largest remaining operational hurdles that is keeping the Polymer Electrolyte Membrane (PEM) fuel cells from being introduced in commercial markets in a wide variety of applications is effective water and thermal management. The limiting factor of the PEM fuel cell at higher current densities is due to mass transport limitations. These limitations are brought on by the production of liquid water in the cathode diffusion and catalyst layer¹. At high current densities liquid water blocks the pores in the diffusion media and covers the

catalyst reaction sites quickly reducing the cell potential and overall efficiency. Removal of water from these layers is easiest in the gaseous phase. Therefore understanding the production of water and its phase as well as how the water in a fuel cell shifts between the liquid and vapor phases is paramount to the design and optimization of better, more efficient, and more reliable fuel cells.

In order to maintain water balance in a fuel cell, operating at optimal conditions is required. To determine these conditions the physical processes that occur inside the cell need to be well understood. One of the key issues necessary to understanding these processes that can be used in system development is water and thermal management¹². Liquid water distribution depends heavily on the evaporation rates, this is why understanding evaporation is critical to development of fuel cell technology and its water management. Operational experience has indicated that flooding can even occur at low current densities and may be difficult to control at practical current densities¹³.

In a fuel cell there are only a few modes in which the product water is removed from the catalyst layer. These modes include evaporation with vapor diffusion and capillary dominated liquid water flow through the porous transport layer (PTL) and gas channel. There are a large variety of system-level fuel cell models ranging from zero dimensional to three dimensional. There is not a standard method for incorporating evaporation and condensation into these models.

1.1.1 Zero-Dimensional Models

A model is classified as zero dimensional if the polarization curves can be described by a single equation. This makes the zero dimensional model the simplest of the fuel cell models. The zero-dimensional term comes from how the fluid transport is considered, since the transport losses are only accounted for in an empirically determined voltage loss. No or “zero,” dimensions of the fluid flow are modeled. Evaporation is accounted for in the mass transport limitations or losses. An example of a zero dimensional model is,

$$V_c = E_r - i_c r_a - A_r \ln \left(\frac{i_c + i_n}{i_0} \right) - m_l \exp(n_l i_c) \quad (1.2)$$

where E_r is the reversible open circuit voltage, i_c is the current density, i_n is the internal fuel crossover equivalent current density, A_r is a semi-empirically value determined by the rate of the electrochemical reaction, i_0 is the exchange current density, m_l and n_l are empirical values that describe losses due to mass-transfer, and r is the area-specific resistance¹. The voltage loss due to mass transfer (1.3) is purely empirical and the variables n_l and m_l are fitting parameters determined by non-linear regression¹⁴.

$$\Delta E_r = m_l \exp(n_l i) \quad (1.3)$$

Another approach to modeling this mass transfer loss that is more theoretically based can

be seen in equation 1.4. However, this only applies to fuel cells that are supplied with pure oxygen as opposed to air. This method also neglects the production and removal of water¹.

$$\Delta V_{\text{trans}} = -B_l \ln \left(1 - \frac{i_c}{i_l} \right) \quad (1.4)$$

In this equation the constant B_l is empirically determined for the fuel cell operating state. Transient modeling is difficult using this approach. Zero dimensional equations are good for initial estimates, and appropriate for calculating voltages. However, zero-dimensional models cannot be used for optimizing or predicting performance other than cell voltage for very specific operating conditions. Figure 1.2 shows an example of a polarization curve along with the losses associated with mass transfer, activation overvoltage and internal resistance, calculated using Equation 1.2.

1.1.2 One Dimensional Models

One dimensional models, sometimes referred to as the sandwich models¹⁵, are the next step in complexity after the zero-dimensional models. There exist many variations of one-dimensional models but each variation is based on the same general approach. One dimensional models treat the fuel cell stack as a single directional flow perpendicular to each of the layers. The typical sandwich model assumes there are at least five layers, anode and cathode electrode and catalyst layers, and the membrane. The microporous layer of

the diffusion layer is occasionally treated as an individual layer¹⁶. Each of these layers has a separate set of governing equations describing flow of water (vapor and/or liquid), reactants, electrons, and/or protons through each modeled layer.

A number of sub-models exist for each layer and each sub-model requires a unique set of assumptions and their own strengths and weaknesses. Many of these individual layer sub-models can be combined to create a stack-level model that investigates a very specific phenomenon. Selected models for the membrane, catalyst layer and PTL, sub-models are examined for their individual strengths and weaknesses in determining evaporation rates and, subsequently, mass transport limitations.

1.1.2.1 Membrane Modeling

The polymer electrolyte membrane of a PEM fuel cell is responsible for conducting protons, separating reactions¹⁷. A typical membrane is a copolymer of polytetrafluoroethylene and perfluorosulfonic acid. There are a number of different approaches used for a one dimensional membrane model, microscopic and physical, diffusive, hydraulic, hydraulic-diffusive, and combination models are some of the more popular approaches.

Diffusive membrane modeling is also common, because its simplicity and ease of integration into a system level model. Diffusive models are almost always single phase, and the transport of water is normally either neglected or it is assumed constant^{16,18–22}. The

proton transport through the membrane is explained using Ohm's law (1.5) and the Nernst-Planck equation, which when combined these are able to be directly applied to the polarization equation. The drawback of the diffusive membrane model is that little information is provided about the membrane and how it is operating because of the vast number of simplifying assumptions. Typical examples are treating the water movement as a known constant, the membrane is modeled as a single phase that usually corresponds to the vapor-equilibrated membrane, and the application of Schröder's paradox are just a few of these²³. When the membrane is modeled as a single phase it is assumed that no water exists in the membrane and a source term for water is added at the interface of the catalyst layer and the membrane. These models are good for situations where the area of interest is not the membrane and is more the system level outputs. Ohm's law is defined as

$$i_c = -\kappa \nabla V_p \quad (1.5)$$

where i_c is current, κ is the ionic conductivity, an V_p is the cell potential¹⁶.

Hydraulic models allow for modeling the membrane layer as two-phase, as opposed to the single phase in the diffusive membrane models. The two phases modeled are the membrane phase and the water phase. This separates the water and the membrane into two separate phases accounting for the proton transport as part of the water phase. To make up for the added complexity by the added phase, these models assume that the water content in the membrane layer is constant which renders the pressure gradients linear and the transport

properties constant, in a similar manner as the diffusive models.

Hydraulic-Diffusive models are a combination of the hydraulic models and the diffusive models. Hydraulic models are pressure driven, while diffusive models are diffusion driven. The hydraulic-diffusive models account for both of these driving forces. The concentration of water is considered constant and water is assumed to be in the gas phase in order to use the gas pressure as a driving force. These models operate very much like the diffusive models computationally, however they yield a greater flux of water from the cathode to the anode¹⁶.

Microscopic and physical models are a very common approach to local modeling of the electrolyte. The majority of these models rely on statistical mechanics and molecular dynamics which are applied to the macroscopic membrane^{17,24–29}. These models are not commonly used in system level modeling. The predictions made by these models can be useful in determining the diffusion rates and more importantly the proton conduction. Due to the nature of the molecular dynamics and statistical mechanics these types of models are capable of investigating the effects of different pore size and pore distribution, as well as different types of electrolytes^{30,31}. Microscopic models are the only membrane modeling approaches where nearly all treat this layer as a two-phase system modeling water and membrane phases¹⁶. The primary focus of this type of membrane model is how the membrane structure is affected by the membranes water content. The membrane models can account for phase change, but the complexity requires significant computational resources

when incorporated into a system level model.

1.1.2.2 Catalyst Layer Modeling

The catalyst layer in most cells is the thinnest of the layers modeled in a fuel cell ($10\ \mu\text{m}$ - $35\ \mu\text{m}$), but possibly the most complicated. Since the PTL governing equations are typically the same with the addition of the electrochemical reaction equations^{16,32–36}. The modeling for this layer of the fuel cell falls into two categories, the microscopic models and the macrohomogenous models.

The microscopic models are much like in the membrane modeling and are statistical mechanics and molecular dynamics based. Also like with the membrane modeling these models are rarely used in multilayer simulations as they are very computationally demanding. These models excel at simulating the transfer reactions as well as the reaction mechanism that occur in this layer.

Macrohomogenous models, the most common of the multilayer models, are typically designed for the cathode. This is because the cathode catalyst layer experiences slower reaction rates than the anode side catalyst layer due to the diffusion rates of oxygen being lower than that of hydrogen, the presence of liquid and vapor water decrease effective diffusivities as well as the production of water on the cathode side making the mass transfer effects significantly more dominant¹⁶. The anode catalyst layer is usually a simplified version of

the cathode catalyst layer model. One issue that makes modeling this layer of the fuel cell very complex is that in this layer many different phases exist, liquid, gas, various different solids, and the membrane. With this complexity additional assumptions must be made in order to reduce the computational load this could add to a model. Some of these assumptions may include, but are certainly not limited to neglecting the ohmic drop in the solids due to their high conductivity, assuming that there is no water flux through the membrane, assuming that double-layer charging does not exist and assuming that this layer is infinitely thin¹⁶. The obvious simple approach to macrohomogeneous catalyst layer modeling is to assume they are infinitely thin, which allows for the structure of this layer to be ignored.

1.1.2.3 Porous Transport Layer Modeling

The PTL of the fuel cell is where much of the transport to and from the catalyst layer occurs, liquid and gaseous phases as well as the conduction of the electrons. When modeling the PTL the majority of models only account for the gas diffusion layer and neglect the presence of a MPL, a few models do exist where both layers are accounted for, these models are few in numbers and usually very computationally demanding¹⁶.

Two main types of transport occur in this layer of the fuel cell, gas phase and liquid phase. Nearly every accepted model treats the gas phase transport using the Stefan-Maxwell equations in some form. To simplify the Stefan-Maxwell equations most models use Fick's Law with the assumption that the system is of only two components³⁵. The simplified

Stefan-Maxwell equation is described as

$$\nabla x_i = \sum_{j \neq i} \left[\frac{(x_i N_j - x_j N_i)}{c_T D_{i,j}^{\text{eff}}} \right] \quad (1.6)$$

where x_i is the molar fraction of species i , c_T is the molar density of all species, $D_{i,j}^{\text{eff}}$ is the effective diffusion rate of species i into j , and N_i is the superficial flux density of species i .

Faraday's law is sometimes used to simulate the generation of water in this layer when models opt to neglect the catalyst layer. Nearly all models take evaporation into account by determining a molar rate of evaporation. This evaporation rate (1.7) is largely determined by the difference between the partial pressure of the water (p_w) and the vapor pressure of the water (p_v^{sat}), when these two values are equal ($p_v = p_v^{\text{sat}}$) the evaporation is switched off and at this point it is assumed that zero net evaporation takes place. Commonly used evaporation equations take the form of

$$\dot{m}^{\text{ev}} = k_m a_{G,L} (p_v - p_v^{\text{sat}}) \quad (1.7)$$

where \dot{m}^{ev} is the evaporation rate, k_m is the evaporation rate constant, $a_{G,L}$ is the gas-liquid interfacial surface area per unit volume, p_v is the partial pressure of the water vapor, and p_v^{sat} is the saturation pressure¹⁶. A more in-depth discussion of the existing evaporation models will be addressed in section 1.2.

The gas-phase transport, as mentioned earlier, is typically described using Fick's Law.

What differs among the models is how smaller pore sizes are accounted for. Gas diffusion layers have pore sizes that range from 0.5 to 20 μm in radius^{37,38}, for these length scales Fick's law of diffusion is an adequate representation, however as the pore sizes become smaller (as they are in the microporous layer) this becomes less accurate of an assumption. For smaller pore sizes (0.5 to 2 μm)^{39,40}, like that of the microporous layer, Knudsen diffusion must be considered. The Knudsen diffusion is added directly into the Stefan-Maxwell equation for models that do consider the microporous layer.

$$\nabla x_i = -\frac{N_i}{c_T D_{i,j}^{\text{eff}}} + \sum_{j \neq i} \left[\frac{(x_i N_j - x_j N_i)}{c_T D_{i,j}^{\text{eff}}} \right] \quad (1.8)$$

The liquid-phase transport is approached with several different methods in one dimensional models, the largest simplification that is sometimes used is to model the transport of the liquid phase as water droplets that reduces effective diffusivities and travel through the PTL with the same velocity as the gas-phase¹⁶. Other methods of approaching this problem are to assume it as a solid in the sense that it will occupy space in the diffusion media which in turn reduces the gas-phase volume and the ability for the gas-phase to diffuse through the media. This approach accounts for the liquid water by reducing the value of $D_{i,j}^{\text{eff}}$ which is no different that reducing the porosity of the PTL. This approach does not consider the transport of liquid water it merely acknowledges that the liquid phase is present and that it is reducing the diffusion coefficients as well as reducing the gas-phase volume. The volume fraction of water is used as a fitting parameter for the mass transfer losses⁴¹. This type of modeling can be problematic in determining accurate mass fluxes as the liquid water is

modeled as stationary and the only flow that is accounted for is the gas-phase mass flux.

Truly two-phase models, an approach that models the movement of both the liquid and gas-phase water separately, are one of a few limited options modelers have to accurately account for the liquid-water flows within the PTL. Various different approaches exist to account for the liquid water, vapor water and the solid PTL. One of the more simple modeling approaches is to assume that a certain percentage of the pores are hydrophobic while the rest remain hydrophilic. This assumption is applied to the model by having a portion of pores that are dedicated to only transporting liquid-phase water, and the remaining portion dedicated to the gas-phase transport⁴². Other treatments of the two-phase flow is to view the two-phases as a mixture, modeling them as a single-phase two-component mixture. These types of models improve the calculations of the mass flux, however since both liquid and gas phases are modeled together their individual velocities are the same, creating a discrepancy in the liquid pressure because it is dependence on its velocity.

Better approaches to modeling two-phase flow in a single capillary are available, however these models, due to computational cost, are not easily applied to the diffusion media. This type of model is very effective at predicting the liquid saturation with respect to position, which allows for a good prediction of flooding. A few of these models use the Leverett *J*-function^{21,22,43–47} as an empirically determined function to describe the capillary pressure as a function of water saturation, while others neglect the capillary pressure by assuming purely hydrophobic diffusion media.

1.2 Evaporation in the Multi Dimensional Model

The equations used to treat evaporation take on quite a range of approaches in the different models. Many models choose to ignore evaporation,^{35,48–51} which reduces the computational demand of the model however this can create large errors in the models accuracy. When evaporation is ignored the inlet conditions are assumed to be fully humidified, thus the partial pressure of water vapor equals its saturation pressure and the evaporation rate equations then drop to zero. This assumption is certainly not true for all operating fuel cells. Figure 1.3 shows that a model assuming 100% humidity at the inlet will tend to underestimate the polarization curves when the actual inlet humidity is not fully saturated. The equations that follow are some of the ways that evaporation, and condensation are treated in fuel cell modeling.

Natarajan and Nguyen²⁰ introduced equation 1.9 which make use of an isothermal switching function to toggle the evaporative terms on and off. This switching function operates with a fluctuating molar fraction of water vapor. The evaporation rate constant ($k_e = 0.00099 \text{ }^1/(\text{Pa}\cdot\text{s})$) in this model was chosen to be the same as determined in He et al.¹⁹, where it was chosen such that the rates (evaporation and condensation) were sufficiently fast. Another example of how the evaporation rate coefficients are chosen is presented in equation 1.13 by Meng⁵². In this model the condensation rate coefficient was first selected

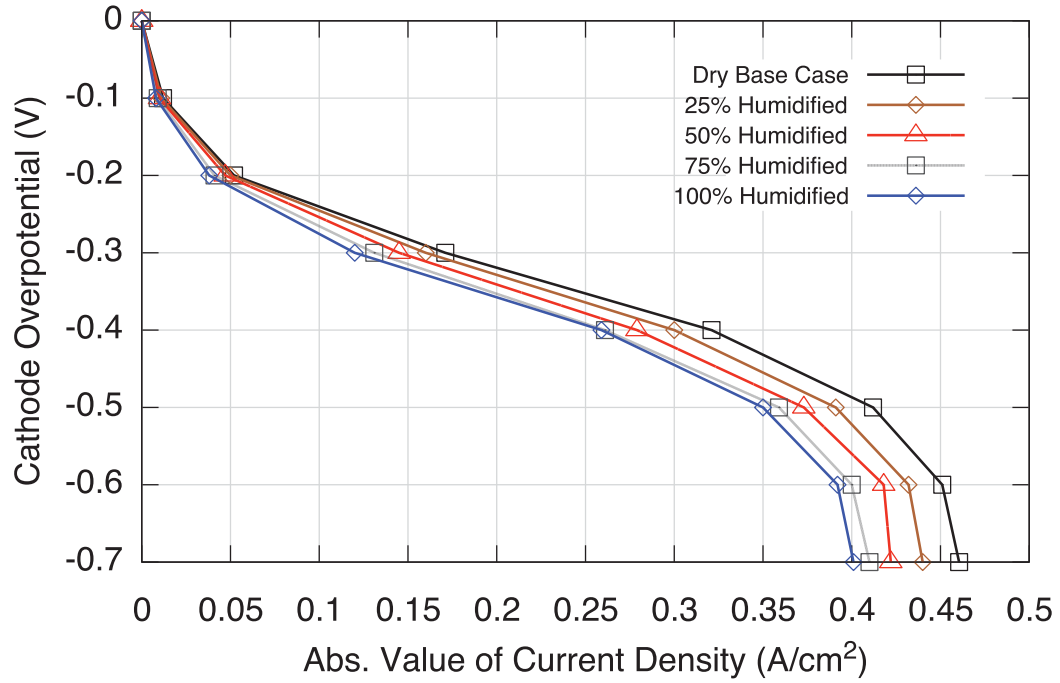


Figure 1.3: Fuel cell polarization curves showing the effect of inlet humidity on cathode performance. Data obtained from Natarajan and Nguyen²⁰ and replotted.

by increasing its value until the results became independent of the condensation rate coefficient, then the evaporation rate coefficient was chosen so that both rates, condensation and evaporation, were of the same magnitude. This method, although yields a decent overall result for specific conditions, may severely hinder this models ability to observe the phenomena that drives evaporation and thus restrict its use in the development of components

and their ability to better water management of a fuel cell.

$$\begin{aligned} \dot{m}^{\text{ev}} = & \frac{k_e \varepsilon \rho_w}{M_w} s (p_v^{\text{sat}} - x_v p) \times \text{switch} \\ & - [k_c \varepsilon (1 - s) x_v (p_v^{\text{sat}} - x_v p)] \times (1 - \text{switch}) \end{aligned} \quad (1.9)$$

$$\text{switch} = \left[\frac{1}{2} + \frac{|p_v^{\text{sat}} - x_v p|}{2(p_v^{\text{sat}} - x_v p)} \right], \quad (1.10)$$

where \dot{m}^{ev} is the interfacial production rate of water, k_e is the evaporation rate coefficient, ε is the porosity, M_w is the molecular weight of water, s is the phase saturation, p_v^{sat} is the saturation pressure, x_v is the molar fraction of water vapor, p is the pressure, and k_c is the condensation rate coefficient, and the switching term is defined in equation 1.10.

Cordiner et al.⁵³ added the effect of temperature as shown in equation 1.11. The approach by Cordiner et al.⁵³ is said to be non-isothermal because of the inclusion of the temperature term in the first term, the condensation portion of the model. Condensation in this approach is instantly turned on over the entire liquid surface when the gas becomes fully saturated. With the exception of temperature on the condensation calculations, equations 1.9 and 1.11 are identical. As with Natarajan and Nguyen²⁰ the values for the condensation and evaporation rate coefficients were taken from He et al.¹⁹.

$$\dot{m}^{\text{ev}} = \left[k_c \frac{\varepsilon(1-s)}{R_g T} (x_v p - p_v^{\text{sat}}) \mathbf{q} + k_e \frac{\varepsilon s \rho_w}{M_w} (x_v p - p_v^{\text{sat}}) (1 - \mathbf{q}) \right] M_w, \quad (1.11)$$

$$\mathbf{q} = \left[\frac{1}{2} + \frac{|(x_v p - p_v^{\text{sat}})|}{2(x_v p - p_v^{\text{sat}})} \right] \quad (1.12)$$

where R_g is the universal gas constant, T is the operating temperature, and ρ_w is the density of liquid water.

A model presented by Meng⁵², also referred to as non-isothermal, is formulated by merely factoring parts of the main evaporation equation 1.11 from Cordiner et al.⁵³ to the switching function as shown in equation 1.13. In this computation the value for the evaporation rate constant is assumed to be $k_e = 1 \times 10^{-4} \text{ (Pa} \cdot \text{s)}^{-1}$. This along with the condensation rate constant were chosen to bring the states of liquid water and water vapor close to their equilibrium⁵².

$$\dot{m}^{\text{ev}} = \left\{ \frac{k_e \mathcal{E} (1-s) x^v}{2RT} \left[1 + \frac{|p_v - p_v^{\text{sat}}|}{p_v - p_v^{\text{sat}}} \right] + \frac{k_e \mathcal{E} \rho_w}{2M_w} \left[1 - \frac{|p_v - p_v^{\text{sat}}|}{p_v - p_v^{\text{sat}}} \right] \right\} (p_v - p_v^{\text{sat}}) \quad (1.13)$$

where p_v is the partial pressure of water vapor.

An alternative approach to a switching function used in determining the interfacial mass transport is programming the model to have an if/then statement based evaporation switch. Equation 1.14 and 1.15 show examples of this type of approach. In the formulation by Hwang⁵⁴ the switch is based on the partial pressure of water vapor. If the partial pressure of the water vapor increases to or above the saturation pressure of water the model assumes condensation and the first part of equation 1.14 is used. If however the partial pressure of water vapor is less than the saturation pressure this model assumes the fuel cell is evaporating its liquid water. In this model the rate of phase change is used to compute the energy

equation as well as the momentum equations. Thus any error in this method will be exaggerated in the polarization curves. The values for the evaporation and condensation rate constants, much like the previous models, were taken from He et al.¹⁹

$$\dot{m}^{\text{ev}} = \begin{cases} k_c \mathcal{E} (1-s) x^v \frac{(p_v - p_v^{\text{sat}})}{RT} & \text{if } p_v - p_v^{\text{sat}} \geq 0 \\ k_e \mathcal{E} s \frac{\rho_w}{M_w (p_v - p_v^{\text{sat}})} & \text{if } p_v - p_v^{\text{sat}} < 0 \end{cases} \quad (1.14)$$

Similarly Sui et al.³⁴ use a computationally driven switch. This condensation switch is toggled off when the vapor pressure drops below the saturation pressure while the interfacial mass transport is positive or is said to be condensing. This is a very interesting formulation as it doesn't include a condensation or an evaporation rate constant, instead it uses as phase change characteristic time (τ_{pc}). There is very little detail on how the phase change characteristic time used in this model is developed and how it relates to the evaporation and condensation rate constants.

$$\dot{m}^{\text{ev}} = \begin{cases} \mathcal{E} \rho (\bar{x}_v^{\text{sat}} - \bar{x}_v) / \tau_{pc} \\ 0; \end{cases} \quad \text{if } s \leq 0 \text{ and } \dot{m}_w > 0 \quad (1.15)$$

In the model presented by Eikerling⁵⁵ (Equation 1.16) the elementary charge of an electron (e_0) as well as the ratio of distributed liquid/vapor interfacial area to apparent electrode surface area as a function of position ($\xi^{lv}(S_r)$) are used to determine the rate of overall water production and area of the evaporating surface respectively. These terms distinguish

this model from the previously discussed models⁵⁵. The elementary charge of an electron that is included in this formulation ($e_0 = 1.6022 \times 10^{-19}C$) is the reason the evaporative rate constant is assumed to be significantly higher than that used in the other models ($k_e = 1.4 \times 10^{18}atm^{-1}cm^{-2}s^{-1}$). The purpose for including the electron charge in the phase change equation is to tie the water production rates from the cell reaction to the evaporation rate. The value for the evaporative rate constant in this model is the most experimental of these types of constants, it was estimated from pure water evaporation from porous silica^{56,57}. The computation done to determine this value was completed for pore diameters and lengths ranging from 5 - 50 nm and $10\mu m$ respectively⁵⁵,

$$\dot{m}^{ev}(z) = \frac{e_0 k_e}{L} \xi^{lv}(S_r) [p_v^{sat}(T) - p_v(z)] \quad (1.16)$$

with L being the thickness of the cathode catalyst layer. This model is limited to the cathode catalyst layer and the PTL is modeled with a stationary liquid water approach.

In the model originally introduced by Nam and Kaviany²¹, and more recently used by Matamoros and Brüggemann⁵⁸, the only phase change equation used calculates a condensation rate. To determine the evaporation rate, Matamoros and Brüggemann⁵⁸ take the inverse of the condensation equation. This model also considers the area of the liquid water interface with respect to the volume of the liquid water that already exists.

$$\dot{m}_{con} = K_{GL} M_{H_2O} \frac{A_{LG}}{V_w} \frac{p_{H_2O} - p_{H_2O}^{sat}}{RT} \quad (1.17)$$

The K_{GL} term is a factor that accounts for the diffusion and evaporative rate coefficients, and A_{GL}/V_w is the gas-liquid interfacial area, which is assumed to be constant in this formulation⁵⁸.

A much older approach introduced by Nguyen and White uses a similar approach to the other models that have been discussed. This model calculates the molar mass flux with respect to position, however instead of incorporating a switching function this model assumes that when the value of $\dot{M}_{H_2O}^w$, the molar rate of water production, is negative the liquid water is said to be evaporating, and if this value is positive the model is said to be condensing.

$$\dot{m}^{ev}(x) = \frac{d\dot{M}_{H_2O}^w}{dx} = \left(\frac{k_c h_c d}{RT} \right) \left(\frac{\dot{M}_{H_2O}^v}{\dot{M}_{H_2O}^v + \dot{M}_{H_2/O_2}} p - p_v^{sat} \right), \quad (1.18)$$

where h_c and d are the width and height of the channel respectively, $\dot{M}_{H_2O}^w$ is the molar rate of water production, $\dot{M}_{H_2O}^v$ is the molar flow rate of water vapor, and \dot{M}_{H_2/O_2} is the molar flow rate of H_2 and O_2 . This approach was implemented with the intent of capturing the effects of condensation on saturation in the PTL.

Nearly all of the models that were presented use some sort of fitting parameter, an evaporation or condensation rate constant. Table 1.1 shows a list of the evaporation and condensation rate constants used. These can be seen to differ greatly from model to model.

Table 1.1
Collection of evaporation rate coefficients from different fuel cell models

Author	k_e	Units	k_c	Units
Khajeh-Hosseini-Dalasm et al. ⁵⁹	9.8×10^{-6}	$1/(Pa \cdot s)$	100	s^{-1}
Meng ⁵²	1×10^{-4}	$1/(Pa \cdot s)$	5000	s^{-1}
Cordiner et al. ⁵³	0.00099	$1/(Pa \cdot s)$	100	s^{-1}
Hwang ⁵⁴	100	$1/(ATM \cdot s)$	100	s^{-1}
Natarajan and Nguyen ²⁰	100	$1/(ATM \cdot s)$	100	s^{-1}
Eikerling ⁵⁵	1.4×10^{18}	$1/(cm^2 ATM \cdot s)$	N/A	—
Nguyen and White ⁶⁰	1.0	s^{-1}	1.0	s^{-1}
Berning and Djilali ⁴⁵	N/A	—	10^{-5}	non-dim

These models have all been introduced to increase the knowledge on how and where the liquid phase water is traveling through the fuel cell system. By understanding this phenomenon, a better design of the PTL could be implemented to reduce the water management issues facing the PEM fuel cell.

1.3 Film Evaporation

It has been shown by many researchers that by introducing a curvature on a liquid-vapor interface the evaporation rate is greatly affected. This is mainly due to the pressure drop

created from the curvature and demonstrated in the Young-Laplace equation (1.19).^{61–67}

$$\Delta p_{\text{surf}} = \left(\frac{1}{R_1} + \frac{1}{R_2} \right) \sigma \quad (1.19)$$

Many computational models use the Hertz-Knudsen-Schrage equation for a flat liquid surface as a basic starting point⁶⁸:

$$J = \alpha \left(\frac{M}{2\pi R} \right)^{1/2} \left[\frac{p_{vlv}}{T_{lv}^{1/2}} - \frac{p_v}{T_v^{1/2}} \right], \quad (1.20)$$

where J is the evaporative flux, α is the accommodation coefficient, M is the molecular weight, R is the universal gas constant, p_{vlv} is the saturation vapor pressure at the interfacial temperature T_{lv} , and p_v is the vapor pressure at the vapor temperature T_v . In nearly all recognized methods used for calculating interfacial mass transport an accommodation coefficient is used. The use of this coefficient for evaporation was introduced in this area by Schrage⁶⁸, where it is explained that the accommodation coefficient shows certain anomalies in its behavior, some of which include the accommodation coefficients dependence on the fluid-substrate material pairings. Currently the mass accommodation coefficient is taken from experimental data, which only applies to very specific conditions such as the fluid and substrate materials. The effect of the intermolecular forces on a localized evaporative flux is far from being fully understood. Values for this mass accommodation coefficient lie between zero and approximately unity. Some reported values from Marek and Straub⁶⁹ and Cammenga⁷⁰ for water have a range of up to three orders of magnitude

($\alpha = 0.0001$ to 1.05) depending on the experimental methods or the researcher performing these experiments.

The original Hertz-Knudsen-Schrage equation (equation 1.20) was derived for a flat surface. Preiss and Wayner Jr.⁶² expanded this equation to include the effects surface tension have on liquid pressure, and Wayner Jr.⁷¹ added surface curvature through the use of the Clapeyron equation:

$$J = \alpha \left(\frac{M}{2\pi RT_{lv}} \right)^{1/2} \left[\frac{p_v M h_{fg}}{RT_v T_{lv}} (T_{lv} - T_v) - \frac{V_l p_v}{RT_{lv}} (\Pi + \sigma \kappa) + \frac{M g p_v}{RT_v} x \right] \quad (1.21)$$

where the V_l is the liquid molar volume, g is the gravitational acceleration, x is the height of the interface, Π is the disjoining pressure (the net pressure reduction within the film due to the solid-liquid intermolecular forces), and the remaining terms are equivalent to those used in Equation 1.20. Despite the addition of curvature to Equation 1.20, errors in the accommodation coefficient continue to cause problems in the calculation of the interfacial mass transport due to the dependence on fluid-substrate pairings. In more recent studies in the thin film region the accommodation coefficient was assumed to be unity. This assumption is justified by studying non-polar liquids. However, as stated by Wang et al.⁷², “in order to acquire more accurate values more detailed experiments are required.”

The accommodation coefficient (α) has been examined by many researchers in the past, however the values these researchers have found have varied by at least three orders of

magnitude. For water alone the values have varied by at least two orders of magnitude depending on the researcher, or the method used to determine this coefficient. Table 1.2 shows a list of values used in the literature for the accommodation coefficient. The experimental procedures for some of the cited accommodation coefficients vary slightly, for example, Rideal⁷³ evaporated water in a closed and inverted and evacuated glass U-tube while controlling the temperatures of each limb (one limb was cooled and the other limb was heated) then measuring the condensation to determine the evaporation rates. Alty⁷⁴ also used a glass vessel while evaporating into a vacuum with surface temperature determined by a thermocouple and the mercury bath temperature was determined by the thermostat. Also Hickman and Torpey⁷⁵ and Narusawa and Springer⁷⁶ also used glass substrates to evaporate the water from and all developed accommodation coefficients in the range of 0.0037 – 0.0155. Cammenga et al.⁷⁷ however used a glass U-tube for the initial experimentation and recorded an accommodation coefficient of 0.002, when changing from glass to a copper capillary, and then a copper block in the same apparatus the accommodation coefficient was reported to be 0.248 and 0.38, respectively.

When considering the evaporation rates from the copper capillaries Cammenga et al.⁷⁷ reported higher accommodation coefficients for smaller capillary diameters. As the contact line length to surface area ratio increased so did the accommodation coefficient and ultimately the evaporation rates. The qualitative trend between contact line length to surface area ratio to the accommodation coefficient and subsequently the evaporation rate is consistent throughout the literature for constant fluid/substrate pairings. For example, analyzing

the data presented by Cammenga et al.⁷⁷, as the ratio of contact line length and surface area increases the accommodation coefficient also increase. In the experiment with copper capillaries it was found that as the capillary reduced in size the accommodation coefficient increased while the surface area decreased proportional to the radius squared the contact line length only reduced proportionally to the radius of the capillary. Table 1.3 demonstrates how both the accommodation coefficient and the contact-line length to surface area ratio increase non-linearly with the change in radius. When altering the fluid/substrate pairing the disjoining pressure, contact angle and liquid surface curvature (as well as several other parameters) all change leading to different evaporation rates and accommodation coefficients for differing fluid/substrate pairing.

Table 1.2
Cited values for the accommodation coefficient found in the literature.

Year	Author	Accommodation Coefficient (α)	Temperature ($^{\circ}\text{C}$)	Fluid/Substrate	Evaporating Area (cm^2)
1925	Rideal ⁷³	0.0037 – 0.0042	25 – 35	Water/Glass U-Tube	1.0
1931	Alty ⁷⁴	0.0083 – 0.0155	5.9 – 32	Water/Glass U-Tube	0.66
1954	Hickman and Torpey ⁷⁵	0.0047	1.2	Water/Glass Vessel	1700.
1967	Maa ⁷⁸	1.00	2	Water/Air*	
1971	Cammenga et al. ⁷⁷	0.002	24 – 30	Water/Glass Vessel	18.0
		0.228	18	Water/Copper Capillary	0.029
		0.273	18	Water/Copper Capillary	0.017
		0.355	18	Water/Copper Capillary	0.006
		0.38	18	Water/Copper Block**	0.03
1975	Narusawa and Springer ⁷⁶	0.038	18 – 27	Water/Metallic Dish	38.5
1995	Schonberg et al. ⁶⁶	2	100	Water/Metallic Capillaries	3.14×10^{-8}
2005	Wee et al. ⁷⁹	2.0	90	Non-Experimental	
2007	Wang et al. ⁷²	1.00	70	Non-Experimental	

* Experiment run on free liquid jet as in a jet tensiometer.

** Area given is the wetted area of the fluid, not the surface area of the fluid.

Table 1.3
Contact-line length to surface area in relation to the accommodation
coefficient. Data found in Cammenga et al.⁷⁷

Contact-line Length (<i>cm</i>)	Contact-line Length Surface Area (<i>cm</i> ⁻¹)	Accommodation Coefficient
0.6037	20.817	0.228
0.4622	27.1882	0.273
0.2746	45.7667	0.355

The verification of equations 1.20 and 1.21 for this thin film region have been limited in part by the ability to observe fluid flow in this area, especially for non-wetting liquids. The very small thickness of this film does not allow for optical microscopy under normal gravity, as the wavelength of light is too large to see all these effects. Scanning electron microscopy (SEM) is limited to solids because of the extremely low pressure requirements the SEM demands for operation. Although Environmental Scanning Electron Microscopy (ESEM) does have the ability to image liquids, there is little literature available that explores this avenue of imaging to determine evaporation rates^{21,80}. Nam and Kaviany²¹ used an ESEM to examine the liquid water distribution while condensing. Due to the nature of SEM and ESEM obtaining accurate evaporation rates through this form of imaging is difficult because to obtain suitable resolutions the frame rate must be low.

In summary, previous researchers have shown that for very specific fluids the interfacial mass transport can be modeled with large uncertainties. However, without very controlled and specific experimentation, the values for the accommodation coefficient can vary up to three orders of magnitude. It has also been shown that the verification of the applicability

of the current models for interfacial mass transport is quite limited by the lack of imaging technology. Many researchers agree that there currently exists insufficient research to determine the mass accommodation coefficient. Until this is better understood, the current models can only be applied accurately to very specific, non-polar, wetting fluids. An indication of why there may be such a large discrepancy in the mass accommodation coefficient is in the details of some experiments. As was first described by Cammenga et al.⁷⁷ and again reiterated in Marek and Straub⁶⁹, an evaporation coefficient of 0.002 was found for water in a glass vessel, but when the glass vessel was replaced with a copper vessel, the capillary evaporation coefficients were increased by two orders of magnitude, to value between 0.25 and 0.38. The experiments with the glass and copper vessels were both conducted in the same apparatus. The only physical change that occurred was in the contact angle between the liquid surface and the solid surface. Thus our hypothesized connection between the contact angle and the mass accommodation coefficient is introduced.

1.4 Summary

In this chapter a basic overview of a fuel cell and its operation were discussed along with a detailed background on the computational modeling efforts. The primary focus was the methods in which each of these models consider the water management aspects of fuel cell operation. For a more detailed background on this matter the books by Mench⁸¹ and Larminie and Dicks¹

The zero dimensional models were briefly discussed, here it was shown that although the system level models can fairly accurately predict the polarization curve the methods used in calculating mass transport are mainly empirical and are unable to be used to aid in understanding the underlying phenomenon that drive this transport. Because of the empirical nature of the mass transport terms in a zero dimensional model, experimental data is required in order to tune the fitting parameters that describe this transport.

Two dimensional models were then discussed in much greater detail, with the main focus on how evaporation is treated in the mass transport terms of various different models. It was clearly shown that several different approaches exist when addressing the evaporation. Some models choose to ignore that evaporation occurs entirely^{35,48–51}, while others tend to follow a derivation of the models listed in the previous section. Due to the typical operating temperature of a PEM fuel cell ($\approx 80^\circ\text{C}$), and the geometry of the internal components ignoring evaporation is clearly not a valid assumption. In nearly all models that do consider evaporation and condensation a rate coefficient is used as a fitting parameter to fit the model predicted polarization curves with the experimental polarization curves. However, as operating conditions and morphology change, the level of flooding increases or decreases and the temperature of the cell fluctuates meaning the evaporation rate coefficients may not necessarily be constant. Many of the models in use today employ a value for the evaporation rate coefficient introduced by He *et al.*¹⁹ where $k_e = 100 \text{ atm}^{-1}\text{s}^{-1}$ and chosen to assure that both the evaporation and condensation rates are fast enough^{19,54,80,82,83}.

Currently little research has been attempted to relate the value of the evaporation and condensation rate coefficients to a physical parameter for use in any level fuel cell models. It has been discussed how many of the current methods used in determining and employing the rate coefficients have only selected the values to fit models to experimental data, and have no physical relation to the properties of the fluids themselves. With a better understanding of how the physical properties of the liquid and vapor water affect these rate coefficients, more accurate, robust, and versatile models can be developed which can in turn help the development of more efficient, less expensive fuel cells that can operate in a much larger range of environmental conditions.

Chapter 2

Transition Film Evaporation Model

This chapter will discuss the development, validation and results of the transition film model. This is a kinetic phase-change model which has been adapted from the work of Wee et al.⁸⁴ to accept a different formulation for disjoining pressure that includes a contact angle input. The new disjoining pressure results in new formulations for interface temperatures, initial film thickness, and the evaporation rate terms. The primary goal of developing a model with these properties was to capture the enhanced evaporation rates at the contact line within the porous media for an evaporating liquid front. The contact line effects are very important in this type of domain as the contact line length to surface area ratio can be orders of magnitude larger than that of a pool evaporation domain.

2.1 Transition Film Model Development

The transition film model is a highly non-linear third order ordinary differential equation with a free boundary. This type of model is selected due to the large influence that transition liquid films have on evaporation rates for porous and non-porous applications^{63,85–87}. The solution is for a steady state condition so it is assumed that between time steps a steady non-deformed liquid surface is obtained. All of the thermodynamic and fluid properties are derived and expressed in terms of a film thickness/profile in the equations that follow. The formulation used in this work is a variation on the work done by Wee et al.⁷⁹. This is a one-sided formulation developed for the liquid side as the liquid properties of density, viscosity, and thermal conductivity are more dominant than those of the vapor phase. A one-sided model updates the liquid and interface properties only, making the assumption that the gas-phase properties remain constant over the domain. This approach is beneficial in reducing the computational expense as the thermal flow fields and convection currents need not be calculated⁸⁸.

Due to the size of the pores under consideration the effects of gravity are neglected, this is a good assumption since the largest Bond number (gravitational forces / surface forces) expected is $Bo < 2.5 \times 10^{-4}$ which is much less than one.

$$Bo = \frac{\rho_l g r_{ij}^2}{\sigma} \quad (2.1)$$

In this microscale flow the fluid velocities near the transition region are much less than the bulk fluid velocities and can be neglected, thus also removing the inertial terms from the formulation.

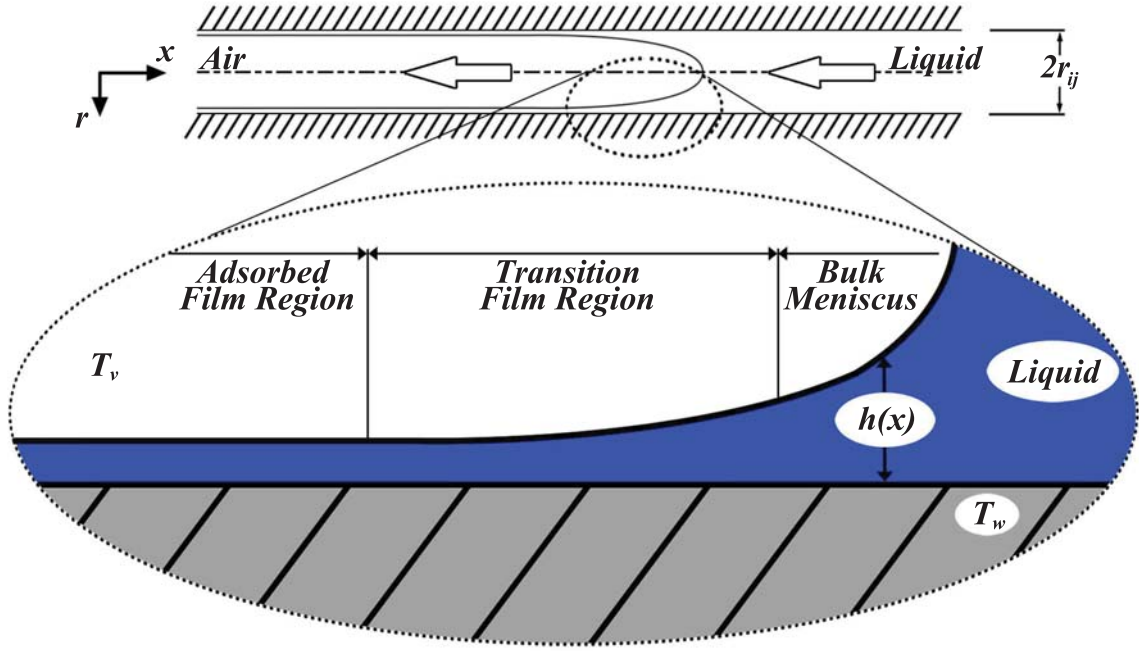


Figure 2.1: Schematic depicting the extended evaporating meniscus including the adsorbed film, transition film, and bulk meniscus.

The geometry for the modeling domain extends along the substrate as seen in Figure 2.1. The non-evaporating adsorbed film region is the x origin and the centerline of the pore being the radial origin making the film thickness along the interface $r_{ij} - h(x)$. The modeling domain then extends from the adsorbed film region to the bulk meniscus. To keep the model in a steady-state mode the mass flux across the interface due to evaporation from the transition film transition region is assumed to be replenished by the fluid in the bulk meniscus continuously during each time step. This keeps the curvature in this region constant

throughout each time step. Figure 2.2 illustrates the conservation of mass for a differential element and the replenishment of the evaporated fluid.

The capillary pressure is typically determined by the Laplace-Young equation (Equation 3.2). To accurately model the pressure balance in this transition film region a modified version of the Laplace-Young equation is to be used. With the addition of the intermolecular interaction forces through the disjoining pressure term the Augmented Laplace-Young equation is obtained⁷¹.

$$p_v - p_l = \sigma K + \Pi \quad (2.2)$$

The variable K is the curvature of the liquid-vapor interface in all planes. In this case since there are two planes of curvature the variable has two curvatures, one due to the radius of the pore and the other because of the meniscus.

$$K = \left(\frac{1}{r_{ij} - h} \right) (1 + h_x^2)^{-1/2} + h_{xx} (1 + h_x^2)^{-3/2} \quad (2.3)$$

In the curvature equation h , h_x and h_{xx} are the liquid film thickness and its first and second derivatives respectively.

The disjoining pressure of a flat, perfectly wetting ($\theta = 0$) liquid surface is

$$\Pi = \frac{A}{h^3} \quad (2.4)$$

Where A is the dispersion constant set to 3.11×10^{-21} Joules for water per Wayner Jr. et al.⁸⁹. Other formulations for the disjoining pressure term have been explored for water through the literature. Holm and Goplen⁹⁰ developed a disjoining pressure for polar water

$$\Pi = \rho_l R_g T_i \ln(mh(x)^n) \quad (2.5)$$

Where $m = 1.49$ and $n = 0.0243$. This formulation is for polar water on quartz. To change this model of disjoining pressure for a different substrate/fluid pairing another set of coefficients m and n would need to be experimentally determined. Unfortunately no set of coefficients exists in the literature capable of modeling the higher contact angles and materials seen within the PTL.

For this work a non-zero contact angle and a smaller radius of curvature are more accurate depictions of the physical scenario and are required to capture the appropriate disjoining pressure in these high contact angle micropores. Many evaporating film models have been presented in the literature^{61,65,66,91–94}, but few models consider non-zero contact angles. Wu and Wong⁹⁵ present a model that accounts for both, a non-zero contact angle and the higher radius of curvature.

$$\Pi = -\frac{B}{h^3} (\theta^4 - h_x^4 + 2hh_x^2 h_{xx}) \quad (2.6)$$

In this formulation instead of using a dispersion constant, a material constant is used which

is a function of the liquid properties.

$$B = \frac{3\pi n_f^2 \beta_{ff} (1 - \phi)}{16} \quad (2.7)$$

The terms n_f , ϕ , and β_{ff} are the number density of the fluid component, the relative humidity of the air and the strength of van der Waals potentials, respectively. For coefficients on the disjoining pressure term, values published by Hiemenz and Rajagopalan⁹⁶ were used resulting in a number density of $n_f = 33.3679 \times 10^{27}$ and a van der Waals strength potential of $\beta_{ff} = 2.1 \times 10^{-77} J \cdot m^3$. In this formulation the disjoining pressure term is dependent on the macro contact angle with by accepting the film curvature and measured contact angle as inputs. This allows for the potential expansion of this model by implementing a stochastic distribution of contact angles that could be applied to the individual pores thus accounting for the effects a changing contact angle distribution has on evaporation rates within the PTL.

The internal flows of the liquid are modeled using the lubrication approximation of the Navier-Stokes momentum equations in polar coordinates to accommodate for the curvatures created in both the cross-pore and parallel-pore directions.

$$\frac{1}{r} \frac{\partial}{\partial r} \left(r \frac{\partial u}{\partial r} \right) = \frac{1}{\mu_l} \frac{dp_l}{dx} \quad (2.8)$$

Here μ_l is the liquid phase viscosity, r is the distance from the pore centerline to the liquid

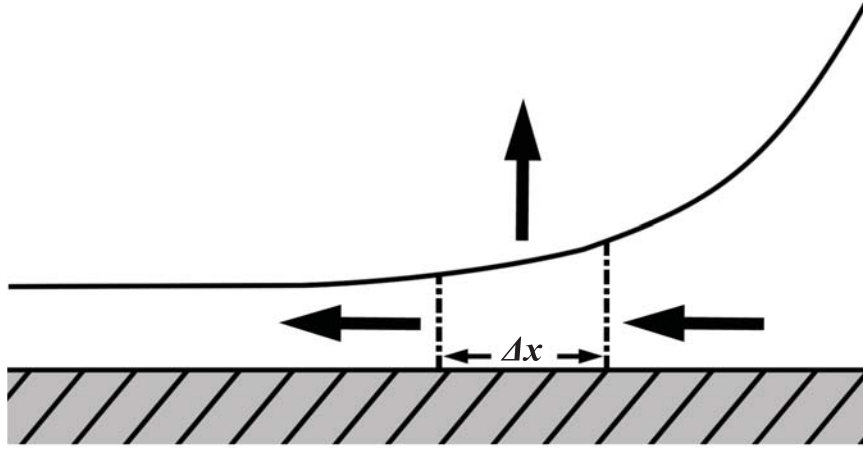


Figure 2.2: The conservation of mass applied to a differential volume of the film meniscus.

vapor interface, dp_l/dx is the driving pressure gradient and u is the fluid velocity. An exact solution to this partial differential equation can be obtained when applying the no slip boundary condition at the wall where the radial position is set to r_{ij} the pore radius. The free surface boundary condition is applied at the liquid-gas interface which is determined by the pore radius minus the film thickness (h) and balances the viscous terms with the surface tension terms.

$$\text{at } r = r_{ij}, u = 0 \quad (2.9)$$

$$\text{at } r = r_{ij} - h, -\mu \frac{\partial u}{\partial r} = \frac{d\sigma}{dx} \quad (2.10)$$

Applying the boundary conditions and solving yields

$$u(r) = \frac{1}{4\mu_l} \frac{dp_l}{dx} r^2 + C_1 \ln r + C_2 \quad (2.11)$$

where the constants of integration are

$$C_1 = -\frac{1}{\mu_l} \frac{d\sigma}{dx} (r_{ij} - h) - \frac{1}{2\mu_l} \frac{dp_l}{dx} (r_{ij} - h)^2 \quad (2.12)$$

$$C_2 = -\frac{1}{4\mu_l} \frac{dp_l}{dx} r_{ij}^2 - C_1 \ln r_{ij} \quad (2.13)$$

By integrating equation 2.11 across a liquid cross section the mass flux feeding the evaporation can be determined.

$$\Gamma = \int_{r_{ij}-h}^{r_{ij}} \rho_l \left[\frac{1}{4\mu_l} \frac{dp_l}{dx} r^2 + C_1 \ln r + C_2 \right] 2\pi r dr \quad (2.14)$$

Evaluating the definite integral in equation 2.14 results in the mass flux over a cross sectional area in the fluid phase that is in terms of the pore radius (r_{ij}), the film thickness and the physical properties of water (μ_l , ν_l , ρ_l). For ease of handling this complex equation it has been broken up into several variables (F_{1-5}) that are functions of constant material properties and pore dimensions.

$$\Gamma = F_1 \frac{dp_l}{dx} + F_2 \frac{d\sigma}{dx} \quad (2.15)$$

where

$$F_1 = \frac{\pi}{8\mu_l} \left\{ \left[r_{ij}^4 - (r_{ij} - h)^4 \right] - 4 (r_{ij} - h)^2 F_5 \right\} + \pi \rho_l (2r_{ij}h - h^2) F_3 \quad (2.16)$$

$$F_2 = -\frac{\pi}{v_l} (r_{ij} - h) F_5 + \pi \rho_l (2r_{ij}h - h^2) F_4 \quad (2.17)$$

$$F_3 = \frac{1}{2\mu_l} \left[(r_{ij} - h)^2 \ln r_{ij} - \frac{r_{ij}}{2} \right] \quad (2.18)$$

$$F_4 = \frac{1}{\mu_l} (r_{ij} - h) \ln r_{ij} \quad (2.19)$$

$$F_5 = r_{ij}^2 \left(\ln r_{ij} - \frac{1}{2} \right) - (r_{ij} - h)^2 \left[\ln (r_{ij} - h) - \frac{1}{2} \right] \quad (2.20)$$

The simplified energy balance for the liquid is described by equation 2.21, with k_l being the thermal conductivity of the liquid phase.

$$k_l \frac{\partial}{\partial r} \left(r \frac{\partial T}{\partial r} \right) = 0 \quad (2.21)$$

The boundary conditions used to solve this differential equation include a constant wall temperature (T_s) and a Neumann condition constant heat flux at the free surface which accounts for conductive heat loss as well as the energy lost due to the enthalpy of vaporization.

$$\text{at } r = r_{ij}, \quad T = T_s \quad (2.22)$$

$$\text{at } r = r_{ij} - h, \quad k_l \frac{dT}{dr} = \dot{m}_{evp} h_{fg} \quad (2.23)$$

Here the evaporation rate is determined by using a form of the Hertz-Knudsen-Schrage equation⁶³

$$\dot{m}_{evp} = a(T_i - T_v) + b(p_l - p_v) \quad (2.24)$$

where T_i is the liquid-gas interface temperature, T_v is the vapor temperature, and coefficients a and b are

$$a = \alpha \left(\frac{M_w}{2\pi R_g T_i} \right)^{1/2} \left(\frac{p_v M_w h_{fg}}{R_g T_v T_i} \right) \quad (2.25)$$

$$b = \alpha \left(\frac{M_w}{2\pi R_g T_i} \right)^{1/2} \left(\frac{V_l p_v}{R_g T_i} \right) \quad (2.26)$$

Integrating equation 2.21 from the wall (r_{ij}) to the liquid-gas interface ($r_{ij} - h(x)$) at each discrete x location results in an interfacial temperature equation 2.28 that is a function of the x -position along the transition film.

$$T_i = -\frac{h_{fg}}{k_l} (r_{ij} - h) \ln \left(\frac{r_{ij}}{r_{ij} - h} \right) \dot{m}_{evp} + T_s \quad (2.27)$$

Now substituting the augmented Laplace-Young equation (equation 2.2) into the evaporative flux equation (equation 2.24) and solving equation 2.27 for the interfacial temperature:

$$T_i = \frac{T_s + G_1 b (\Pi + K \sigma) + T_v a G_1}{a G_1 + 1} \quad (2.28)$$

where

$$G_1 = \frac{h_{fg} (r_{ij} - h) \ln \left(\frac{r_{ij}}{r_{ij} - h} \right)}{k_l} \quad (2.29)$$

Differentiating the augmented Laplace-Young equation with respect to the distance from the adsorbed film region results in the liquid pressure gradient.

$$\frac{dp_l}{dx} = -\sigma \frac{dK}{dx} - K \frac{d\sigma}{dx} - \frac{d\Pi}{dx} \quad (2.30)$$

Finally by replacing the curvature terms from equation 2.30 with the definition of the curvature in equation 2.3 and taking the derivative with respect to the distance from the adsorbed film region the equation for the film thickness can be obtained. With the solution to the film thickness other parameters such as the interface temperature, liquid pressure, curvature, evaporation fluxes, disjoining pressures and liquid velocity profiles can be solved as

they have been written in terms of film thickness.

$$h_{xxx} - \frac{3h_{xx}^2 h_x}{1 + h_x^2} - \frac{h_{xx} h_x}{r_{ij} - h} + \frac{h_x (1 + h_x^2)}{(r_{ij} - h)^2} + \frac{\gamma}{\sigma} \left\{ \frac{1 + h_x^2}{r_{ij} - h} + h_{xx} \right\} \frac{dT}{dx} + \frac{1}{\sigma} (1 + h_x^2)^{1/2} \left(\frac{dP_l}{dx} + \frac{d\Pi}{dx} \right) = 0 \quad (2.31)$$

The film thickness equation (equation 2.31) is solved using a 6th order Runge-Kutta-Fehlberg method which is implemented in FORTRAN 95. The solution to the conservation of mass equations, specifically the interfacial mass transfer, is integrated over the liquid interface within the pore. Despite this formulation assuming a constant evaporation rate over the bulk meniscus, it is an adequate representation of evaporation since the internal temperatures of PTL rarely exceed 90°C. At these temperatures it is said that between 50% to 95% of the total evaporation takes place in the transition film region^{63,70,77}.

The uneven evaporation across the liquid interface is why adding such a computationally expensive method for modeling evaporation in the porous network is necessary. The evaporation modeling that is discussed in Section 1.1.2.3 are referred to as diffusive models herein. With the diffusive evaporation model the surface area of the cross-section of the pore is what controls how much evaporation takes place thus assuming a constant evaporation rate across the entire liquid surface and neglecting the increased liquid surface area due to the interface curvature. In the transition film evaporation model the contact line area is

the primary determining factor. This subtle difference increase the total area of the liquid-gas interface and some cases can create very large differences in the mass of evaporated liquid. For example Figure 2.3 shows the net evaporation rates from both the transition film and diffusive evaporation models for a liquid interface surface area of $\pi \times 10^{-8} m^2$ divided amongst a varying amount of pores with radii ranging from $10\mu m$ to $1\mu m$.

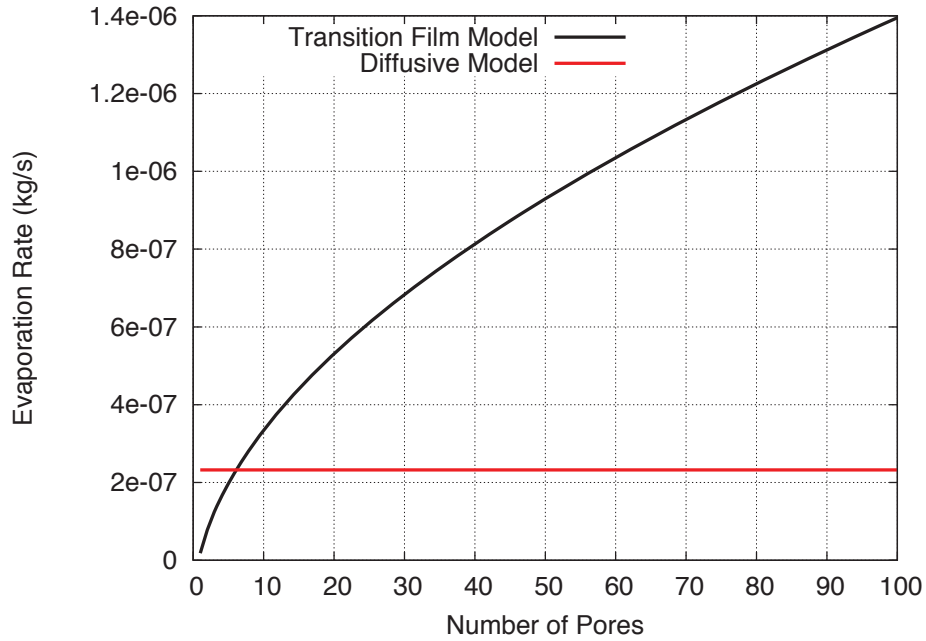


Figure 2.3: Evaporation rates for the transition film and diffusive evaporation models from $\pi \times 10^{-8} m^2$ surface area liquid interface divided into a varying number of pore radii ranging from $10\mu m$ to $1\mu m$.

As the number of pores a constant liquid-gas interface surface area is divided into increases, the contact line length to surface area ratio is increased, therefore increasing the evaporation rates calculated by the transition film model. For the diffusive modeling approach the

increased liquid-gas interface area is not accounted for thus the overall evaporation rates are independent of the number of pores a liquid-gas interface is divided into. Figure 2.3 illustrates that for a constant liquid-gas interface area evaporation rates will increase, the increased evaporation rates are due to the higher evaporation rates near the liquid-solid interface. The transition film model accounts for these effects while the diffusive modeling approach does not. With the transition film evaporation model there is a greater accuracy, especially when the pore size varies making this type of formulation more robust for modeling a porous media with non constant pore radii.

Figure 2.3 shows the evaporation rates as an evaporating surface is split into equally sized pores. With the increasing number of pores the evaporating surface is split into the evaporation rates increase for the transition film model while the diffusive model remains constant. This is due to the inclusion of contact line effects in the transition film model. The diffusive evaporation model becomes less accurate as the pore size is reduced due to the increase in the contact line to surface area ratio, the larger this ratio the less accurate the diffusive model becomes. For every set of operating parameters a pore size, or contact line length to surface area ratio exists, the diffusive modeling approach becomes such a significant source of error when trying to determine the liquid phase distribution and can be misleading when determining the level of flooding the PTL experiences for a given set of operating parameters.

2.2 Evaporation Rate Boundary Conditions

The evaporation rate is determined through many variables that all rely on the solution to the film thickness equation. At the origin the initial film thickness is found using a Newton-Raphson iteration method on equation 2.28 to solve for h_0 with the interface temperature (T_i) set to the wall temperature (T_s). This solution has a strong dependence on the disjoining pressure. A small perturbation ($1 \times 10^{-14}m$) is applied to the initial film thickness to avoid a constant film thickness solution. The slope, or first derivative of the film thickness, is set to zero at the non-evaporating adsorbed film region. Again a small perturbation is also applied. Finally the second derivative of film thickness is also set to zero. The solution to the film thickness model, equation 2.31, is very sensitive to the initial perturbation in the first derivative of film thickness. Thus the Newton-Raphson iterative technique is again applied to solve for the initial perturbation of the film thickness slope that will result in a stable solution that matches the specified contact angle in the bulk meniscus region. As stated earlier the routine is solved using the Runge-Kutta-Fehlberg 6th order solver. This solver was chosen because non-dimensionalization was not an option due to some of the complex models for disjoining pressure.

2.3 Transition Film Evaporation Results

The transition film evaporation model that was based off the work by Wee et al.⁸⁴ and was modified to accept a non-zero contact angle. The results match the model presented in Wee et al.⁸⁴ for the zero degree contact angle cases. This modification allows for the higher contact angles seen in the PTL to be considered while calculating the evaporation rates in each pore. Figure 2.6 demonstrates how the evaporative mass flux changes with the contact angle. To obtain the evaporation rate, these mass fluxes must be integrated around the perimeter the pore.

The results for the film thickness of a fluid evaporating at 80°C with a 90° contact angle can be seen in Figure 2.4. When compared to the results of the evaporative fluxes in Figures 2.6 and 2.7 the region with the highest curvature can be seen to have the highest evaporative fluxes.

Figure 2.5 shows the interface temperature at the liquid-gas interface as calculated by the transition film model. The interface temperature begins at the substrate temperature and as the film thickness begins to grow the interface temperature can be seen to asymptote to the vapor temperature. The high temperature is seen as the film thickness is close to that of the adsorbed film thickness due to the proximity of the heated substrate. As the film thickness grows the temperature drop that can be seen is due to the conductive resistance of the fluid.

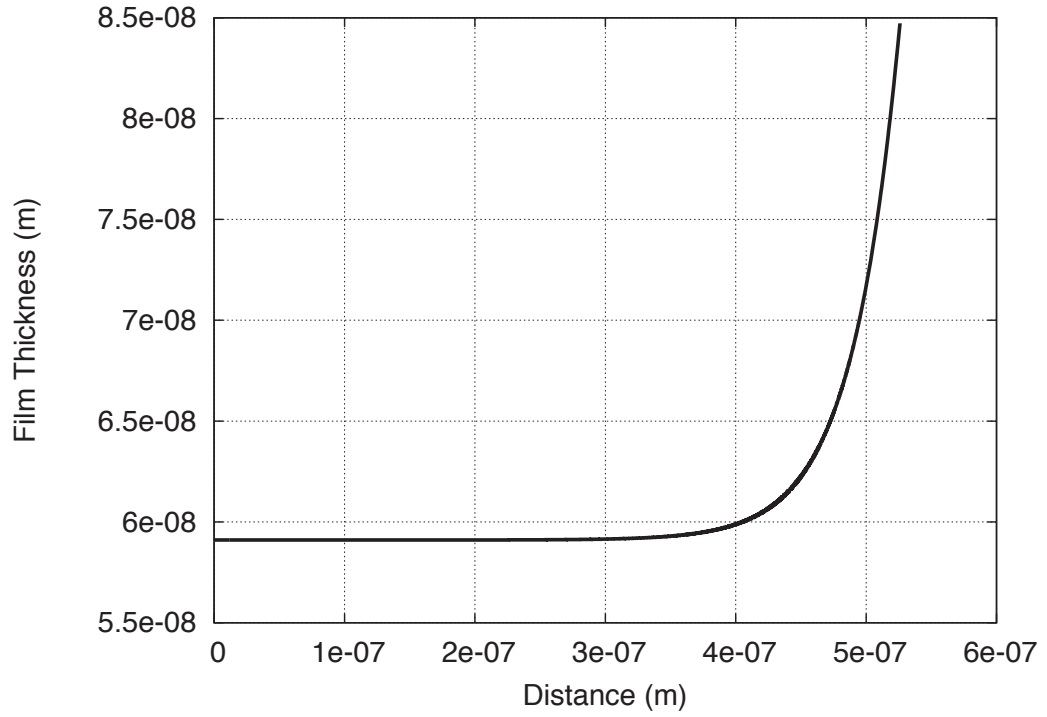


Figure 2.4: Film thickness for the $\theta = 90^\circ$ case as modeled by the transition film model.

For the $\theta = 90^\circ$ contact angle case in Figure 2.6, a constant evaporative mass flux is seen over the bulk meniscus region. This is due to the higher curvature present in bulk meniscus due to the higher contact angles. As the temperature increases the evaporative fluxes found in the bulk meniscus presents itself at the lower contact angle cases. These results in the case of a zero degree contact angle match the work performed by Wee et al.⁸⁴ exactly.

Figure 2.7 shows the evaporative mass flux for the varying contact angle at 80°C . As expected the mass fluxes are higher, and a constant bulk evaporative flux is beginning to

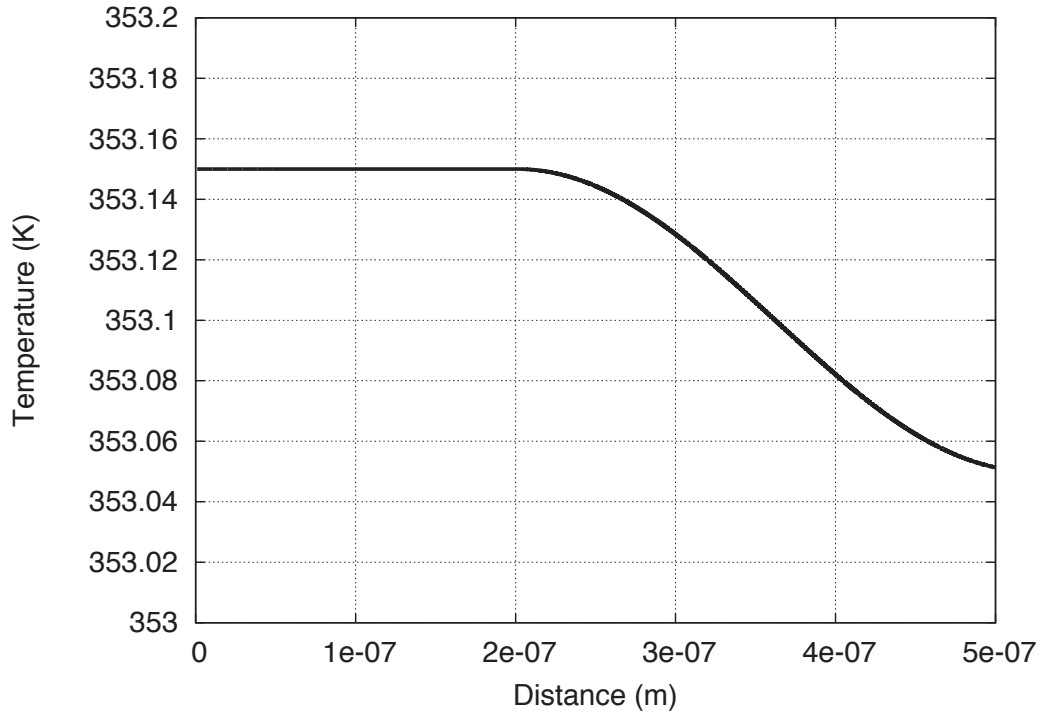


Figure 2.5: Interface temperature for the $\theta = 90^\circ$ and $T_s = 80^\circ\text{C}$ case as modeled by the transition film model.

appear at lower contact angles when the contact line length remains the same. This has been demonstrated experimentally in the literature, especially when examining pore evaporation⁹⁷. Plawsky et al.⁹⁸ demonstrate that as the contact angle decreases the transition film region lengthens providing a larger area for evaporation. The discontinuity that appears near the peak of the evaporative mass flux plots is seen for all of the evaporation cases involving water. The polarity of water causes the disjoining pressure term to drop abruptly, changing approximately five orders of magnitude over 150nm . As the disjoining pressure approaches zero the mass flux exhibits a discontinuity. For example in Figure 2.7,

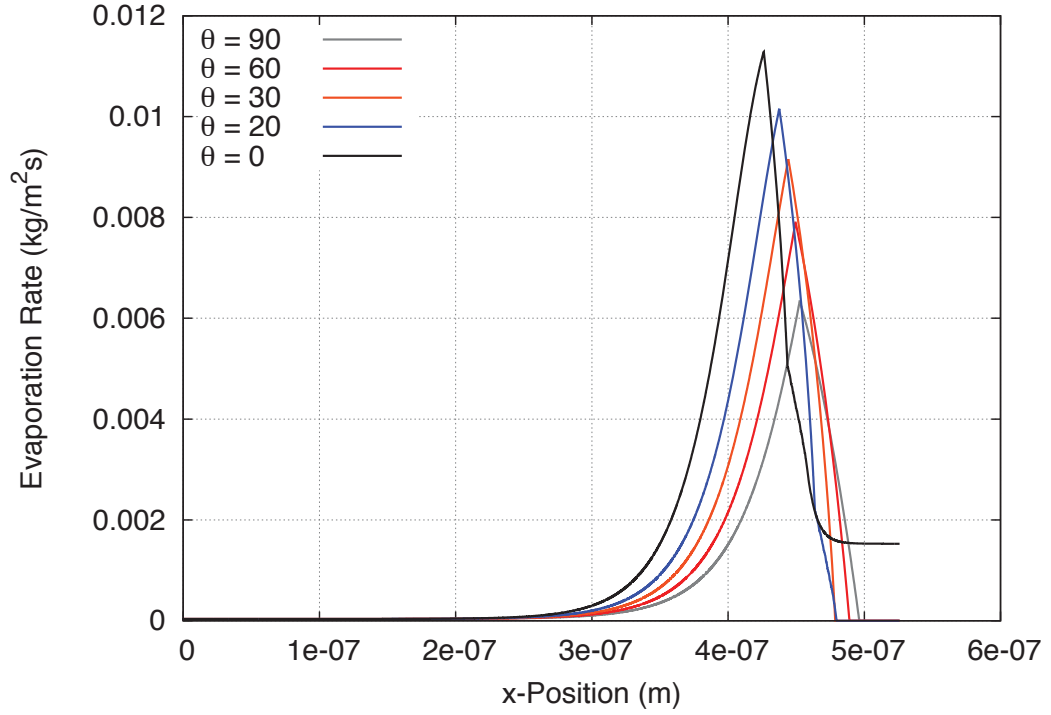


Figure 2.6: Transition film evaporation mass fluxes at varying contact angles at 70°C

the end of the transition film region (the point at which the disjoining pressure reaches zero) for the $\theta = 90^{\circ}$ case is located at $4.07 \times 10^{-7} \text{ m}$.

Evaporation rate versus contact angle data found in the literature that explores evaporation rates in wetting/non-wetting scenarios use a heated substrate sessile drop evaporation experiment and must be read with caution^{99–101}. If the contact line lengths for the different contact angle cases are not the same several parameters will change aside from the contact angle that will affect the evaporation rate. The typical sessile drop experiment for varying

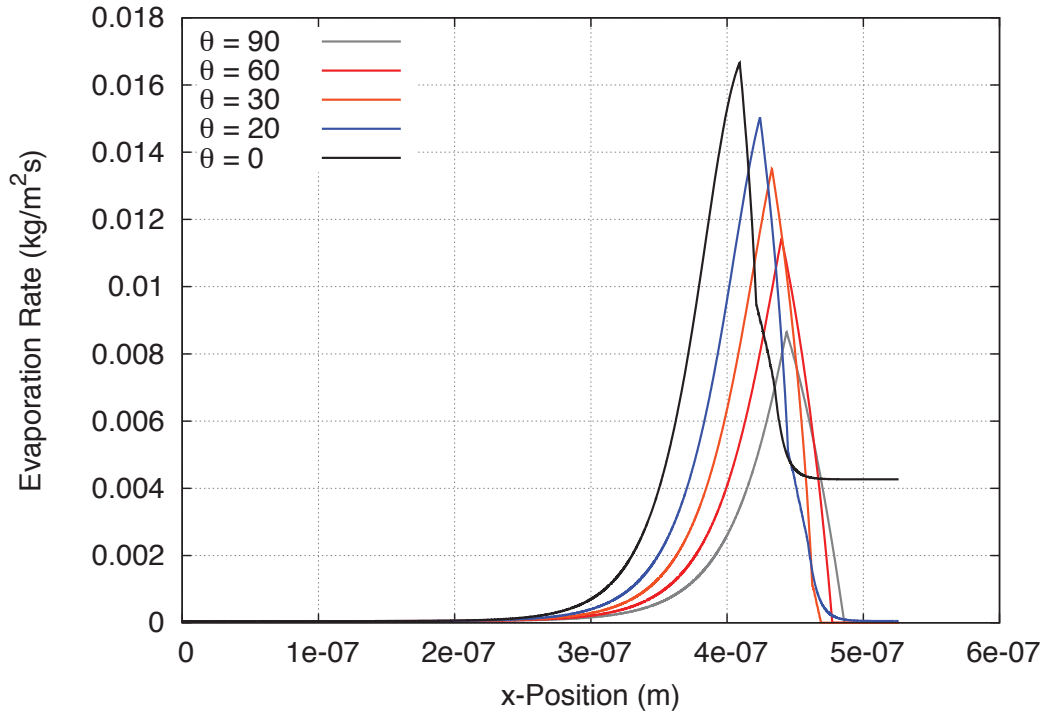
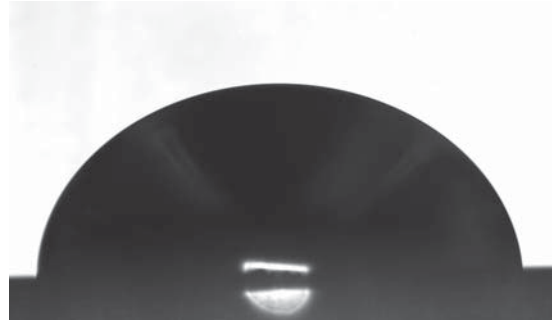


Figure 2.7: Transition film evaporation mass fluxes at varying contact angles at 80°C

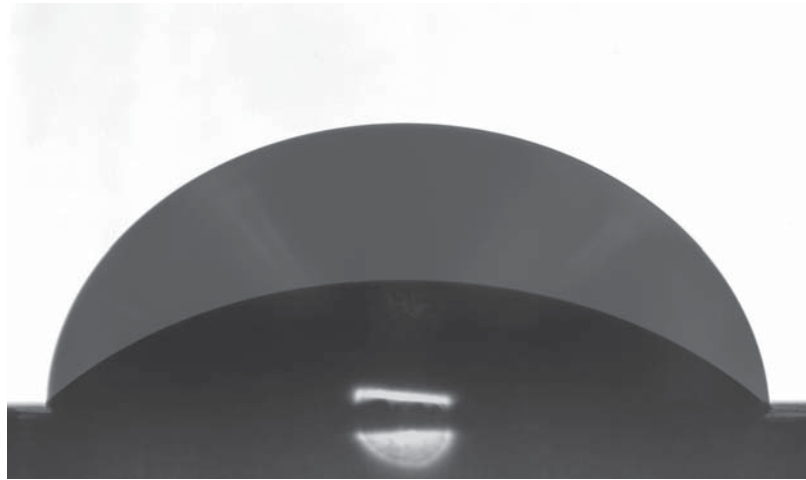
contact angle will compare two drops of the same volume, for higher contact angle cases the wetted area and contact line length will be lesser than the case of the lower contact angle. This will produce lower evaporation rates in the high contact angle case because of a shorter contact line length, and a smaller wetted area. Having a smaller wetted area will allow for less heat transfer from the substrate to the sessile droplet and will not be an accurate comparison of the two evaporation rates the fluids will experience inside a pore. In a pore the contact line length remains constant with respect to the surface area¹⁰². This is problematic because the results showing different evaporation rates for different contact



(a) Low contact angle experiment



(b) High contact angle experiment



(c) High and low contact angle images superimposed

Figure 2.8: Images from the evaporation rate validation experiment with various contact angles. (a) illustrates the lower contact angle validation experiment, (b) shows the higher contact angle experiment and (c) is the two sessile drops superimposed showing that both experiments at the same contact line length.

angles do not consider the changes in surface area, contact line length and the higher heat transfer rates from the larger wetted area. Figure 2.8 shows an example of two sessile drops superimposed with the same contact line length as their radii are the same. In most cases the experimentation involves two sessile drops with equivalent masses but different contact angles and this normally results each droplet having a different contact line length. The work by Picknett and Bexon¹⁰³ examines the constant contact line case with their constant

contact area evaporation mode and find that for the cases with a higher interface curvature produce higher evaporation rates.

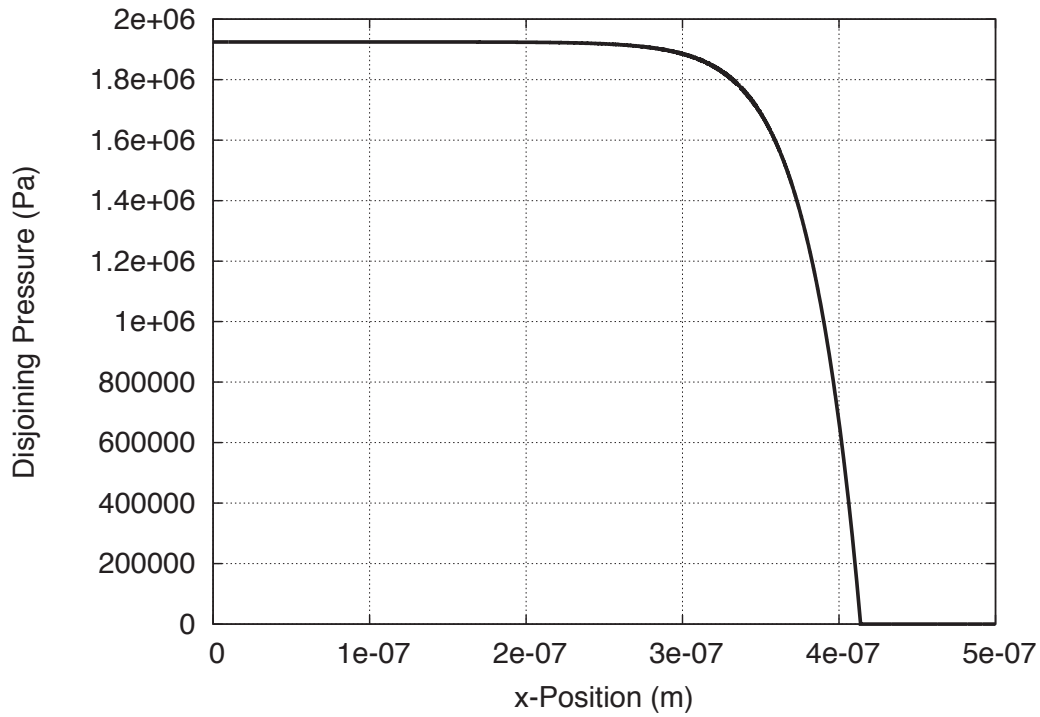


Figure 2.9: Disjoining pressure with a contact angle of 90° and at 80°C wall temperature.

The disjoining pressure, which is responsible for the discontinuity in the mass flux plots is shown in Figure 2.9. As the film thickness increases the disjoining pressure drops to zero and this term no longer affects the evaporative mass flux, leaving only the curvature terms, temperature and relative humidity of the vapor to determine the mass flux. At lower temperatures and higher relative humidities the bulk meniscus will experience reduced evaporation rates. When higher temperatures and lower relative humidities are present the bulk

meniscus will see a constant evaporative mass flux over the entire pore.

The consideration of the transition film evaporation is what sets this model apart from the others found in the literature using a diffusive style evaporation model. The transition film model is what allows the pore network model results presented in the next section to predict the liquid water distribution accurately for any mean pore size and any pore distribution. Something that cannot be obtained with a standard diffusive evaporation model. The upcoming sections will compare the results from the pore network model at the extreme cases, which will show the conditions that create the largest and smallest differences between these two evaporation models.

2.4 Transition Film Evaporation Validation

To capture the evaporation rates of a non-zero contact angle fluid, a heated substrate sessile drop configuration with passive humidity control was used. The experimental setup and procedure follow what has been outlined in Konduru¹⁰⁴. A Köhler illumination of the sessile droplet was used in conjunction with a microscope to accurately determine the liquid-air interface of the droplet. The experimental setup utilizes an Axisymmetric Drop Profile Analysis (ADPA) to fit theoretical drop profiles to a drop edge obtained using images^{104,105} which can be seen in figure 2.10.

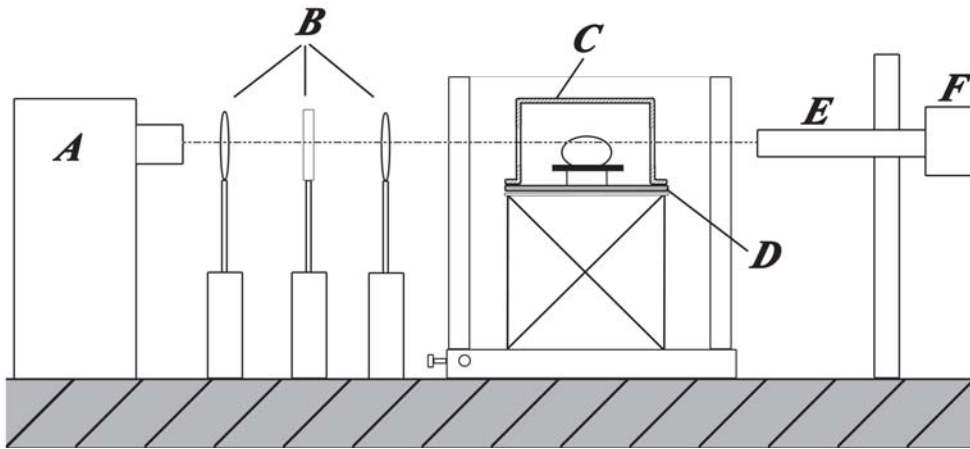


Figure 2.10: Diagram of the experimental setup used to collect the evaporation data from non-zero contact angles. **A** is the Köhler light source, **B** is the lens array responsible for columnating the light source, **C** is the enclosure responsible for maintaining a constant air temperature and humidity, **D** is the heating plate, **E** is the long microscope lens and **F** is the Polnix CCD which records the images.

A set of experiments were run at varying temperatures that captured images of an evaporating sessile droplet at short time intervals for varying temperatures. The relative humidity was held at $20\% \pm 2.1\%$ for all of the simulations. The relative humidity was controlled by a steady flow of distilled water into a wick within the environmental enclosure. The humidity was then monitored with VWR digital hygrometer. The flow rates of the syringe pump supplying the water to the system were set to the lowest value as the water evaporating from the droplet itself was nearly enough to maintain a 20% relative humidity. This control method was without feedback and thus resulting in the error of $\pm 3\%$ on the relative humidity measurements. Figure 2.11 demonstrates one of the images acquired by the apparatus, these images are timed and used to calculate evaporation rates that are then compared to evaporation rates estimated by the transition film evaporation model. Once captured the

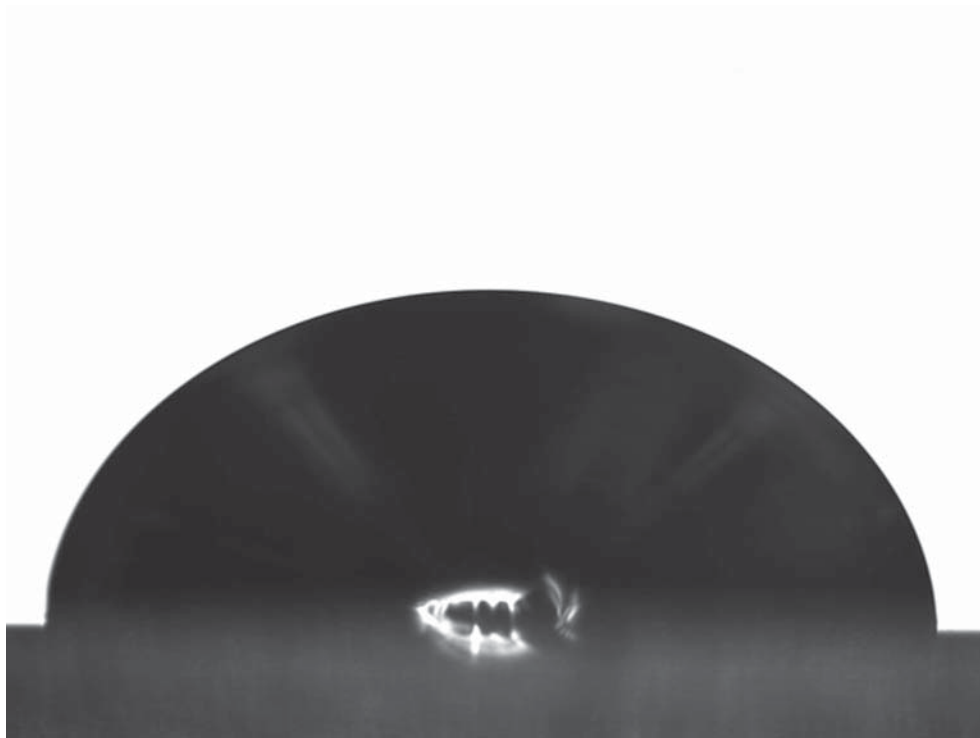


Figure 2.11: An image from the 57°C non-zero contact angle evaporation experiment illustrating the images capture and analyzed for the calculation of mass transfer rates.

images are post processed using a software developed by Konduru¹⁰⁴ to determine the remaining mass in the droplet after each image thus allowing for the calculation of mass loss from image to image.

The initial contact angle and wetted radius of the droplet (outputs of the ADPA code) are then fed into the transition film evaporation model. The transition film evaporation model will then calculate an estimated mass loss for the time between images and predict what the new mass of the droplet should be at the next image. The calculated mass from the transition film model is then used to calculate a laplacian curve that plots the new drop profile. From this profile the wetted radius can be calculated and fed back into the

transition film model for the next time step. Figure 2.12 shows an example of the predicted drop mass from the transition film evaporation model compared to the actual drop mass which was calculated by the ADPA code.

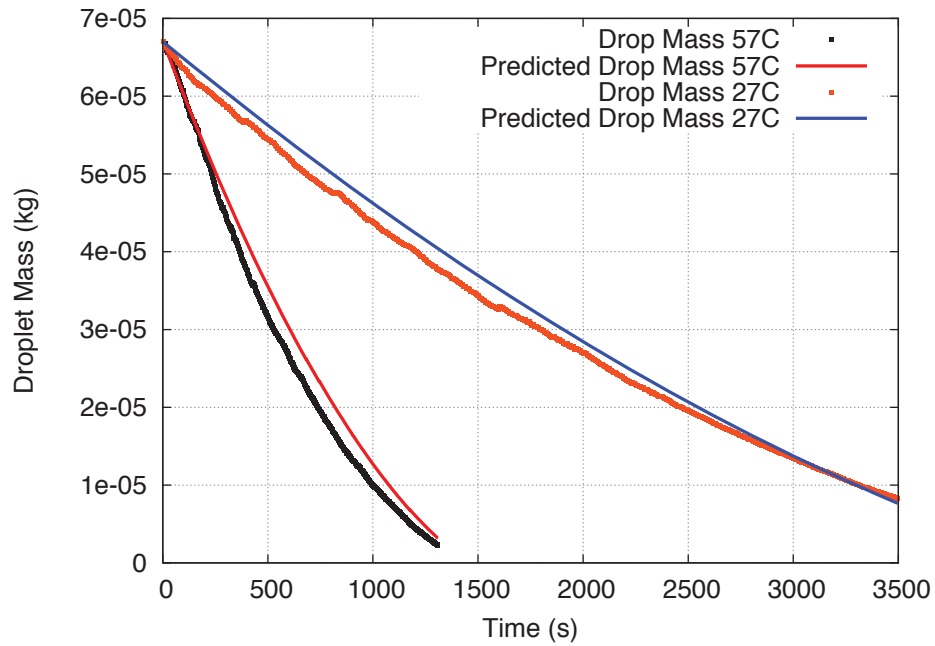


Figure 2.12: A comparison of the experimental mass of an evaporating non-zero contact angle deionized water droplet to the mass estimated by the transition film evaporation model over the duration of the experiment. Both cases started with the same initial droplet mass.

Figure 2.12 demonstrates how closely the transition film evaporation model is capable of predicting the evaporation rates. In the actual experiment there are circulating flows within the sessile droplet that enhance its evaporation rate^{106–109}, these are neglected in the transition film model thus causing the predicted evaporation rates to be slightly slower than that of the physical droplet. The transition film evaporation model prediction is shown for

two temperature cases, 27°C and 57°C . Both of these experiments show that the transition film evaporation model is a good predictor of the evaporation rates of a sessile droplet evaporating in 20% relative humidity. The large change in temperature between the two experiments shown illustrates the models ability to adapt to varying temperatures.

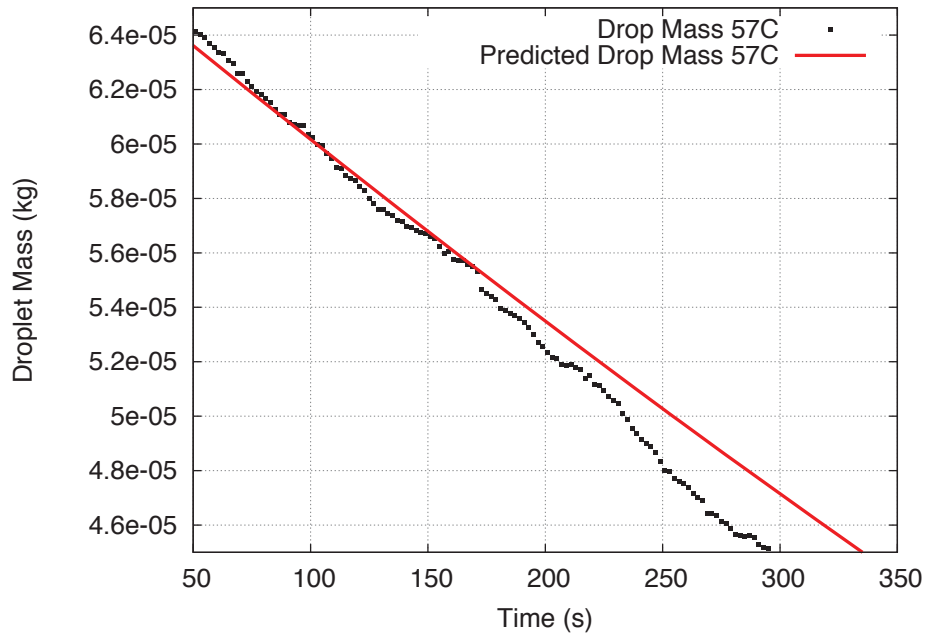


Figure 2.13: Close-up of the pinning/depinning event 220 seconds into the 57°C validation test.

Figures 2.13 and 2.14 show a closer look at an area where there is a sudden drop in droplet mass. In Figure 2.13 at 220 seconds into the experiment the change in curvature is due to the depinning of the contact line on the sessile drop. The sudden change in curvature the depinning caused is also partly responsible for the deviation in the model prediction and the experimental data. This pinning/depinning can be seen three times in the 27°C case at

375, 805 and 1540 seconds and Figure 2.14 shows the first of these events.

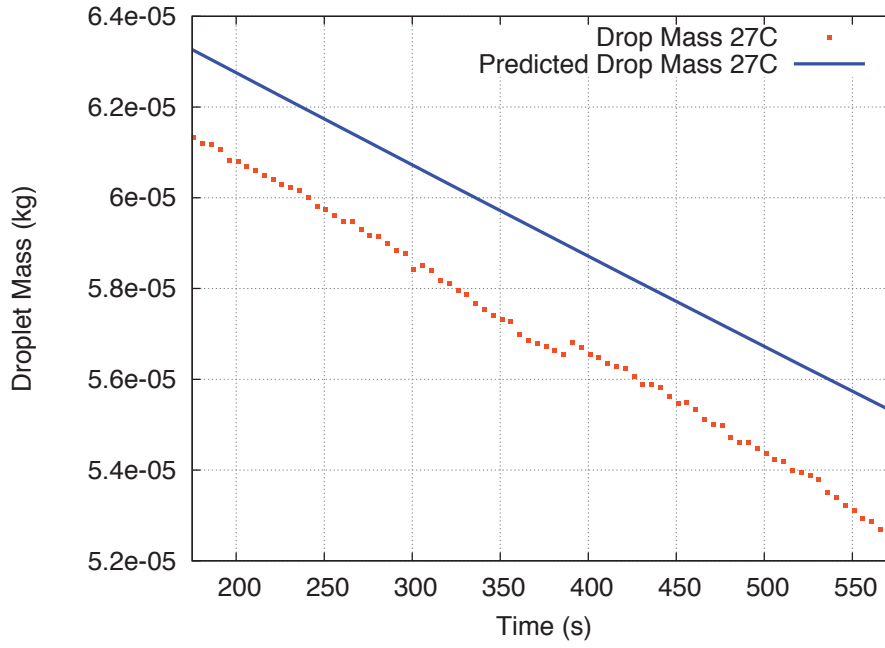


Figure 2.14: Close-up of a pinning/depinning event 375 seconds into the 27°C validation test.

To determine the mass of the drop first the volume is determined by fitting a Laplacian curve to the interface. The Laplace equation which has been derived for a pore earlier is now presented in terms of a sessile droplet, this formulation takes into account the gravity forces and the surface tension forces¹⁰⁴.

$$\left(\frac{1}{r_1} + \frac{1}{r_2} \right) \sigma = \Delta p \quad (2.32)$$

The pressure term is defined as the sum of all the pressures acting on the droplet and this

can be described adequately to generate a film profile by specifying the gravitational and surface tension based terms. In the cases where the Bond number (equation 2.1) becomes much less than zero the gravitational terms become negligible.

$$\Delta p_g = \rho_l g z \quad (2.33)$$

$$\Delta p_\sigma = \frac{2\sigma}{r_a} \quad (2.34)$$

Combining the pressure terms and the Laplace equation results in an equation that can be used to predict the drop shape and more importantly its volume and mass.

$$\left(\frac{1}{r_1} + \frac{1}{r_2} \right) \sigma = \rho_l g z + \frac{2\sigma}{r_a} \quad (2.35)$$

Substituting for the radii of curvature their definitions with respect to arc lengths and tangents results in equations 2.36 and 2.37

$$\frac{1}{r_1} = \frac{d\theta}{dl_s} \quad (2.36)$$

$$\frac{1}{r_2} = \frac{\sin(\theta)}{x} \quad (2.37)$$

Here the term l_s is the arc length along the surface of the drop. Replacing the curvature terms back into the Laplace equation will yield the differential equation that needs to be

solved in order to predict the droplet interface.

$$\frac{d\theta}{dl_s} = \frac{2}{r_a} + \frac{\rho_l g z}{\sigma} - \frac{\sin(\theta)}{x} \quad (2.38)$$

The capillary constant is then used to scale this equation so that it can easily be solved using an ordinary Runge-Kutta fourth order solver.

$$c_a = \frac{\rho_l g}{\sigma} \quad (2.39)$$

Combining the square root of the capillary constant with the length terms in equation 2.38 the non-dimensional terms used in solving this differential equation are made.

$$X = x\sqrt{c_a} \quad (2.40)$$

$$Z = z\sqrt{c_a} \quad (2.41)$$

$$R_a = r_a\sqrt{c_a} \quad (2.42)$$

$$L_s = l_s\sqrt{c_a} \quad (2.43)$$

The new non-dimensional differential equation to be solved becomes

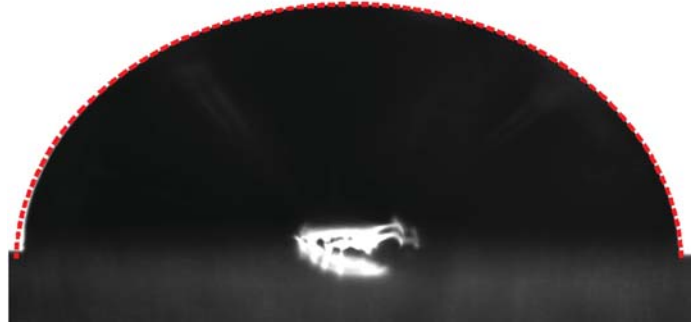
$$\frac{d\theta}{dL_s} = \frac{2}{R_a} + Z - \frac{\sin(\theta)}{X} \quad (2.44)$$

Where the geometrical relations shown in equation 2.45 and 2.46 that form the set of differential equations that are solved to determine the drop profile¹⁰⁴.

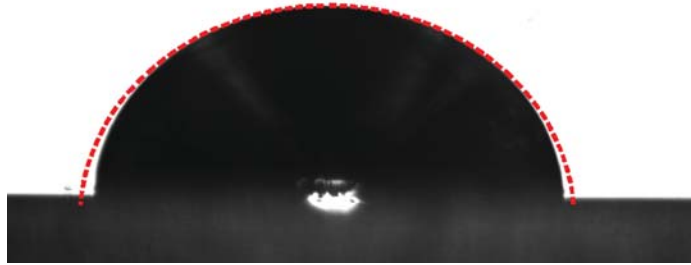
$$\frac{dX}{dL_s} = \cos(\theta) \quad (2.45)$$

$$\frac{dZ}{dL_s} = \sin(\theta) \quad (2.46)$$

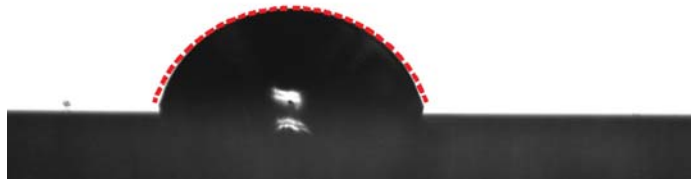
The shape, and therefore the volume of a sessile droplet can be solved. To make the appropriate comparisons the drop profile is solved with the new drop mass as an input calculating the new wetted radius which is used as an input for the transition film model. Figure 2.15 shows the predicted drop profile from the transition film model compared to the actual drop from the experiment. Much like figure 2.12, this is showing the difference in the size of the actual droplet and that estimated by the transition film evaporation model.



(a) $t = 0$



(b) $t = 600s$



(c) $t = 1180s$

Figure 2.15: An example of a sessile drop volume calculated by the transition film evaporation model compared to the actual drop volume of a sessile drop evaporating with a non-zero contact angle. (a) illustrates the estimated drop volume at $t = 0$ using the contact angle measurement technique, (b) and (c) are the estimated drop volumes using the transition film evaporation model at $t = 600s$ and $t = 1180s$ respectively.

2.5 Summary

In this chapter a validation was performed on the individual components of the overall model. For example the incorporation of the contact angle as well as the transition film

model were validated by evaporating sessile droplets at varying temperatures, relative humidities, and contact angles. The pore network model was validated primarily in the work of Medici¹¹⁰, however some visual, non-quantitative results have been presented to illustrate the pore network models capabilities. The evaporation rate data follows the theoretical values well. A direct validation of the half-cell model presented herein cannot be done with the equipment available, thus with the individual portions of the half-cell model validated the complete half-cell model is validated by the sum of its parts.

Chapter 3

Modeling Transport in the PTL

The primary objective of this research was to develop a kinetic model of phase change and incorporate that model into a pore-level transport model for fuel cell porous media. The pore-network model used herein originally developed as an isothermal model by Medici¹¹⁰ and was experimentally validated¹¹¹. This model was extended to include thermal transport using a diffusion-limited model for phase change¹¹².

This chapter describes this model and the subsequent modifications implemented in order to incorporate the kinetic model of phase-change. The main modifications are:

1. Treatment of solid phase distribution in the network domain (Sec. 3.3).
2. Variation of the thermal boundary condition at the channel interface (Sec. 3.5.3).

3. Incorporation of kinetic model of evaporation that accounts for surface wettability and interface curvature (Sec. 2).

The water transport through the porous transport layer (PTL) of a fuel cell are represented in this work as a rectangular grid network. This network is comprised of equal length pores with varying radii and is geometrically modeled as cylindrical tubes. The distribution of radii (r) are determined through the application of a Weibull function whose coefficients were tested and verified in Medici and Allen¹¹³. A modified version of the Poiseuille flow assumptions was used to include the effects of the two-phase flow and capillary pressures¹¹⁴.

3.1 The Porous Transport Layer Domain

The PTL is a complex array of teflonated carbon fibers joined together to create a porous, conductive, non-wetting medium for the transport of gases, liquids and electrons to and from the reaction sites in the catalyst layer. For this research the pores created in the PTL are modeled as cylindrical tubes of equal length. The pore size distribution used in the modelling is derived from the Weibull Probability Distribution Function (PDF) 3.1

$$f(x) = \left\{ \frac{k}{\psi} \left(\frac{x - \delta}{\psi} \right)^{(k-1)} \right\} \exp \left(- \frac{x - \delta}{\psi} \right)^k \quad (3.1)$$

where k is a scale factor, ψ is a shape factor, and δ is the minimum pore radius. These variables used as fitting parameters based on mercury standard porosimetry data from Gostick et al.¹¹⁵. Figure 3.1 shows several data sets of porosimetry data which can be used to

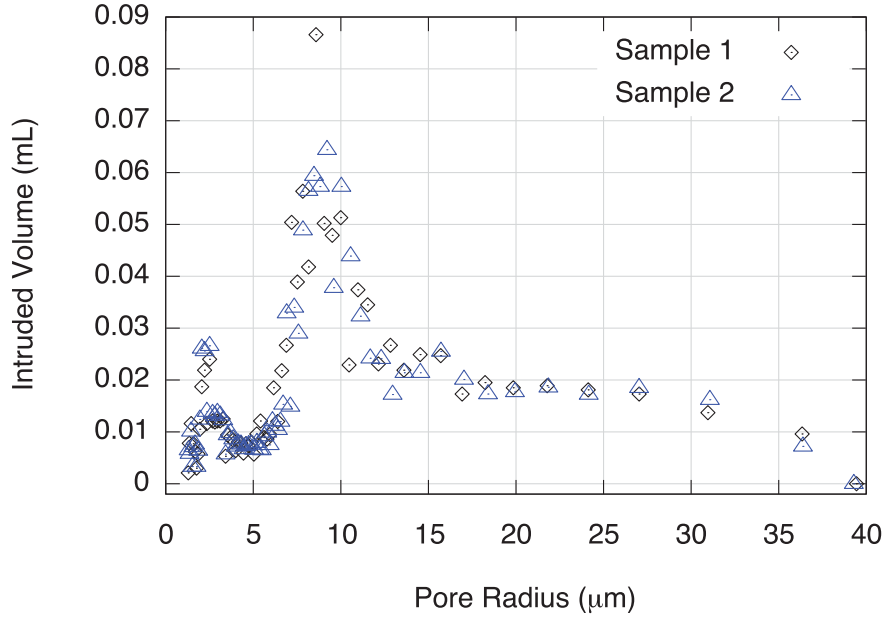


Figure 3.1: Mercury intrusion porosimetry data for two different 230 μm Ballard Material Products (BMP) PTL samples. The contact angle between mercury and the PTL was recorded at 145° . Data supplied by Ballard Power Systems.

calculate pore size distributions, porosities, pore area and the number of pores at each intrusion step. Mercury intrusion porosimetry (MIP) uses the concept of capillary pressures to determine pore size distributions in porous media. When an experiment is run, the pressure forcing the mercury into the porous specimen is increased allowed to equilibrate. The volume of intrusion and pressures are then recorded, this allows for the calculation of the average pore diameter that has been intruded during that step¹¹⁶. The pressures required to

flow into a pore of diameter D is determined by equation 3.2.

$$p_c = \frac{-(4\sigma \cos \theta)}{D}, \quad (3.2)$$

where p_c is the pressure applied to overcome the capillary pressure, σ is the surface tension, and θ is the contact angle between the mercury and the substrate, in this case a teflonated porous transport layer. Figure 3.1 illustrates this test performed on a Toray PTL with a thickness of $230 \mu m$ and an apparent contact angle of 145° , denoting a very non-wetting behavior. A peak of intrusion volume can be seen at the $9 \mu m$ pore radius which signifies that the majority of volume in this porous media exists at pores with a $9 \mu m$ radius.

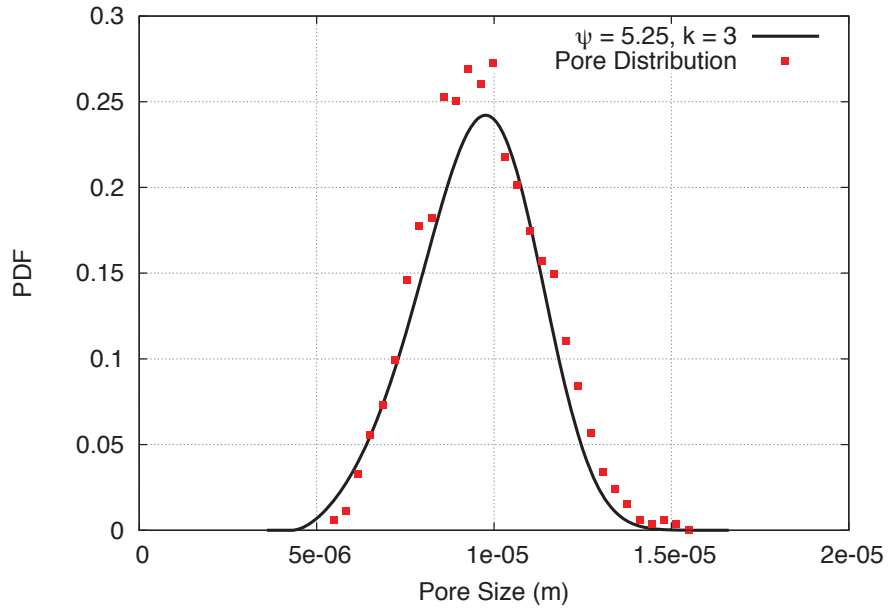


Figure 3.2: Weibull probability distribution function for the PTL pore size distribution with scale and shape factors of $\psi = 5.25$, and $k = 3$ respectively.

The experimental data from the MIP testing is then used to develop a statistical distribution of pore sizes for the PTLs computational domain. The Weibull function shown in Figure 3.2 is then applied to each of the pores in the domain to create a distribution that closely matches a realistic PTL.



Figure 3.3: An example of the 2-Dimensional porous network generated using the Weibull function using $\psi = 5.25$ and $k = 3$ as the coefficients.

Figure 3.3 shows an example of a PTL domain created for the porous transport network model used in this research. For this domain the injection occurs at a point at the center of the domain and is run for a simulated amount of time, as opposed to the in-cell simulation domain where the injection occurs over the entire catalyst layer - microporous layer boundary. In both domains the pores are assumed to be cylindrical and the average pore radius is $9.6\mu m$. These values match the experimental results as well as values for mean pore size distribution found in the literature^{37,39,111,113,117,118}.

The pores are represented in this network model according to the domain shown in Figure 3.3 and the schematic shown in Figure 3.4. A square grid of nodes is first created, each node is placed in equal intervals throughout the domain, the distance between two adjacent nodes is l . The pore radii are then determined by assigning the random output of a Weibull distribution that follows the aforementioned shape and scaling parameters ($\psi = 5.25$, $k = 3$).

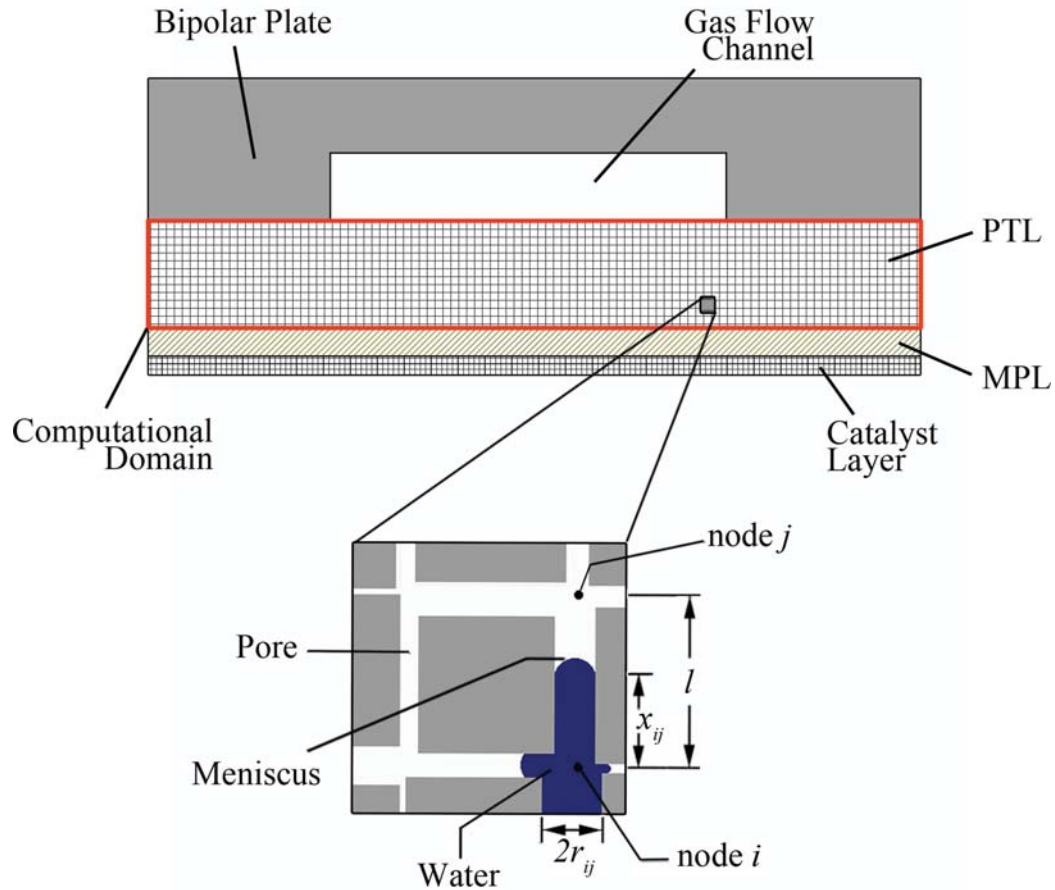


Figure 3.4: The full computational domain for this work shown here outlined in red, the fluid injection begins at the MPL/Catalyst layer interface and propagates to the gas channel. Also shown in this Figure are several nodes in the computational domain, non-wetting water, wetting gas and the fibers.

3.2 PTL Water Transport

Medici¹¹⁰ used a modified Poiseuille flow technique is used to model the volumetric flow rates through the individual pores. The standard Poiseuille formulation for the volumetric

flow rate through a cylinder is shown in equation 3.3 as derived through the Navier-Stokes equations.

$$q_{ij} = \frac{\pi r_{ij}^4}{8l\mu} (p_j - p_i) \quad (3.3)$$

For equation 3.3, r_{ij} is the radius of the pore between nod i and j , μ is the dynamic viscosity, and $p_j - p_i$ is the pressure difference across the length l of the pore. This Poiseuille flow formulation is then modified to include the two fluids or phases present. As a fluid passes through a pore, the location of the interface is tracked and this information can then be used to create an transition viscosity for the pore by applying a weighted average of the wetting and non-wetting fluid viscosities. The modified Poiseuille flow equation then becomes

$$q_{ij} = \frac{\pi r_{ij}^4}{8l\mu_{ij}^e} (p_j - p_i - p_{ij}^c) \quad (3.4)$$

where μ_{ij}^e is the transition viscosity and p_{ij}^c is the capillary pressure term which arises from the fluid interface. In the unlikely case that the capillary pressure (p_{ij}^c) is greater than the driving pressure (Δp_{ij}) the volumetric flow rate becomes negative signifying a retreating liquid phase. The transition viscosity is described as

$$\mu_{ij}^e = (\mu_{nw} - \mu_w) \frac{1 - \cos(\pi x_{ij}/l)}{2} + \mu_w \quad (3.5)$$

where μ_{nw} is the viscosity of the non-wetting fluid (liquid), μ_w is the viscosity of the wetting fluid (gas), and x_{ij} is the position of the meniscus measured from the i node. The transition viscosity is a combination of both the wetting and non-wetting fluids, this helps to provide a smooth transition between the non-wetting and wetting fluids¹¹³. Equation 3.5 shows that as a pore is occupied by only one fluid the transition viscosity (μ_{ij}^e) becomes equal to that fluids viscosity.

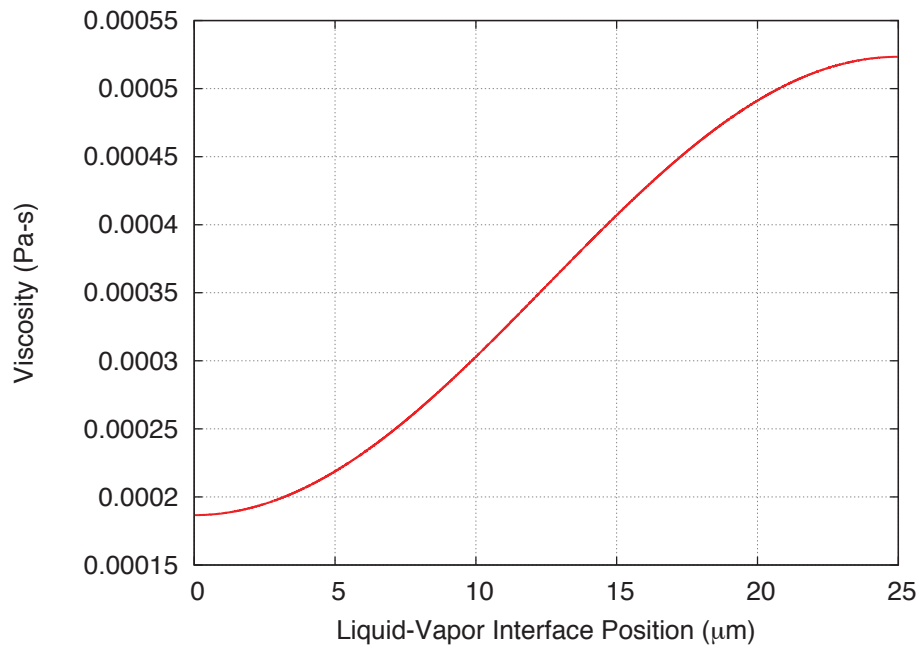


Figure 3.5: The transition viscosity as the liquid-vapor interface progresses through the pore.

As the liquid is injected and progresses through the pore the viscosity is calculated from equation 3.5. When the pore is completely void of liquid the viscosity becomes that of the gas phase, and when the pore is completely saturated the viscosity becomes that of the

liquid phase. Figure 3.5 illustrates how the viscosity varies as fluid progresses the pore.

The capillary pressure term like the transition viscosity term is dependent on the location of the meniscus in the pore. This relation is to deal with possible large changes in capillary pressure at the pore junctions or nodes. When meniscus reaches the node the radius used to calculate the capillary pressure is the average radius of the intersecting pores. For the 2-dimensional case this would be the average of four pore radii and for the 3-dimensional case this would be the average of the six intersecting pore radii. The modified capillary pressure formulation was derived by Medici and Allen¹¹³.

$$p_{ij}^c = \sigma \cos(\theta) \left[\left(1 - \frac{r_{ij}}{2\bar{r}_i} - \frac{r_{ij}}{2\bar{r}_j} \right) \frac{1 - \cos(2\pi x_{ij}/l)}{r_{ij}} + \frac{1 + \cos(\pi x_{ij}/l)}{\bar{r}_i} + \frac{1 - \cos(\pi x_{ij}/l)}{\bar{r}_j} \right] \quad (3.6)$$

where \bar{r}_i and \bar{r}_j are the average of the intersecting pore radii at the respective nodes i and j . As in equation 3.2, σ and θ are the surface tension and contact angle respectively. To prevent sharp changes in the capillary pressure terms and computational instabilities while approaching the nodes cosine functions were applied to the capillary pressure formulation from equation 3.2 to produce the smooth transition that is obtained in equation 3.6^{110,113}.

After the fluid progressing through a pore reaches the next node the capillary pressure simulates a change in contact angle to account for the pinning of the liquid interface at the pore opening. Figure 3.6 illustrates a typical capillary pressure as the fluid interface

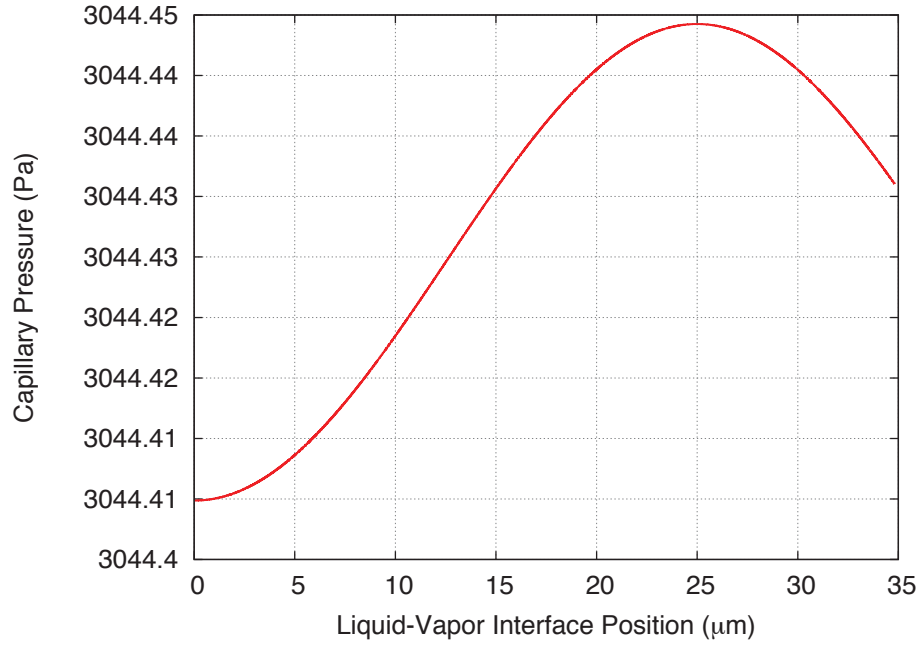


Figure 3.6: The capillary pressure as the liquid-vapor interface progresses through a single pore of $25 \mu\text{m}$, the pressures after $25 \mu\text{m}$ are designed to simulate the contact line pinning at the exit of the pore.

position flows through the pore and reaches the node. The decrease in capillary pressure noticed after the liquid reaches the node is due to the effect of contact line pinning at that node.

The effective capillary pressure are calculated for each pore in the domain that contains liquid, or could contain liquid on the next time step and the viscosities are calculated for each pore within the domain. These values are then applied to the flow rate calculation from equation 3.4 for each pore. This yields an accurate account of the capillary pressure and the viscosities for each pore as the liquid progress through the domain.

To conserve mass in this model the application of equation 3.7 is applied to the Poiseuille flow formulation. This states that the mass flux into a node equals the mass flux exiting the node. This balance is applied at every time step of the simulation.

$$\sum_{j=1}^n q_{ij} = 0 \quad (3.7)$$

Here $j = 1$ to n is the summation of flux from all of the pores at a given node intersection, n is the number of pores at this intersection and can be either 4 or 6 for a 2-dimensional or 3-dimensional pore network respectively. The conservation of mass is applied to the individual pores resulting in equation 3.8, a flux balance for each node within the domain.

$$\sum_{j=1}^n \frac{r_{ij}^4}{\mu_{ij}^e} (p_j - p_i - p_{ij}^c) = 0 \quad (3.8)$$

Equation 3.8 is the discretized modified Poiseuille flow equation used to describe the fluid transport in the modeled cylindrical tubes.

3.3 Thermal Transport

Medici and Allen¹¹² used a variation of the Surasani et al.¹¹⁹ model was used to model the heat transport from node to node. In this model all heat transfer is considered to transport

through conduction. The conservation of energy is then applied around each node

$$(v\rho c_p) \frac{dT_i}{dt} = - \sum_{j=1}^n \dot{Q}_{ij} - \sum_{j=1}^m (\dot{m}^{ev} \Delta h_{fg})_{ij} \quad (3.9)$$

where $(v\rho c_p)_{ij}$ is the total heat capacity at node i which is a function of the water, air and carbon content of the surrounding pores, \dot{m}^{ev} is the evaporation rate at the liquid-gas interface, and Δh_{fg} is the enthalpy of formation which is determined empirically by linear regression of published enthalpy data¹²⁰.

$$\Delta h_{fg} = 3187.47 - 2.49489T_i \quad (3.10)$$

By expanding equation 3.9 with the volumes associated with each of the three phases present in each of the pores connecting to a node the total heat capacity of each node can then be calculated.

$$(v\rho c_p)_i = \frac{l}{2} \sum_{j=1}^n \left\{ \left[\pi \left(1.1 \frac{l}{2} \right)^2 - \pi r_{ij}^2 \right] (\rho c_p)_s + s_{ij} \pi r_{ij}^2 (\rho c_p)_l + (1 - s_{ij}) \pi r_{ij}^2 (\rho c_p)_g \right\} \quad (3.11)$$

The saturation of a pore (s_{ij}) is the ratio of liquid volume in the pore ij to the total volume of that pore. When $s_{ij} = 1$ the pore is completely full with the wetting phase (liquid water) and when $s_{ij} = 0$ the pore is filled completely with the wetting phase (humidified air).

The area distribution in the solid phase was modified from the work of Medici and Allen¹¹² to create a more realistic relationship between pore size and the surrounding solid phase. The model presented by Medici and Allen¹¹² calculated the area of the solid phase conducting material by using a cross-section of a square that has an edge length of two times the radius of the pore. This would cause the solid phase volume for a pore to be larger in the larger pores and small in the small pores. Intuitively the opposite is true, the larger the pore the smaller the solid phase conductive area. To address this the geometry was modified from that of a square with circular cut-out to an annulus. The outer radius (as seen in Figure 3.7) is set to be just over half the distance between parallel pores while the inner radius is that of the pore. This creates an inverse relationship to the pore size, a larger pore means less solid-phase.

The thermal transport properties of this model are based off a thermal resistance model that is applied to the solid fiber lattice structure generated from the same Weibull PDF that creates the pore size distribution. The conduction area for the solid phase is taken to be $\pi(1.1 \cdot l_{ij}/2)^2$, where the 1.1 accommodating factor and is chosen such that the effective porosity remains at 0.7 for the PTL and l_{ij} is the length of every pore. With a 1.1 multiplying factor the overall carbon volume occupies 30% of the volume thus accounting for an accurate carbon to air ratio throughout the PTL. The thermal conductivity is greatly controlled by the carbon volume in the PTL and this is modeled by assuming each pore is encapsulated by a carbon cylinder forming an annulus of carbon around the pore space.

The outer radius of the annulus is set to be $r_f = 1.1 \cdot l_{ij}/2$ and the inner radius is r_{ij} as illustrated in Figure 3.7. This is a modified version of the thermal model presented by Surasani et al.¹¹⁹

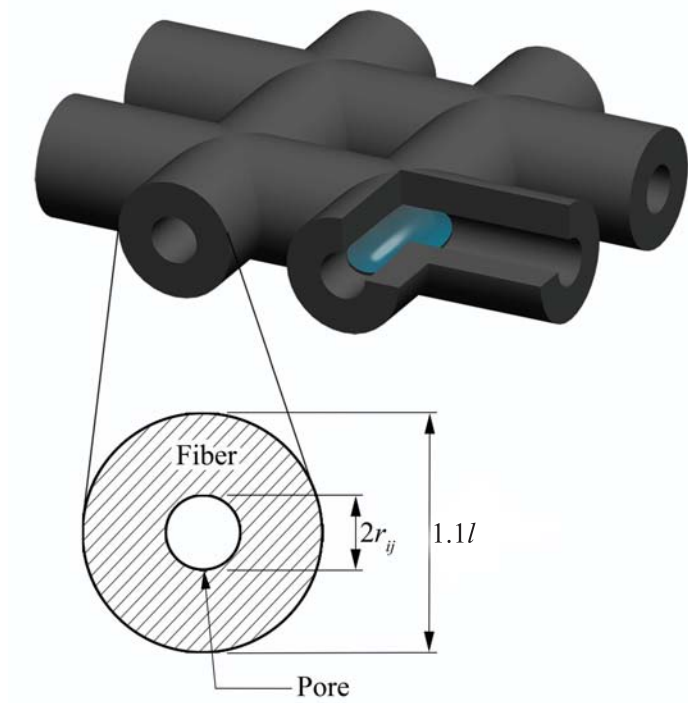


Figure 3.7: A visualization of the thermal transport domain for the 2-dimensional pore network model. The scales chosen in this illustration are to better illustrate the conduction in the solid and liquid states and not to scale.

The basic thermal resistance model for conduction can be seen in equation 3.12, here k is the thermal conductivity of the conductor, A is the conductive area and l is the length of the

pore.

$$R_{t,cond} = \frac{l}{kA} \quad (3.12)$$

This conductive thermal resistance model is then applied to the components present in the models domain, the solid phase (carbon fibers), the liquid phase (water), and the gas phase (humidified air) resulting in a thermal resistance circuit shown in Figure 3.8. For this model the thermal resistances R_s , R_l and R_g are the equivalent thermal resistances for the solid, liquid and gas phases respectively. In the case that a pore is occupied by a single phase the lower branch of the resistive circuit become equal to the thermal resistance of only the phase that is present.

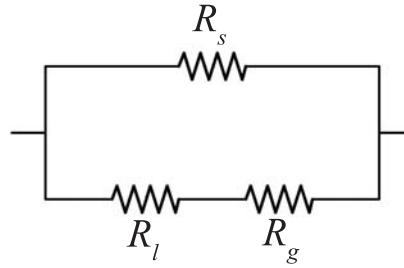


Figure 3.8: Equivalent thermal resistance circuit for a pore containing liquid and gas phases.

Solving the circuit for its equivalent thermal resistance is done by using equation 3.13

yielding an effective thermal resistance for the pore and its surrounding fiber¹²¹.

$$R_{ij}^{tot} = \frac{R_s(R_l + R_g)}{R_s + (R_l + R_g)} \quad (3.13)$$

Finally the heat transfer rate can be calculated with

$$\dot{Q}_{ij} = \frac{T_i - T_j}{R_{ij}^{tot}} \quad (3.14)$$

where ΔT_{ij} is the temperature difference between nodes i and j . For this model the heat transfer rates are set to be constant at the catalyst layer representing the heat generated from the reaction occurring during the fuel cell operation. Equation 3.14 can then be solved in terms of T_j and when applied at every pore will result in the temperature profile of the domain at each time step as illustrated in Figure 3.9, the temperature distribution for a land temperature of 80°C and a minimum channel temperature of 79.72°C .

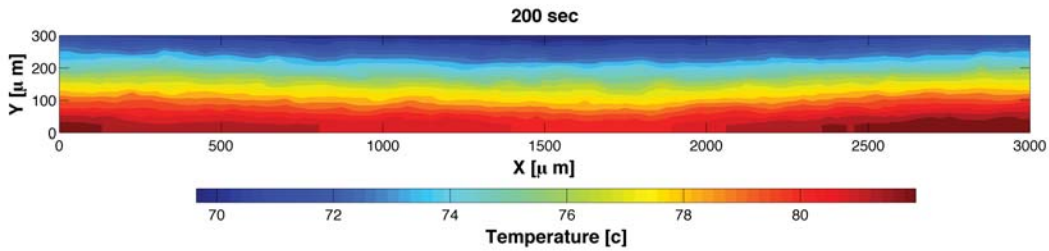


Figure 3.9: The final temperature distribution of the PTL after a 200 second simulation with the land temperature set to 80°C and a relative humidity in the channel of 70%.

3.4 Vapor Transport

The vapor transport in this model is accounted for by modeling the concentration gradients. The driving force of the vapor in the PTL is the concentration gradient between the liquid front and the gas channel. The sharper this gradient the more effectively the vapor produced from the vapor source, the evaporating liquid water is carried away from the interface and to the gas channel. The two vapor phase generation models investigated are the diffusive and the transition film model. The diffusive model is strictly based on the surface area of the fluid and the relative humidity in the pore. In the case of a fuel cell the porous media allows for a large contact line length to volume ratio, this is the reason a thin-film model is preferred. While the diffusive model only considers the surface area the transition film model considers the contact line area, contact angle, liquid curvature and it has been shown across the literature that the transition film region near the contact line is responsible for 50% – 95% of the overall heat and mass transfer of an evaporating fluid^{77,79,84,88,122–124}. To compare the results of the two evaporation models employed herein the primary diffusive vapor transport model, derived from the work of Yiotis et al.¹²⁵, is employed to transport the water vapor generated from the evaporation models to the gas channel. Here a convection-diffusion equation used to account for this vapor phase mass transfer.

$$\frac{\partial C}{\partial t} = D \nabla^2 C \quad (3.15)$$

In the diffusion equation 3.15 C is the vapor concentration, and D is the binary diffusivity of water vapor in air. This equation is applied to the gas phase and is used to determine the concentration and location of the water vapor. The results of this concentration are then directly used as an input for the phase change models. Equation 3.15 can be discretized and applied on a per pore basis thus solving locally the concentration of the water vapor in the respective pore^{111,125}.

$$V_i \frac{dC_i}{dt} = D_i \pi r_{ij}^2 \frac{C_i - C_j}{l} \quad (3.16)$$

Here the term V_i is the volume of the pores surrounding node i , and D_i is the binary diffusivity of water vapor in air at the temperature of node i . The diffusion constant is a function of the local temperature and for this model is approximated by equation 3.17 which is a linear regression of the water vapor in air diffusion coefficient as reported in Bolz and Tuve¹²⁰ with units of cm^2/s .

$$D_i = 0.168828 + 0.00152943T_i \quad (3.17)$$

The volume of the pores surrounding a node i is calculated using equation 3.18 which is a sum of the volumes of each node joining with node i .

$$V_i = \frac{l}{2} \sum_{j=1}^n \pi r_{ij}^2 \quad (3.18)$$

In a 3-Dimensional simulation the number of pores connected at the node is 6 and for 2-Dimensional simulations the value of n is 4.

3.4.1 Diffusive Evaporation Model

Medici and Allen¹¹² used the diffusive evaporation model based of the work of Yiotis et al.¹²⁵. The liquid is evaporating at the gas-liquid interface of each pore containing the non-wetting fluid

$$m_{ij}^{ev} = \pi r_{ij}^2 \Delta t D_j \frac{C_i^{ev} - C_j}{l} \quad (3.19)$$

where m_{ij}^{ev} is the mass of evaporated liquid water, C_i^{ev} is the maximum vapor concentration allowable in air at T_i ($RH = 100\%$), Δt is the time step, and C_i is the concentration of water vapor in air at node i . To determine the maximum vapor concentration the humidity ratio is calculated at the saturation pressure

$$\omega^{ev} = 0.622 \frac{p_{sat}}{p_{atm} - p_{sat}} \quad (3.20)$$

where p_{atm} is the air pressure in the pore, and p_{sat} is a function of temperature (T_i) that is empirically determined from published data¹²⁰. The input temperature units for this

formulation are $^{\circ}C$ and the output saturation pressure is in $mmHG$.

$$\log_{10} p_{sat} = \left(8.07131 - \frac{1730.63}{233.426 + T_i} \right) \quad (3.21)$$

Finally the maximum vapor concentration can be calculated from the humidity ratio by multiplying by the density of dry air.

$$C^{ev} = \omega^{ev} \rho_{air} \quad (3.22)$$

The vapor concentration of the gas phase can be determined in a similar fashion, starting with the partial pressure of water vapor in the gas phase at node i . The relative humidity (ϕ_i) is specified at the channel as a boundary condition.

$$p_{v,i} = \phi_i p_{sat} \quad (3.23)$$

The humidity ratio at the channel can then be determined by

$$\omega_i = 0.622 \frac{p_{v,i}}{p_{v,i} - p_{sat}} \quad (3.24)$$

and used to calculate the concentration at the channel boundary which is then used as a boundary condition.

$$C_i = \omega_i \rho_{air} \quad (3.25)$$

Using the evaporated mass (equation 3.19), the new location of the meniscus in the pore can be calculated as

$$x_{ij} = \frac{m_{ij}^l - m_{ij}^{ev}}{\pi r_{ij}^2 \rho_l} \quad (3.26)$$

, where m_{ij}^l is the mass of the liquid phase, ρ_l is the density of the liquid phase and m_{ij}^{ev} is the mass of evaporated liquid as described in equation 3.19.

3.5 Boundary Conditions

The pore network model analyzes only the cathode side of the fuel cell and neglects transport through the membrane and the gas channel. The membrane and gas channel transport have been neglected to keep this model computationally inexpensive. These assumptions do however eliminate the ability to model the effects of back-diffusion through the membrane to the anode and plug formation in the gas channel. The simulation ends either when the liquid phase reaches the gas channel or if the liquid reaches a steady state situation where the rate of injection is tantamount to the rate of evaporation.

Table 3.1 is a summary of the boundary conditions applied in the pore network model for the liquid percolation, vapor concentration, and thermal transport. The selection and application of these boundary conditions will be discussed in greater detail in the following

Table 3.1

Boundary conditions used in solving the pore network model simulations.

	North		South	East/West
	Land	Channel		
Liquid	<i>Neumann/Wall</i> $q_{ij} = 0$	<i>Dirichlet</i> $p_{\text{air}} = p_{\text{atm}}$	<i>Neumann</i> $q_{ij} = 1.2 \times 10^{-7} \text{ mL/s}$	<i>Symmetry</i>
Saturation	<i>Isolated</i> $C(\infty) = 0$	<i>Dirichlet</i> $\phi = \text{const}$	<i>Saturation*</i> $\phi = 1$	<i>Symmetry</i>
Thermal	<i>Dirichlet</i> $T_l = \text{const}$	<i>Dirichlet</i> $T_c = T_l \cdot f(x)^{**}$	<i>Neumann</i> $\dot{Q}_{ij} = 0.144 \text{ W}$	<i>Symmetry</i>

* The “Southern” boundary condition for saturation is set at the liquid-vapor interface and not the bottom of the domain.

** $f(x)$ is a parabolic function that fits the temperature boundary with the results found in Shimpalee and Dutta¹²⁶.

sections.

The evaporation rates are calculated on a per pore basis and each pore has a unique set of input parameters to the evaporation model which calculates the evaporation rate based on the transition film evaporation model discussed in section 2. With this the evaporation in every pore is subject to a unique set of boundary conditions that is determined by the radius of that individual pore, the wall temperature of that pore and the vapor phase saturation in that pore.

3.5.1 Liquid-phase Boundary Conditions

The boundary conditions used to determine the liquid phase flow are referred to herein as the “North” and “South” boundary for the top and bottom of the simulated domain,

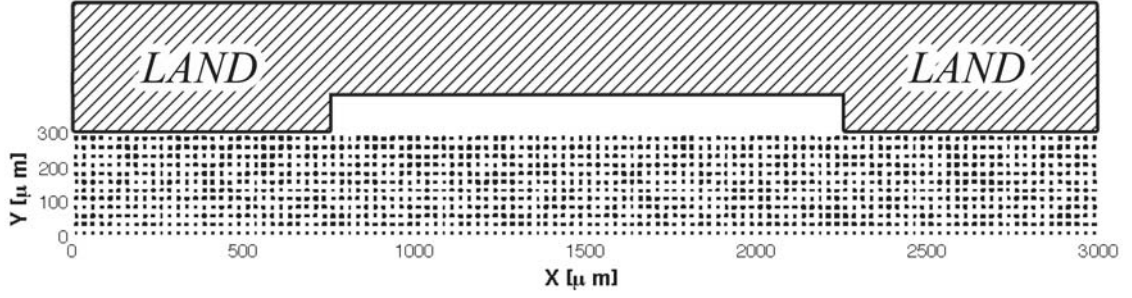


Figure 3.10: The computational domain of the PTL transport model illustrating the location of the land area and the boundary conditions used in this simulation. Note that the channel is not included in the computational domain, thus its height is not drawn to scale.

and the “East” and “West” boundary for the left and right sides of the simulated domain respectively. At the north boundary as seen in Figure 3.10 the wall or Neumann boundary condition is applied under the land which in this case is from $0 - 750\mu m$ and $2250 - 3000\mu m$, this boundary condition simulates the impermeable bipolar plate and is set at zero injection rate. Also on the north boundary is the open channel which resides in the area from $750 - 2250\mu m$ along the x-domain, the Dirichlet boundary condition here is set to 0 gauge pressure. This allows all vapor water that reaches the channel to be removed from the simulation. To maintain this boundary condition the simulation is stopped when the liquid phase water reaches any portion of the channel.

Since the gas pressure at the channel is set to 0 gauge pressure the assumption is made that the anode side gas pressure is the same as the cathode side, this model is capable of applying a pressure differential between the cathode and anode side gas channels by adjusting the cathode boundary condition at the channel to reflect the difference in pressures. For the purposes illustrated in this work a pressure differential between the anode and cathode

is not required. A wall boundary condition is also set at the southern boundary making the assumption that the membrane is completely impermeable to the liquid water. This assumption is valid since the liquid phase permeability of the membrane is very low and on time scales several orders of magnitude greater than the duration of these simulations. A symmetry boundary condition is set on both the east and the west boundaries.

On the southern boundary a Neumann boundary condition is set to a constant influx of water. The rate at which this boundary condition is set at $1 \times 10^{-9} \text{ mL/s}$ at each pore. This injection rate was determined from the water generated in a fuel cell operating at 2.0 A/cm^2 and 0.2 V . The reason for choosing such a high current density in these simulations was to capture the mass transport losses that are most prevalent at high current densities (see Figure 1.2).

Initially the domain is occupied by only air at a relative humidity set equal to that of the gas channel. Once the simulation begins the liquid water begins with its injection rate constant across the southern boundary. The water generated in this model is generated purely in the liquid phase like that of Weber and Darling¹²⁷. It has been shown in the literature that a constant water influx across the catalyst layer may not be accurate representation of how the reaction takes place, as water builds up blocking passage to reaction sites the water production in certain areas may decrease, this is not modeled due to the inconsistency in the literature what sort of profile the water generation might take across the catalyst layer. This model has the ability to input such a function across the catalyst layer however, until a

better understanding of how this production takes place a constant influx of water has been used.

The network of this model consists of pores that are of equal length ($25\ \mu m$) with varying radii, as discussed previously in section 3.1. Although a constant pore length may not be physically accurate to describe the PTL the pore size distribution was selected to take this in account. By varying the locations of the different pore sizes according to the Weibull distribution the effect of different pore lengths is captured making this a model physically accurate in water transport while keeping the computational costs at a minimum.

3.5.2 Saturation Boundary Conditions

The saturation boundary conditions are initially set as input parameters to this model. Along the north boundary the land portions ($0 - 750\mu m$ to $2250\mu m$) in the model shown in Figure 3.10) are set to isolated boundaries while under the channel a constant relative humidity is specified as an input parameter. At the beginning of the model the entire domain is assumed to be equal to that set as an input for the channel relative humidity. As the water is injected the southern boundary becomes saturated with liquid water forcing the boundary to a fully saturated state. The east and west boundaries, like those of the liquid-phase boundary conditions, is set to a symmetry boundary condition. In the results presented in chapter 4 the effects of four different relative humidity cases are explored,

$\phi = 60\%, 70\%, 80\%$ and 90% .

3.5.3 Thermal Boundary Conditions

For the thermal boundary conditions along the land section of the north boundary a constant temperature is set. At the channel on the north boundary the temperature profile is set to simulate a cooling effect from the constant air flow that travels through the channel. The profile was chose to match the results from Shimpalee and Dutta¹²⁶ in which the temperature distributions throughout a fuel cell were studied. The resulting profile yields a minimum temperature in the center of the channel as can be seen in Figure 3.11 that is 0.5% lower than the constant temperature boundary condition of the land. This value was chosen to fit published data for the temperature distribution of the flow channel on the cathode side of a PEM fuel cell^{82,126}. In the results presented in chapter 4 the effects of three different land temperature boundary conditions are explored, $T = 70^{\circ}\text{C}, 75^{\circ}\text{C}, 80^{\circ}\text{C}$.

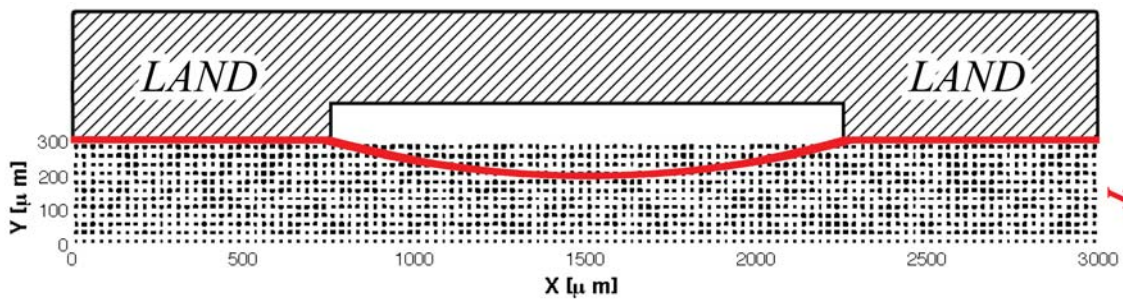


Figure 3.11: A schematic showing how the temperature profile varies along the north boundary.

The east and west boundaries are again set to symmetric conditions, while the southern

boundary consists of a Neumann boundary condition of constant heat flux. Just as in the liquid-phase boundary condition the heat flux is generated from a source term that produces heat from the electrochemical reaction determined by the cell operating conditions of $2A/cm^2$ and $0.2V$. The heat production associated with such a condition is $1.2 \times 10^{-3}W$ per pore along the southern boundary or catalyst layer.

3.6 Fluid Transport Validation

The fluid transport for this model has been validated using a pseudo-Helle-Shaw experiment. This is referred to as the “pseudo” Helle-Shaw because it is comprised of two parallel plates however, for this setup instead of just two parallel plates there is a PTL sandwiched between the plates. For the validation tests the model is changed from a thin PTL with fluid injection all along the bottom to a PTL with the fluid injected in the center. This allows for various different flow regimes (capillary fingering, viscous fingering and stable displacement) to be simulated and tested for to prove the physics behind the model are correct¹¹³. For more information on the validation of the flow regimes and the PTL fluid transport models see the work by Medici¹¹⁰.

Figure 3.12 demonstrates a simulation/experimental set with the fluid injected in the center

of the PTL, the percolation in this test shows the capillary fingering that is found experimentally by Medici¹¹⁰. The experiments run to verify this output were done at low temperatures ($\approx 22^\circ\text{C}$) in an environment where the top and bottom of the PTL were covered with transparent plates to minimize the effects of evaporation and to keep the flow in the plane of the PTL, thus for this simulation run the effects of evaporation were toggled off. The

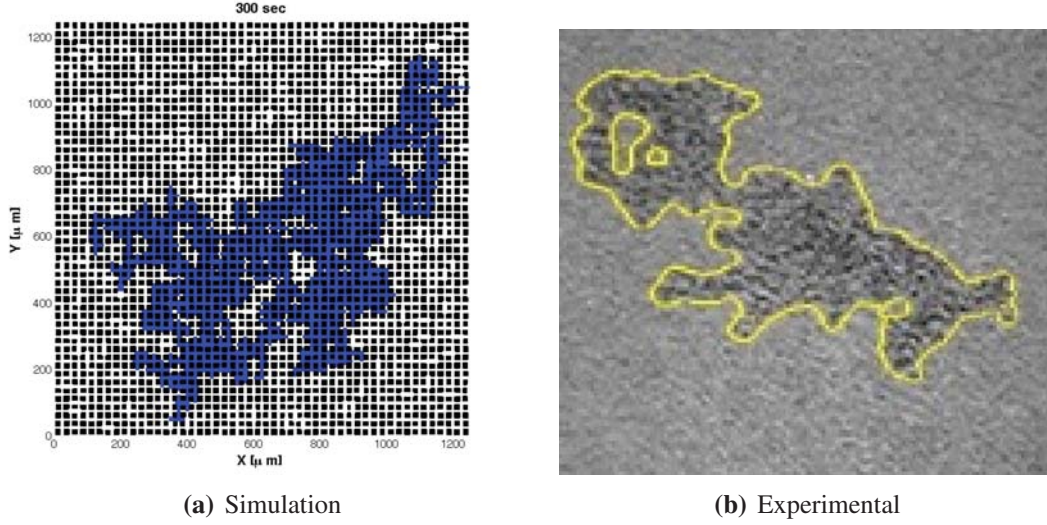


Figure 3.12: Validation simulation of the liquid transport model. The injection rates in 3.12(b) were performed with a $C_a = 3.1 \times 10^{-8}$, the outline represents the liquid air interface.

capillary numbers on both the experiment and the simulation were set to $C_a = 3.1 \times 10^{-8}$ a value in the range of an operating fuel cell. Comparing the simulation and the experimental data the subtle differences that can be noticed are due to differences in pore distribution. Although the mean pore size distributions for both the PTL and the simulation domain are very closely matched, the stochastic nature of the pore distribution cause differences in the experimental and simulated percolations. For example, although very unlikely, the randomly applied Weibull distribution could result in the largest diameter pores falling in a

line ranging from the injection point to the edge of the simulation causing the percolation to quickly progress along that line.

3.7 Summary

In this chapter a pore network model was presented that can utilize two different approaches on phase change. The diffusive model, which assumes uniform flux across the interfacial area and the transition film model which considers curvatures, disjoining pressures and capillary pressures to determine the phase change fluxes in the areas of the meniscus that have the highest curvature. Both of the modeling approaches presented consider the entire surface area, however it is only the transition film model that has the added considerations near the contact line. The transition film model, although more accurate does increase the computational time from the order of minutes to tens of minutes. These two different approaches introduced in this chapter will be discussed and compared in the following chapters.

The pore network model boundary conditions used for the simulations presented have been set to a very high current density fuel cell situation. This is due to the dominance of the mass transport losses at such operating conditions. By simulating the operating conditions that create the mass transport problems, a better understanding of the phenomena responsible for causing these losses may be more closely examined.

Chapter 4

Modeling Results

This chapter will examine the results obtained from the pore network model with both the transition film and the diffusive models for evaporation. These comparisons will be made with several different pore distributions to demonstrate how each model behaves when the morphology is changed. The simulations will also indirectly examine how the morphology of the PTL changes the distribution of liquid water and temperature gradients in the modeling domain. Figure 4.1 shows the three different pore distributions. The mean

Table 4.1
Pore size distribution Weibull PDF parameters for the three morphological cases under investigation.

Scale factor (ψ)	Shape factor (k)	Mean Pore Size
5.25	3	$9.7\mu m$
5.25	10	$9.7\mu m$
9.25	4	$8.7\mu m$

pore size and Weibull scale/shape factors for the three different PDFs that generate the pore network can be seen in table 4.1. These values were chosen from the mercury intrusion porosimetry data by Gostick et al.¹¹⁵. When the pore distribution is changed while keeping

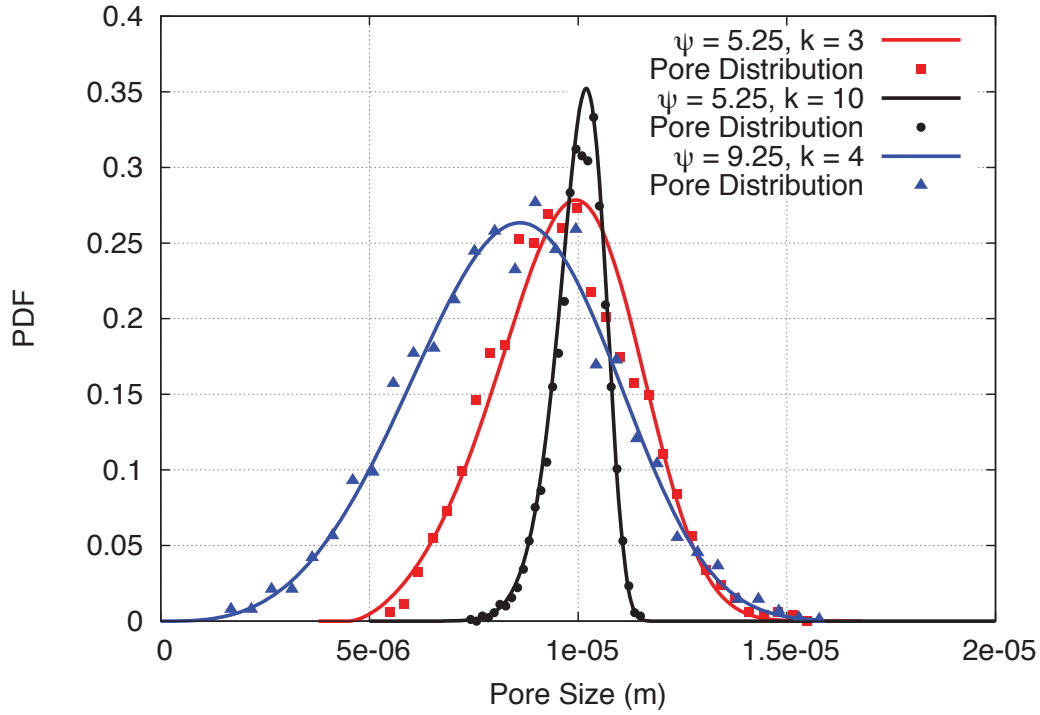


Figure 4.1: Three pore size distributions tested all with a mean pore size and distributions shown in table 4.1.

the mean pore size constant the liquid percolation changes and the results from the diffusive and transition film evaporation models show very similar results. It isn't until the mean pore size and its distribution are changed that results from the two different evaporation models begin to differ. With a smaller mean pore radius the contact line to surface area ratio is increased which will physically lead to higher expected evaporation rates¹²⁸. This

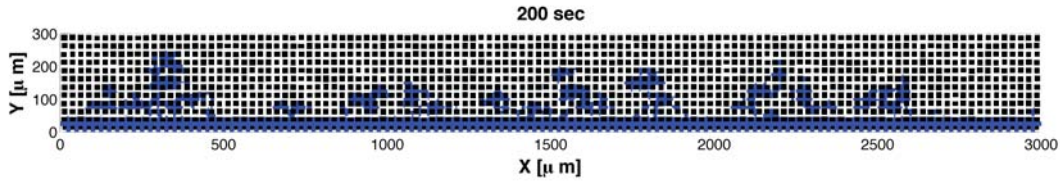
phenomenon is captured with the transition film evaporation model however, the diffusive model is unable to capture these effects.

4.1 Diffusive/Transition Film Model Comparison at 60% Relative Humidity and 70°C

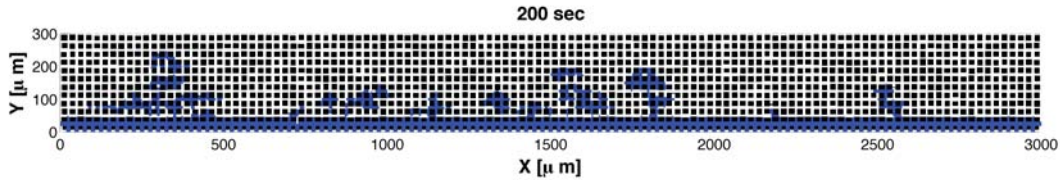
The differences between the two evaporation models in the pore network model are examined in this section for low relative humidity and low temperature conditions ($\phi = 60\%$ and $T_l = 70^\circ\text{C}$). These simulations are run with two different pore distributions and mean pore radii. The first distribution under investigation has a mean pore size of $9.7\ \mu\text{m}$ and the Weibull scale and shape parameters used to generate this distribution are $\psi = 5.25$ and $k = 3$ respectively. The other distribution examined has a mean pore size of $8.7\ \mu\text{m}$ and Weibull scale and shape parameters of $\phi = 9.25$ and $k = 4$. The change in mean pore size is to illustrate the ability of the transition film model to capture the effects curvature has on the overall evaporation rates out of porous media.

Figure 4.2 shows the percolation of water through the pore network model for both the diffusive and transition film evaporation models. Here a slight difference in the liquid water front can be noticed with more liquid water present in the diffusive model than the transition film model. Figures 4.3 and 4.4 give a more quantitative look at how these models compare, these are referred to herein as the liquid phase water saturation plots. The liquid phase

water saturation shows the front length, occupied volume, evaporated volume and wetted area and are all in terms of a percentage. These curves are shown as a percentage so direct comparisons between simulations with varying fuel cell operating conditions and pore distributions can be made. The percentage of front length is the two-dimensional liquid water-air interface length with respect to the summation of the pore diameters throughout the domain. The percentage of occupied volume is the volume of liquid phase water in the PTL with respect to the total pore volume in the modeling domain. The percentage of evaporated volume is the volume of liquid water that has evaporated with respect to the total volume of liquid water.



(a) Diffusive model percolation at 60% RH and 70°C with a 9.7 μm mean pore size.



(b) Transition film model percolation at 60% RH and 70°C with a 9.7 μm mean pore size.

Figure 4.2: Percolation of liquid water from the catalyst layer at 60% RH and 76°C for the 9.7 μm mean pore size. (a) Diffusive evaporation model, (b) transition film evaporation model.

The liquid phase water saturation plots show the progression of the liquid water finger and

illustrate the liquid water distribution, but they do not allow the two evaporation models to be compared directly. In some cases these are very close, especially in the cases with a mean pore size near $10\ \mu m$. To help distinguish the differences in the results from each model table 4.2 shows the percent evaporated volume at the end of the simulation and the average occupied volume and front length for the last 20 seconds of the simulation when the model nears steady state.

Many of the liquid saturation plots exhibit oscillations, dips and fluctuations that are most prevailing in the front length curves. In Figure 4.3 at about 90 seconds into the simulation an almost sudden change in the front length occurs. These fluctuations are a function of the current liquid water distribution and the pore size distribution.

The sequence of percolation and vapor concentration plots shown in Figure 4.5 demonstrate the liquid water distribution at 4 second intervals for the duration of the dip seen in the liquid saturation plot, Figure 4.3. Through this sequence the liquid water front appears to be receding and vapor concentration plots show that as the liquid front gets close to the gas channel the steep concentration gradient that is formed aids in the removal of water as a vapor. The removal of water vapor through the gas channel helps to increase the evaporation rates seen at the liquid interface thereby causing the liquid water front to retreat.

With the low temperature and low relative humidity operating conditions the transition film model is predicting a higher evaporation rate. This can easily be seen by not only the larger percentage of evaporated volume but the occupied volume and front length are considerably

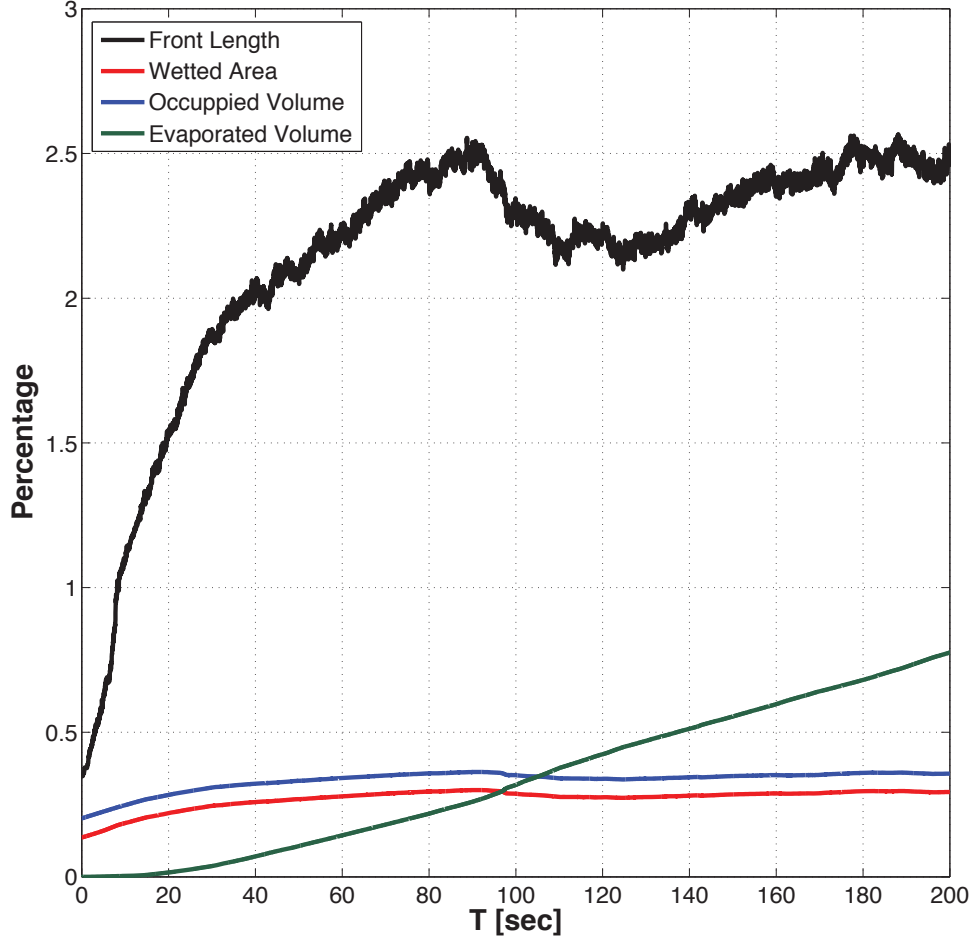


Figure 4.3: PTL saturation of liquid water from the catalyst layer at 60% RH and 70°C for the 9.7 μm mean pore size with the diffusive evaporation model.

lower than that of the diffusive model as well.

The temperature distributions shown in figure 4.6 demonstrate a few of the differences in the temperature distribution because of the different evaporation rates calculated by the two models. The transition film model has predicted higher evaporation rates than the diffusive model, the effects of this can be noticed in the difference in maximum temperatures for the

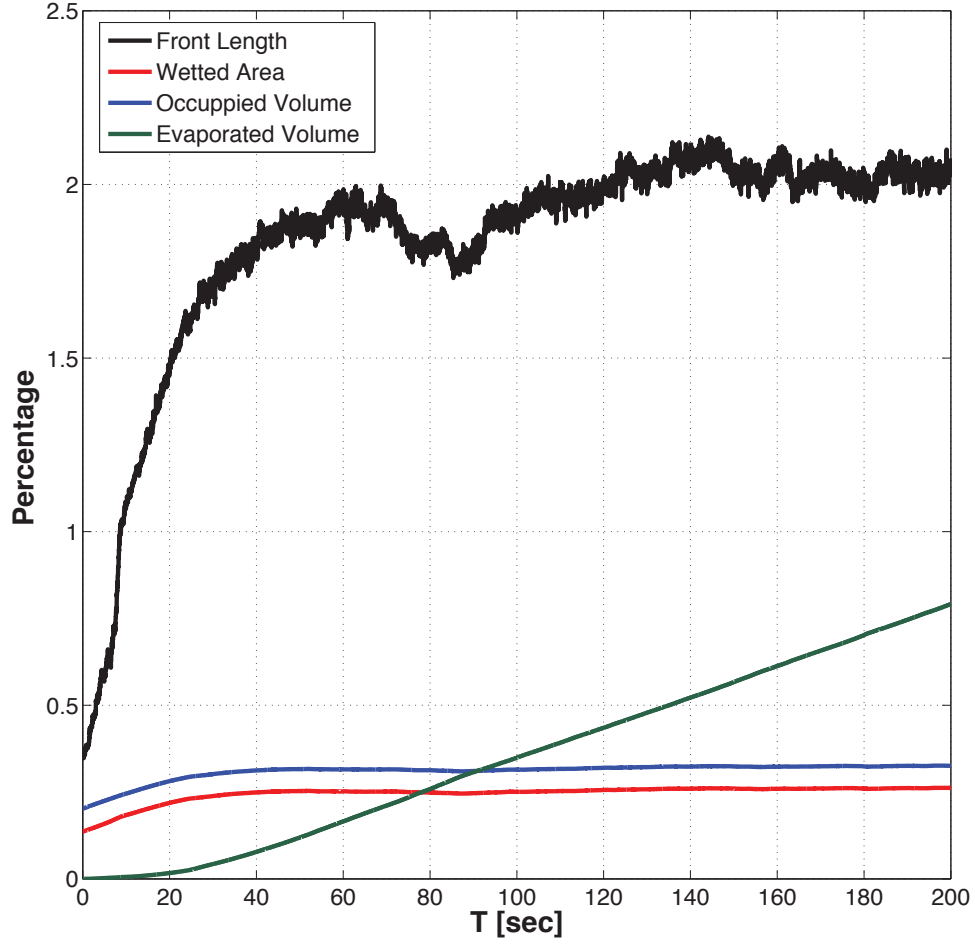


Figure 4.4: PTL saturation of liquid water from the catalyst layer at 60% RH and 70°C for the 9.7 μm mean pore size with the transition film evaporation model.

temperature distributions. Figure 4.6(a) is the final temperature distribution for the network model with the diffusive evaporation model. This is similar when compared to the transition film model (figure 4.6(b)) however, the higher evaporation rates and different liquid water distributions have slightly changed the mean domain temperature and temperature distributions.

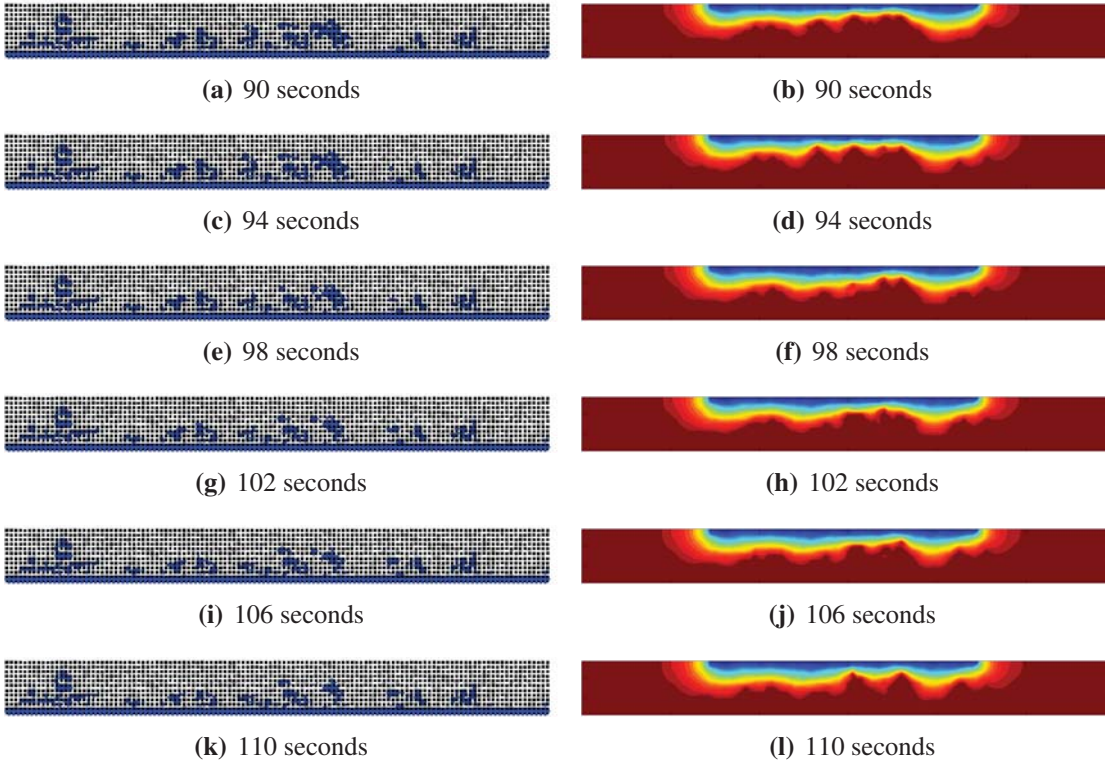


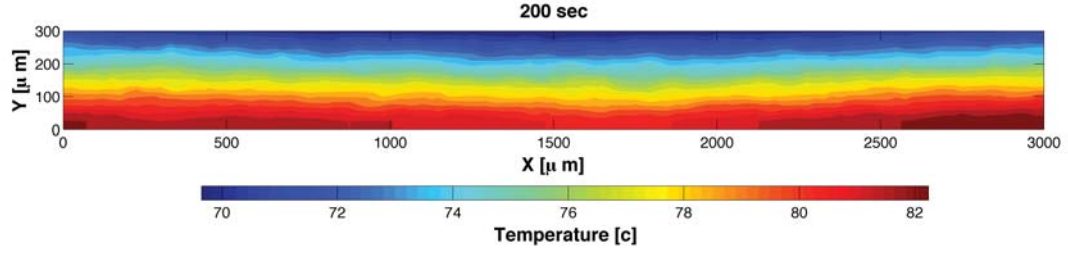
Figure 4.5: Liquid water percolation (left) and vapor saturation (right) of the receding front at 90 seconds to 110 seconds in the diffusive model 60% RH and 70°C case.

Table 4.2

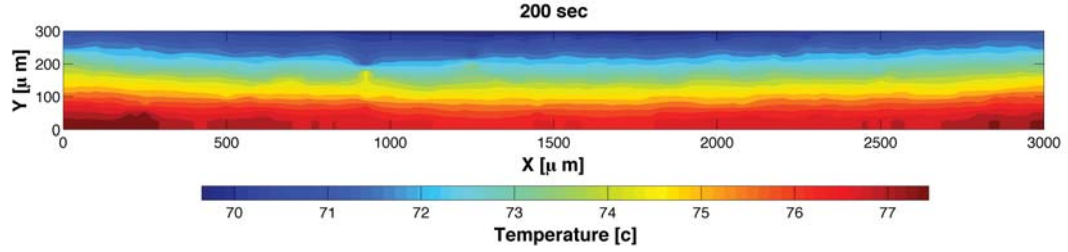
Comparison of the liquid water saturation data for the diffusive and transition film models with an $9.7\mu m$ mean pore size.

	Diffusive Model	Transition Film Model
Total Evaporated Volume	0.75%	0.76%
Occupied Volume	0.357%	0.326%
Front Length	2.46%	2.03%

The mean temperatures as the simulation progresses can be seen in figure 4.7, here the transition film model is predicting several degrees lower average temperature than the diffusive model. This is entirely due to the higher evaporation rates, more heat energy is removed



(a) Diffusive model temperature distribution at 60% RH and 70°C with an 9.7 μm mean pore size.



(b) Transition film model temperature distribution at 60% RH and 70°C with an 9.7 μm mean pore size.

Figure 4.6: Temperature distribution for the 60% relative humidity, 80°C and 9.7 μm mean pore size.

due to phase change thus resulting in a lower mean temperature. The higher evaporation rates affect the water distribution which in turn changes the thermal conductivity of the domain.

Figure 4.8 shows the water vapor concentration over the domain at the final time step, here the dark red area is near fully saturated while the dark blue is the relative humidity of the channel (in this case 60% RH). In these two examples the transition film model appears to have a slightly smaller saturated area than the diffusive model. In these the sharper the gradient from fully saturated to the channel relative humidity the faster the water vapor from the evaporating pores is driven to the channel.

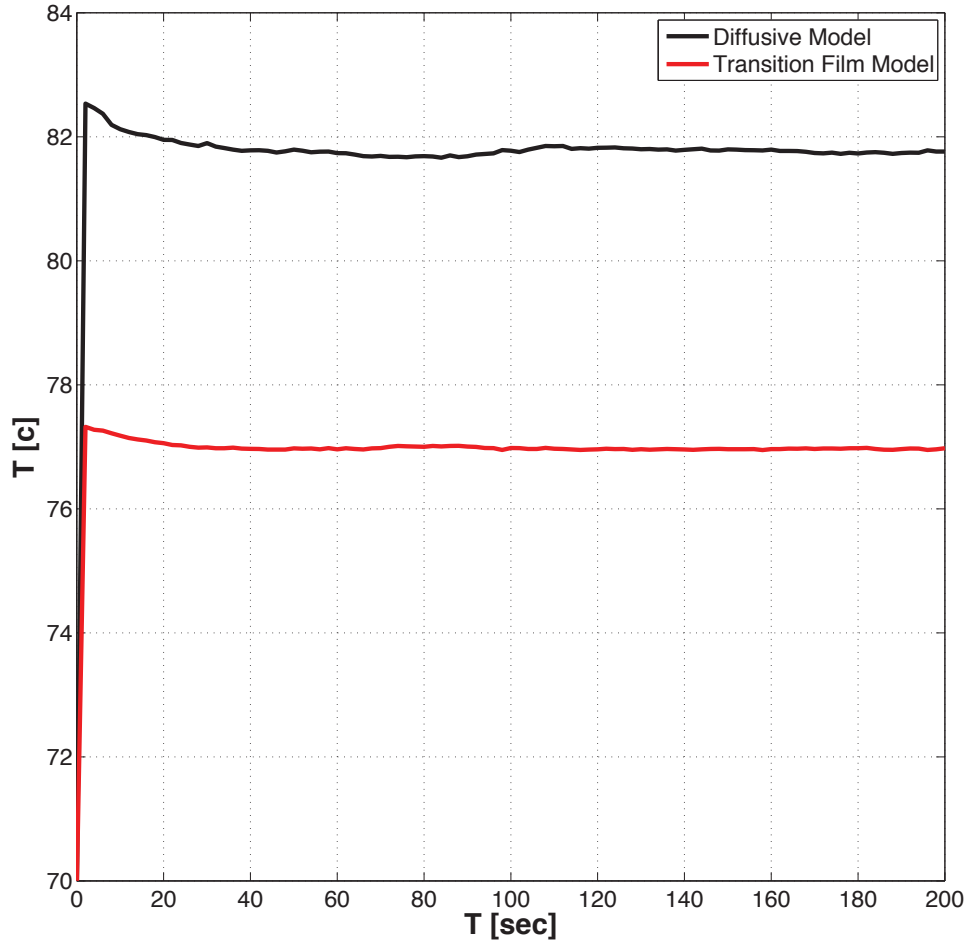
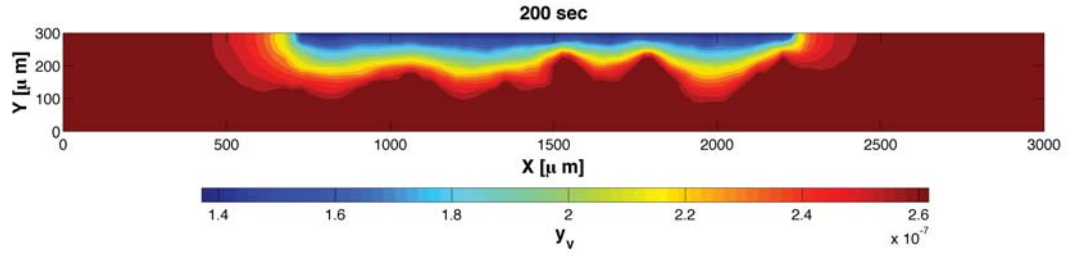
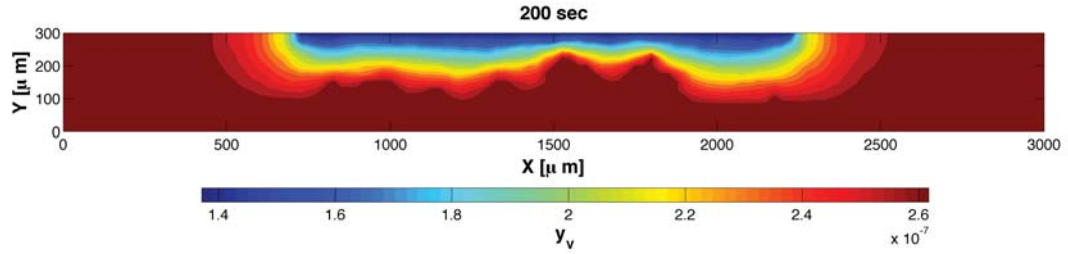


Figure 4.7: Average temperature of the domain throughout the simulation for both the transition film and diffusive models with a mean pore size of $9.7\mu m$.

The pressure distributions plots can be difficult to obtain useful information from. The largest issue is that when the percolating liquid reaches a node with several small pores the pressure will increase substantially at that specific node while the others at that time remain fairly low, this causes a “hotspot” on the surface plot which reduces the visibility of everything except one or two nodes that have abnormally high pressures. Figure 4.9 shows



(a) Diffusive model saturation distribution at 60% RH and 70°C with an 9.7 μm mean pore size.

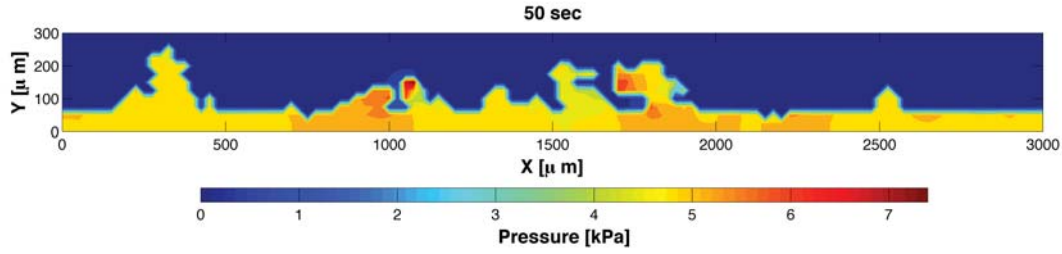


(b) Transition film model saturation distribution at 60% RH and 70°C with an 9.7 μm mean pore size.

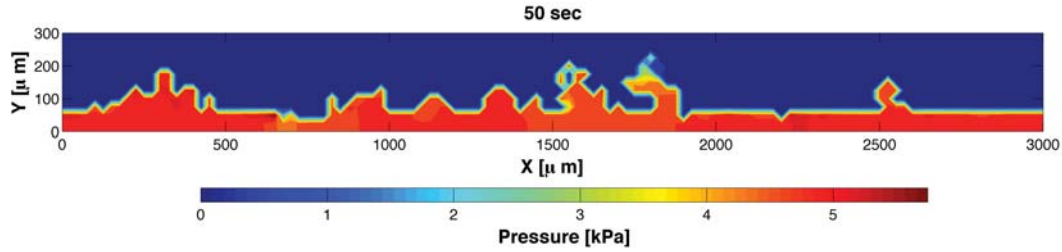
Figure 4.8: Saturation distribution for the 60% relative humidity, 80°C and 9.7 μm mean pore size.

the pressure distribution for both models. The presence of liquid water is the primary factor in these plots, so when comparing the two evaporation rate models this is no more useful than the percolation plots. The pressure distribution plots do however aid in the understanding of the liquid water transport through the PTL.

Figure 4.10 illustrates the water distribution for both the diffusive and the transition film evaporation models in the pore network model for a smaller mean pore size. The diffusive model in this case is stopped at 70 seconds when the liquid finger reached the gas channel. With the transition film model the liquid phase does not reach the gas channel through the duration of the simulation. In this morphology, with the smaller pore size and thus the smaller pore volume, more flooding is expected. This is seen with both of the evaporation



(a) Diffusive model pressure distribution at 60% RH and 70°C with an 9.7 μm mean pore size.

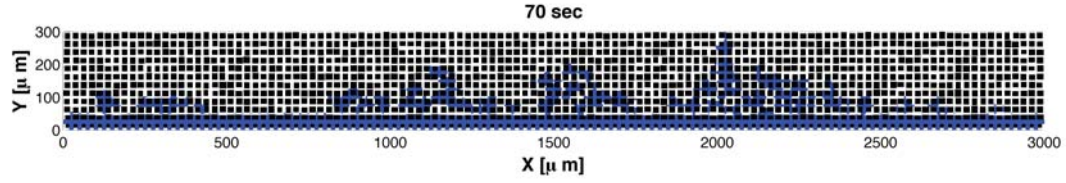


(b) Transition film model pressure distribution at 60% RH and 70°C with an 9.7 μm mean pore size.

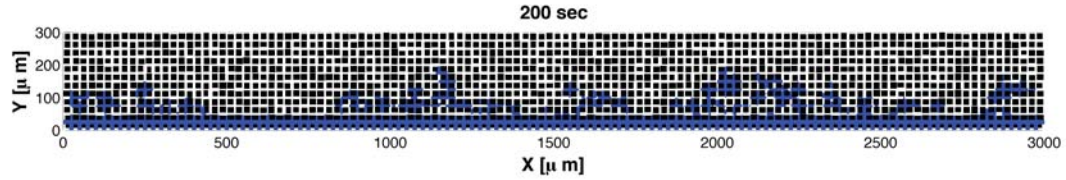
Figure 4.9: Pressure distribution for the 60% relative humidity, 80°C and 9.7 μm mean pore size.

models. However, the flooding is exaggerated by the under-prediction of evaporation rates when using the diffusive model.

In the liquid phase water saturation plots for the 8.7 μm mean pore radius much larger differences can be seen. At 70 seconds the diffusive evaporation model reaches the gas channel and the simulation is stopped which can be seen in Figure 4.11 when all the parameters plotted flat-line. The flat-line is caused by the computational model freezing the results for the remainder of the simulation to reduce computational time on a simulation that has reached the gas channel. For comparison purposes the values of both models are evaluated at the point where the liquid reaches the gas channel in the diffusive model and after 200 seconds has elapsed in the transition film model.



(a) Diffusive model percolation at 60% RH and 70°C with an 8.7 μm mean pore size.



(b) Transition film model percolation at 60% RH and 70°C with an 8.7 μm mean pore size.

Figure 4.10: Percolation of liquid water from the catalyst layer at 60% RH and 70°C for the 8.7 μm mean pore size. (a) Diffusive evaporation model, (b) transition film evaporation model.

Table 4.3 shows the values for the final evaporated volume as well as the evaporated volume at 70 seconds, for the diffusive model these values are the same. It can again be noticed that the evaporation rates predicted by the transition film model are larger than that predicted by the diffusive model, this is the primary reason why the diffusive model had percolated through to the gas channel and the transition film model did not.

Table 4.3

Comparison of the liquid water saturation data for the diffusive and transition film models with an 8.7 μm mean pore size.

	Diffusive Model	Transition Film Model at 70s	Transition Film Model
Total Evaporated Volume	0.23%	0.25%	0.91%
Occupied Volume	0.393%	0.379%	0.388%
Front Length	2.24%	2.01%	2.12%

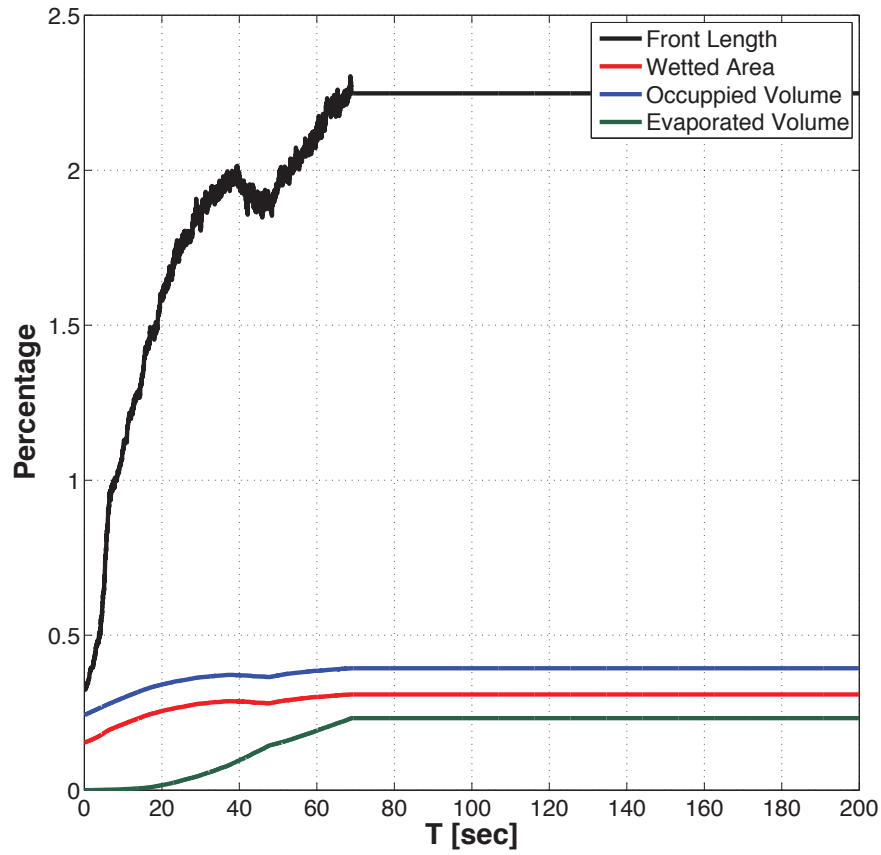


Figure 4.11: PTL saturation of liquid water from the catalyst layer at 60% RH and 70°C for the 8.7 μm mean pore size with the diffusive evaporation model.

Looking at the temperature distribution for the smaller mean pore size with the larger pore distribution results in nearly identical temperature profiles. This is likely due to the much larger solid volume in this pore size distribution. Because there is a larger volume of solid, or carbon, in this simulation the thermal resistance circuit becomes dominated by the solid component thus the liquid/air components of the thermal resistance model become much larger than the solid phase.

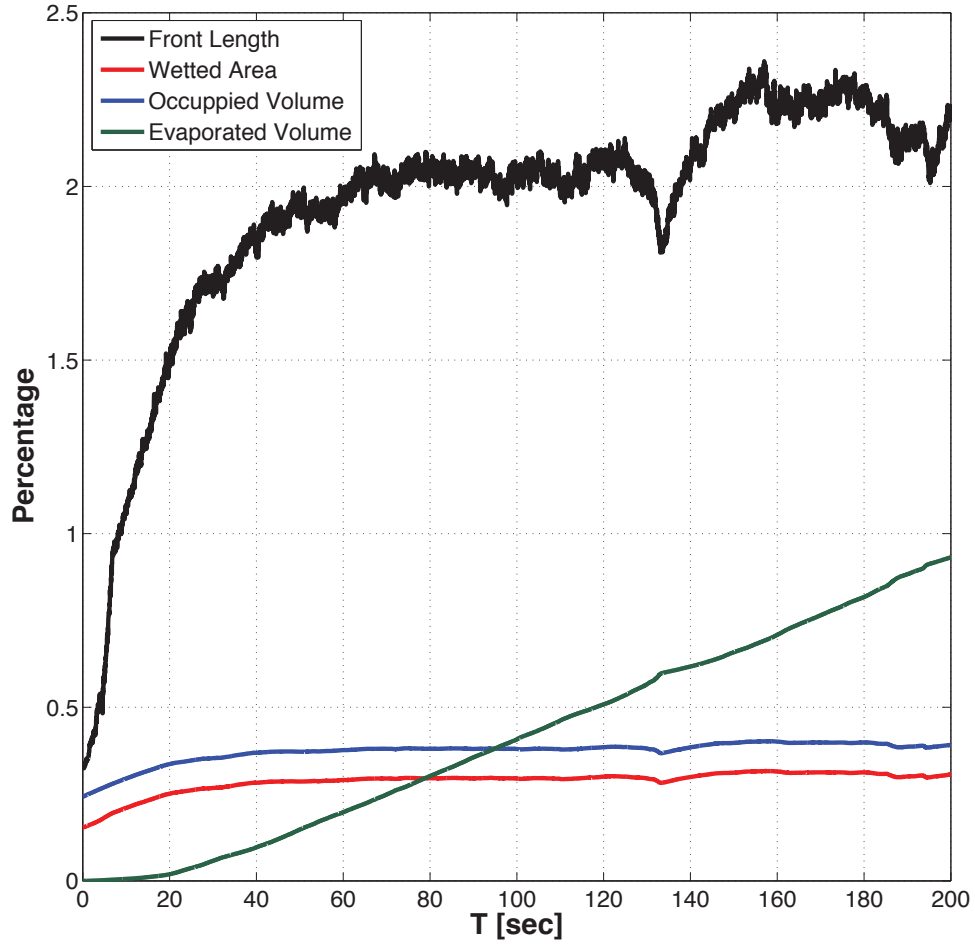
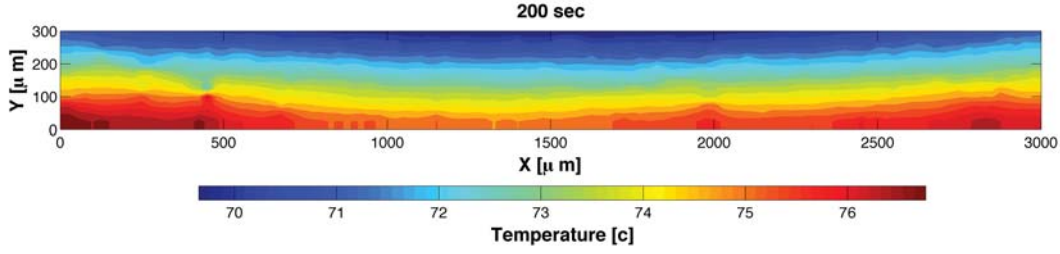
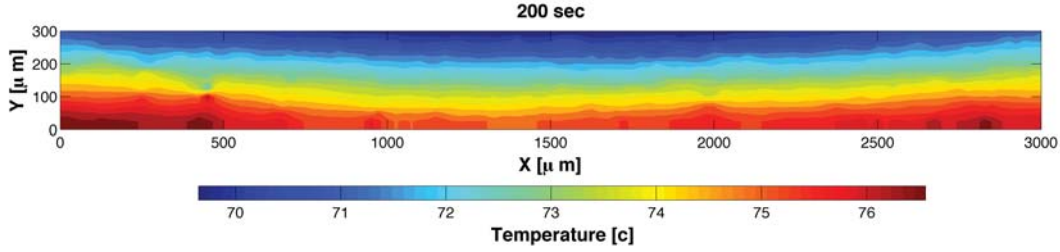


Figure 4.12: PTL saturation of liquid water from the catalyst layer at 60% RH and 70°C for the 8.7 μm mean pore size with the transition film evaporation model.

The effect of the evaporating water is greatly reduced, aside from the thermal conductivity being dominated by the solid phase the interface area becomes much smaller which will result in an overall reduction in total heat loss due to phase change compared to the slightly larger pore size. This can be seen in figure 4.14 where the average temperature profiles for both models become very close. This is mostly due to the dominance of the R_s term in the



(a) Diffusive model temperature distribution at 60% RH and 70°C with an 8.7 μm mean pore size.



(b) Transition film model temperature distribution at 60% RH and 70°C with an 8.7 μm mean pore size.

Figure 4.13: Temperature distribution for the 60% relative humidity, 80°C and 8.7 μm mean pore size.

thermal resistance model.

In the saturation distribution plots for the 8.7 μm mean pore size simulations the liquid water reaches the channel. In Figure 4.15(a) the fully saturated area can be seen to almost reach the channel, this is because of the strictly enforced boundary conditions of 60% RH in the channel. This is why the simulation must stop once the finger reaches the gas channel.

Finally in the 60% RH and 80°C case there are the pressure distribution plots. As discussed earlier the transition film pressure distribution is showing a “hotspot” on the pressure distribution from the liquid water finger reaching a node with smaller pores. This has caused the pressure to spike locally making the rest of the percolating front more difficult to see.

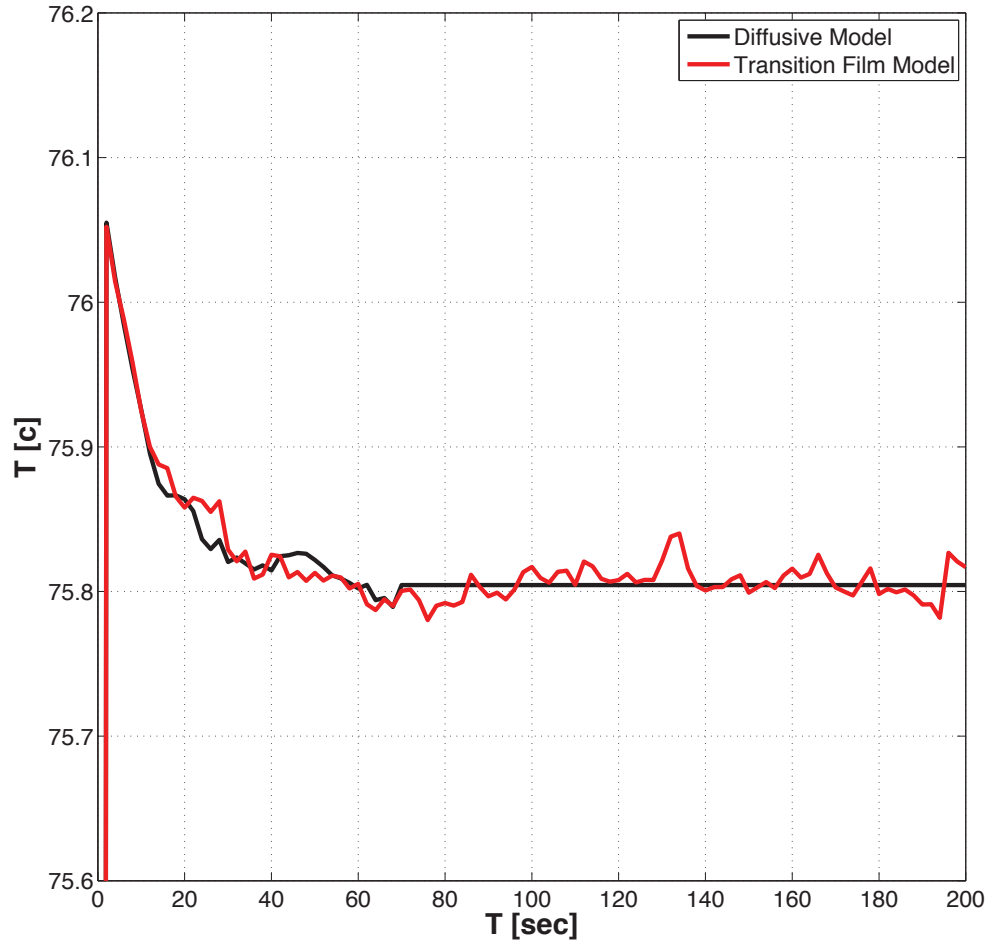
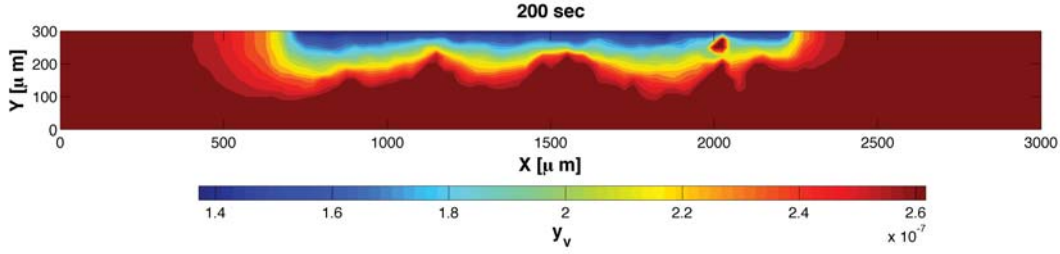


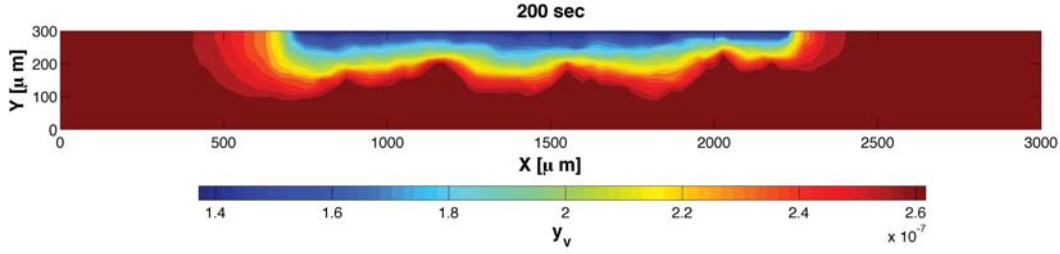
Figure 4.14: Average temperature of the domain throughout the simulation for both the transition film and diffusive models with a mean pore size of $8.7\mu m$.

It is because of this that the intensities of each plot cannot be compared to one another as the pressure range can differ greatly from one simulation to the next.

Figure 4.17 shows a typical average pressure plot created by the pore network model. Here the red curve illustrates the average pressure across the liquid vapor interface which is a



(a) Diffusive model saturation distribution at 60% RH and 70°C with an 8.7 μm mean pore size.

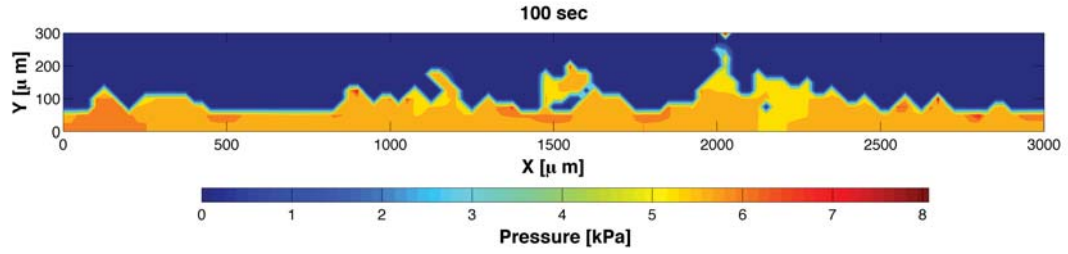


(b) Transition film model saturation distribution at 60% RH and 70°C with an 8.7 μm mean pore size.

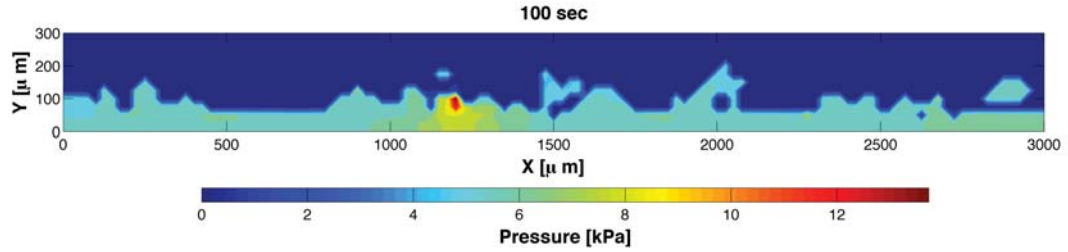
Figure 4.15: Saturation distribution for the 60% relative humidity, 80°C and 8.7 μm mean pore size.

function of the radii of the pores the liquid occupies. The average pressure at the liquid-vapor interface exhibits so a range of “noise” because at each time step the liquid front has a wide range of new pore radii which in turn can change the average pressure seen at the liquid front significantly. The black curve is the injection pressure at the catalyst layer, this is a result of the amount of pressure required to inject the quantity of water that is produced at each time step from the chemical reaction at the catalyst layer.

The next sections will discuss more simulations comparing the two evaporation models. The simulations will examine a moderate temperature and relative humidity as well as a high temperature and high relative humidity case. For these simulations only the percolation plots, and the liquid saturation curves will be shown as the temperature, pressure



(a) Diffusive model pressure distribution at 60% RH and 70°C with an 8.7 μm mean pore size.



(b) Transition film model pressure distribution at 60% RH and 70°C with an 8.7 μm mean pore size.

Figure 4.16: Pressure distribution for the 60% relative humidity, 80°C and 8.7 μm mean pore size.

and saturation distributions remain similar in trend to the 60% RH and 70°C case, these plots are also not necessary for this investigation. The extreme cases are modeled to show a range of results that best represents the overall trend on the differences between the two models. Other simulations that have been tested have results that lie within the confines of the three simulations presented in this chapter. Some of the simulated operating conditions that are not presented in this chapter can be found in the Appendix.

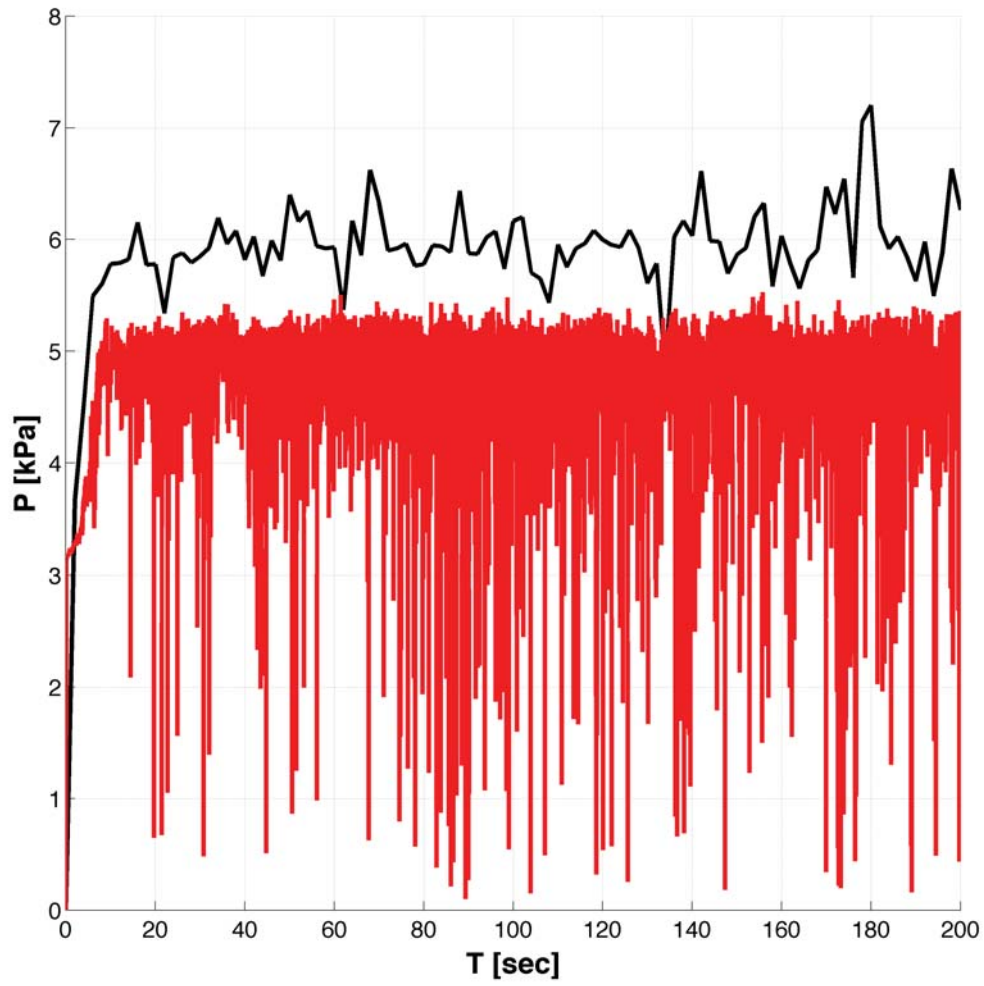
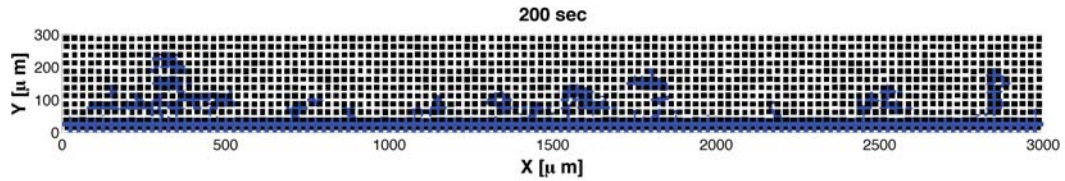


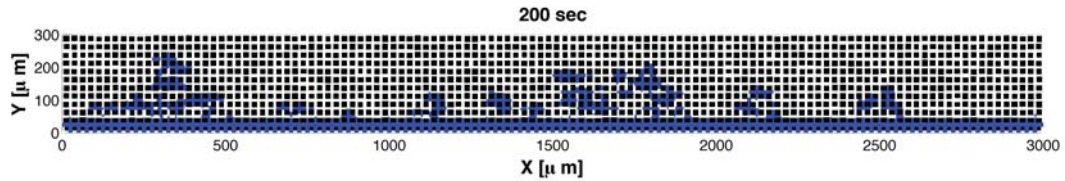
Figure 4.17: Injection pressure at the catalyst layer (black) and pressure at the liquid vapor interface (red) for the transition film model at 60% RH and 70°C with the 8.7 μm mean pore size.

4.2 Diffusive/Transition Film Model Comparison at 70% Relative Humidity and 75°C

The differences in the diffusive model and the transition film model will be explored, presenting in this section a moderate case ($\phi = 70\%$ and $T = 75^\circ\text{C}$) for two different pore size distributions. Figure 4.18 demonstrates the percolation of liquid water as calculated by the diffusive model 4.18(a), and the transition film model 4.18(b).



(a) Diffusive model percolation at 70% RH and 75°C with a 9.7 μm mean pore size.



(b) Transition film model percolation at 70% RH and 75°C with a 9.7 μm mean pore size.

Figure 4.18: Percolation of liquid water from the catalyst layer at 70% RH and 75°C for the 9.7 μm mean pore size. (a) Diffusive evaporation model, (b) transition film evaporation model.

Upon inspection of the percolation plots in Figure 4.18 the difference between the two models is difficult to discern. A small difference in liquid water distribution is evident, but the quantity of liquid water cannot be determined. To analyze these subtle differences the

Table 4.4

Comparison of the liquid water saturation data for the diffusive and transition film models with a $9.7\mu m$ mean pore size.

	Diffusive Model	Transition Film Model
Total Evaporated Volume	0.81%	0.78%
Occupied Volume	0.335%	0.339%
Front Length	2.10%	2.18%

liquid saturation plots must be evaluated. Figures 4.19 and 4.20 show the liquid saturation curves, here the front length curve is a percentage of the two-dimensional interface length normalized with the total of all the pore diameters. The wetted area is the percentage of two-dimensional area occupied by the liquid phase which is normalized with the area of all the pores in the domain. The occupied volume is the percentage of the total pore volume occupied by liquid water normalized with the total pore volume in the domain. The evaporated volume is the percentage of the total volume of liquid water that has evaporated throughout the simulation. These values are all given as a percentage of the total possible within the domain to make direct comparisons between simulations with different pore distributions and mean pore sizes possible.

It can be seen in table 4.4 that the diffusive model has predicted higher evaporation rates than the transition film model, this is because the mean pore size with a liquid water interface is larger than the mean pore size of the entire domain. This makes sense as the flow of

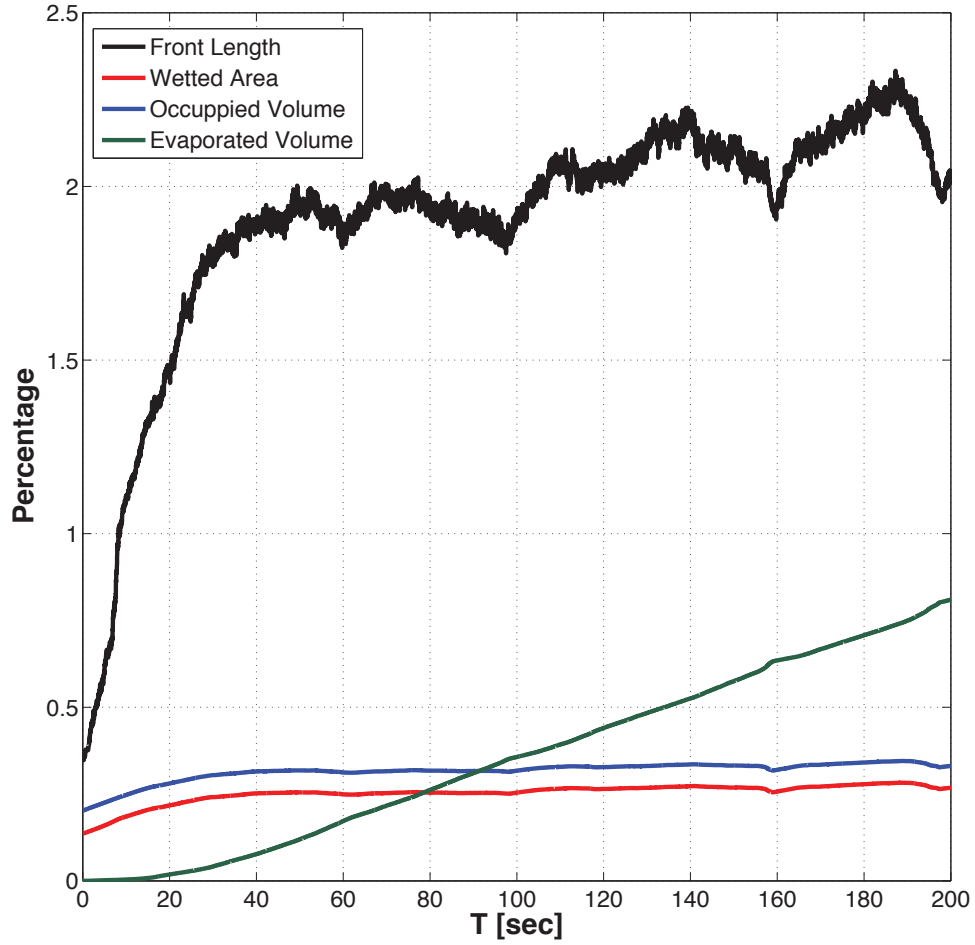


Figure 4.19: PTL saturation of liquid water from the catalyst layer at 70% RH and 75°C for the 9.7 μm mean pore size with the diffusive evaporation model.

liquid water is determined by the driving pressure and the pores that have the lowest resisting capillary forces, and the pores with the lowest capillary forces happen to be the largest pores. The larger-than-average pore size occupied by the liquid phase water is causing the diffusive model to predict higher evaporation rates. The data shown in table 4.4 for front length and occupied volume is the average of the final 20 seconds of the simulation, this is

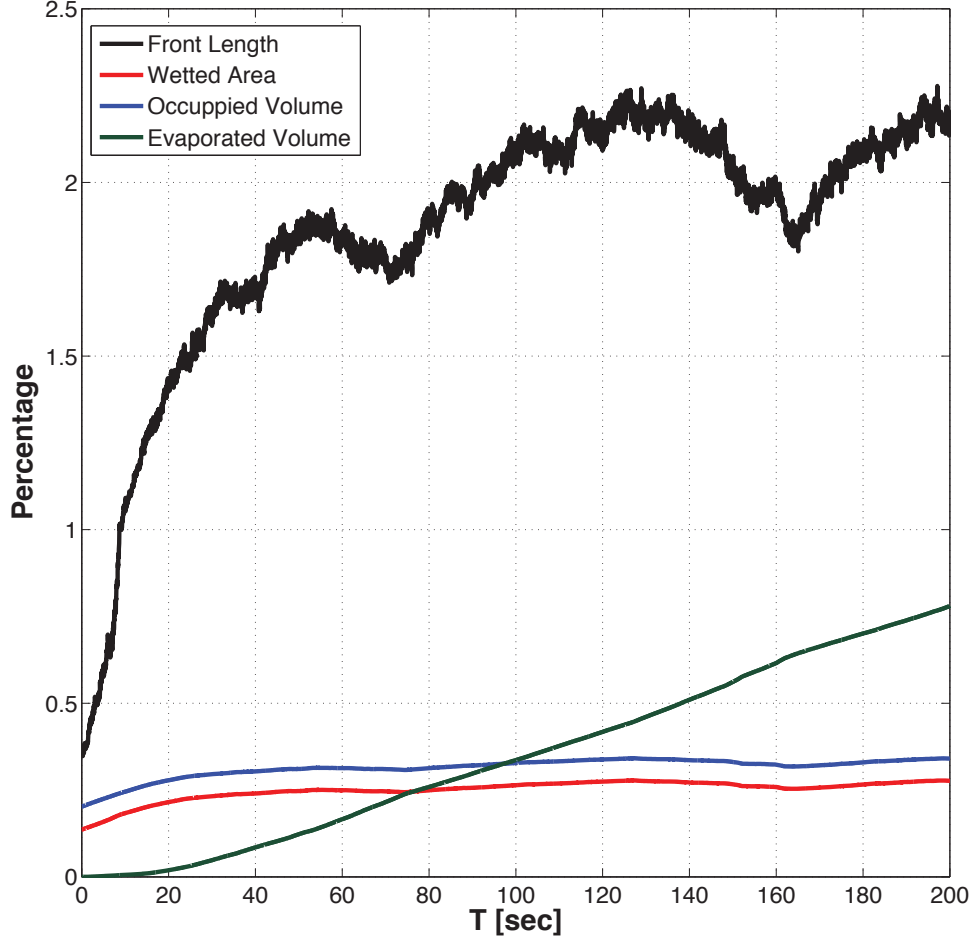
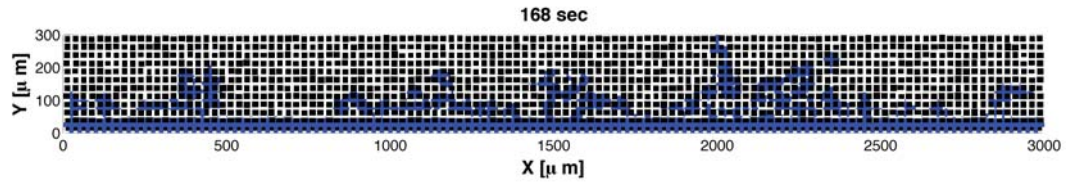


Figure 4.20: PTL saturation of liquid water from the catalyst layer at 70% RH and 75°C for the 9.7 μm mean pore size with the transition film evaporation model.

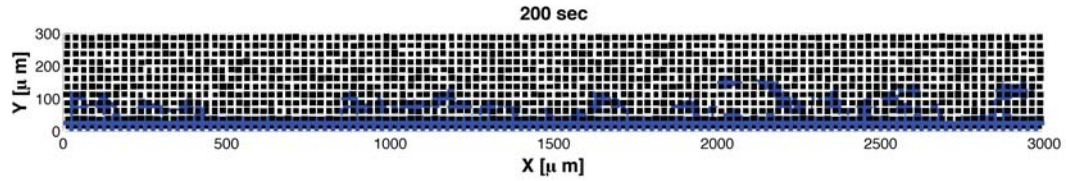
done to make a fair comparison as using just the final point could be misleading due to the sinusoidal nature of these parameters.

The mean pore size was reduced to 8.7 μm with a distribution that follows the Weibull PDF shown in figure 4.1 and a shape and scale value of $k = 4$ and $\psi = 9.25$ respectively. The reduction of the mean pore size from 9.7 μm to 8.7 μm effectively reduces the porosity of

the PTL by 0.54%. From the simulation with an $8.7\mu\text{m}$ mean pore size shown in figure 4.21



(a) Diffusive model percolation at 70% RH and 75°C with an $8.7\mu\text{m}$ mean pore size.



(b) Transition film model percolation at 70% RH and 75°C with an $8.7\mu\text{m}$ mean pore size.

Figure 4.21: Percolation of liquid water from the catalyst layer at 70% RH and 75°C for the $8.7\mu\text{m}$ mean pore size. (a) Diffusive evaporation model, (b) transition film evaporation model.

a clear difference in liquid water distribution and quantity can be seen. Without studying the liquid water saturation plots an obvious difference in evaporation rates can be noticed as after 168 seconds the diffusive evaporation model was stopped because the liquid water had reached the gas channel while the transition film evaporation models liquid water had never reached the gas channel through the duration of the simulation.

Both the transition film and the diffusive models have shown that there are certain areas of the PTL that are prone to the build up of liquid water, however the smaller pore size causes the diffusive model to grossly under-predict the evaporation rates and this flooding phenomenon is greatly exaggerated by the diffusive model. As discussed previously the

transition film model is capable of accurately modeling any pore size and thus the over/under prediction problems that plague the diffusive model are addressed with the transition film model.

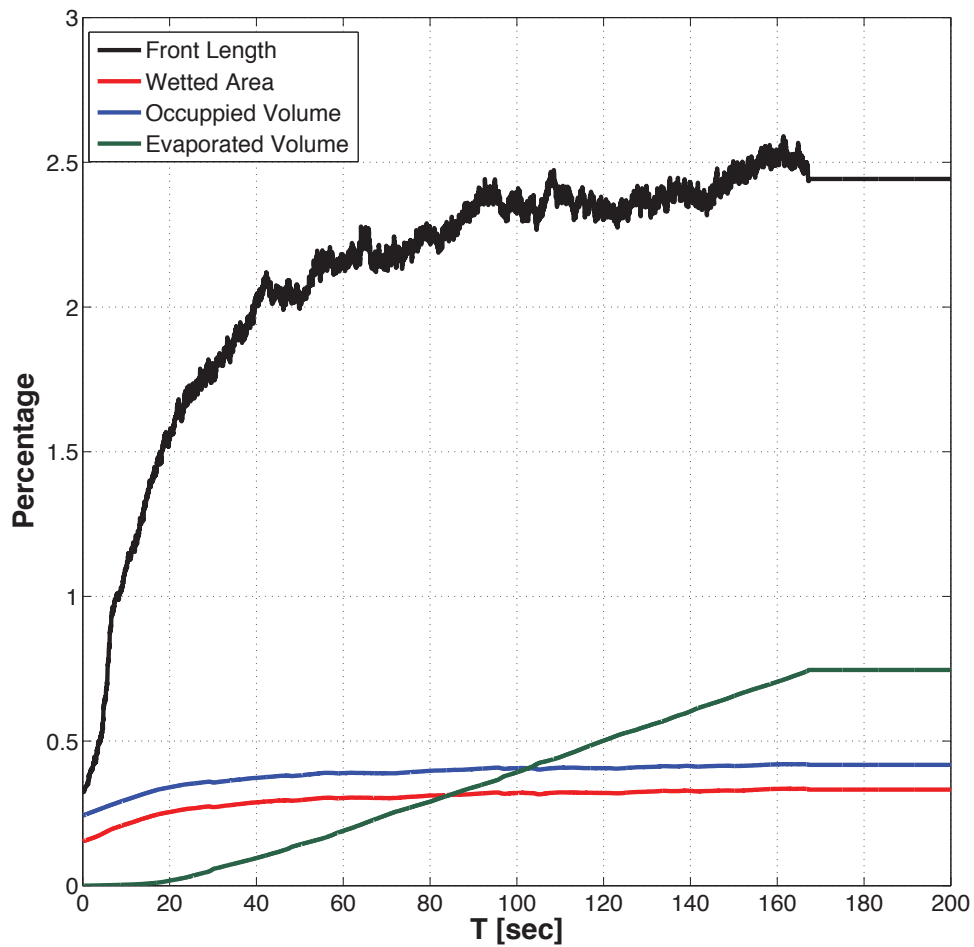


Figure 4.22: PTL saturation of liquid water from the catalyst layer at 70% RH and 75°C for the 8.7 μ m mean pore size with the diffusive evaporation model

For continuity table 4.5 shows the values of the total mass evaporated and the average of

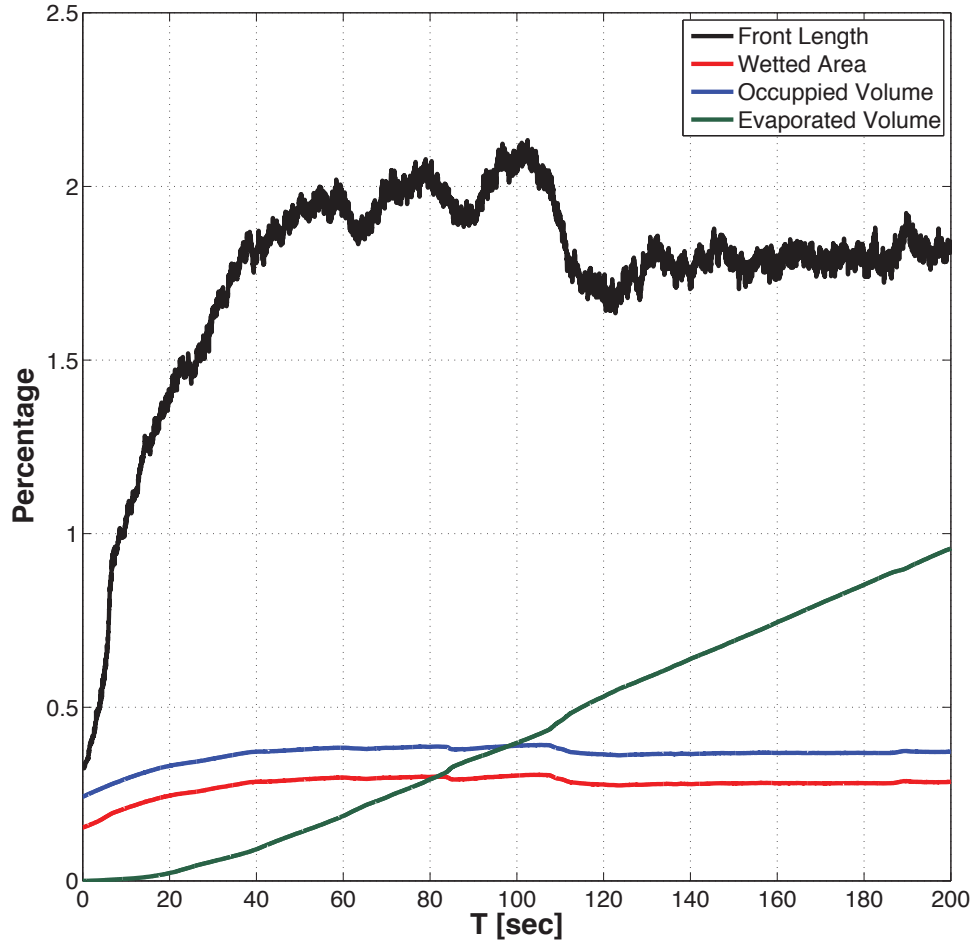


Figure 4.23: PTL saturation of liquid water from the catalyst layer at 70% RH and 75°C for the 8.7 μm mean pore size with the transition film evaporation model.

the last 20 seconds of simulation (in the case of the diffusive model the last 20 seconds of simulation prior to the breaching of the gas channel was used) for the occupied volume and front length curves. These results, as expected, show that the transition film model predicts much higher evaporation rates while the diffusive model is under-predicting the evaporation rates.

Table 4.5

Comparison of the liquid water saturation data for the diffusive and transition film models with an $8.7\mu m$ mean pore size.

	Diffusive Model	Transition Film Model at 168s	Transition Film Model
Total Evaporated Volume	0.75%	0.79%	0.93%
Occupied Volume	0.418%	0.369%	0.372%
Front Length	2.44%	1.79%	1.82%

For the moderate temperature and relative humidity simulations in a reduced porosity PTL the transition film model shows clear advantages over diffusive models. The results shown in table 4.5 are for two different times of the transition film simulation as the diffusive model had percolated into the gas channel at 168 seconds. The transition film 168 second column illustrates the liquid saturation outputs at the time the diffusive model reaches the gas channel. This is necessary for a direct comparison because at this point total injected liquid throughout the simulation is the same. An even larger difference between front length and occupied volumes is noticed between the two models when comparing them at the same time in the simulation.

To compare the distribution of the liquid phase water, the ratio of occupied volume to front length is introduced in figure 4.24. The percent volume to percent front length, or surface area, shows how distributed the liquid water phase is for each model. A smaller volume to surface area would mean that the liquid water is more evenly distributed over the PTL, and as expected the diffusive model appears to be more evenly distributed than the transition

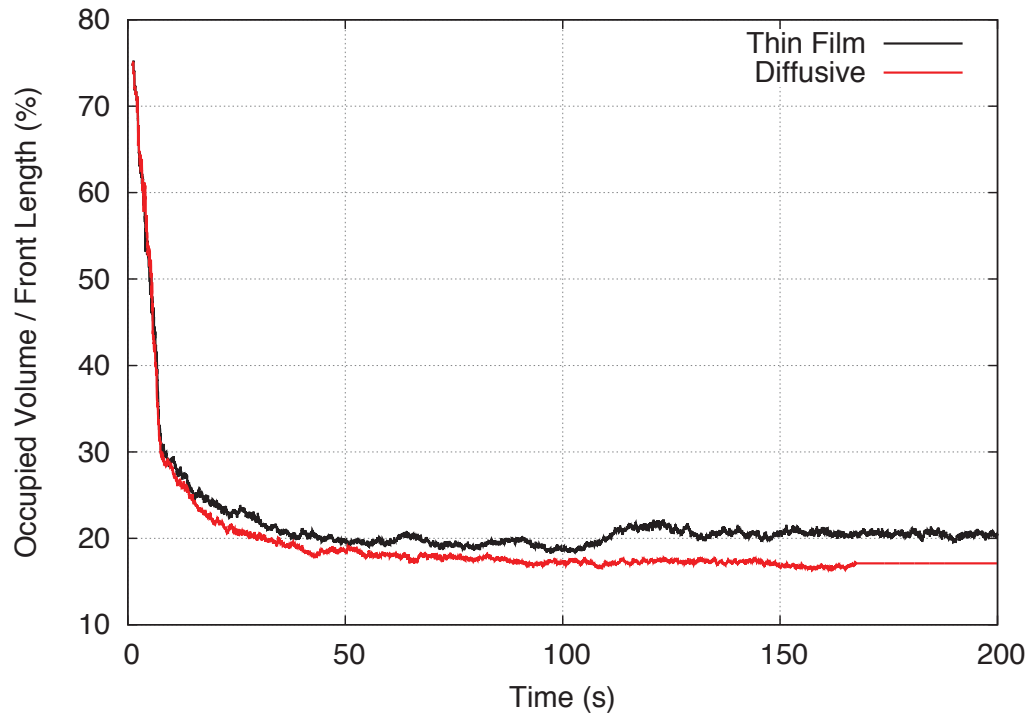
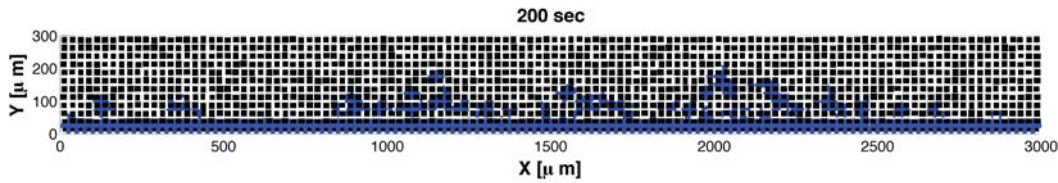


Figure 4.24: Comparison of the ratio of percent occupied volume to percent front length, illustrating the distribution of liquid water in the PTL.

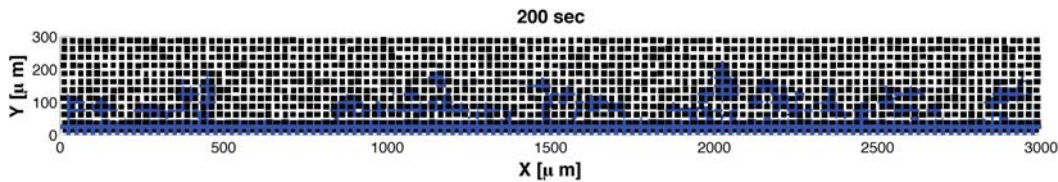
film model. The reason for this is due to the higher evaporation rates achieved by the transition film model when the liquid water gets isolated in a few pores the evaporation rates will increase causing the water to retreat to areas of greater liquid water content.

4.3 Diffusive/Transition Film Model Comparison at 80% Relative Humidity and 80°C

The results in the high relative humidity and high temperature simulation are similar to the previous cases where the changes in morphology are better captured by the transition film model. For this simulation the temperature of the land was set to 80°C and the relative humidity was set to 80%. As the relative humidity approaches 100% the two evaporative models converge, this is expected as the mechanism that is responsible for transporting the water vapor away from the liquid interface becomes less effective at higher humidities.



(a) Diffusive model percolation at 80% RH and 80°C with a 9.7 μm mean pore size.



(b) Transition film model percolation at 80% RH and 80°C with a 9.7 μm mean pore size.

Figure 4.25: Percolation of liquid water from the catalyst layer at 80% RH and 80°C for the 9.7 μm mean pore size. (a) Diffusive evaporation model, (b) transition film evaporation model.

The percolation plots show a similar trend for both the transition film and the diffusive

evaporation models with these operating conditions. The distributions are close as well as the overall liquid water present. This is expected with the higher relative humidities for the cell operating conditions.

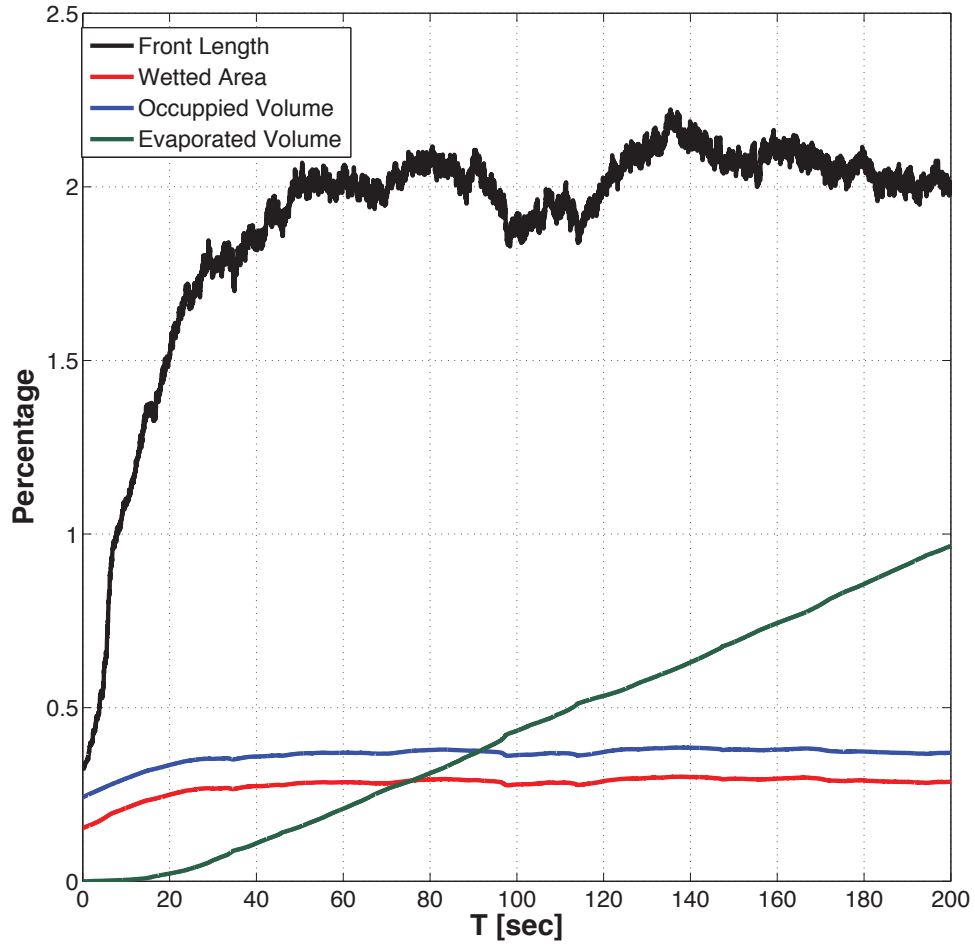


Figure 4.26: PTL saturation of liquid water from the catalyst layer at 80% RH and 80°C for the 9.7 μ m mean pore size with the diffusive evaporation model.

Table 4.6 shows the final total evaporated volume and the average of the final 20 seconds of simulation. The diffusive model is again over-predicting the evaporation rates because

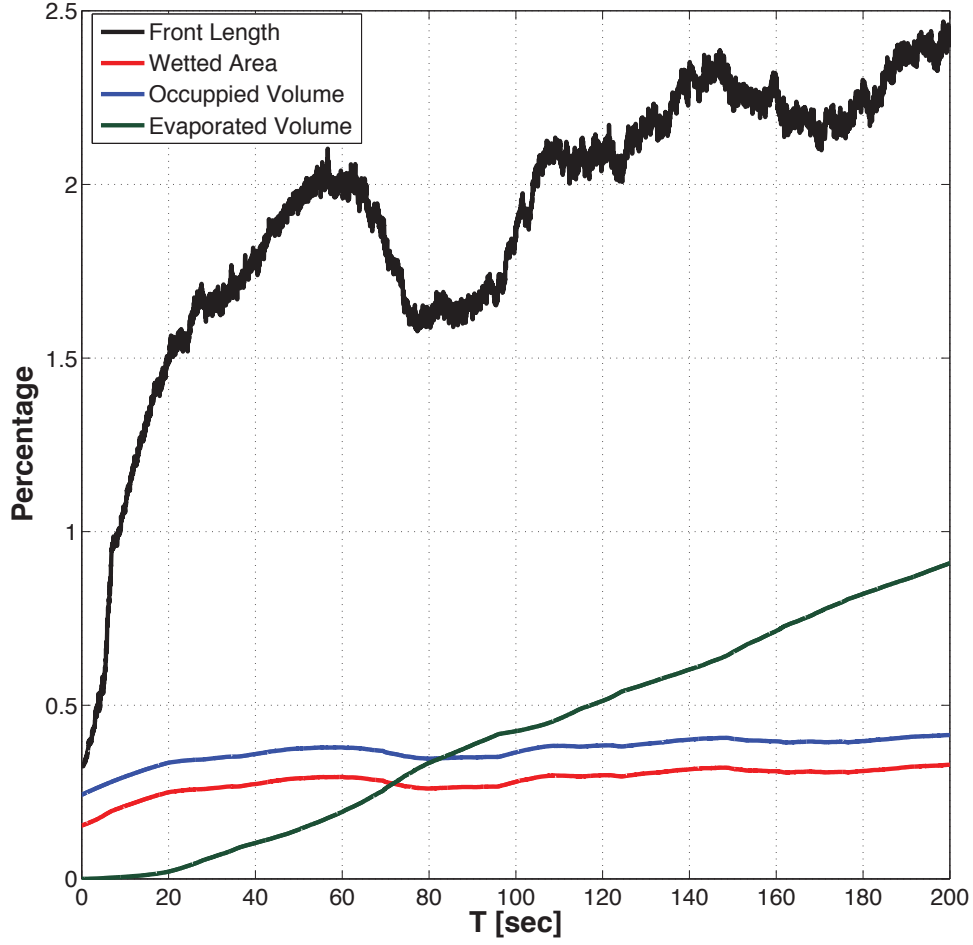


Figure 4.27: PTL saturation of liquid water from the catalyst layer at 80% RH and 80°C for the 9.7 μm mean pore size with the transition film evaporation model.

though the mean pore size is 9.7 μm the average pore size that has a liquid-air interface that is greater than 9.7 μm due to the nature of the liquid percolation filling the largest pores first.

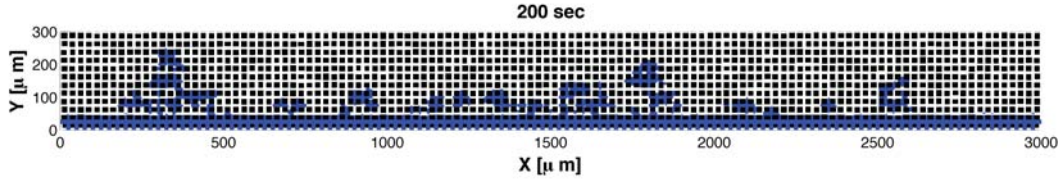
With the smaller mean pore size at 8.7 μm the evaporation rates are again higher for the transition film model however, due to the higher relative humidity in this simulation the

Table 4.6
Comparison of the liquid water saturation data for the diffusive and transition film models with an $9.7\mu m$ mean pore size.

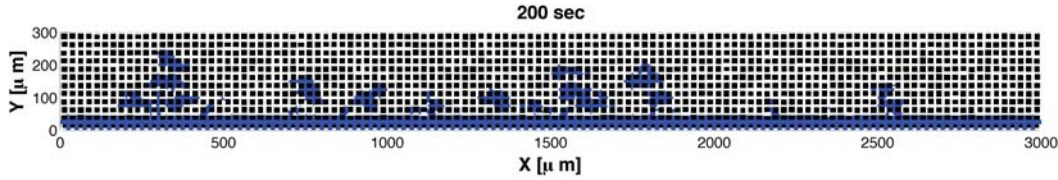
	Diffusive Model	Transition Film Model
Total Evaporated Volume	0.97%	0.90%
Occupied Volume	0.369%	0.411%
Front Length	2.01%	2.39%

results are much closer than under the previously examined operating conditions. The overall effect of evaporation is dampened by the higher humidity in this simulation and the results reflect this. The evaporation models are responsible for transferring the liquid phase into the vapor phase, but it is the concentration gradients and the vapor phase modeling that is responsible for transporting the evaporated vapor from the liquid water interface to the gas channel. With higher relative humidities the concentration gradient is much lower creating a lower driving force removing the evaporated vapor thus slowing the evaporation rates for both models. If the relative humidities were to increase to 100% both evaporation models would be essentially shut off and the pore network model would be only modeling the liquid percolation through the PTL.

The liquid phase saturation plots (figures 4.29 and 4.30) show there is less liquid water present after the simulation in the transition film model than found in the diffusive model. The distribution of the liquid water is also more spread out in the diffusive model, consistent with the previous simulations.



(a) Diffusive model percolation at 80% RH and 80°C with an 8.7 μm mean pore size.



(b) Transition film model percolation at 80% RH and 80°C with an 8.7 μm mean pore size.

Figure 4.28: Percolation of liquid water from the catalyst layer at 80% RH and 80°C for the 8.7 μm mean pore size. (a) Diffusive evaporation model, (b) transition film evaporation model.

In both of the models, the transition film and the diffusive model, for the 80% relative humidity 70°C and temperature case the liquid water saturation plots show multiple dips as the simulation runs. These like in the earlier cases are due to the liquid phase getting close to the lower relative humidity gas channel. In the gas channel the humidity is constant which causes sharp gradients in the concentration as the liquid approaches the channel. Under these operating conditions the frequency of the advancement and retraction are higher, this is because in this simulation the relative humidity is higher than in the earlier simulations. The pore distribution and the location of the liquid phase water also plays a role in how much and when the advancing fluid will retract. As the liquid phase approaches the gas channel the concentration gradient may become large enough to increase the evaporation rates and cause the fluid front to retreat.

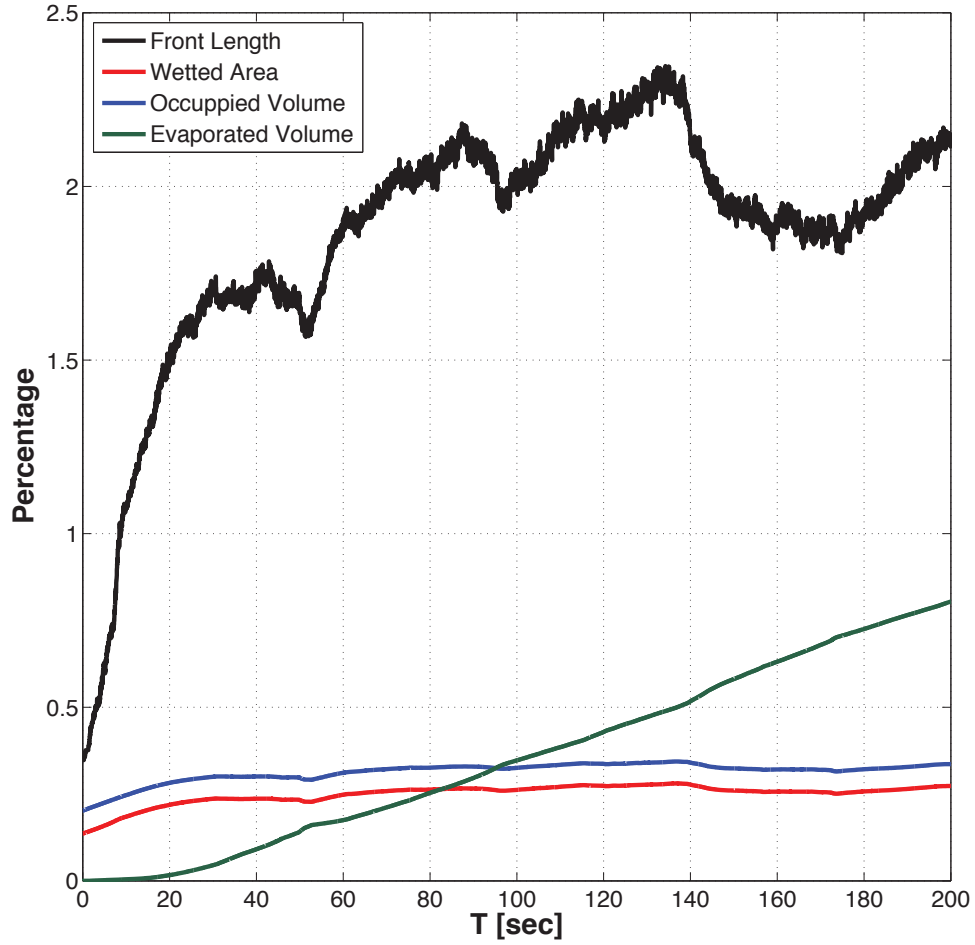


Figure 4.29: PTL saturation of liquid water from the catalyst layer at 80% RH and 80°C for the 8.7 μm mean pore size with the diffusive evaporation model.

Table 4.7 shows that the evaporation models under investigation here become very close under the higher humidity operating conditions. The results for this simulation are the closest of all under consideration. Despite the high humidities the transition film model still predicts evaporation rates more accurately, especially when the pore size varies. Having this ability in an evaporation model is very important when modeling the phenomenon in

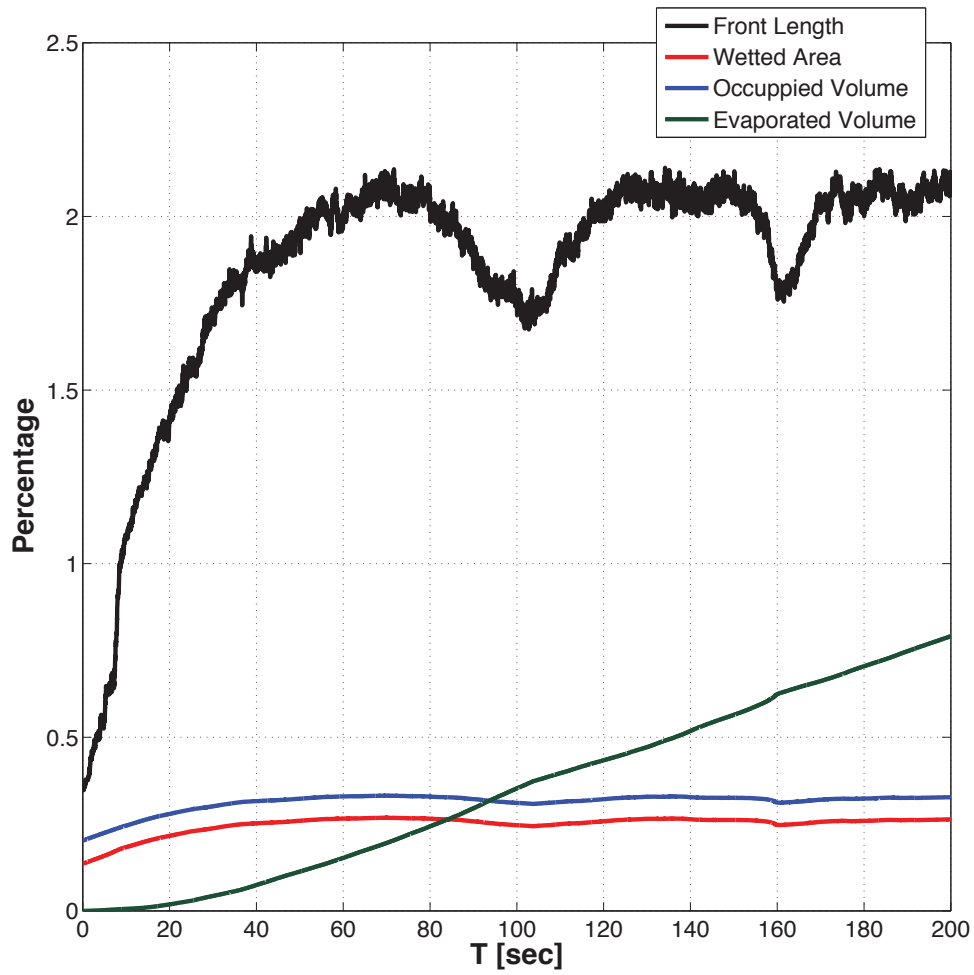


Figure 4.30: PTL saturation of liquid water from the catalyst layer at 80% RH and 80°C for the 8.7 μm mean pore size with the transition film evaporation model.

a fuel cell. The added versatility that the transition film model brings to the pore network model is essential when modeling a PTL, especially one that has a microporous layer as this layer introduces a large variation in the pore size seen in the modeling domain.

Table 4.7
Comparison of the liquid water saturation data for the diffusive and transition film models with an $8.7\mu m$ mean pore size.

	Diffusive Model	Transition Film Model
Total Evaporated Volume	0.79%	0.80%
Occupied Volume	0.333%	0.326%
Front Length	2.10%	2.07%

4.4 Diffusive/Transition Film Model Comparison at 80% RH and 75°C With a Microporous Layer

The MPL is added to a fuel cell to reduce losses, improve overall performance and increase the range of external operating conditions. This is achieved by focusing on the mass transport losses and the water management. Through the use of an MPL the membrane has better hydration levels and the flooding in the PTL is reduced^{129,130}. Experimentally the MPL has been shown to significantly improve the overall PEM fuel cell performance^{129–134}. Chen and Gao¹³⁵ have found that at 0.2V the current density produced by a cell with an MPL is nearly $2 A/cm^2$ greater than the same cell without an MPL. Many other researchers have found similar results^{39,40,136,137}.

To examine the effects an MPL has on the water transport through the PTL the distribution shown in Figure 4.31 was created. This distribution has three major modes, the first mode,

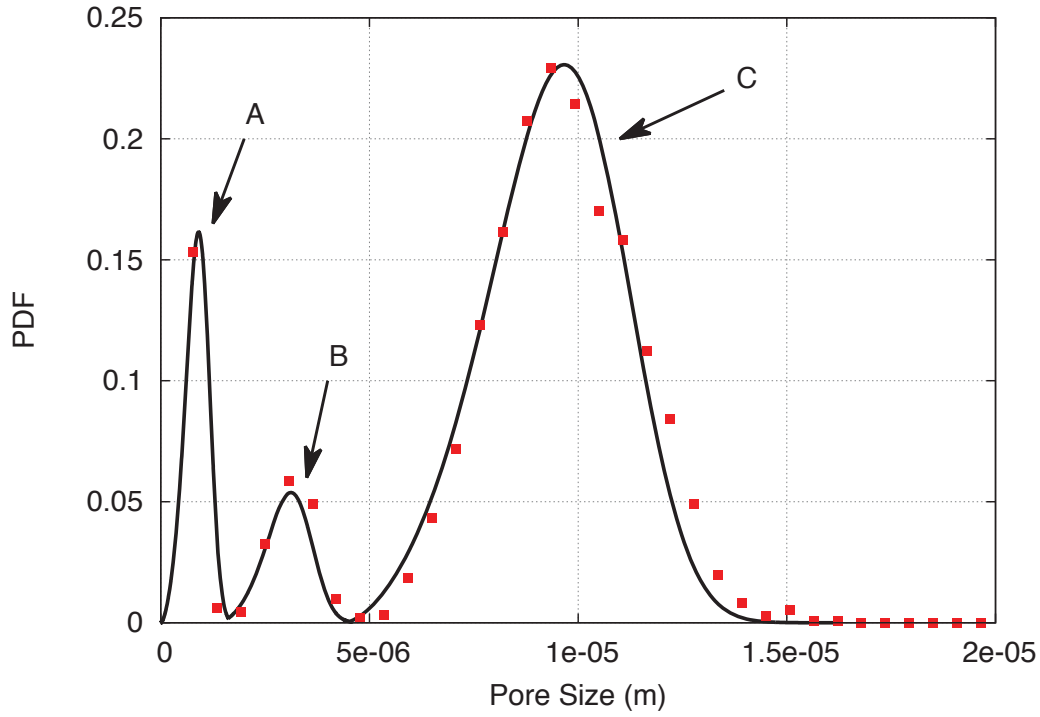


Figure 4.31: Pore size distribution for the MPL simulation. A) Pore size distribution of the MPL. B) Pore size distribution of the MPL imperfections. C) Pore size distribution of the PTL

denoted by A in Figure 4.31, is the distribution of the MPL layer. The mean pore size of the MPL layer was set to be $1.5 \mu m$ which conforms with the experimental results from Kong et al.³⁹ and Lee et al.¹³⁸. Mode B signifies the cracks and imperfections in the MPL and is found to be necessary for realistic simulations in the morphology study by Medici and Allen¹¹³. Without the existence of the imperfections the injection pressure noticed in the simulations becomes three to four times greater than the experimental results and the simulated injection pressures for a MPL that has imperfections. Finally mode B is the pore

size distribution for the PTL and pore size and distribution for this area is identical to the simulations run previously with the $9.7\mu\text{m}$ mean pore radius, only the MPL was modeled at the southern boundary.

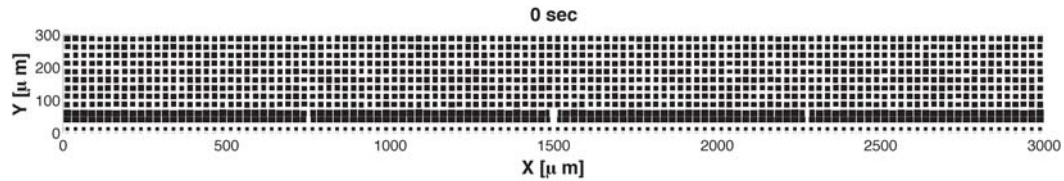
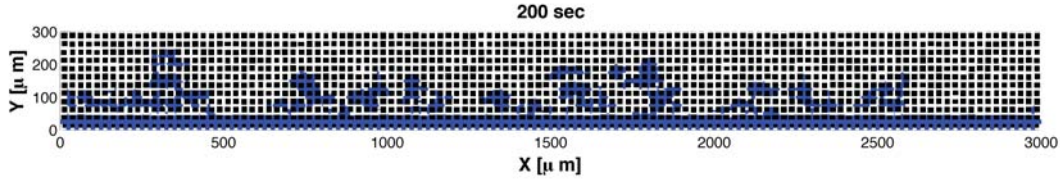


Figure 4.32: Modeling domain with MPL in the southern boundary.

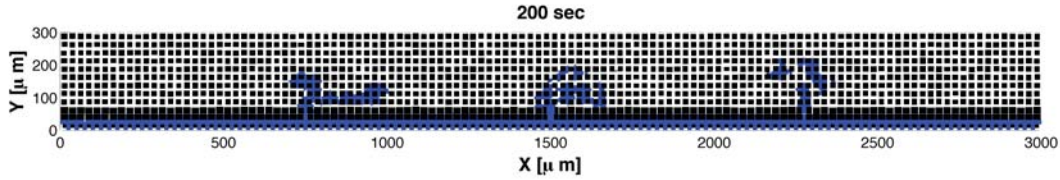
The MPL layer used in the simulations can be seen in Figure 4.32 on the southern boundary. The larger of the imperfections, or cracks can be seen in the middle of the modeling domain and the other larger imperfections are evenly distributed throughout the domain.

Investigating the percolation plots (Figure 4.33) a very large difference in water distribution can be seen especially in the case without a MPL (Figure 4.33(a)). The diffusive model has three liquid fingers all located at the large imperfections in the MPL while the transition film model exhibits three fingers that are quite small in comparison. The drastic differences in water content is expected from the results shown in the experimental work on MPLs and can be seen in the liquid phase saturation plots, Figures 4.34 and 4.35.

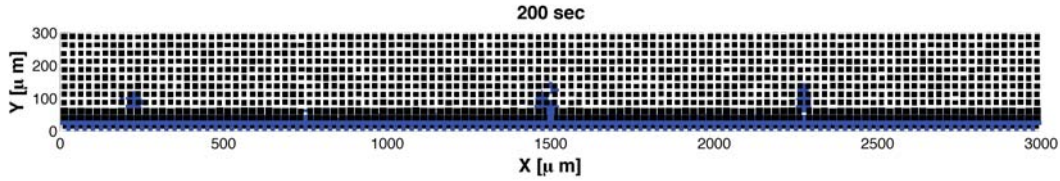
The liquid water saturation plots, Figures 4.34 and 4.35 show that the transition film model is predicting the liquid water content to be much lower than the diffusive model results. Part of the reason for this is the role the MPL takes in reducing the liquid waters ability



(a) Transition film model percolation at 80% RH and 70°C with a 9.7 μm mean pore size and no MPL



(b) Diffusive model percolation at 80% RH and 70°C with a 9.7 μm mean pore size and a MPL.



(c) Transition film model percolation at 80% RH and 70°C with a 9.7 μm mean pore size and a MPL.

Figure 4.33: Percolation of liquid water from the catalyst layer at 80% RH and 70°C for the 9.7 μm mean pore size with a MPL. (a) Transition film model with no MPL, (b) diffusive evaporation model with MPL and (c) transition film evaporation model with MPL.

to easily find a path through the PTL and restricting the injected water to the imperfection areas of the MPL. This causes a large portion of the water to enter the PTL from the MPL as a vapor, and because the amount of liquid water in the PTL is low the vapor concentration is low allowing for easier transport of the vapor to the gas channel.

The differences in the transition film and the diffusive evaporation models has been thoroughly examined, for the remainder of this section the transition film model will be

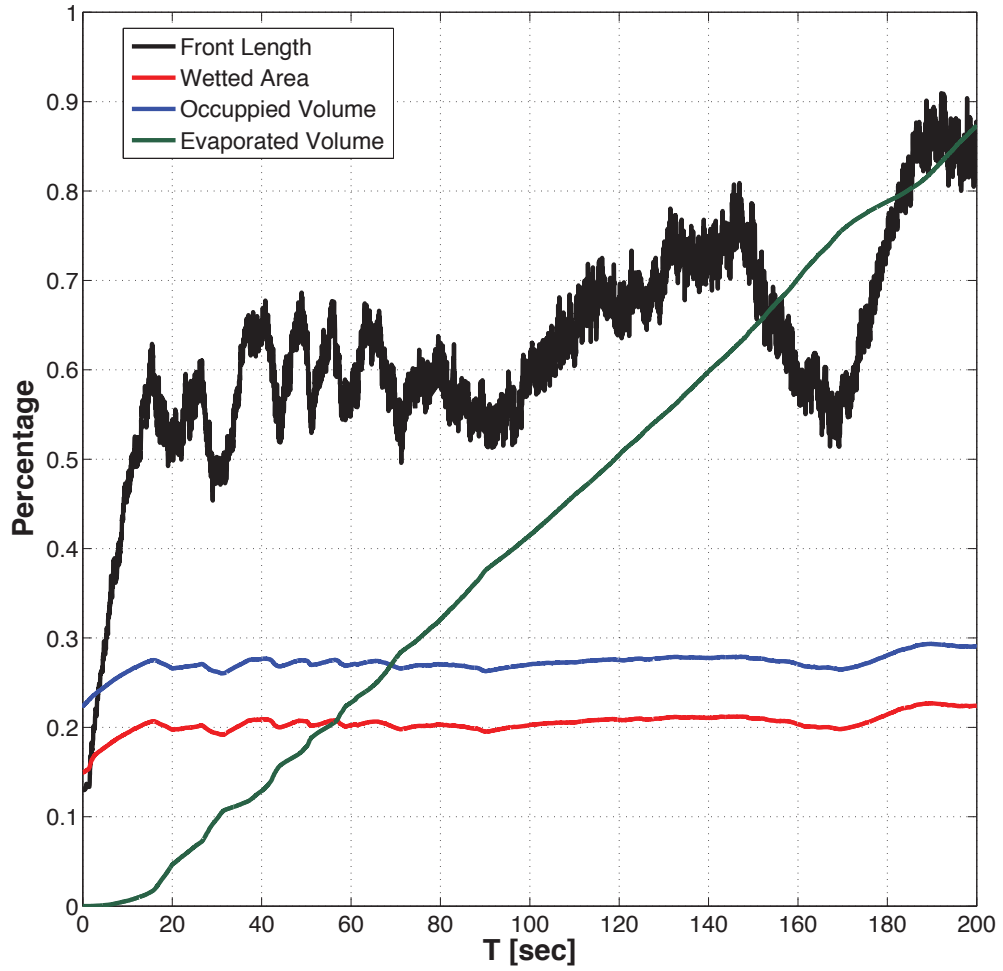


Figure 4.34: PTL saturation of liquid water from the catalyst layer at 80% RH and 80°C for the 9.7 μm mean pore size with the diffusive evaporation model.

used to examine the differences between the cases with and without the MPL. The 80% relative humidity and 70°C simulation has been chosen because the case without the MPL illustrated issues with flooding of the PTL and the ability of the MPL to reduce flooding is being explored.

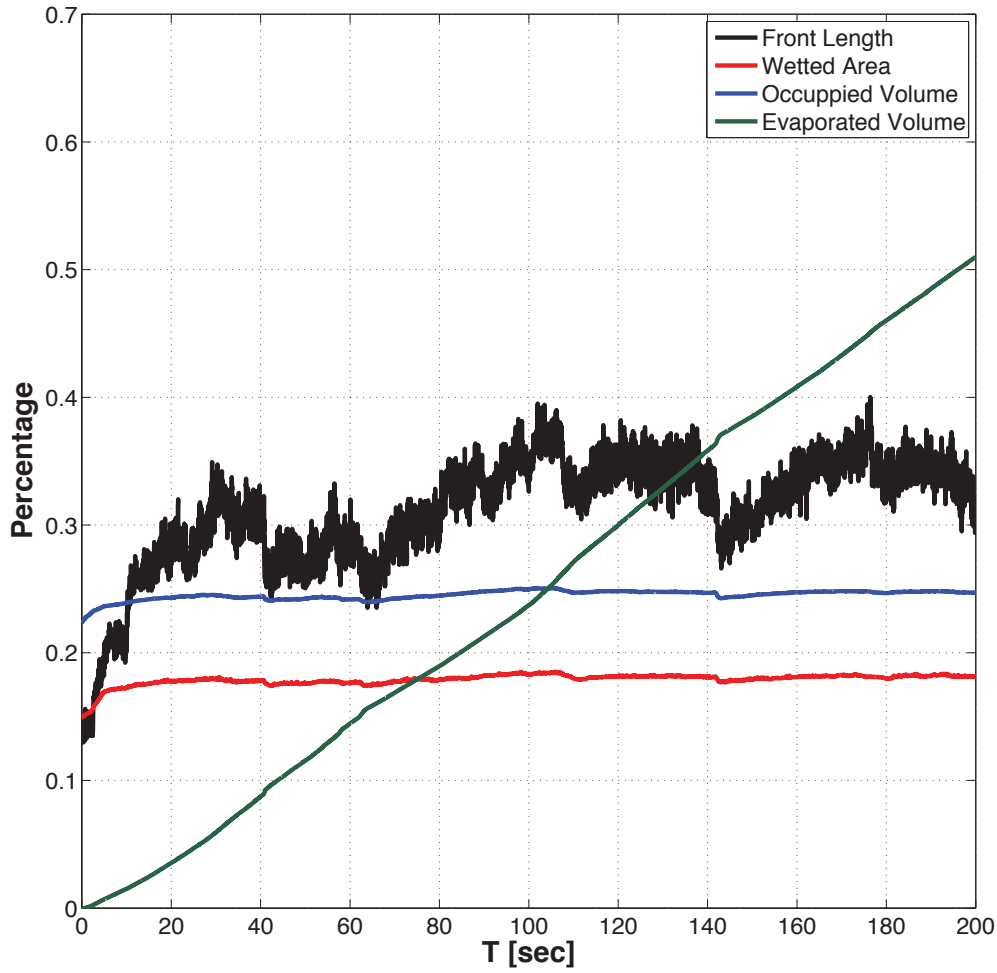
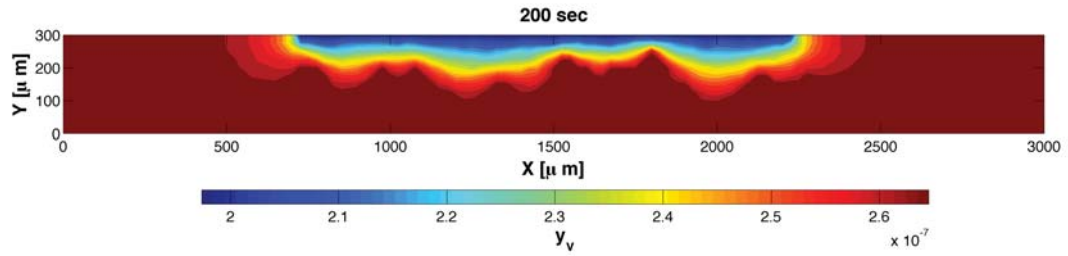


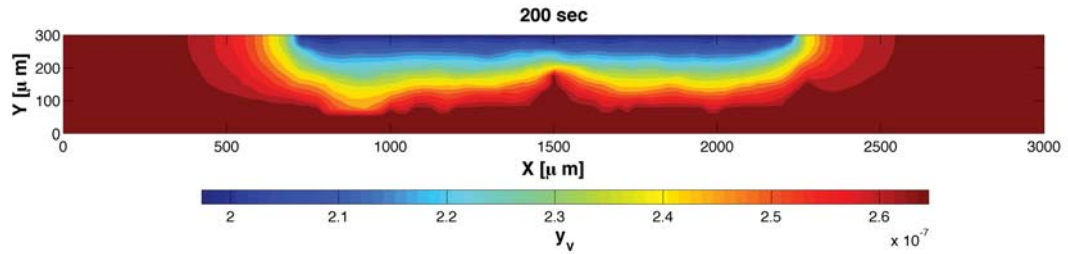
Figure 4.35: PTL saturation of liquid water from the catalyst layer at 80% RH and 80°C for the 9.7 μm mean pore size with the transition film evaporation model.

To examine why there might be such a difference in the percolation plots from the simulation with the MPL to this simulation without a MPL the vapor concentration plots can be used. These show how the MPL greatly reduces the vapor concentration throughout the PTL thereby enhancing the evaporation rates of the liquid fingers. Figure 4.36 compares the vapor concentration results of the transition film models for the cases with and without

MPLs.



(a) Transition film model vapor concentration at 80% RH and 70°C with a 9.7 μm mean pore size and no MPL.

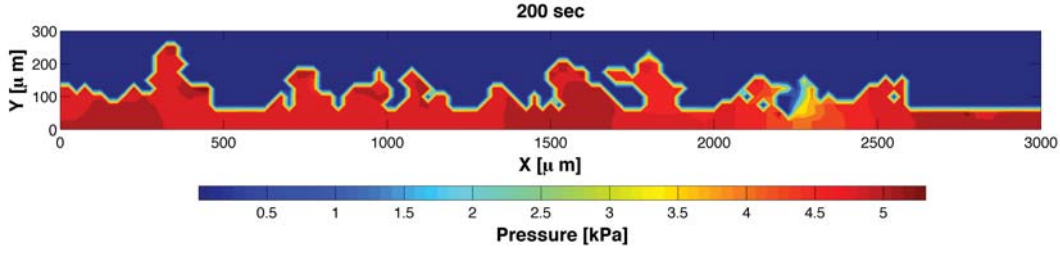


(b) Transition film model vapor concentration at 80% RH and 70°C with a 9.7 μm mean pore size and a MPL.

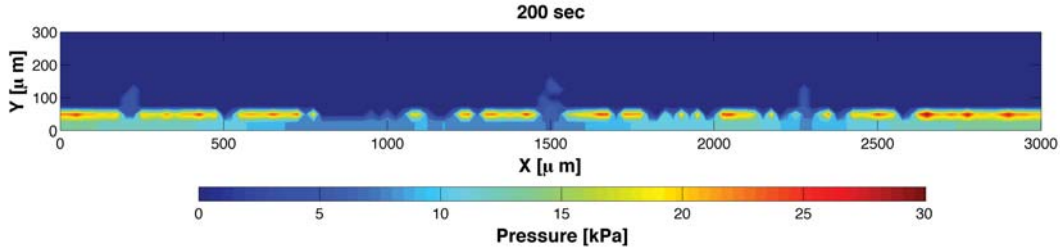
Figure 4.36: Percolation of liquid water from the catalyst layer at 80% RH and 70°C for the 9.7 μm mean pore size with a MPL. (a) without MPL, (b) with MPL.

The vapor concentration plots have show how the MPL creates a lower average relative humidity throughout the PTL. Chen et al.¹³⁹ has shown that with similar operating temperatures the MPL can reduce the overall relative humidity in the PTL by just over 20%. In this particular case 20% is the maximum difference the models could experience due to the channel relative humidity which has been set to 80%. The transition film model predicts a difference in average relative humidity through the course of the simulation of 10.4% which is expected with an 80% relative humidity.

The pressure distribution plots in Figure 4.37 show not only a large difference in maximum



(a) Transition film model pressure distribution at 80% RH and 70°C with a $9.7\mu\text{m}$ mean pore size and no MPL.



(b) Transition film model pressure distribution at 80% RH and 70°C with a $9.7\mu\text{m}$ mean pore size and a MPL.

Figure 4.37: Pressure distribution at 80% RH and 70°C for the $9.7\mu\text{m}$ mean pore size with a MPL. (a) without MPL (b) with MPL.

pressure but also how the pressure is distributed. For the case with the MPL the pressure builds up all along the MPL and is significantly lower in the percolating fluid fingers. On the contrast the simulation without a MPL has an almost evenly distributed pressure throughout the liquid phase.

4.5 Summary

A phenomenological model for evaporating transition films was implemented into a pore network model simulating two-phase flow with evaporation. This transition film model has

been shown to capture the effects of a varying pore size, effects that are not considered in the industry standard diffusive evaporation models. The simulations tested were for several different fuel cell operating conditions with two different pore distributions both with different mean pore sizes. The data presented herein was for three operating conditions that were chosen to demonstrate a wide range of conditions that would be seen in a fuel cell and show the differences between the two modeling approaches at these conditions. The range selected also illustrated how the transition film and diffusive models converge as the relative humidities become closer to saturation.

The transition film modeling approach incorporates contact line length and contact angle, both of which have proven to be large factors in determining the evaporation rates. Varying pore size and contact angles changes the curvature of the transition film region which in turn directly affects the evaporation rates. The morphology of the PTL yields a very large contact line area to volume ratio and because evaporation from the transition film region at temperatures below boiling is the primary location of phase change, this is an important inclusion in modeling evaporation in porous media. With this model contact line area, contact angle and transition film evaporation have been included into a half-cell cathode-side fuel cell model for the first time.

Chapter 5

Membrane Permeability

PEM fuel cells typically utilize a perfluorinated polymer membrane, which is responsible for the conduction of protons and the insulation of both electrons and diatomic hydrogen cross-over. The polymer membrane in a PEMFC needs to be fully hydrated to effectively achieve these responsibilities. The process of hydration is referred to as water uptake, and the level of hydration during operation is important to the life of the PEM^{2,140–142}. The length of time a membrane requires to reach a “fully saturated” state varies depending on many variables, including the phase of the water in contact with the membrane which is known as Schröder’s paradox^{143,144}. In recent work there has been conflicting results on Schröder’s paradox, and whether or not it affects the PEM ionomer^{143–148}.

To ensure the possible effects of Schröder’s paradox are accounted for Zawodzinski Jr

et al.¹⁴⁹ allowed 10 days of water vapor exposure at 30°C for their membranes to reach equilibrium, however it was mentioned that between day 5 and day 10 very little change was recorded¹⁴⁹. When the membrane reaches the fully saturated state the membranes properties are considered to be constant when in contact with water.

Many cell and stack level models use this constant property assumption for the permeability of the ionomer^{42,150}. Costamagna¹⁵⁰ derives their hydraulic permeability constant from Darcy's law in a formulation that was first used in Fales et al.¹⁵¹. Weber and Newman⁴² also assume a constant hydraulic permeability, here the value is chosen as an average of values that have been cited in the literature. Although the cited permeability values range several orders of magnitude they found that $4.7 \times 10^{-15} \text{ cm}^2$ best matched the experimental results with the simulation⁴².

Adachi et al.¹⁵² tested Nafion NR-211 pretreated as prescribed by DuPont and as received, in the protonic (H^+) state. It was found that not only is the permeability not affected by the pretreated state of the membrane, but also that the liquid equilibrated, liquid-liquid permeability coefficients are by far the largest permeation modes¹⁵².

5.1 Experiment

An experiment was designed to test the permeability of Nafion membranes as a function of both temperature and hydraulic pressure. A U-Tube configuration was built to apply a hydrostatic pressure head across the membrane with external heating lamps to increase the temperature of the entire system. The temperature can be ranged from room temperature to 80°C while the pressure can be adjusted from $\Delta p = 0 \text{ kPa}$ to $\Delta p = 10.6 \text{ kPa}$ for deionized water and $\Delta p = 19.4 \text{ kPa}$ for 3M Fluorinert FC-3283.

5.1.1 Membrane and fluids tested

The material under investigation was Nafion NR-211 and its permeability was tested with deionized water and 3M's Fluorinert (FC-3238). NR-211 is a chemically stabilized perfluorosulfonic acid / polytetrafluoroethylene (PTFE) copolymer which in these studies is tested as received, in the H^{+} state. Adachi et al.¹⁵² showed that the permeability of the Nafion membrane is identical in the H^{+} state as it is after undergoing the standard pretreatment¹⁵². The nominal thickness of the NR-211 membrane is $25.4 \mu\text{m}$ at 23°C and 50% RH. Although only a single thickness of the Nafion membrane is tested, Majsztrik et al.¹⁵³ report that the permeation rates of water through Nafion are independent of the thickness of the membrane.

The tests involving water were run using deionized water with a resistivity of $> 20\text{ M}\Omega \cdot \text{cm}$. The deionized water was used to equilibrate the Nafion membrane for a period of 14 days at room temperature prior to testing to ensure full hydration.

5.1.2 Testing apparatus

A system was designed to test the permeability of a perfluorosulfonic acid based polymer electrolyte membrane (PEM) by applying a hydraulic pressure gradient at various temperatures. A schematic of the experimental setup can be seen in Figure 5.1. The two arms of the U-tube containing the testing fluid are separated by a 3.85 cm diameter sample of Nafion NR-211 membrane. This system is closed to the atmosphere and the experiments are run with the gas phase at atmospheric pressure. This is done by connecting a small tube to each arm of the U-tube apparatus. The purpose for closing this system is to minimize the mass loss that could be caused by evaporation of the working fluid to the environment.

To create the hydrostatic pressure head the liquid columns are set at different heights. The high pressure side has a 1 meter column of liquid which is used to drive the permeation through the membrane. Due to the height limitations the pressures are relatively low and there is no need for a backing to support the membrane. To change the temperature in this system there is an array of external heaters which heat the entire system during operation which is monitored through the use of 10 K-type thermocouples placed throughout the

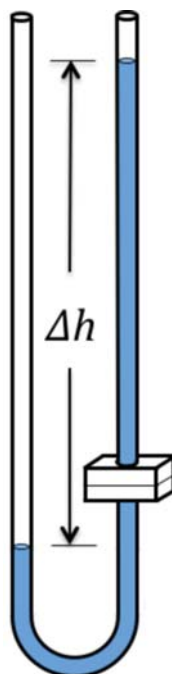


Figure 5.1: Schematic of the experimental apparatus used to test membrane permeability

system.

5.2 Uncertainty Management

The membrane permeability testing apparatus is remarkably simple, it is in its simplicity that several uncertainties may arise that must be accounted for. The correction factors applied are done so to account for a change in height on the low side of the apparatus as this is where the imaging is done. The Nikon D1X is positioned at the low side meniscus and images the height as the testing progresses.

5.2.1 Height Correction

Throughout a test run the temperature varies slightly, this variation in temperature can cause the amount of thermal expansion of the fluid being tested to change. The temperature fluctuations are typically only a few degrees centigrade however because the permeabilities are low the thermal expansion of the fluid can skew the results. To account for the thermal expansion the apparatus has been fitted with seven K-type Omega thermal couples spaced close near the membrane manifold and further apart near the high side meniscus.

To determine the change in volume from the thermal expansion equation 5.1 is used.

$$\Delta V = \beta V_0 \Delta T \quad (5.1)$$

Here ΔV is the change in volume, V_0 is the initial volume before the temperature change, ΔT is the change in temperature and β is the thermal expansion coefficient. For water the value for β is not constant for all temperatures and a look-up table is used to determine the thermal expansion for water. With the expanded volume and the dimensions of the U-tube the change in measured height can be determined.

The drawn glass U-tube has some variability in the inner diameter, this variation was tested

Table 5.1
Thermal expansion of water and FC-3283 used in the temperature correction

Fluid	Thermal Expansion (β) ($10^{-6} K^{-1}$)
Water (20°C)	207
Water (80°C)	640
FC-3283	1300

and applied to the volume calculation for the permeability. To measure the inner diameter fluid was injected using a syringe, the remaining fluid in the syringe was weighed. From this, the volume of injected fluid could be calculated resulting in an accurate mapping of the inner tube diameter. The volume changes due to the variability of inner diameter are then applied through the velocity term in the permeability equation (Equation 5.2).

Finally, due to the length of the experiments at lower temperatures a correction has to be made for the small amount of fluid that escapes through the seals of the closed system. This was done by monitoring the levels of fluid in both arms over an extended period of time for multiple temperature conditions to determine the rate of leakage. A correlation was then made to accommodate for the escaped fluid.

The permeability of the membrane can be calculated using Equation 5.2. The permeability is calculated using Darcy's Law.

$$\kappa_m = v \frac{\mu \Delta x}{\Delta p} \quad (5.2)$$

where κ_m is the permeability of the membrane, v is the superficial fluid velocity through

the medium, μ is the fluids dynamic viscosity, Δx is the thickness of the membrane and Δp is the pressure applied across the membrane.

Applying the correction factors to the permeability equation 5.2 becomes

$$\kappa_m = (v + v_{\text{loss}} + v_{\text{exp}}) \frac{\mu \Delta x}{\Delta p} \quad (5.3)$$

where v_{loss} is the reduction in measured fluid velocity due to the mass loss from the system and v_{exp} is the change in measured velocity due to the thermal expansion of the fluid. To calculate the velocity adjusted for varying U-tube radius

$$v = \frac{\Delta V}{\pi r(x)^2 \Delta t} \quad (5.4)$$

where ΔV is the volume of fluid that permeates through the membrane over a time step, $r(x)$ is the variability in the U-tube radius as a function of position and Δt is the time between measurements.

5.3 Data Processing

The height data was recorded by imaging the meniscus at a set time interval. Each image was then post processed in an automated Matlab program to determine the height of the meniscus for each image. Figure 5.2 demonstrates a typical image that is used for this

processing. To determine the temperature and the meniscus height the Matlab software has

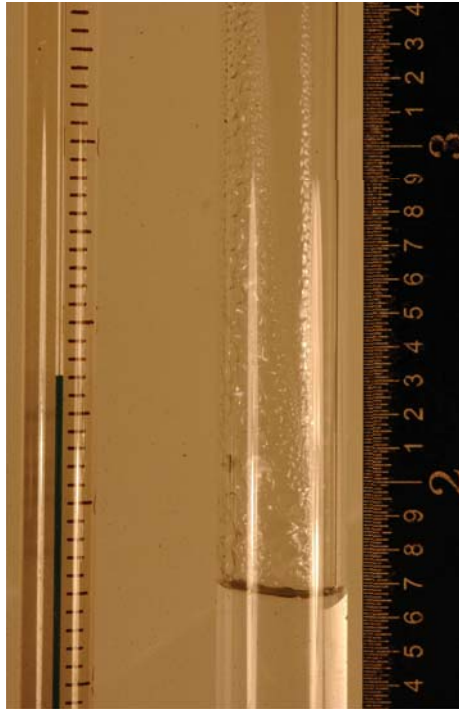


Figure 5.2: Image from a FC-3283 permeability test currently at 67°C

been developed to average the image background data and analyze only the areas that have changed from image to image. The software then scans the pixels inside the U-tube or thermometer for the interface of either the fluid permeating through the membrane or the alcohol from the thermometer. This algorithm is capable of detecting either the meniscus or the temperature even in cases where the path of the fluid may be obstructed by reflecting lights from the heating system or the graduations from the thermometer. This is possible due to the averaging of a range of images before and after the current image to subtract the background image and anything that is constant between images, such as graduations or reflections. Since this whole process is automated the only user input is the calibration

of the thermometer and the height, this is made very simple as well as the user only needs to click a pixel with in the graduation and the center point is automatically calculated to ensure that the pixel a user selects does not vary from case to case.

5.4 Results and Discussion

The permeabilities of the deionized water and FC-3283 through Nafion NR-211 are given in table 5.2 for a range of temperatures. It can be seen that a correlation between temperature and permeability exists, more importantly though with FC-3283 the permeation ceases below 58°C . When processing the image data slight variations occur from the condensing vapor and evaporating meniscus that cause the height readings to sometimes be negative. This is not desirable as this would make the permeability for this step to be negative. To account for this a curve is fit to the height data and the residuals are logged. The permeabilities are then calculated from the fitted curve and the height residuals are converted to permeabilities and added back in, resulting in a permeability curve on the log scale.

5.4.1 Deionized Water Results

The water permeability tests for Nafion NR-211 in the protonic state were performed with high quality deionized water ($R > 20\text{M}\Omega \cdot \text{cm}$) over a range of temperatures likely to be seen

Table 5.2
Permeabilities of Nafion NR-211 for FC-3283 and deionized at various temperatures.

Fluid	Temperature (°C)	Permeability (cm²)
DI Water	78.25	1.884×10^{-13}
DI Water	69.75	1.353×10^{-13}
DI Water	47.50	2.307×10^{-15}
DI Water	23.50	2.173×10^{-15}
FC-3283	68.50	4.306×10^{-15}
FC-3283	63.25	2.080×10^{-15}
FC-3283	61.25	8.869×10^{-16}
FC-3283	59.50	6.226×10^{-16}
FC-3283	< 58	0.00

in typical PEM fuel cell operation. Along with a dependence to temperature it can also be seen in figure 5.3 that the permeability of the Nafion membrane has a dependence to the time of exposure to the fluid. When this testing begins the membrane is in the protonic state and has not been exposed to the DI water until loaded into the testing apparatus. Some of the scatter noticed in the data can be attributed to the evaporation/condensation processes taking place near the fluid interface, the accuracy of the scale and the limitations brought on by the size of a pixel in the interface tracking images. For these tests the pixel size was however smaller than the accuracy of the scale. The effects of these inaccuracies can be seen as the permeability becomes smaller thus creating a larger scattering of the data and confidence intervals.

To examine how temperature affects the permeability of the Nafion membrane an experiment was run where the deionized water would permeate at room temperature through the membrane until the permeation stops. The heating lamps were then turned on allowing for

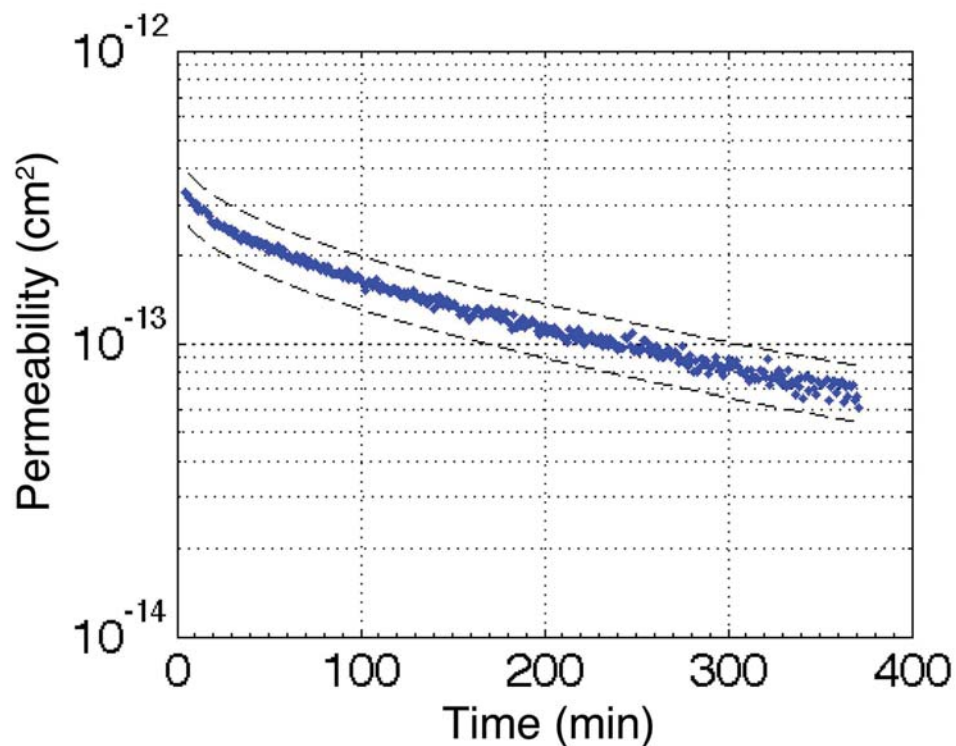


Figure 5.3: Permeability of Nafion NR-211 with $20M\Omega \cdot cm$ deionized water tested at $69.75^{\circ}C$.

the system to heat up. Figure 5.4 illustrates the displacement of deionized water through the Nafion membrane plotted along with the temperature of the system. When the heating lamps were started at 2170 minutes a sudden increase in permeability caused the height of the meniscus to rise. After a relatively short period of time the system equilibrated to a new, slightly higher permeability than existed at room temperature.

Figure 5.5 shows a similar trend to the experiment run at $58^{\circ}C$ however, a significantly larger increase in overall displacement is noticed. The permeability is proportional to the

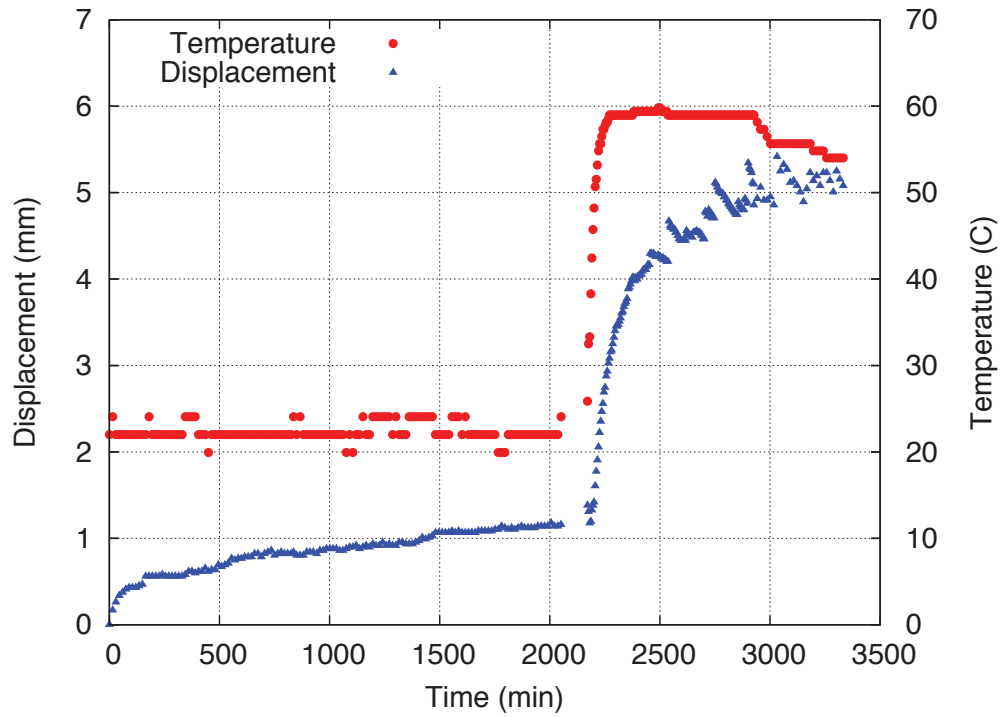


Figure 5.4: Deionized water displacement results starting at room temperature then at 2170 minutes increasing the temperature to 58°C.

slope of the displacement curves and a significant change in slope is noticed after the system temperature reaches a steady state. The change in permeabilities between the room temperature and 80°C points on the curve are several orders of magnitude in difference.

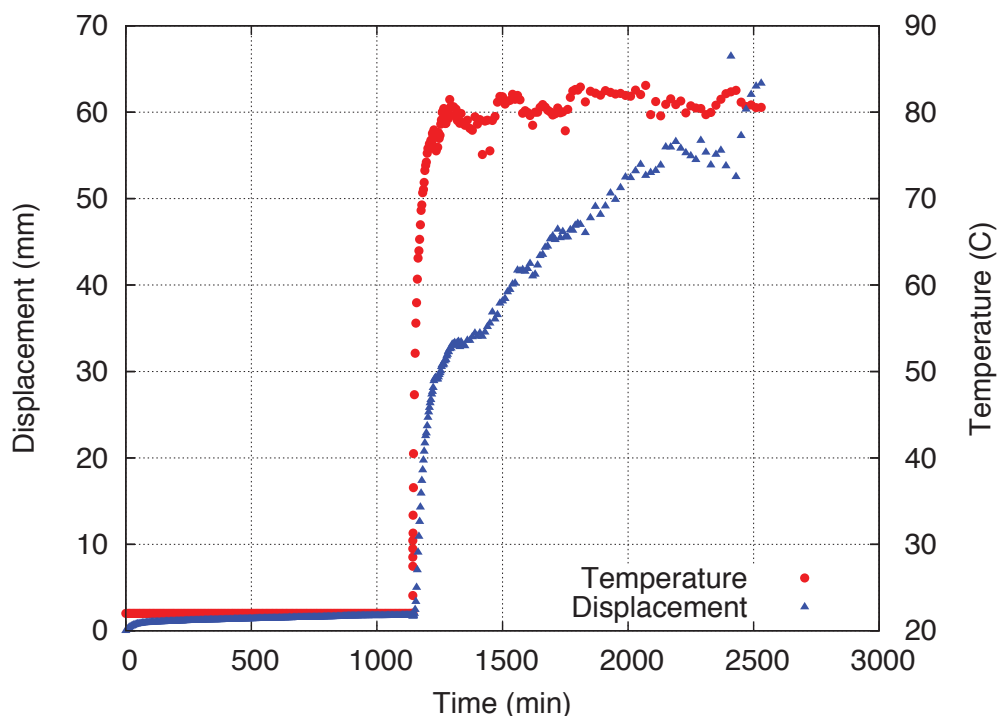


Figure 5.5: Deionized water displacement results starting at room temperature then at 1185 minutes increasing the temperature to 80°C.

5.4.2 3M Fluorinert FC-3283 Results

The fluid tested, FC-3283 is an electronic liquid that is clear, colorless, thermally and chemically stable, non-polar and fully-fluorinated. The liquid state range for this fluid is from -50°C to 128°C at standard atmospheric pressure and temperature. FC-3283 is derived from a single compound making its composition stable thus keeping the transport properties constant over time. FC-3283 was also tested for its compatibility with the Nafion

Table 5.3
Fluid properties of 3M Fluorinert FC-3283.

Properties	FC-3283
Molecular Weight	521 <i>kg/kmol</i>
Vapor Pressure	1.44×10^3
Liquid Density	1820 <i>kg/m³</i>
Kinematic Viscosity	0.75 <i>cSt</i>
Absolute Viscosity	1.4 <i>cP</i>
Coefficient of Expansion	0.0014 $^{\circ}\text{C}^{-1}$
Solubility in Water	< 5 <i>ppm</i>

membrane for possible changes in structure and state. A Nafion NR-211 sample was submerged in FC-3283 and massed daily for the first week, then weekly for the next month. These tests showed that the Nafion did not uptake any amount of the FC-3283, nor did it exhibit any visible degradation. The FC-3283 was selected because it is a non-polar fluid and with the exception of density its properties are similar to those of water without the uptake and the possibility of Schröder's paradox. By testing both deionized water and FC-3283 the ionic interaction between the fluid and the membrane can be examined. The water uptake times and the time scale for the Nafion membrane to reach a constant permeability are in close proximity. It is that prompted the permeability testing of FC-3283, without a water uptake the effects of the uptake rates may have on the permeability of the membrane will be eliminated.

The permeability of FC-3283 through Nafion NR-211 was tested for a range of temperatures ($22^{\circ}\text{C} - 63^{\circ}\text{C}$). The testing began at room temperature and was gradually increased

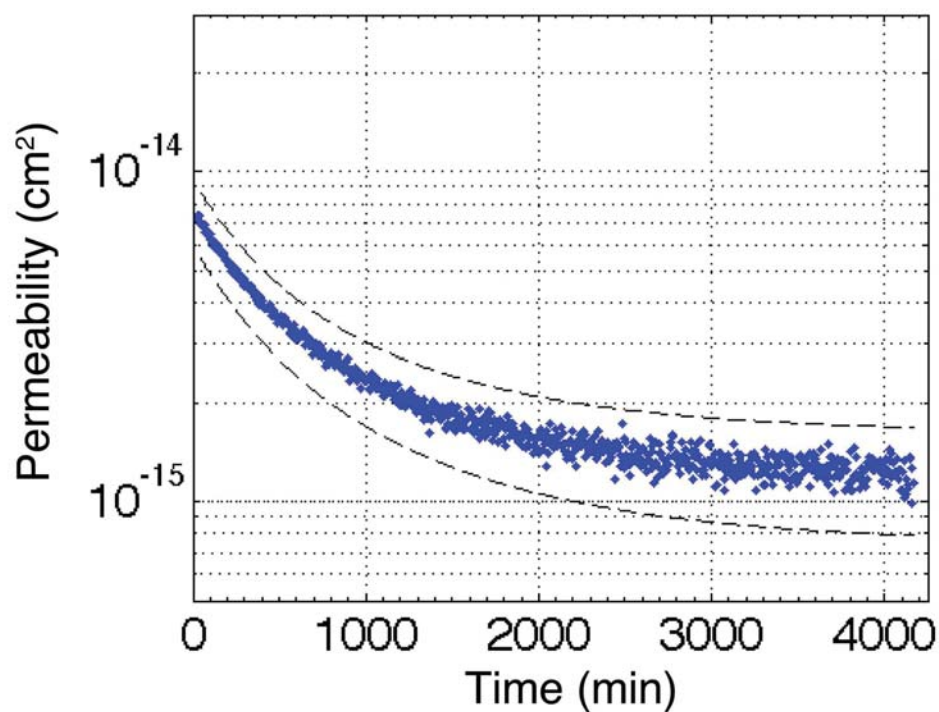


Figure 5.6: Permeability of Nafion NR-211 with 3M Fluorinert FC-3283 tested at 61.25°C.

until reaching approximately 63°C. It was found that at temperatures below 58°C the membrane was completely impermeable to FC-3283, while above 58°C yielded average permeabilities a few orders of magnitude less than that of deionized water.

5.5 Summary

It has been shown that there are some anomalies in the behavior of the membrane when in contact with a liquid. As time passes the permeability of the Nafion NRE-211 membrane reduces, and in some cases comes to a complete stop. For the lower temperature cases the permeability of the membrane is greatly reduced and in the cases with the FC-3283 the membrane becomes impermeable.

There is a definite temperature dependence to the permeability of the Nafion membrane. A temperature exists near 60°C at which a significant change in how the Nafion membranes transport fluids. This is important to understand as the typical operating temperatures seen within a PEM fuel cell are greater than 60°C .

The FC-3283 testing has shown that the change in permeability over time is not a function of the water uptake, or the water uptake rates. The initial hypothesis was that due to the similar times required for water uptake and the membrane permeability to reach a constant value the permeability was a function of the membranes water uptake. Since the FC-3283 and the deionized water exhibited similar order of magnitude reductions in permeability as the experiment elapsed the permeability is not a function of water uptake.

Chapter 6

Conclusions and Recommendations

The inclusion of the transition film evaporation model to the pore network model increases the ability to predict evaporation rates and thus the distribution of liquid water in the PTL. These results can be used to gain a better understanding of mechanisms responsible for liquid water and water vapor transport through the PTL. The model presented in this work can be used to develop better water management strategies. For example, with the improved ability to model evaporation in a large range of pore sizes the effects of an MPL on liquid water distribution and saturation can be more closely examined. The high clamping pressures and general manufacturing processes used in building a PEM fuel cell stack lead to inevitable defects in the PTL (including the MPL) and these effects can now be explored.

The simulations that have been presented in this research have shown the strength of the

transition film evaporation model over the diffusive approach. As the pore size changes the diffusive models tend to lose accuracy while the transition film model can account for these variations. The improved accuracies however have come at a slight expense of the computational time, which have increased to approximately one hour depending on the operating parameters being simulated (more liquid water leads to a greater computational time).

The experiments performed in this research were done to measure and validate the evaporation rates produced by the transition film model with a non-zero contact angle. These were performed on a contact angle measurement setup with Köhler illumination, humidity control and a heated substrate. The images of the drop profile were obtained using a microscope, then processed using an ADPA software. These experiments verify that the transition film model is capable of predicting evaporation rates at varying contact angles, temperatures and pore radii with great accuracy.

6.1 Recommendations

The modeling efforts and concepts presented herein are still in the developmental stages and there are areas that are beyond the scope of this research that could be improved to better simulate the complex water transport in porous media. This section will include some ideas on how to improve some of the results generated by this model. This research

was presented with the modeling of a PEM fuel cell in mind however, the concepts and phenomenon modeled here cover a broad spectrum of microfluidics applications such as drug delivery, pharmaceutical development, fluid transport in soil and aggregates as well as any applications of fluids in a porous material. The following is a list of ideas and areas of focus that could improve this model for applications in any of the aforementioned disciplines:

- Condensation is currently not included in the model presented in this research. To include condensation the interface temperature from the transition film model and the vapor saturation from the pore network model can be used along with the air-water vapor psychrometrics to determine condensation rates in each pore.
- Thermal contact resistance could be implemented into this model by applying a probability distribution function to the contact resistance at each pore and adding a resistive element to the thermal circuit as shown in figure 6.1. This would allow for the use of a single fiber conductivity for R_s as opposed to the current bulk PTL conductivity. The effects of the many fibers intersecting at a given pore would be captured within the probability distribution function that is applied to the R_c thermal resistance, much like how the pore radius distribution function captures the effects of varying pore lengths.

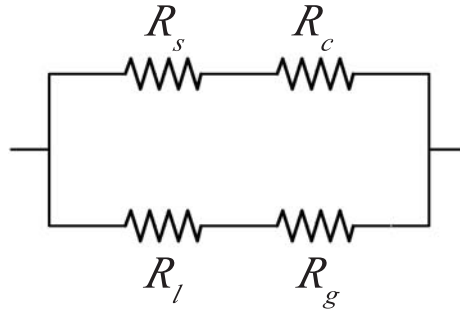


Figure 6.1: Thermal resistance model including fiber contact resistances.

- An oxygen diffusivity model should be implemented in order to obtain a more realistic reaction rate profile along the catalyst layer. This is a difficult parameter to include as the ability for oxygen to reach the catalyst layer depends on vapor saturation, the location of the liquid, the tortuosity of the available path and the temperature. By including this the reaction rates would slow in areas that are starved of oxygen affecting the reaction rates thereby changing the thermal gradients and liquid water generation.
- The inclusion of water generation from the membrane by electro-osmotic drag can be included as a source term at the catalyst layer at each pore. This source term would be dependent on the reaction rates and could be included once the oxygen diffusivity model is implemented.
- Simulate the effects of differing anode and cathode pressures to examine how these operating parameters affect the liquid water distribution in the cathode PTL. The model is currently capable of such a study, this can be done by modifying the cathode gas channels pressure.

- Adapt the disjoining pressure and interfacial temperature terms of the transition film model to accept a contact angle of greater than 90° . This would create a more robust model to account for hydrophobic and hydrophilic pores.
- Modify the current temperature boundary condition along the channel area to account for the convective air flows that occur from the air supply.
- Adjust the PTL morphology to include the MPL and simulate the resulting percolation with evaporation. The domain could also be easily expanded to simulate a three-dimensional PTL domain.

Many of the recommendations listed above would greatly improve the models ability to predict the water liquid and vapor distributions. These increased accuracies would however come at a great cost of computational efficiency especially when applied to a three-dimensional model. The computational time would be increased by a factor for every $25\ \mu m$ modeled in the with-channel axis.

References

- [1] J. Larminie, A. Dicks, Fuel Cell Systems Explained, John Wiley & Sons, 2nd ed. edition, 2003.
- [2] A. Collier, H. Wang, X.Z. Yuan, J. Zhang, D.P. Wilkinson, Degradation of polymer electrolyte membranes, International Journal of Hydrogen Energy 31 (2006) 1838 – 1854. Fuel Cells.
- [3] H.J. Alcock, O.C. White, G. Jegelevicius, M.R. Roberts, J.R. Owen, New high-throughput methods of investigating polymer electrolytes, Journal of Power Sources n/a (2010) n/a.
- [4] S. Banerjee, D.E. Curtin, Nafion perfluorinated membranes in fuel cells, Journal of Fluorine Chemistry 125 (2004) 1211 – 1216. Fluorine in Alternative Energy Sources.
- [5] X. Wang, T.V. Nguyen, Modeling the effects of the microporous layer on the net water transport rate across the membrane in a PEM fuel cell, Journal of the Electrochemical Society 157 (2010) B496–B505.
- [6] A.Z. Weber, J. Newman, Effects of microporous layers in polymer electrolyte fuel cells, Journal of the Electrochemical Society 152 (2005) A677.
- [7] A.Z. Weber, R. Balliet, H.P. Gunterman, J. Newman, Modeling water management in polymer-electrolyte fuel cells, in: M. Schlesinger (Ed.), Modeling and Numerical Simulations, volume 43 of *Modern Aspects of Electrochemistry*, Springer New York, New York, NY, 2009, pp. 273–415.
- [8] V. Mehta, J.S. Cooper, Review and analysis of pem fuel cell design and manufacturing, Journal of Power Sources 114 (2003) 32 – 53.

- [9] S. Shimpalee, S. Greenway, J.V. Zee, The impact of channel path length on pemfc flow-field design, *Journal of Power Sources* 160 (2006) 398 – 406.
- [10] S. Ge, C.Y. Wang, Liquid water formation and transport in the pefc anode, *Journal of The Electrochemical Society* 154 (2007) B998–B1005.
- [11] T.C. Jao, P.H. Chi, S.T. Ke, G.B. Jung, S.H. Chan, Investigation of degradation behavior of membrane electrode assembly with polytetrafluoroethylene/Nafion composite membranes, *Journal of Power Sources* - (2010) –.
- [12] P. Badrinarayanan, PEM Fuel Cell Water and Thermal Management: A Methodology to Understand Water and Thermal Management in an Automotive Fuel Cell System, Master's thesis, University of California Davis, 2001.
- [13] J.J. Baschuk, X. Li, Modeling of polymer electrolyte membrane fuel cells with variable degrees of water flooding, *Journal of Power Sources* 86 (2000) 181.
- [14] J. Kim, S. Lee, S. Srinivasan, Modeling of proton exchange membrane fuel cell performance with an emperical equation, *Journal of the Electrochemical Society* 142 (1995) 2670.
- [15] A.Z. Weber, J. Newman, Transport in polymer-electrolyte membranes ii. mathematical model, *Journal of the Electrochemical Society* 151 (2004) A311.
- [16] A.Z. Weber, J. Newman, Modeling transport in polymer-electrolyte fuel cells, *Chemical Reviews* 104 (2004) 4679.
- [17] P.G. Khalatur, S.K. Talitskikh, A.R. Khokhlov, Structural organization of water-containing nafion: The integral equation theory, *Macromolecular Theory and Simulations* 11 (2002) 566.
- [18] D. Bevers, M. Wöhr, K. Yasuda, K. Oguro, Simulation of a polymer electrolyte fuel cell electrode, *Journal of Applied Electrochemistry* 27 (1997) 1254.
- [19] W. He, J.S. Yi, T.V. Nguyen, Two-phase flow model of the cathode of PEM fuel cells using interdigitated flow fields, *American Institute of Chemical Engineers Journal* 46 (2000) 2053.
- [20] D. Natarajan, T.V. Nguyen, Three-dimensional effects of liquid water flooding in the cathode of a pem fuel cell, *Journal of Power Sources* 115 (2003) 66.

- [21] J.H. Nam, M. Kaviany, Effective diffusivity and water-saturation distribution in single- and two-layer PEMFC diffusion medium, *International Journal of Heat and Mass Transfer* 46 (2003) 4595.
- [22] S. Mazumder, J.V. Cole, Rigorous 3-D mathematical modeling of PEM fuel cells, *Journal of the Electrochemical Society* 150 (2003) A1510.
- [23] A.Z. Weber, J. Newman, *Macroscopic Modeling of Polymer-Electrolyte Membranes*, ELSEVIER, p. 47.
- [24] S.J. Paddison, T.A. Zawodzinski Jr., Molecular modeling of the pendant chain in nafion, *Solid State Ionics* 115 (1998) 333.
- [25] S.J. Paddison, R. Paul, J. Thomas A. Zawodzinski, A statistical mechanical model of proton and water transport in a proton exchange membrane, *Journal of the Electrochemical Society* 147 (2000) 617.
- [26] J.J. Krueger, P.P. Simon, H.J. Ploehn, Phase behavior and microdomain structure in perfluorosulfonated ionomers via self-consistent mean field theory, *Macromolecules* 35 (2002) 5630.
- [27] T. Li, A. Wlaschin, P.B. Balbuena, Theoretical studies of proton transfer in water and model polymer electrolyte systems, *Industrial and Engineering Chemistry* 40 (2001) 4789.
- [28] S.J. Paddison, R. Paul, J. Thomas A. Zawodzinski, Proton friction and diffusion coefficients in hydrated polymer electrolyte membranes: Computations with a non-equilibrium statistical mechanical model, *Journal of Chemical Physics* 115 (2001) 7753.
- [29] R. Paul, S.J. Paddison, A statistical mechanical model for the calculation of the permittivity of water in hydrated polymer electrolyte membrane pores, *Journal of Chemical Physics* 115 (2001) 7762.
- [30] T. Okada, Theory for water management in membranes for polymer electrolyte fuel cells: Part 1. The effect of impurity ions at the anode side on the membrane performances, *Journal of Electroanalytical Chemistry* 465 (1999) 1.

- [31] T. Okada, Theory for water management in membranes for polymer electrolyte fuel cells: Part 2. The effect of impurity ions at the cathode side on the membrane performances, *Journal of Electroanalytical Chemistry* 465 (1999) 18.
- [32] A. Rowe, X. Li, Mathematical modeling of proton exchange membrane fuel cells, *Journal of Power Sources* 102 (2001) 82.
- [33] J.J. Baschuk, X. Li, A comprehensive, consistent and systematic mathematical model of PEM fuel cells, *Applied Energy* 86 (2009) 181.
- [34] P.C. Sui, S. Kumar, N. Djilali, Advanced computational tools for pem fuel cell design part 1. development and base case simulations, *Journal of Power Sources* 180 (2008) 410.
- [35] Y. Wang, Modeling of two-phase transport in the diffusion media of polymer electrolyte fuel cells, *Journal of Power Sources* 185 (2008) 261.
- [36] X. Wang, T.V. Nguyen, Modeling the effects of capillary property of porous media on the performance of the cathode of a PEMFC, *Journal of the Electrochemical Society* 155 (2008) B1085.
- [37] E. Passalacqua, G. Squadrito, F. Lufrano, A. Patti, L. Giorgi, Effects of the diffusion layer characteristics on the performance of polymer electrolyte fuel cell electrodes, *Journal of Applied Electrochemistry* 31 (2001) 449.
- [38] L.R. Jordan, A.K. Shukla, T. Behrsing, N.R. Avery, B.C. Muddle, M. Forsyth, Diffusion layer parameters influencing optimal fuel cell performance, *Journal of Power Sources* 86 (2000) 250.
- [39] C.S. Kong, K.Y. Kim, H.K. Lee, Y.G. Shul, A.H. Lee, Influence of pore-size distribution of diffusion layer on mass-transport problems of proton exchange membrane fuel cells., *Journal of Power Sources* 108 (2002) 185.
- [40] L.R. Jordan, A.K. Shukla, T. Behrsing, N.R. Avery, B.C. Muddle, M. Forsyth, Effect of diffusion-layer morphology on the performance of polymer electrolyte fuel cells operating at atmospheric pressure, *Journal of Applied Electrochemistry* 30 (2000) 641.

- [41] V. Gurau, F. Barbir, H. Liu, An analytical solution of a half-cell model for PEM fuel cells, *Journal of the Electrochemical Society* 147 (2000) 2468.
- [42] A.Z. Weber, J. Newman, Transport in polymer-electrolyte membranes iii. model validation in a simple fuel-cell model, *Journal of the Electrochemical Society* 151 (2004) A326.
- [43] Z.H. Wang, C.Y. Wang, K.S. Chen, Two-phase flow and transport in the air cathode of proton exchange membrane fuel cells, *Journal of Power Sources* 94 (2001) 40.
- [44] L. You, H. Liu, A two-phase flow and transport model for the cathode of PEM fuel cells, *International Journal of Heat and Mass Transfer* 45 (2002) 2277.
- [45] T. Berning, N. Djilali, A 3D, multiphase, multicomponent model of the cathode and anode of a PEM fuel cell, *Journal of the Electrochemical Society* 150 (2003) A1589.
- [46] U. Pasaogullari, C.Y. Wang, Liquid water transport in gas diffusion layer of polymer electrolyte fuel cells, *Journal of the Electrochemical Society* 151 (2004) A399.
- [47] E.C. Kumbur, K.V. Sharp, M.M. Mench, Validated leverett approach for multiphase flow in pefc diffusion media, *Journal of the Electrochemical Society* 154 (2007) B1315–B1324.
- [48] L. Zhang, M. Pan, S. Quan, Model predictive control of water management in PEMFC, *Journal of Power Sources* 180 (2008) 322.
- [49] X. Yu, B. Zhou, A. Sobiesiak, Water and thermal management for Ballard PEM fuel cell stack, *Journal of Power Sources* 147 (2005) 184.
- [50] F. Chen, Y.G. Su, C.Y. Soong, W.M. Yan, H.S. Chu, Transient behavior of water transport in the membrane of a PEM fuel cell, *Journal of Electroanalytical Chemistry* 566 (2004) 85.
- [51] U. Pasaogullari, C.Y. Wang, K.S. Chen, Liquid water transport in polymer electrolyte fuel cells with multi-layer diffusion media, in: ASME.
- [52] H. Meng, A two-phase non-isothermal mixed-domain pem fuel cell model and its application to two-dimensional simulations, *Journal of Power Sources* 168 (2007) 218.

- [53] S. Cordiner, S.P. Lanzani, V. Mulone, M. Chiapparini, A. D'Anzi, D. Orsi, Polymer electrolyte fuel cell design based on three-dimensional computational fluid dynamics modeling, *Journal of Fuel Cell Science and Technology* 6 (2009) 021310.
- [54] J.J. Hwang, A complete two-phase model of a porous cathode of a PEM fuel cell, *Journal of Power Sources* 164 (2007) 174.
- [55] M. Eikerling, Water management in cathode catalyst layers of PEM fuel cells, *Journal of the Electrochemical Society* 153 (2006) E58.
- [56] K.J. Beverley, J.H. Clint, P.D.I. Fletcher, Evaporation rates of pure liquids measured using a gravimetric technique, *Physical Chemistry Chemical Physics* 1 (1999) 149.
- [57] K.J. Beverley, J.H. Clint, P.D.I. Fletcher, S. Thubron, Evaporation rates of water contained within porous silica particles, *Physical Chemistry Chemical Physics* 1 (1999) 909.
- [58] L. Matamoros, D. Brüggemann, Simulation of the water and heat management in proton exchange membrane fuel cells, *Journal of Power Sources* 161 (2006) 203.
- [59] N. Khajeh-Hosseini-Dalasm, K. Fushinobu, K. Okazaki, Transient phase change in the cathode side of a pem fuel cell, *Journal of the Electrochemical Society* 157 (2010) B1358–B1369.
- [60] T.V. Nguyen, R.E. White, A water and heat management model for proton-exchange-membrane fuel cells, *Journal of the Electrochemical Society* 140 (1993) 2178.
- [61] M. Potash Jr., P.C. Wayner Jr., Evaporation from a two-dimensional extended meniscus, *International Journal of Heat and Mass Transfer* 15 (1972) 1851.
- [62] G. Preiss, P.C. Wayner Jr., Evaporation from a capillary tube, *Journal of Heat Transfer* 98 (1976) 178.
- [63] S. DasGupta, J.A. Schonberg, J. P. C. Wayner, Investigation of an evaporating extended meniscus based on the augmented Young–Laplace equation, *Journal of Heat Transfer* 115 (1993) 201.

- [64] S. DasGupta, J.A. Schonberg, I.Y. Kim, P.C. Wayner Jr., Use of the augmented Young-Laplace equation to model equilibrium and evaporating extended menisci, *Journal of Colloid and Interface Science* 157 (1993) 332.
- [65] S. DasGupta, I.Y. Kim, J. P. C. Wayner, Use of the Kelvin-Claapeyron equation to model an evaporating curved microfilm, *Journal of Heat Transfer* 116 (1994) 1007.
- [66] J.A. Schonberg, S. DasGupta, P.C.W. Jr., An augmented young - laplace model of an evaporating meniscus in a microchannel with high heat flux, *Experimental Thermal and Fluid Science* 10 (1995) 163.
- [67] H. Bruus, *Theoretical Microfluidics*, Oxford University Press, 2008.
- [68] R.W. Schrage, *A Theoretical Study of Interphase Mass Transfer*, Ph.D. thesis, Columbia University Press, 1953.
- [69] R. Marek, J. Straub, Analysis of the evaporation coefficient and the condensation coefficient of water, *International Journal of Heat and Mass Transfer* 44 (2001) 39.
- [70] H.K. Cammenga, *Evaporation mechanisms of liquids*, volume 5, North-Holland Publishing Company, Hans-Sommer-Strasse 10 D-3300 Braunschweig, F. R. Germany, p. 335. Section Title: "Evaporation Mechanisms of Liquids".
- [71] P.C. Wayner Jr., The effect of interfacial mass transport on flow in thin liquid films, *Colloids and Surfaces* 52 (1991) 71.
- [72] H. Wang, S.V. Garimella, J.Y. Murthy, Characteristics of an evaporating thin film in a microchannel, *International Journal of Heat and Mass Transfer* 50 (2007) 3933.
- [73] E.K. Rideal, On the influence of thin surface films on the evaporation of water, *Journal of Physical Chemistry* 29 (1925) 1585.
- [74] T. Alty, The reflection of vapour molecules at a liquid surface, in: J. Thomson (Ed.), *Proceedings of the Royal Society*, volume 131 of A, Mathematical and Physical Sciences.
- [75] K.C.D. Hickman, W.A. Torpey, Evaporation of resting water, *Industrial and Engineering Chemistry* 46 (1954) 1446.

- [76] U. Narusawa, G.S. Springer, Measurements of evaporation rates of water, *Journal of Colloid and Interface Science* 50 (1975) 392.
- [77] H.K. Cammenga, H. Klinge, B.E. Rudolph, Untersuchungen über die verdampfungsgeschwindigkeit von flüssigkeiten, *Fortschrittsberichte über Kolloide und Polymere* 55 (1971) 118.
- [78] J.R. Maa, Evaporation coefficient of liquids, *Industrial and Engineering Chemistry* 6 (1967) 504.
- [79] S.K. Wee, K.D. Kihm, D.M. Pratt, J.S. Allen, Microscale heat and mass transport of evaporating thin film of binary mixture, *Journal of Thermophysics and Heat Transfer* 20 (2006) 320.
- [80] D. Gerteisen, T. Heilmann, C. Ziegler, Modeling the phenomena of dehydration and flooding of a polymer electrolyte membrane fuel cell, *Journal of Power Sources* 187 (2009) 165 – 181.
- [81] M. Mench, *Fuel Cell Engines*, John Wiley & Sons, 2008.
- [82] N. Zamel, X. Li, Non-isothermal multi-phase modeling of pem fuel cell cathode, *International Journal of Energy Research* 34 (2010) 568–584.
- [83] H. Meng, Numerical investigation of transient responses of a PEM fuel cell using a two-phase non-isothermal mixed-domain model, *Journal of Power Sources* 171 (2007) 738.
- [84] S.K. Wee, K.D. Kihm, K.P. Hallinan, Effects of the liquid polarity and the wall slip on the heat and mass transport characteristics of the micro-scale evaporating transition film, *International Journal of Heat and Mass Transfer* 48 (2005) 265 – 278.
- [85] F. Plourde, M. Prat, Pore network simulations of drying of capillary porous media. influence of thermal gradients, *International Journal of Heat and Mass Transfer* 46 (2003) 1293 – 1307.
- [86] J.B. Laurindo, M. Prat, Numerical and experimental network study of evaporation in capillary porous media. drying rates, *Chemical Engineering Science* 53 (1998) 2257.

- [87] S. Wang, Y. Utaka, Y. Tasaki, An experimental study on moisture transport through a porous plate with micro pores, *International Journal of Heat and Mass Transfer* 52 (2009) 4386.
- [88] S.K. Wee, Microscale observables for heat and mass transport in sub-micron scale evaporating thin film, Ph.D. thesis, Texas A&M, 2004.
- [89] P.C. Wayner Jr., Y.K. Kao, L.V. LaCroix, The interline heat-transfer coefficient of an evaporating wetting film, *International Journal of Heat and Mass Transfer* 19 (1976) 487 – 492.
- [90] F.W. Holm, S.P. Goplen, Heat transfer in the meniscus thin film transition region, *Journal of Heat Transfer* 101 (1979) 543.
- [91] S.Y. Du, Y.H. Zhao, New boundary conditions for the evaporating thin-film model in a rectangular micro channel, *International Journal of Heat and Mass Transfer* 54 (2011) 3694 – 3701.
- [92] B.V. Derjaguin, S.V. Nerpin, N.V. Churayev, Effect of film transfer upon evaporation of liquids from capillaries, *Bulletin Rilem* 29 (1965) 93.
- [93] V.M. Ha, C.L. Lai, Theoretical analysis of Marangoni instability of an evaporating droplet by energy method, *International Journal of Heat and Mass Transfer* 47 (2004) 3811.
- [94] S.S. Panchamgam, S.J. Gokhale, J.L. Plawsky, S. DasGupta, J. Peter C. Wayner, Experimental determination of the effect of disjoining pressure on shear in the contact line region of a moving evaporating thin film, *Journal of Heat Transfer* 127 (2005) 231.
- [95] Q. Wu, H. Wong, A slope-dependent disjoining pressure for non-zero contact angles, *Journal of Fluid Mechanics* 506 (2004) 157–185.
- [96] P.C. Hiemenz, R. Rajagopalan, *Principles of colloid and surface chemistry*, CRC Press LLC., 1997.
- [97] K. Sefiane, R. Bennacer, Nanofluids droplets evaporation kinetics and wetting dynamics on rough heated substrates, *Advances in Colloid and Interface Science* 147-148 (2009) 263 – 271. Colloids, polymers and surfactants. Special Issue in honour of Brian Vincent.

- [98] J.L. Plawsky, M. Ojha, A. Chatterjee, P.C. Wayner Jr., Review of the effects of surface topography, surface chemistry and fluid physics on evaporation at the contact line, *Chemical Engineering Communications* 196 (2008) 658.
- [99] B. Sobac, D. Brutin, Triple-line behavior and wettability controlled by nanocoated substrates: Influence on sessile drop evaporation, *Langmuir* 27 (2011) 14999–15007.
- [100] S. Chandra, M. di Marzo, Y.M. Qiao, P. Tartarinich, Effect of liquid-solid contact angle on droplet evaporation, *Fire Safety Journal* 27 (1996) 141 – 158.
- [101] R. Ranjan, J.Y. Murthy, S.V. Garimella, A microscale model for thin-film evaporation in capillary wick structures, *International Journal of Heat and Mass Transfer* 54 (2011) 169 – 179.
- [102] S.C. Wong, Y.C. Lin, Effect of copper surface wettability on the evaporation performance: Tests in a flat-plate heat pipe with visualization, *International Journal of Heat and Mass Transfer* 54 (2011) 3921 – 3926.
- [103] R.G. Picknett, R. Bexon, The evaporation of sessile or pendant drops in still air, *Journal of Colloid and Interface Science* 61 (1977) 2.
- [104] V. Konduru, Static and Dynamic Contact Angle Measurement on Rough Surfaces Using Sessile Drop Profile Analysis with Application to Water Management in Low Temperature Fuel Cells, Master's thesis, Michigan Technological University, 2010.
- [105] P. Cheng, D. Li, L. Boruvka, Y. Rotenberg, A. Neumann, Automation of axisymmetric drop shape analysis for measurements of interfacial tensions and contact angles, *Colloids and Surfaces* 43 (1990) 151 – 167.
- [106] D. Chatzikyriakou, S. Walker, C. Hale, G. Hewitt, The measurement of heat transfer from hot surfaces to non-wetting droplets, *International Journal of Heat and Mass Transfer* 54 (2011) 1432 – 1440.
- [107] J.B. Freund, The atomic detail of an evaporating meniscus, *Physics of Fluids* 17 (2005) 022104.
- [108] H. Hu, R. Larson, Fluid Flow in An Evaporating Droplet, Technical Report, University of Michigan, 1997.

- [109] G. Lu, Y.Y. Duan, X.D. Wang, D.J. Lee, Internal flow in evaporating droplet on heated solid surface, *International Journal of Heat and Mass Transfer* 54 (2011) 4437 – 4447.
- [110] E.F. Medici, Water transport in complex, non-wetting porous layers with applications to water management in low temperature fuel cells, Ph.D. thesis, Michigan Technological University, 2010.
- [111] E.F. Medici, J.S. Allen, Scaling percolation in thin porous layers, *Physics of Fluids* 23 (2011) 122107.
- [112] E.F. Medici, J.S. Allen, Incorporation of evaporation and vapor transport in pore level models of fuel cell porous media, *ECS Transactions* 41 (2011) 141–152.
- [113] E.F. Medici, J.S. Allen, The effects of morphological and wetting properties of porous transport layers on water movement in pem fuel cells, *Journal of the Electrochemical Society* 157 (2010) B1505–B1514.
- [114] R. Lenormand, E. Touboul, C. Zarcone, Numerical models and experiments on immiscible displacements in porous media, *Journal of Fluid Mechanics* 189 (1988) 165–187.
- [115] J.T. Gostick, M.W. Fowler, M.A. Ioannidis, M.D. Pritzker, Y. Volfkovich, A. Sakars, Capillary pressure and hydrophilic porosity in gas diffusion layers for polymer electrolyte fuel cells, *Journal of Power Sources* 156 (2006) 375 – 387.
- [116] A. Jena, H. Sanders, J. Miller, R. Wimberly, Comparison of mercury porosimetry and flow porometry for the testing of battery separator materials, *IEEE* (2001) 71–75.
- [117] M.J. Martínez, S. Shimpalee, J.W.V. Zee, A.V. Sakars, Assessing methods and data for pore-size distribution of pemfc gas-diffusion media, *Journal of the Electrochemical Society* 156 (2009) B558–B564.
- [118] J.T. Gostick, M.A. Ioannidis, M.W. Fowler, M.D. Pritzker, Pore network modeling of fibrous gas diffusion layers for polymer electrolyte membrane fuel cells, *Journal of Power Sources* 173 (2007) 277 – 290.

- [119] V. Surasani, T. Metzger, E. Tsotsas, Consideration of heat transfer in pore network modelling of convective drying, *International Journal of Heat and Mass Transfer* 51 (2008) 2506 – 2518.
- [120] R.E. Bolz, G.L. Tuve, *CRC Handbook of tables for applied engineering science*, CRC Press LLC., 1973.
- [121] F.P. Incropera, D.P. Dewitt, *Fundamentals of Heat and Mass Transfer*, John Wiley & Sons, 2002.
- [122] H.B. Ma, P. Cheng, B. Borgmeyer, Y.X. Wang, Fluid flow and heat transfer in the evaporating thin film region, *Microfluid Nanofluid* 4 (2008) 237.
- [123] H.B. Ma, G.P. Peterson, D.M. Pratt, Disjoining pressure effect on the wetting characteristics in a capillary tube, *Microscale Thermophysical Engineering* 2 (1998) 283.
- [124] D.M. Pratt, J.R. Brown, K.P. Hallinan, Thermocapillary effects on the stability of a heated, curved meniscus, *Journal of Heat Transfer* 120 (1998) 220.
- [125] A.G. Yiotis, A.K. Stubos, A.G. Boudouvis, Y.C. Yortsos, A 2-d pore-network model of the drying of single-component liquids in porous media, *Advances in Water Resources* 24 (2001) 439 – 460. Pore Scale Modeling.
- [126] S. Shimpalee, S. Dutta, Numerical prediction of temperature distribution in PEM fuel cells, *Numerical Heat Transfer, Part A: Applications* 38 (2000) 111–128.
- [127] A.Z. Weber, R.M. Darling, Understanding porous water-transport plates in polymer-electrolyte fuel cells, *Journal of Power Sources* 168 (2007) 191. 10th EUROPEAN LEAD BATTERY CONFERENCE - Selected Papers Presented at the 10th EUROPEAN LEAD BATTERY CONFERENCE(10 ELBC) Athens, Greece, 26-29 September 2006.
- [128] J.H. Kim, S.I. Ahn, J.H. Kim, W.C. Zin, Evaporation of water droplets on polymer surfaces, *Langmuir* 23 (2007) 6163–6169.
- [129] G. Janssen, M. Overvelde, Water transport in the proton-exchange-membrane fuel cell: measurements of the effective drag coefficient, *Journal of Power Sources* 101 (2001) 117 – 125.

- [130] F. Lufrano, E. Passalacqua, G. Squadrito, A. Patti, L. Giorgi, Improvement in the diffusion characteristics of low pt-loaded electrodes for pefcs, *Journal of Applied Electrochemistry* 29 (1999) 445–448. 10.1023/A:1026419102310.
- [131] M.S. Wilson, J.A. Valerio, S. Gottesfeld, Low platinum loading electrodes for polymer electrolyte fuel cells fabricated using thermoplastic ionomers, *Electrochimica Acta* 40 (1995) 355 – 363. <ce:title>Polymer electrolyte fuel cells</ce:title>.
- [132] N. Hara, K. Tsurumi, M. Watanabe, An advanced gas diffusion electrode for high performance phosphoric acid fuel cells, *Journal of Electroanalytical Chemistry* 413 (1996) 81 – 88.
- [133] E. Passalacqua, F. Lufrano, G. Squadrito, A. Patti, L. Giorgi, Influence of the structure in low-pt loading electrodes for polymer electrolyte fuel cells, *Electrochimica Acta* 43 (1998) 3665 – 3673.
- [134] A.Z. Weber, J. Newman, Modeling gas-phase flow in porous media, *International Communications in Heat and Mass Transfer* 32 (2005) 855.
- [135] F.C. Chen, Z. Gao, An analysis of black liquor falling film evaporation, *International Journal of Heat and Mass Transfer* 47 (2004) 1657.
- [136] V.A. Paganin, E.A. Ticianelli, E.R. Gonzalez, Development and electrochemical studies of gas diffusion electrodes for polymer electrolyte fuel cells, *Journal of Applied Electrochemistry* 26 (1996) 297–304. 10.1007/BF00242099.
- [137] Z. Qi, A. Kaufman, Improvement of water management by a microporous sublayer for pem fuel cells, *Journal of Power Sources* 109 (2002) 38 – 46.
- [138] S. Lee, S. Mukerjee, J. McBreen, Y. Rho, Y. Kho, T. Lee, Effects of nafion impregnation on performances of pemfc electrodes, *Electrochimica Acta* 43 (1998) 3693 – 3701.
- [139] J. Chen, T. Matsuura, M. Hori, Novel gas diffusion layer with water management function for pemfc, *Journal of Power Sources* 131 (2004) 155 – 161. <ce:title>Selected papers presented at the Eighth Grove Fuel Cell Symposium</ce:title>.

- [140] G. Alberti, R. Narducci, M. Sganappa, Effects of hydrothermal/thermal treatments on the water-uptake of Nafion membranes and relations with changes of conformation, counter-elastic force and tensile modulus of the matrix, *Journal of Power Sources* 178 (2008) 575–583.
- [141] D. Burnett, A. Garcia, F. Thielmann, Measuring moisture sorption and diffusion kinetics on proton exchange membranes using a gravimetric vapor sorption apparatus, *Journal of Power Sources* 160 (2006) 426–430.
- [142] C.E. Evans, R.D. Noble, S. Nazeri-Thompson, B. Nazeri, C.A. Koval, Role of conditioning on water uptake and hydraulic permeability of Nafion membranes, *Journal of Membrane Science* 279 (2006) 521–528.
- [143] C. Vallieres, D. Winkelmann, D. Roizard, E. Favre, P. Scharfer, M. Kind, On schroeder's paradox, *Journal of Membrane Science* 278 (2006) 357 – 364.
- [144] M. Bass, V. Freger, Hydration of nafion and dowex in liquid and vapor environment: Schroeder's paradox and microstructure, *Polymer* 49 (2008) 497 – 506.
- [145] G.S. Hwang, M. Kaviani, J.H. Nam, M.H. Kim, S.Y. Son, Pore-water morphological transitions in polymer electrolyte of a fuel cell, *Journal of the Electrochemical Society* 156 (2009) B1192.
- [146] L. Onishi, J. Prausnitz, J. Newman, Water-Nafion Equilibria. Absence of Schroeder's Paradox, Technical Report, Department of Chemical Engineering, University of California Berkeley, 2005.
- [147] S. Ge, X. Li, B. Yi, I.M. Hsing, Absorption, desorption, and transport of water in polymer electrolyte membranes for fuel cells, *Journal of the Electrochemical Society* 152 (2005) A1149–A1157.
- [148] C.W. Monroe, T. Romero, W. Mérida, M. Eikerling, A vaporization-exchange model for water sorption and flux in Nafion, *Journal of Membrane Science* 324 (2008) 1–6.
- [149] T.A. Zawodzinski Jr, C. Derouin, S. Radzinski, R.J. Sherman, V.T. Smith, T.E. Springer, S. Gottesfeld, Water uptake by and transport through Nafion 117 membranes, *Journal of the Electrochemical Society* 140 (1993) 1041–1047.

- [150] P. Costamagna, Transport phenomena in polymeric membrane fuel cells, *Chemical Engineering Science* 56 (2001) 323 – 332.
- [151] J.L. Fales, N.E. Vanderborgh, P. Strove, The influence of channel geometry on ionic transport, *The Electrochemical Society* 86 (1986) N/A.
- [152] M. Adachi, T. Navessin, Z. Xie, B. Frisken, S. Holdcroft, Correlation of in situ and ex situ measurements of water permeation through Nafion NRE211 proton exchange membranes, *Journal of the Electrochemical Society* 156 (2009) B782–B790.
- [153] P. Majsztrik, A. Bocarsly, J. Benziger, Water permeation through Nafion membranes: The role of water activity, *The Journal of Physical Chemistry B* 112 (2008) 16280–16289.

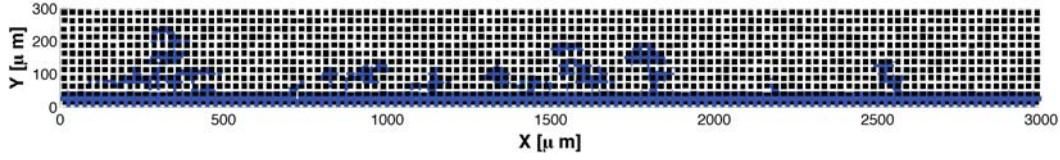
Appendix A

Transition Film Pore Network Model Results

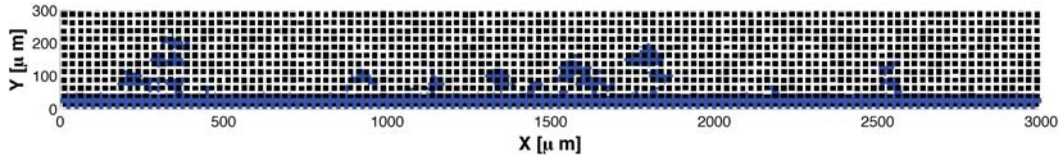
In this chapter the distribution results from the transition film pore network model can be found. The cases tested have a relative humidity range of 60% to 90% and a land temperature boundary condition ranging from 70°C to 80°C. The sections are grouped by the land temperature for the varying relative humidity cases and are arranged in order of increasing relative humidity. All of the results presented in the appendices are for the 9.7 μm mean pore size PTL as explained in Chapter 4. Each of the distributions shown in this chapter are at the end of the simulation, so in the cases where the gas channel is breached by the liquid finger the distribution shown is for the time of the breach, all other cases are at the end of simulation time, 200 seconds.

A.1 70°C Land Temperature Results

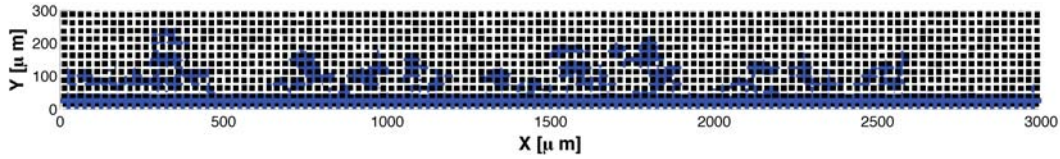
A.1.1 Drainage



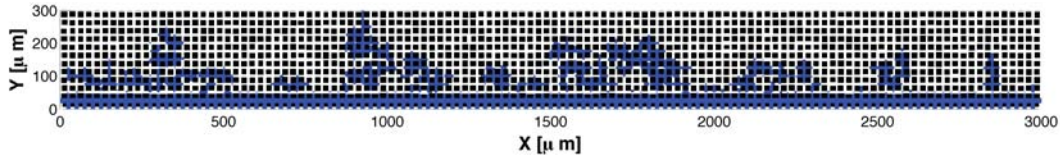
(a) Transition film model 70°C land temperature and a 60% relative humidity.



(b) Transition film model 70°C land temperature and a 70% relative humidity.



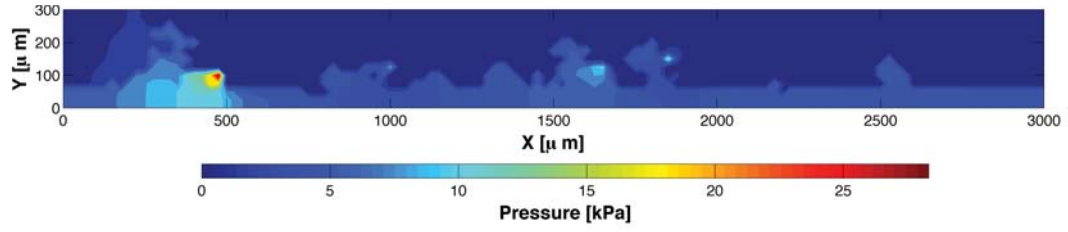
(c) Transition film model 70°C land temperature and a 80% relative humidity.



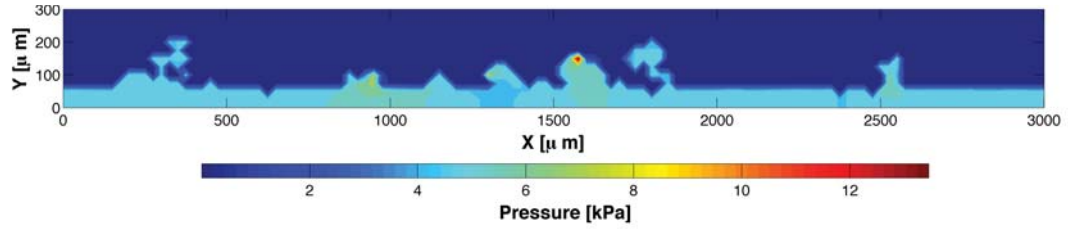
(d) Transition film model 70°C land temperature and a 90% relative humidity.

Figure A.1: Drainage simulations for the transition film model taken at 70°C land temperature and varying relative humidity.

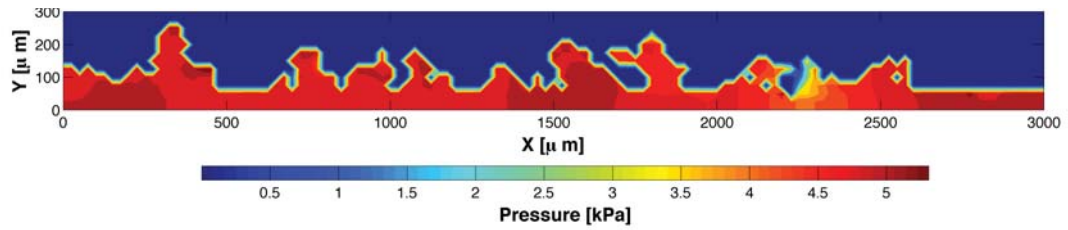
A.1.2 Pressure Distribution



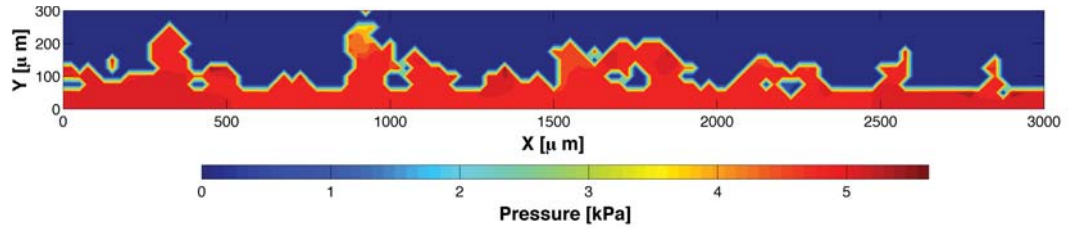
(a) Transition film model 70°C land temperature and a 60% relative humidity.



(b) Transition film model 70°C land temperature and a 70% relative humidity.



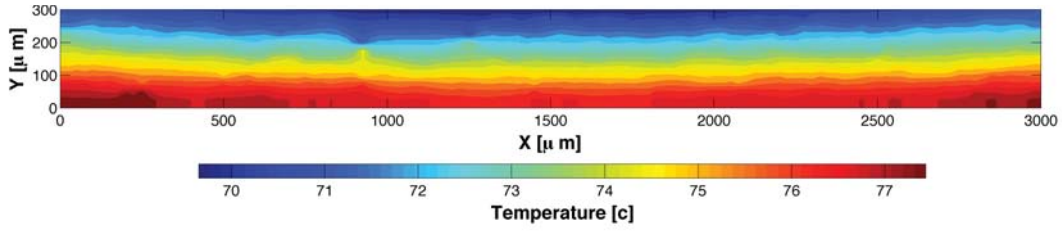
(c) Transition film model 70°C land temperature and a 80% relative humidity.



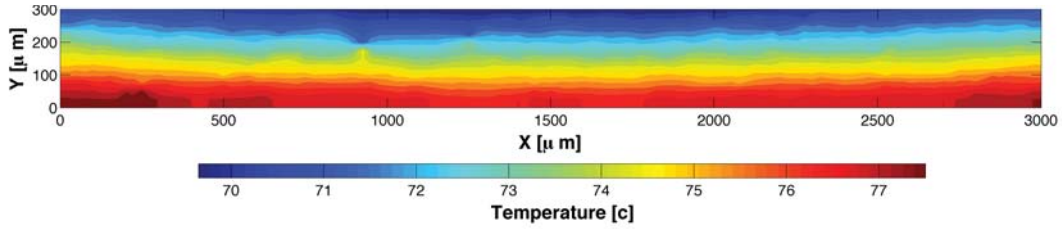
(d) Transition film model 70°C land temperature and a 90% relative humidity.

Figure A.2: Pressure distribution simulations for the transition film model taken at 70°C land temperature and varying relative humidity.

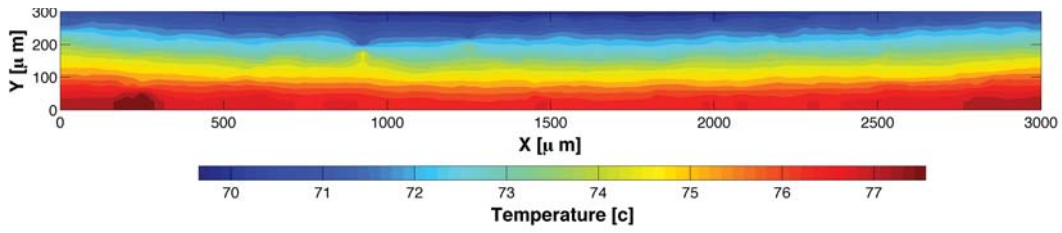
A.1.3 Temperature Distribution



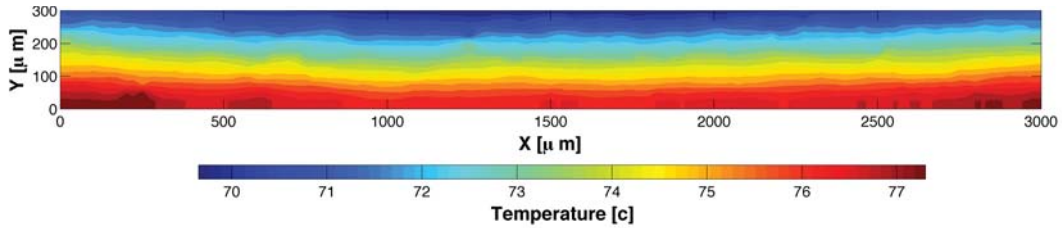
(a) Transition film model 70°C land temperature and a 60% relative humidity.



(b) Transition film model 70°C land temperature and a 60% relative humidity.



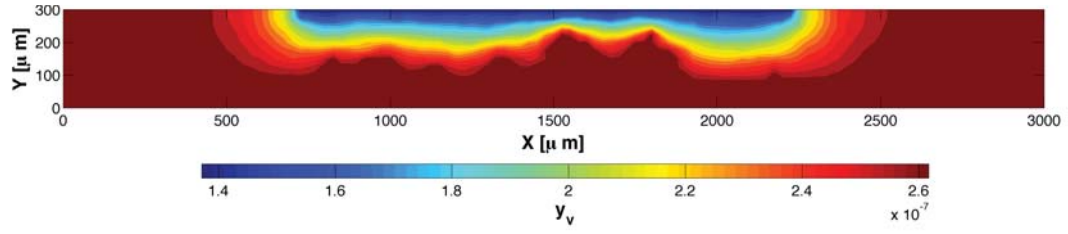
(c) Transition film model 70°C land temperature and a 60% relative humidity.



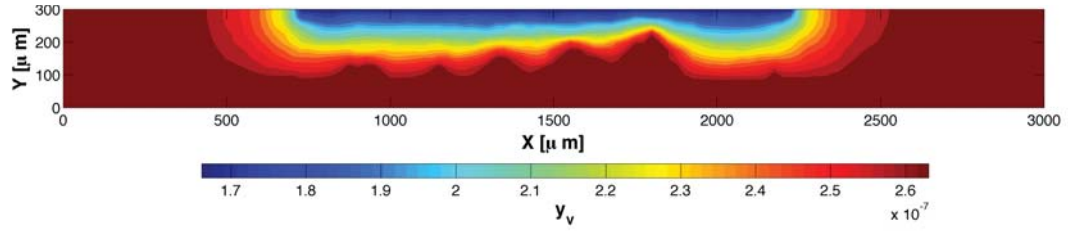
(d) Transition film model 70°C land temperature and a 60% relative humidity.

Figure A.3: Temperature distribution simulations for the transition film model taken at 70°C land temperature and varying relative humidity.

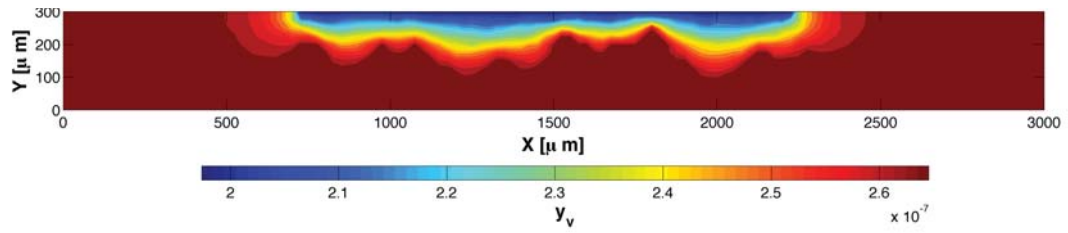
A.1.4 Vapor Concentration Distribution



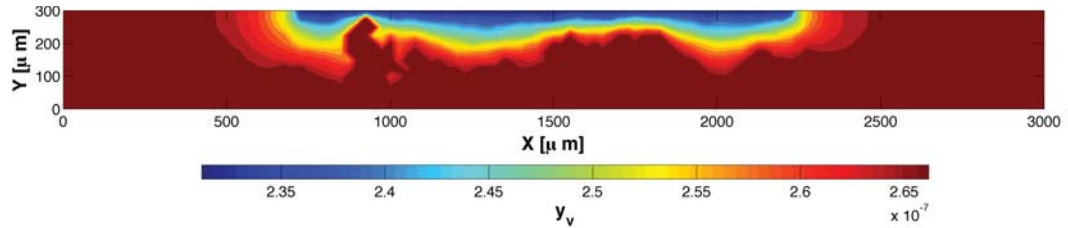
(a) Transition film model 70°C land temperature and a 60% relative humidity.



(b) Transition film model 70°C land temperature and a 60% relative humidity.



(c) Transition film model 70°C land temperature and a 60% relative humidity.

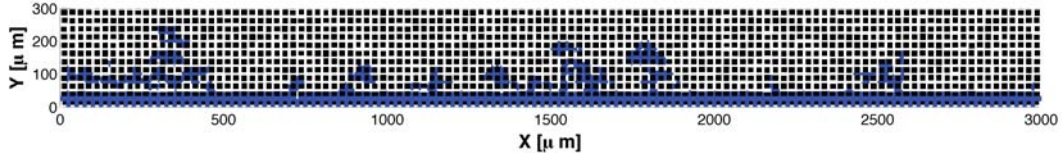


(d) Transition film model 70°C land temperature and a 60% relative humidity.

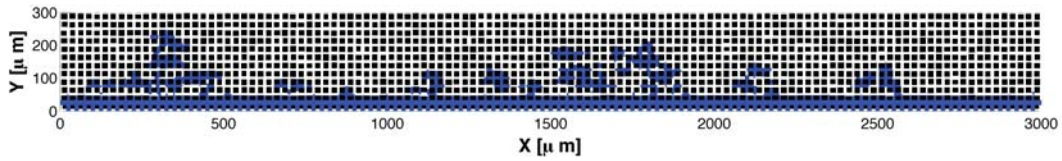
Figure A.4: Vapor concentration distribution simulations for the transition film model taken at 70°C land temperature and varying relative humidity.

A.2 75°C Land Temperature Results

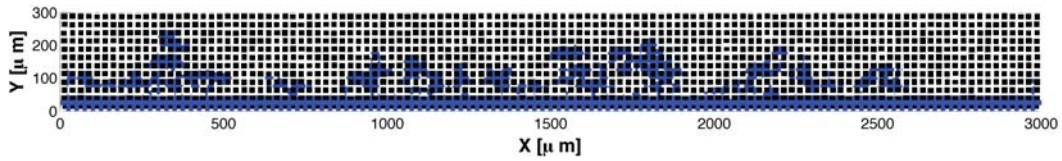
A.2.1 Drainage



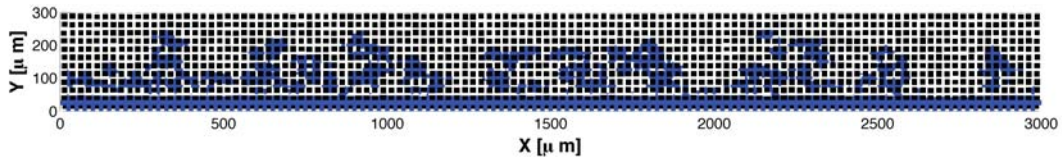
(a) Transition film model 75°C land temperature and a 60% relative humidity.



(b) Transition film model 75°C land temperature and a 70% relative humidity.



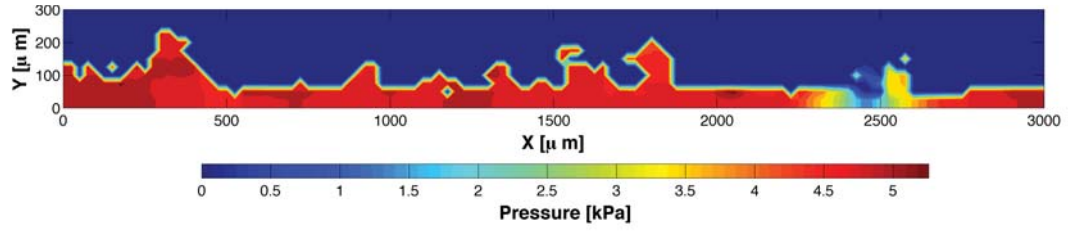
(c) Transition film model 75°C land temperature and a 80% relative humidity.



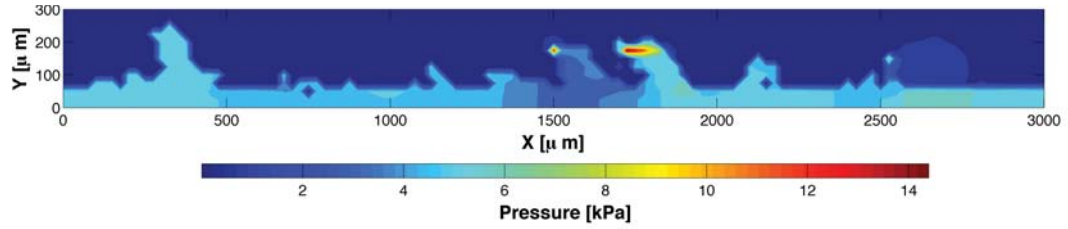
(d) Transition film model 75°C land temperature and a 90% relative humidity.

Figure A.5: Drainage simulations for the transition film model taken at 75°C land temperature and varying relative humidity.

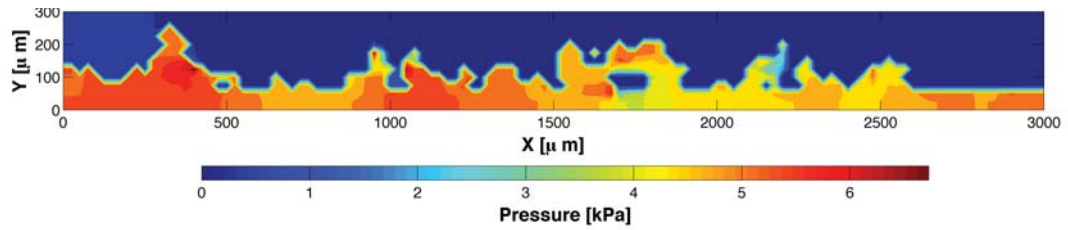
A.2.2 Pressure Distribution



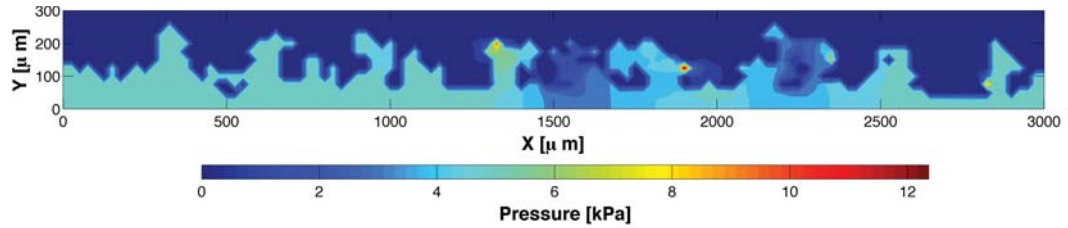
(a) Transition film model 75°C land temperature and a 60% relative humidity.



(b) Transition film model 75°C land temperature and a 70% relative humidity.



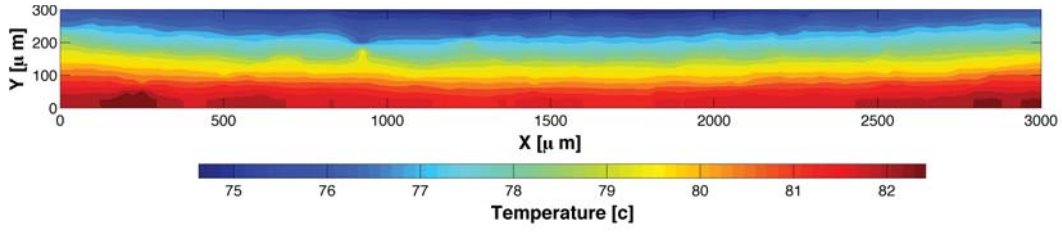
(c) Transition film model 75°C land temperature and a 80% relative humidity.



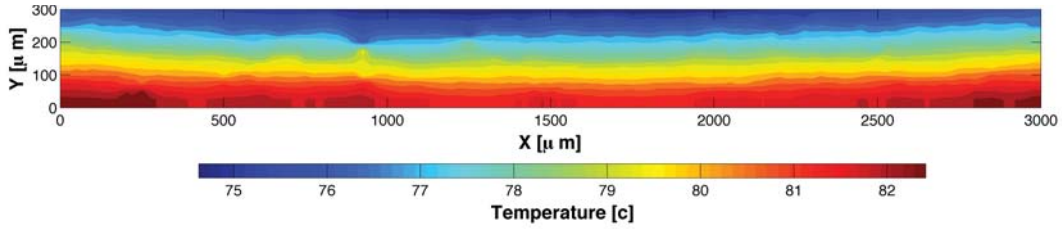
(d) Transition film model 75°C land temperature and a 90% relative humidity.

Figure A.6: Pressure distribution simulations for the transition film model taken at 75°C land temperature and varying relative humidity.

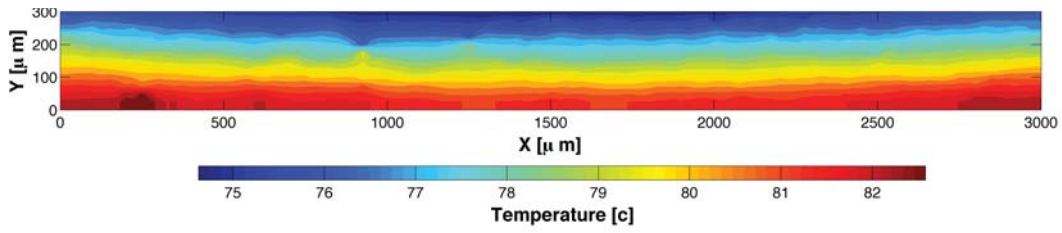
A.2.3 Temperature Distribution



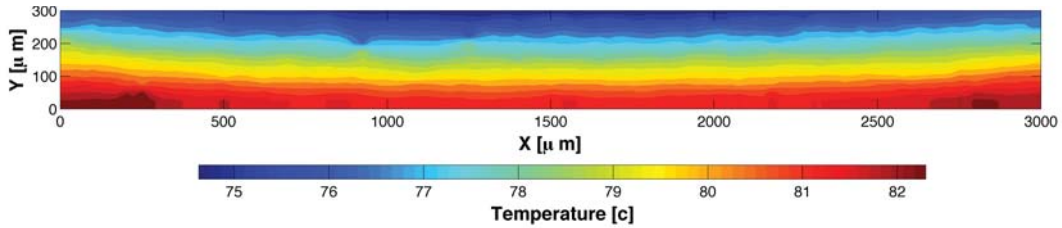
(a) Transition film model 75°C land temperature and a 60% relative humidity.



(b) Transition film model 75°C land temperature and a 60% relative humidity.



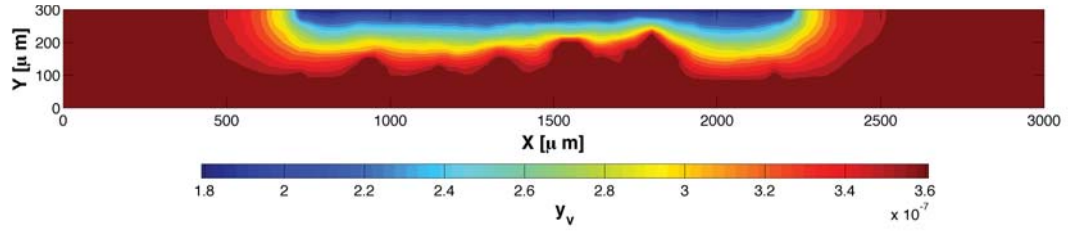
(c) Transition film model 75°C land temperature and a 60% relative humidity.



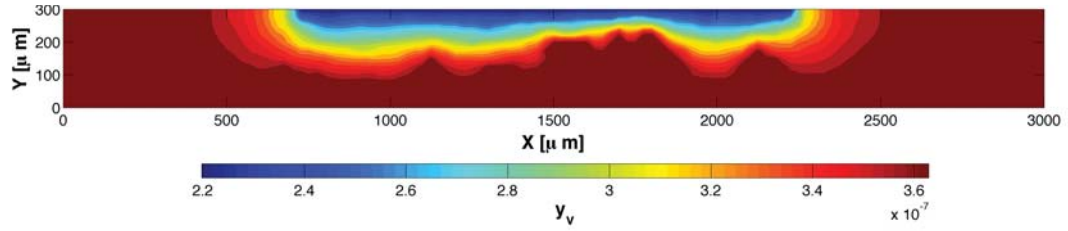
(d) Transition film model 75°C land temperature and a 60% relative humidity.

Figure A.7: Temperature distribution simulations for the transition film model taken at 75°C land temperature and varying relative humidity.

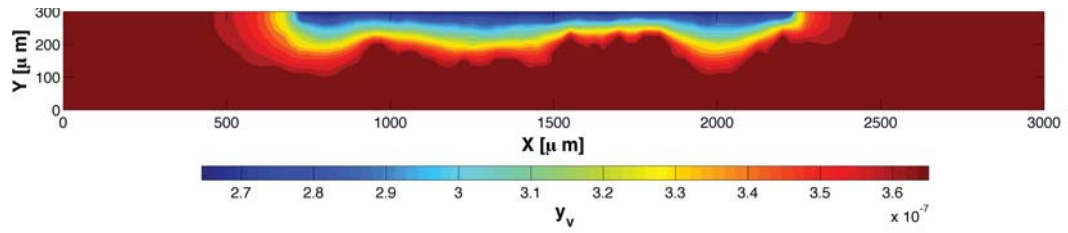
A.2.4 Vapor Concentration Distribution



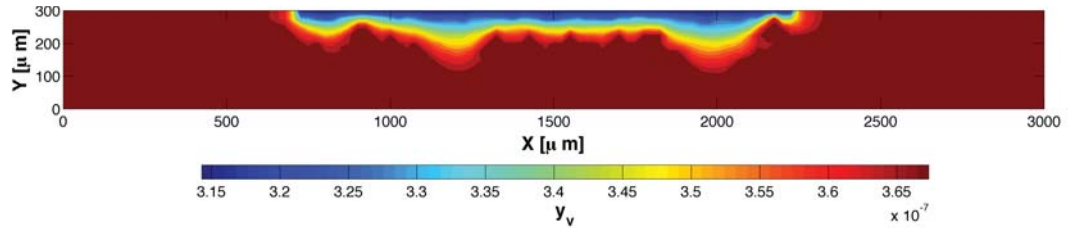
(a) Transition film model 75°C land temperature and a 60% relative humidity.



(b) Transition film model 75°C land temperature and a 60% relative humidity.



(c) Transition film model 75°C land temperature and a 60% relative humidity.

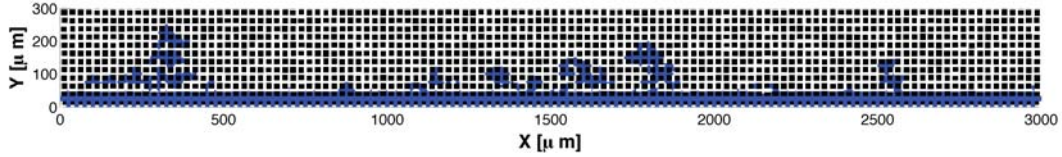


(d) Transition film model 75°C land temperature and a 60% relative humidity.

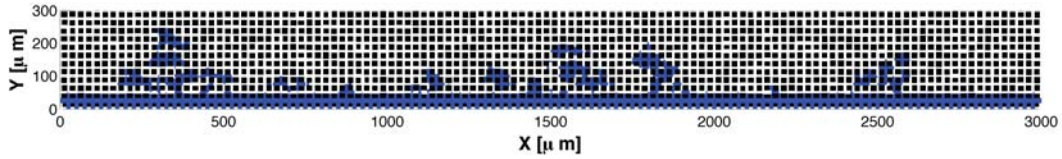
Figure A.8: Vapor concentration distribution simulations for the transition film model taken at 75°C land temperature and varying relative humidity.

A.3 80°C Land Temperature Results

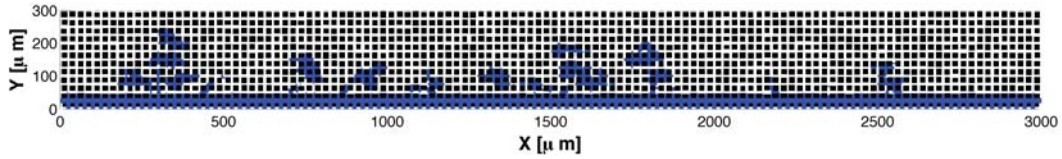
A.3.1 Drainage



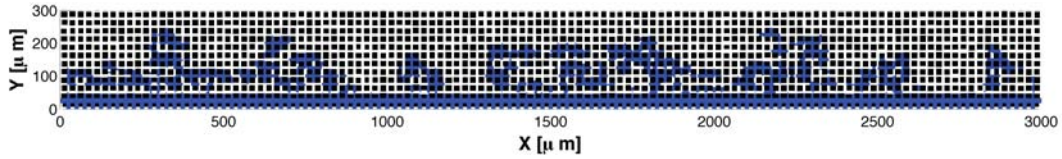
(a) Transition film model 80°C land temperature and a 60% relative humidity.



(b) Transition film model 80°C land temperature and a 70% relative humidity.



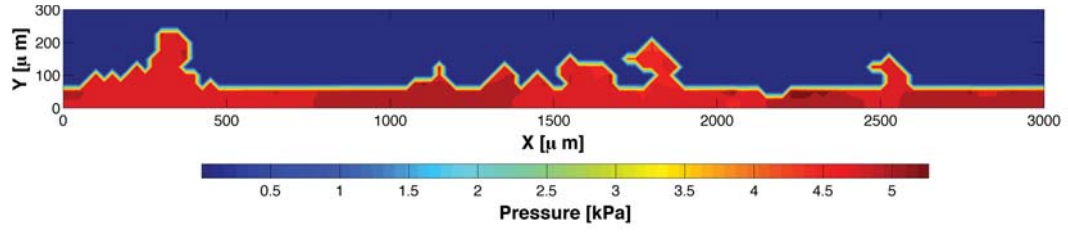
(c) Transition film model 80°C land temperature and a 80% relative humidity.



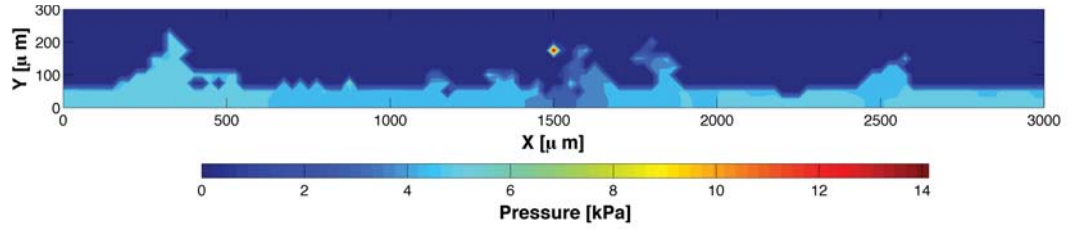
(d) Transition film model 80°C land temperature and a 90% relative humidity.

Figure A.9: Drainage simulations for the transition film model taken at 80°C land temperature and varying relative humidity.

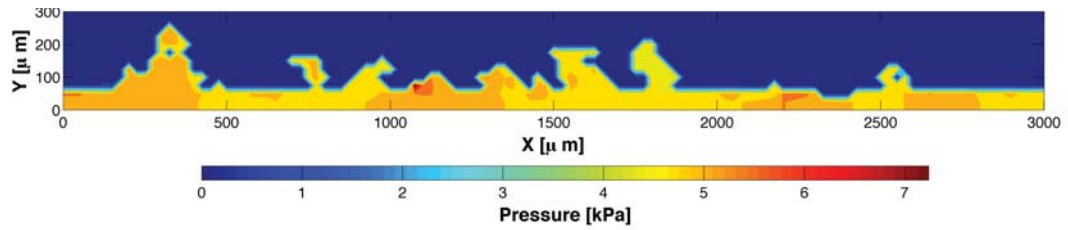
A.3.2 Pressure Distribution



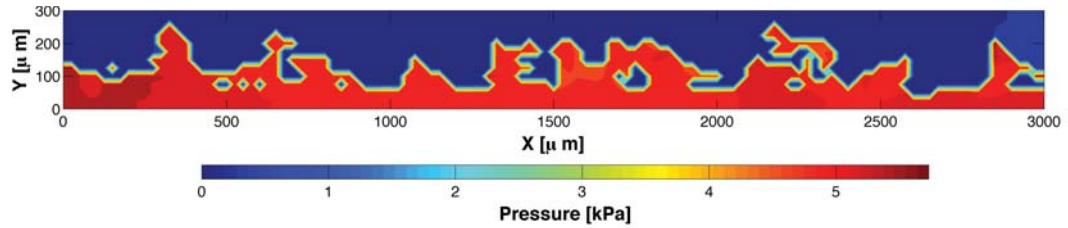
(a) Transition film model 80°C land temperature and a 60% relative humidity.



(b) Transition film model 80°C land temperature and a 70% relative humidity.



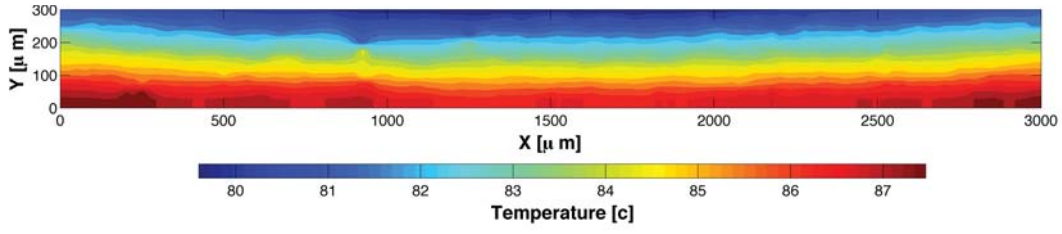
(c) Transition film model 80°C land temperature and a 80% relative humidity.



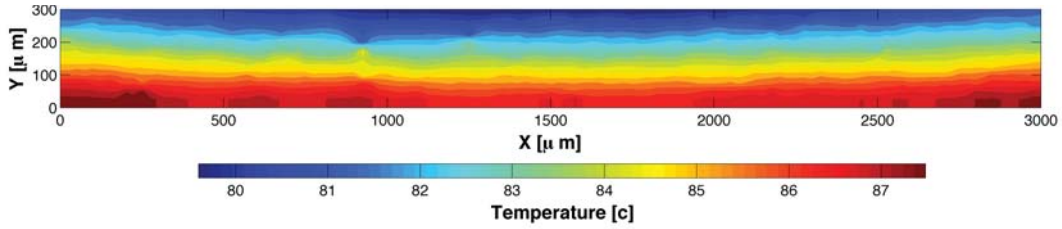
(d) Transition film model 80°C land temperature and a 90% relative humidity.

Figure A.10: Pressure distribution simulations for the transition film model taken at 80°C land temperature and varying relative humidity.

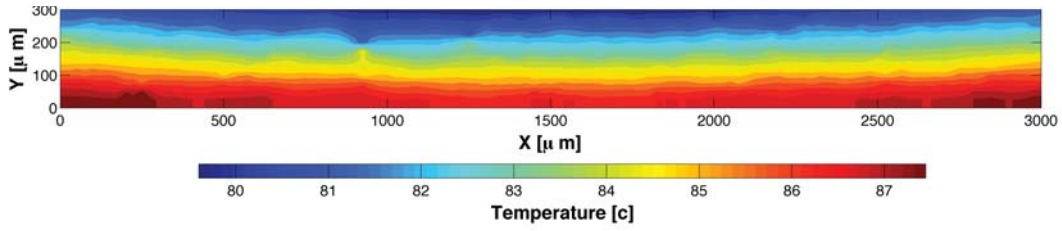
A.3.3 Temperature Distribution



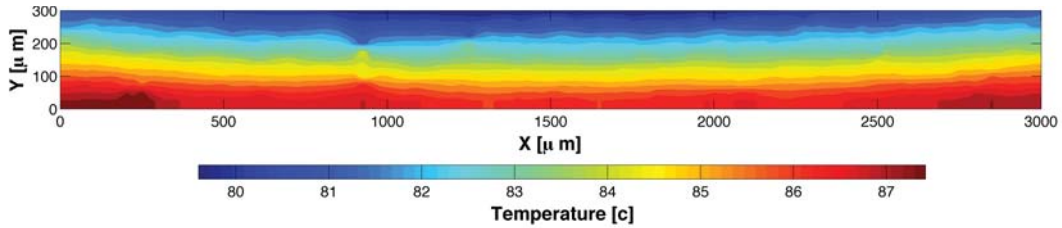
(a) Transition film model 80°C land temperature and a 60% relative humidity.



(b) Transition film model 80°C land temperature and a 60% relative humidity.



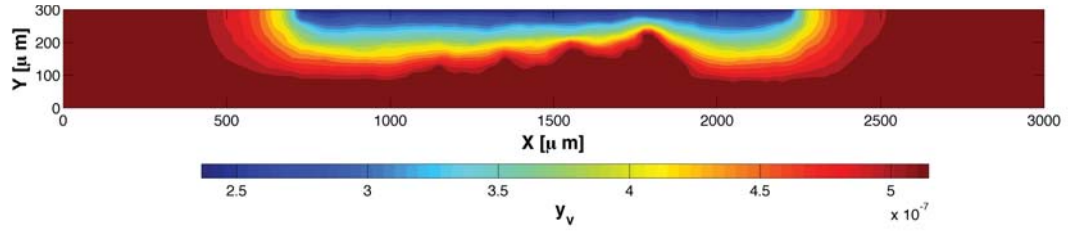
(c) Transition film model 80°C land temperature and a 60% relative humidity.



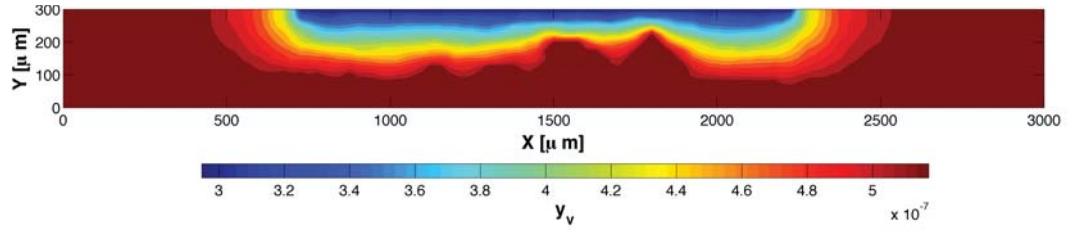
(d) Transition film model 80°C land temperature and a 60% relative humidity.

Figure A.11: Temperature distribution simulations for the transition film model taken at 80°C land temperature and varying relative humidity.

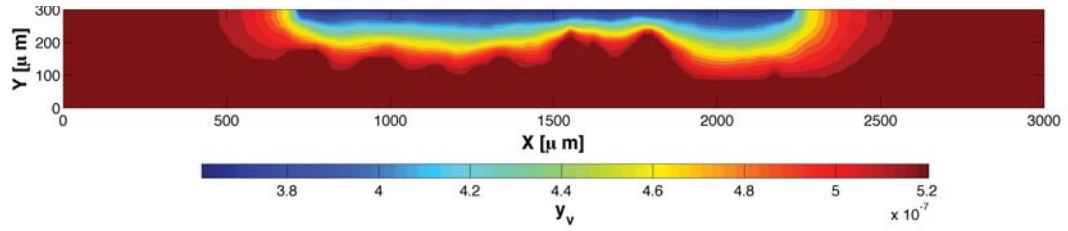
A.3.4 Vapor Concentration Distribution



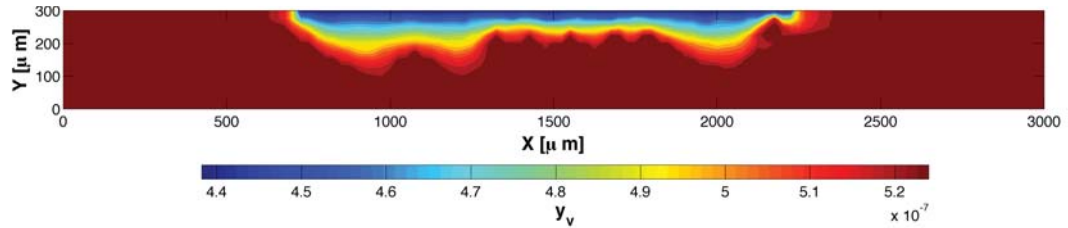
(a) Transition film model 80°C land temperature and a 60% relative humidity.



(b) Transition film model 80°C land temperature and a 60% relative humidity.



(c) Transition film model 80°C land temperature and a 60% relative humidity.



(d) Transition film model 80°C land temperature and a 60% relative humidity.

Figure A.12: Vapor concentration distribution simulations for the transition film model taken at 80°C land temperature and varying relative humidity.

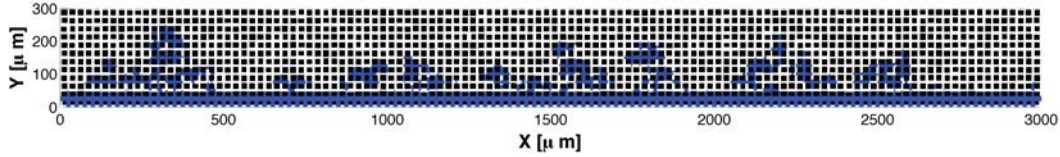
Appendix B

Diffusive Pore Network Model Results

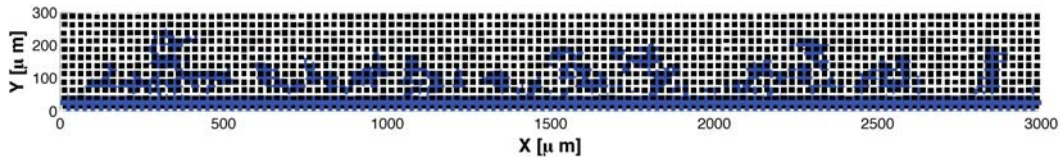
In this chapter the distribution results from the diffusive pore network model can be found. The cases tested have a relative humidity range of 60% to 90% and a land temperature boundary condition ranging from 70°C to 80°C. The sections are grouped by the land temperature for the varying relative humidity cases and are arranged in order of increasing relative humidity. All of the results presented in the appendices are for the 9.7 μm mean pore size PTL as explained in Chapter 4. Each of the distributions shown in this chapter are at the end of the simulation, so in the cases where the gas channel is breached by the liquid finger the distribution shown is for the time of the breach, all other cases are at the end of simulation time, 200 seconds.

B.1 70°C Land Temperature Results

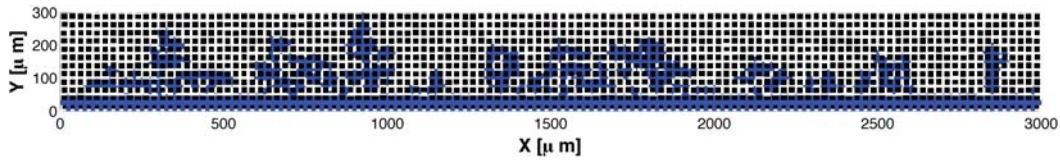
B.1.1 Drainage



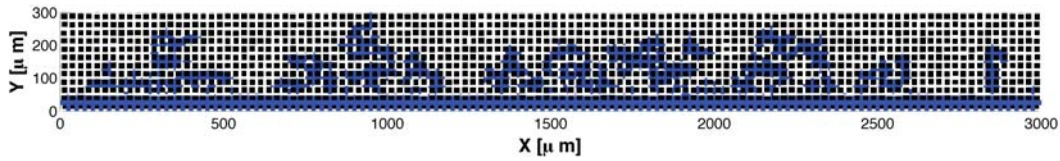
(a) Diffusive model 70°C land temperature and a 60% relative humidity.



(b) Diffusive model 70°C land temperature and a 70% relative humidity.



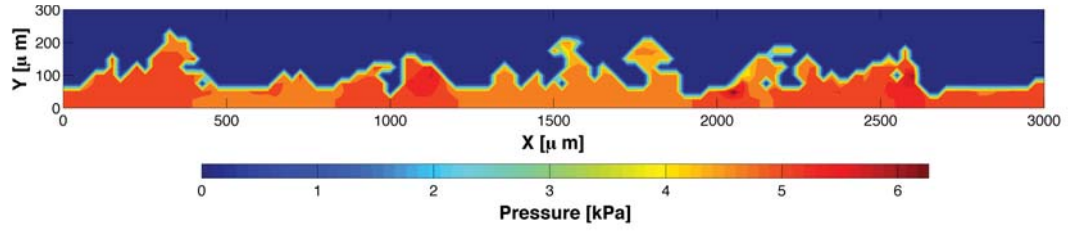
(c) Diffusive model 70°C land temperature and a 80% relative humidity.



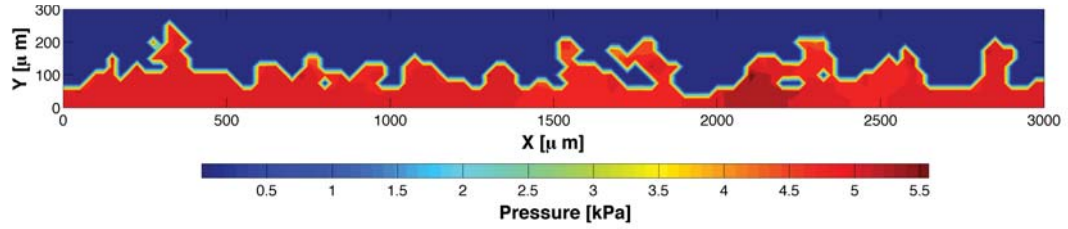
(d) Diffusive model 70°C land temperature and a 90% relative humidity.

Figure B.1: Drainage simulations for the diffusive model taken at 70°C land temperature and varying relative humidity.

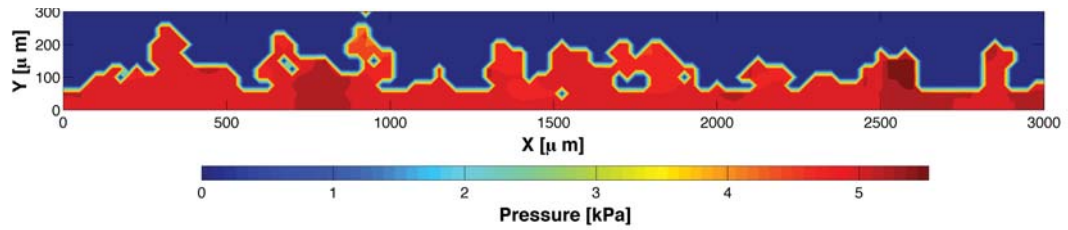
B.1.2 Pressure Distribution



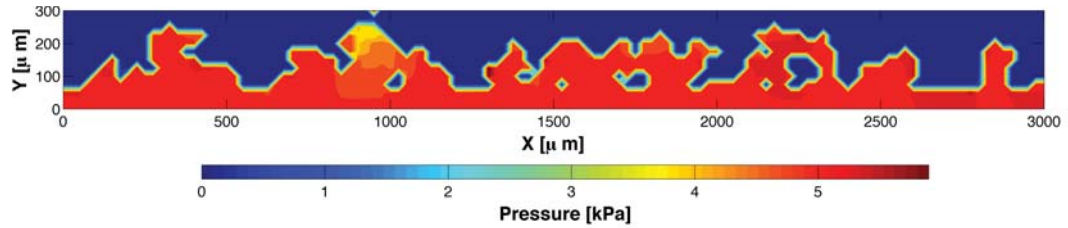
(a) Diffusive model 70°C land temperature and a 60% relative humidity.



(b) Diffusive model 70°C land temperature and a 70% relative humidity.



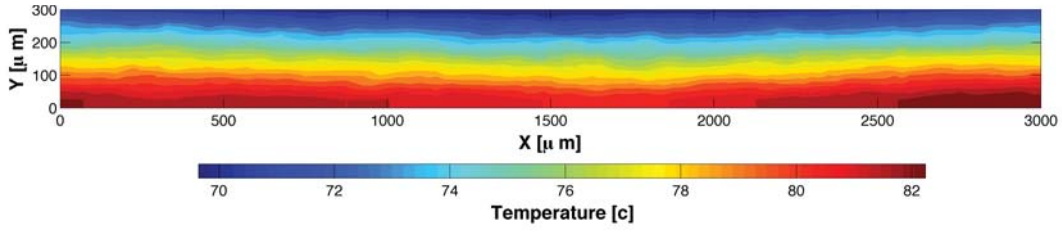
(c) Diffusive model 70°C land temperature and a 80% relative humidity.



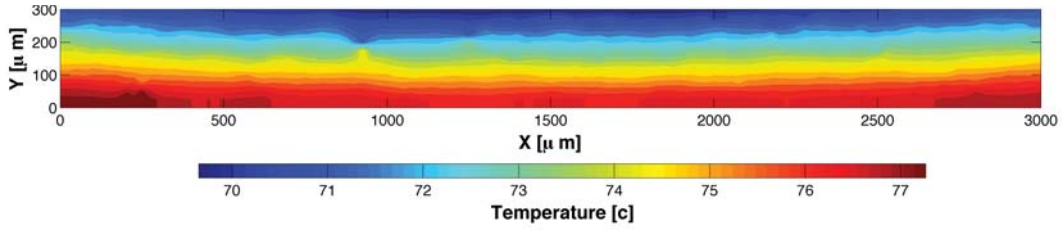
(d) Diffusive model 70°C land temperature and a 90% relative humidity.

Figure B.2: Pressure distribution simulations for the diffusive model taken at 70°C land temperature and varying relative humidity.

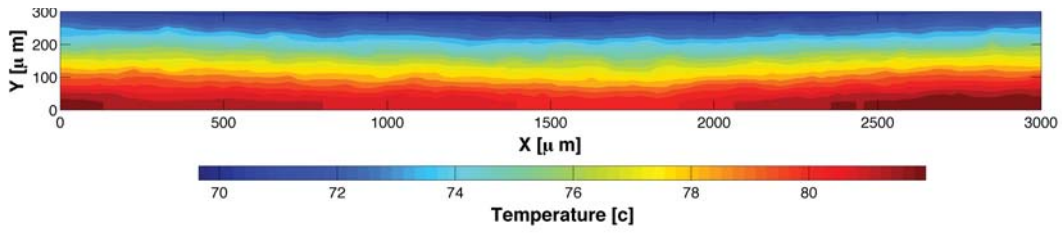
B.1.3 Temperature Distribution



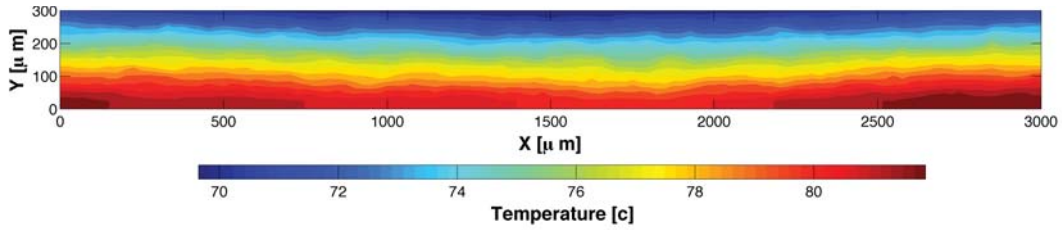
(a) Diffusive model 70°C land temperature and a 60% relative humidity.



(b) Diffusive model 70°C land temperature and a 60% relative humidity.



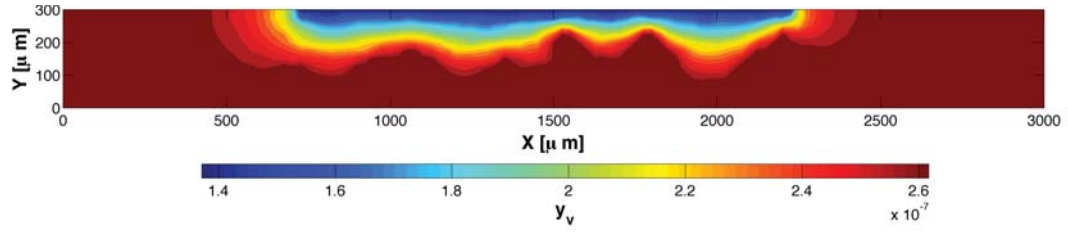
(c) Diffusive model 70°C land temperature and a 60% relative humidity.



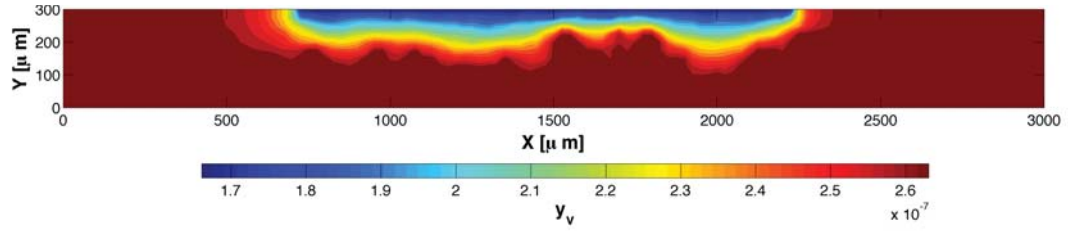
(d) Diffusive model 70°C land temperature and a 60% relative humidity.

Figure B.3: Temperature distribution simulations for the diffusive model taken at 70°C land temperature and varying relative humidity.

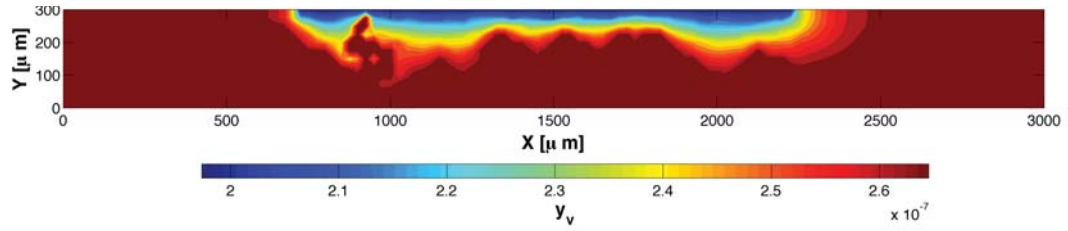
B.1.4 Vapor Concentration Distribution



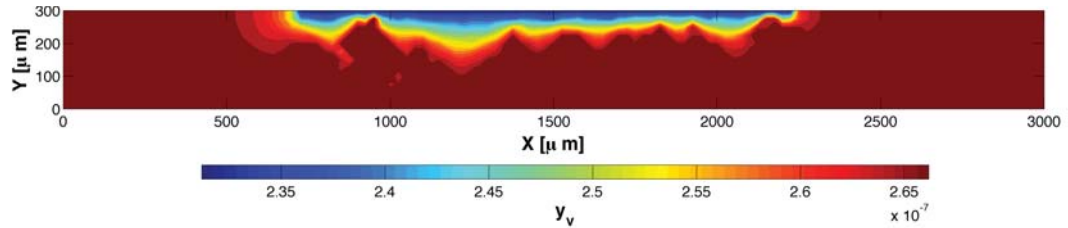
(a) Diffusive model 70°C land temperature and a 60% relative humidity.



(b) Diffusive model 70°C land temperature and a 60% relative humidity.



(c) Diffusive model 70°C land temperature and a 60% relative humidity.

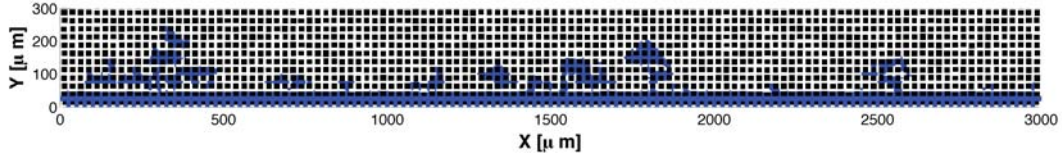


(d) Diffusive model 70°C land temperature and a 60% relative humidity.

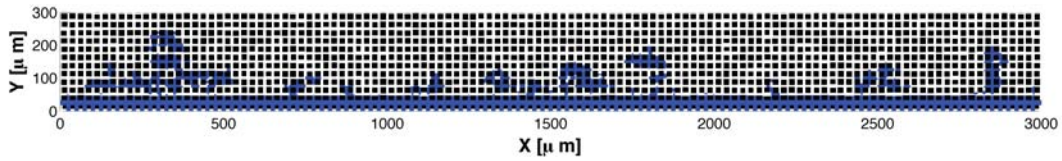
Figure B.4: Vapor concentration distribution simulations for the diffusive model taken at 70°C land temperature and varying relative humidity.

B.2 75°C Land Temperature Results

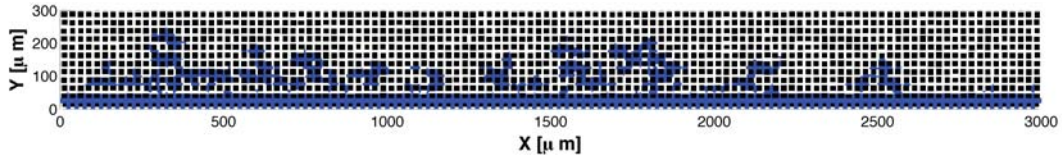
B.2.1 Drainage



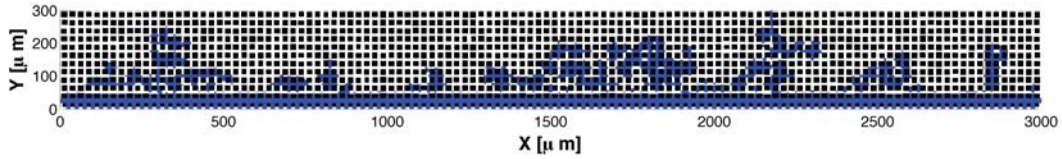
(a) Diffusive model 75°C land temperature and a 60% relative humidity.



(b) Diffusive model 75°C land temperature and a 70% relative humidity.



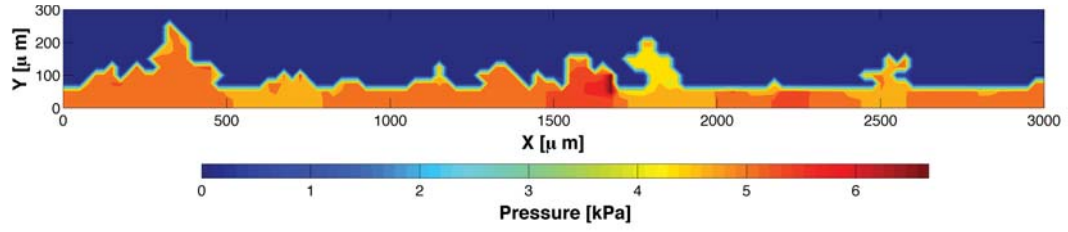
(c) Diffusive model 75°C land temperature and a 80% relative humidity.



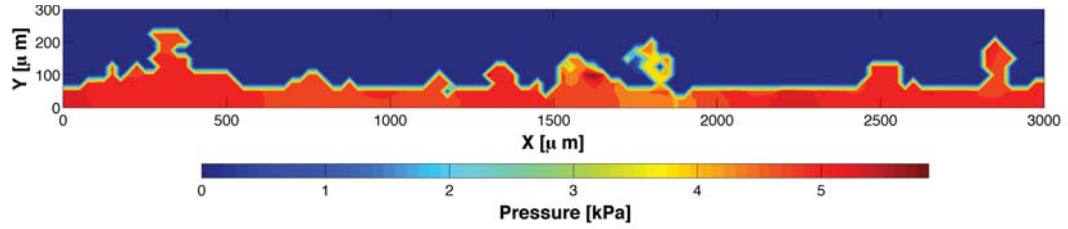
(d) Diffusive model 75°C land temperature and a 90% relative humidity.

Figure B.5: Drainage simulations for the diffusive model taken at 75°C land temperature and varying relative humidity.

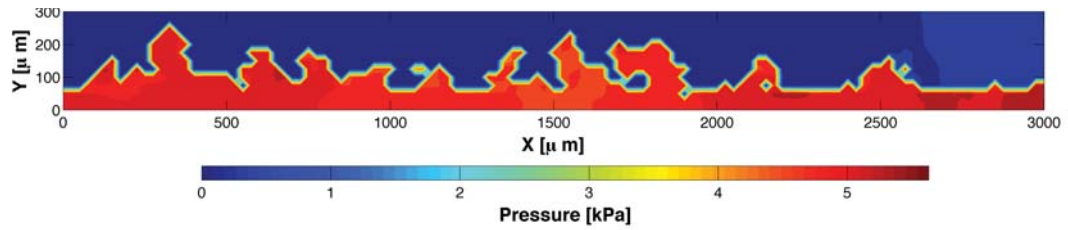
B.2.2 Pressure Distribution



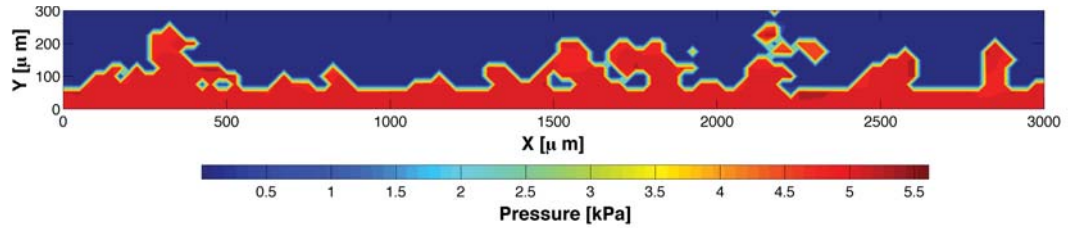
(a) Diffusive model 75°C land temperature and a 60% relative humidity.



(b) Diffusive model 75°C land temperature and a 70% relative humidity.



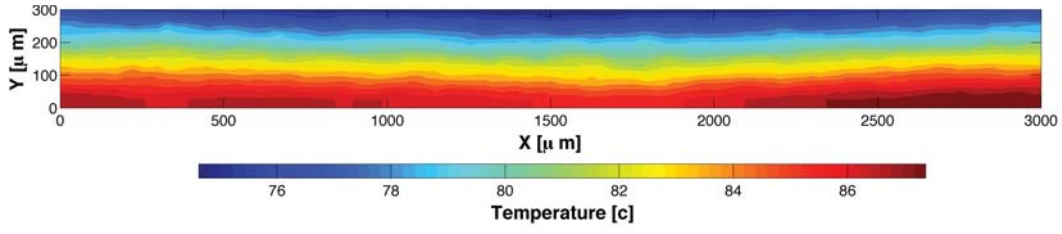
(c) Diffusive model 75°C land temperature and a 80% relative humidity.



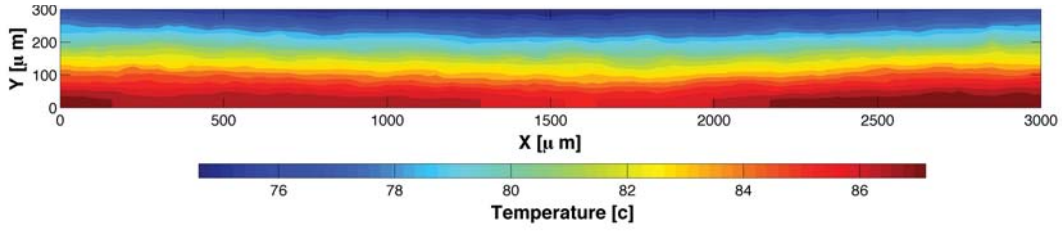
(d) Diffusive model 75°C land temperature and a 90% relative humidity.

Figure B.6: Pressure distribution simulations for the diffusive model taken at 75°C land temperature and varying relative humidity.

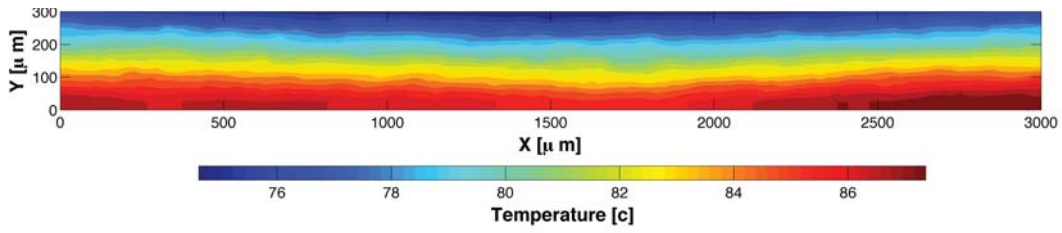
B.2.3 Temperature Distribution



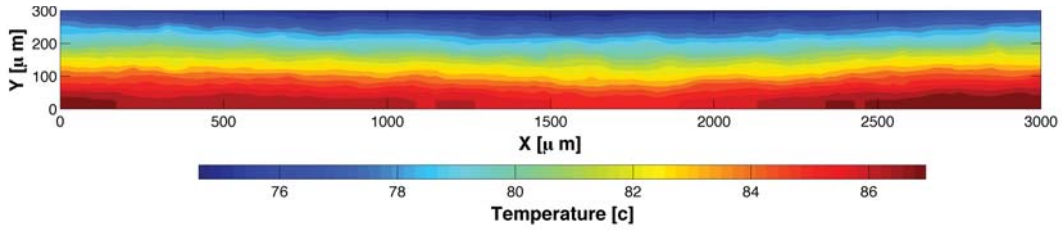
(a) Diffusive model 75°C land temperature and a 60% relative humidity.



(b) Diffusive model 75°C land temperature and a 60% relative humidity.



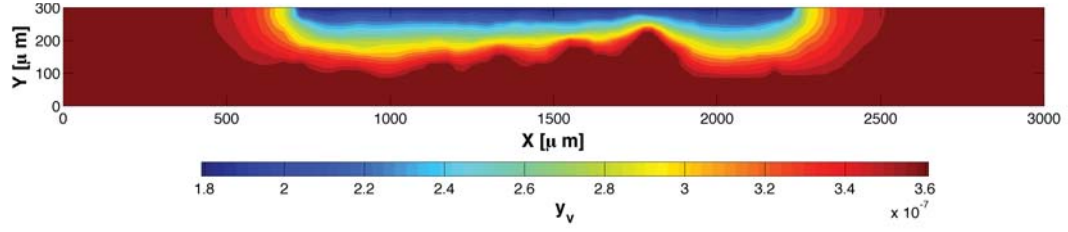
(c) Diffusive model 75°C land temperature and a 60% relative humidity.



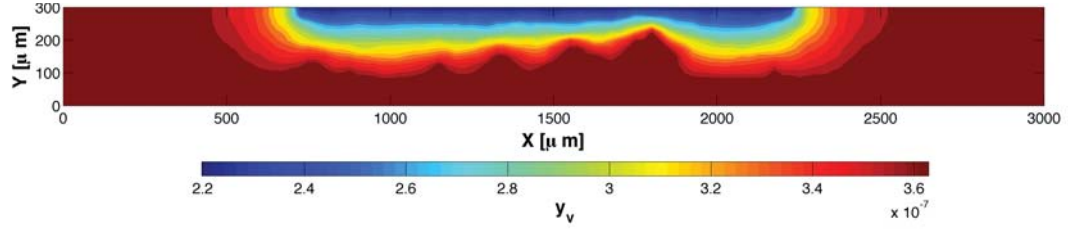
(d) Diffusive model 75°C land temperature and a 60% relative humidity.

Figure B.7: Temperature distribution simulations for the diffusive model taken at 75°C land temperature and varying relative humidity.

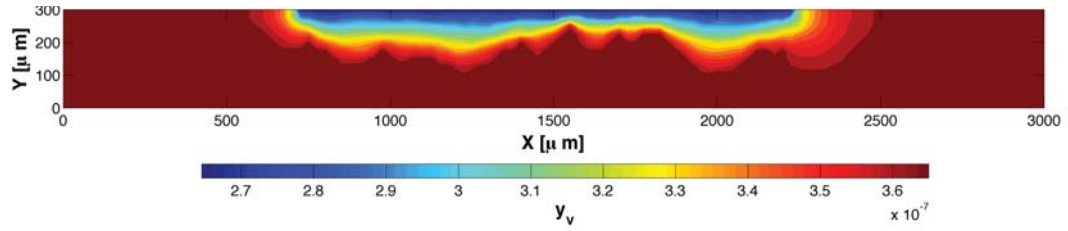
B.2.4 Vapor Concentration Distribution



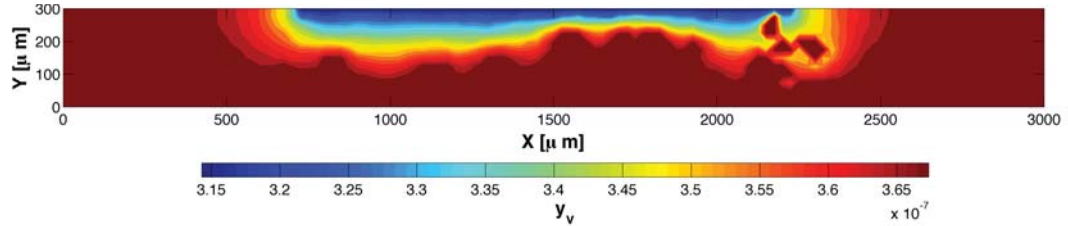
(a) Diffusive model 75°C land temperature and a 60% relative humidity.



(b) Diffusive model 75°C land temperature and a 60% relative humidity.



(c) Diffusive model 75°C land temperature and a 60% relative humidity.

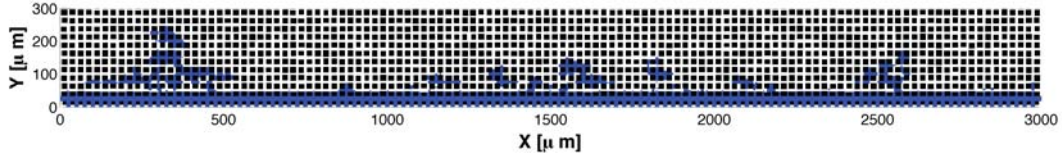


(d) Diffusive model 75°C land temperature and a 60% relative humidity.

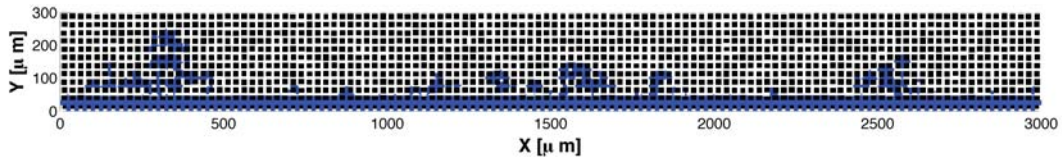
Figure B.8: Vapor concentration distribution simulations for the diffusive model taken at 75°C land temperature and varying relative humidity.

B.3 80°C Land Temperature Results

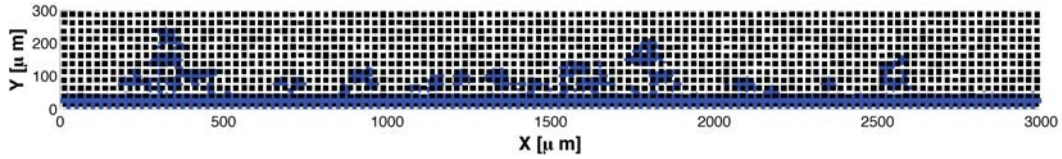
B.3.1 Drainage



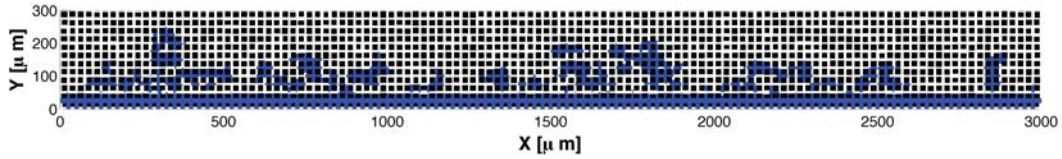
(a) Diffusive model 80°C land temperature and a 60% relative humidity.



(b) Diffusive model 80°C land temperature and a 70% relative humidity.



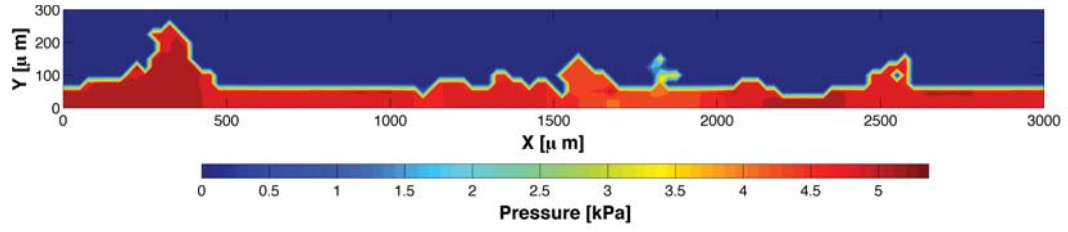
(c) Diffusive model 80°C land temperature and a 80% relative humidity.



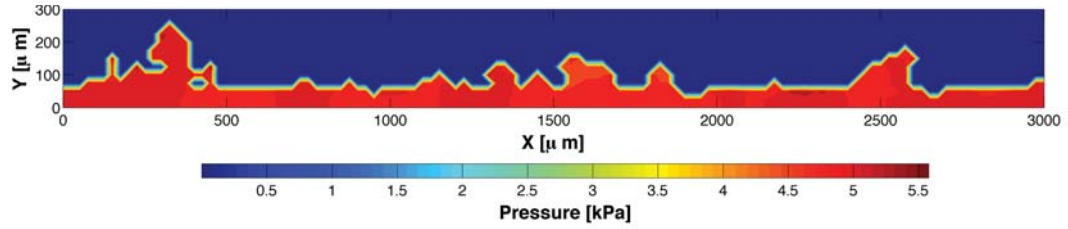
(d) Diffusive model 80°C land temperature and a 90% relative humidity.

Figure B.9: Drainage simulations for the diffusive model taken at 80°C land temperature and varying relative humidity.

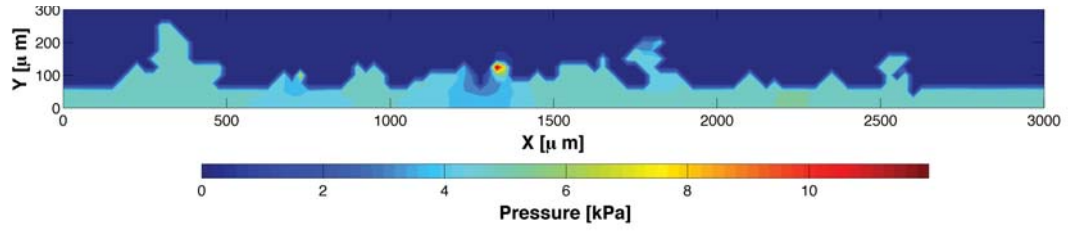
B.3.2 Pressure Distribution



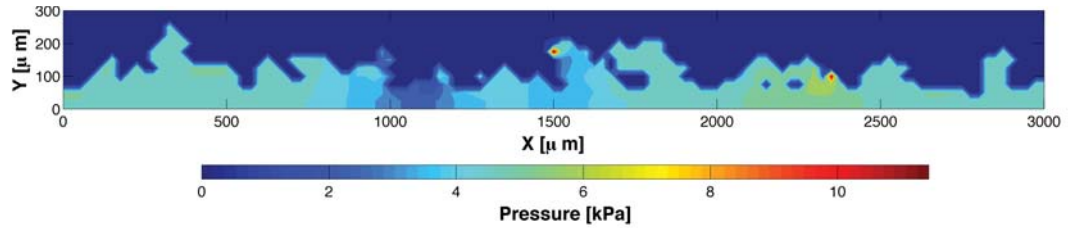
(a) Diffusive model 80°C land temperature and a 60% relative humidity.



(b) Diffusive model 80°C land temperature and a 70% relative humidity.



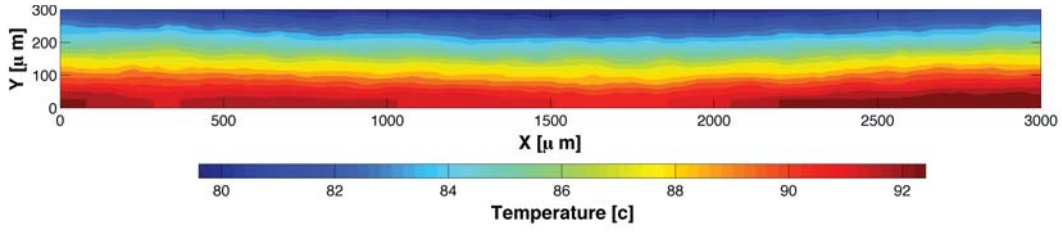
(c) Diffusive model 80°C land temperature and a 80% relative humidity.



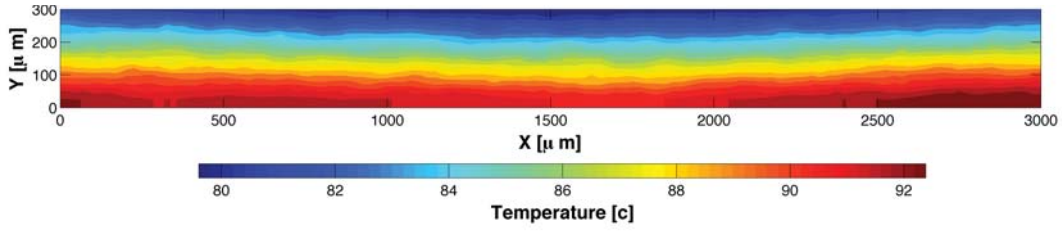
(d) Diffusive model 80°C land temperature and a 90% relative humidity.

Figure B.10: Pressure distribution simulations for the diffusive model taken at 80°C land temperature and varying relative humidity.

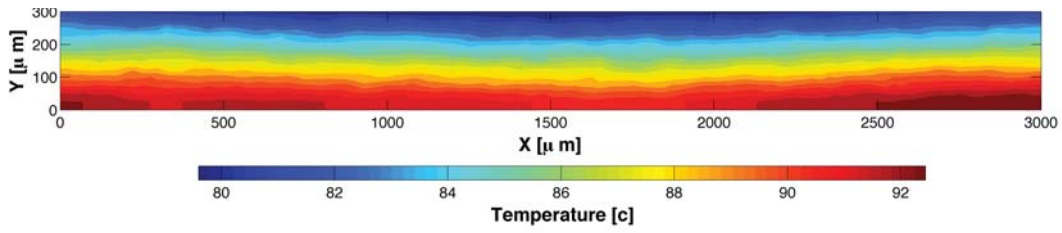
B.3.3 Temperature Distribution



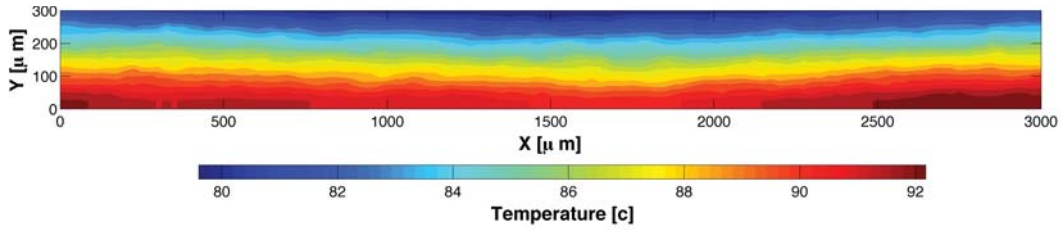
(a) Diffusive model 80°C land temperature and a 60% relative humidity.



(b) Diffusive model 80°C land temperature and a 60% relative humidity.



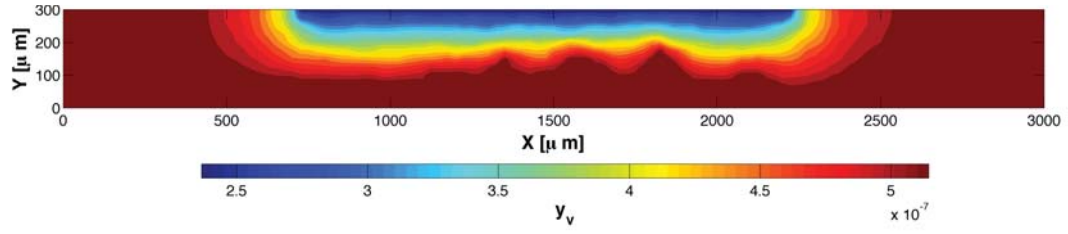
(c) Diffusive model 80°C land temperature and a 60% relative humidity.



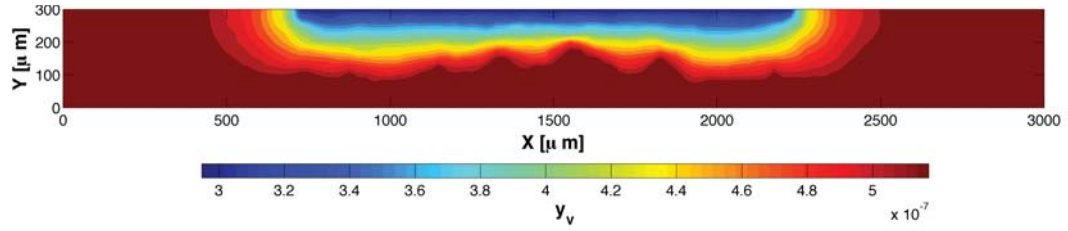
(d) Diffusive model 80°C land temperature and a 60% relative humidity.

Figure B.11: Temperature distribution simulations for the diffusive model taken at 80°C land temperature and varying relative humidity.

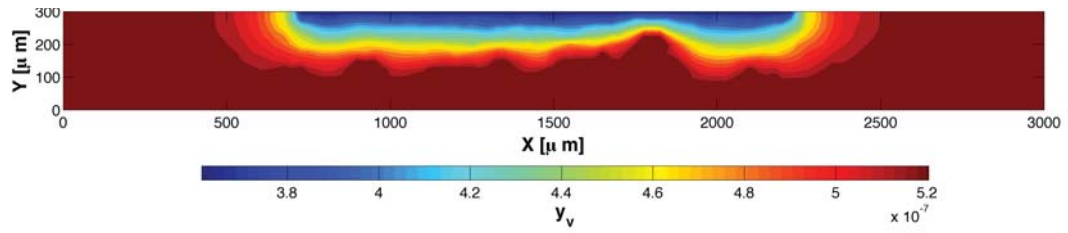
B.3.4 Vapor Concentration Distribution



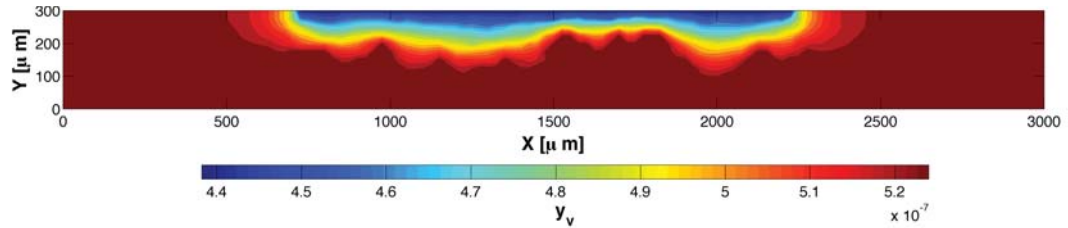
(a) Diffusive model 80°C land temperature and a 60% relative humidity.



(b) Diffusive model 80°C land temperature and a 60% relative humidity.



(c) Diffusive model 80°C land temperature and a 60% relative humidity.



(d) Diffusive model 80°C land temperature and a 60% relative humidity.

Figure B.12: Vapor concentration distribution simulations for the diffusive model taken at 80°C land temperature and varying relative humidity.

Appendix C

Pore Evaporation Subroutine

```
SUBROUTINE PORE_EVAP(R0,Tw)
!*****!
!*
!*          Pore Evaporation Model
!*
5  !*
!*          Written by: David L. Fritz
!*          Contact: dlfriz@mtu.edu
!*
!*          Michigan Technological University
!*          1400 Townsend Drive
10 !*          Houghton, Michigan
!*          49931
!*
!*=====!*
!* VARIABLE DEFINITIONS:
!* -----
15 !*
!*
!*      h    -> Thickness of the film profile in meters, the
!*             initial condition for this must be perturbed
!*             from the adsorbed film thickness to keep from
20 !*             a pure trivial solution.
!*
!*      hx   -> Slope of the film thickness or the first deri-
!*             vative of the film thickness. When setting in-
!*             itial conditions this initial value must be
!*             perturbed in order to keep from solving for
25 !*             the trivial solution of a constant film thick-
!*             ness. The selection of this parameter is very
!*             sensitive to the convergence of the film thic-
!*             kness ODEs. A trial and error method must be
!*             employed.
30 !*
!*      hxx  -> Second derivative of the film thickness the
!*             initial condition is set as 0 in this subrout-
!*             ine and is not adjustable in the accompanying *
```



```

!*          VARS.dat file .                                *!
!*          hxxx -> Third derivative of the film thickness , the *!
35  !*          initial condition is set as 0 in this subrout-*!
!*          ine and is not adjustable in the accompanying *!
!*          VARS.dat file .                                *!
!*          Ti  -> Liquid-vapor interface temperature , this value*!
!*          is greatly affected by the evaporation rate of*!
40  !*          the fluid .                                *!
!*          DP  -> Disjoining pressure which is caused by the mo-*!
!*          lecular forces in transition films . The two fitting *!
!*          parameters alpha and beta in the formulation *!
!*          are currently set to water on quartz . These *!
45  !*          will need to be adjusted to appropriate values*!
!*          for a non-wetting system. The values alpha and*!
!*          beta are adjustable in the VARS.dat file .      *!
!*          *!
!*=====*!
50  !*          *!
!*  CONSTANTS:                                           *!
!*  -----                                           *!
!*          *!
!*          Rg  -> The Specific Gas Constant (J/(kgK))    *!
55  !*          rhol -> Liquid density (kg/m^3) adjusted to the inter-*!
!*          face temperature, updated every iteration . Fl-*!
!*          uid data taken from webbook.nist.gov        *!
!*          Tv  -> Vapor temperature set in the VARS.dat input *!
!*          file .                                       *!
60  !*          DT0 -> Superheat condition , this is the temperature *!
!*          difference between the wall and the vapor *!
!*          Tw  -> Wall temperature, this value is calculated fr-*!
!*          om the vapor temperature (Tv) given in the *!
!*          VARS.dat input file and the Superheat (DT0) *!
65  !*          condition also specified in VARS.dat.    *!
!*          *!
!*=====*!
!*          *!
!*  INPUTS:                                           *!
70  !*  -----                                           *!
!*          *!
!*          R0  -> Pore radius (m), currently input through dum-*!
!*          my main program however upon completion this *!
!*          will be an input for the subroutine from the *!
75  !*          Porous Network Model.                    *!
!*          *****!

IMPLICIT NONE
EXTERNAL      :: FEX
80  DOUBLE PRECISION, &
ALLOCATABLE, &
DIMENSION (:)      :: h, hx, hxx, hxxx, Ti, DP, x, y, mdot, K, &
                    Pl, dpdx, dpidx, dTdx, sig, work, xout

```

```

85      DOUBLE PRECISION :: Rg, R0, rho1, alp, bet, gam, c1, c2, &
      c3, c4, c5, c6, c7, c8, Tw, Tv, a, b, kl, &
      M, R, Pv, hfg, nul, mul, rho1, rho2, &
      rho3, mu1, mu2, mu3, mu4, DT0, aerr, &
      rerr, sig1, ph, phx, V1, th, Pc, Psv1, &
90      Psv2, Psv, hnew, hold, h1, h2, dh, acc, &
      hfin, F1, stp, dTx, dpx, dpix, dsdx, &
      lamda, ds, xold, xnew, dom

      COMMON hfin
      DOUBLE PRECISION, &
      PARAMETER      :: pi=4.D0*DATAN(1.D0)
95      INTEGER, &
      ALLOCATABLE, &
      DIMENSION(:)   :: iwork
      INTEGER         :: res, i, j, neqn, iflag
      CHARACTER (LEN=100) :: TITLE
100

      !*****!
      !*                                           *!
      !*      Initialization /Reading of the VARS.dat input file .    *!
105    !*                                           *!
      !*****!

      OPEN(unit=13,file="VARS.dat")
      REWIND 13
110

      READ(13,*)
      READ(13,*)
      READ(13,*) TITLE

115      READ(13,*)
      READ(13,*)
      READ(13,*) M, rho1, rho2, rho3

      READ(13,*)
120      READ(13,*)
      READ(13,*) mu1, mu2, mu3, mu4

      READ(13,*)
      READ(13,*)
125      READ(13,*) Psv1, Psv2, acc

      READ(13,*)
      READ(13,*)
      READ(13,*) sig1, gam, th
130

      READ(13,*)
      READ(13,*)
      READ(13,*) DT0, kl, hfg

```

```

135      READ(13,*)
      READ(13,*)
      READ(13,*) ph, phx, hold

      READ(13,*)
140     READ(13,*)
      READ(13,*) alp, bet

      READ(13,*)
      READ(13,*)
145     READ(13,*) res, dom, aerr , rerr

CLOSE(13)

!*****!
150  !*                                     *!
!*      Pre-allocating space for the vectorized variables that *!
!*      will be updated each iterative step in the X domain. *!
!*      The length of these variables is determined by the res *!
!*      variable in the VARS.dat input file . *!
155  !*                                     *!
!*****!

ALLOCATE (h(res), hx(res), hxx(res) , hxxx(res) , Ti(res) , DP(res))
ALLOCATE (x(res), mdot(res), K(res) , Pl(res) , dpdx(res) , sig(res))
160  ALLOCATE (dpidx(res), dTdx(res), y(3) , work(21), iwork(5))
ALLOCATE (xout(res))

!*****!
165  !*                                     *!
!*      Initialization of the non-adjustable constants *!
!*                                     *!
!*****!

170  R = 8.3144621D0      !* Universal Gas Constant (J/(molK))..

!*****!
175  !*                                     *!
!*      Initial Conditions for the ODE solver *!
!*                                     *!
!*****!

i      = 1      !* Initial step .....
180  neqn = 3      !* Number of ODEs to solve for .....
iflag = -1      !* RKF45 Solver "Normal" Setting .....
hx(i) = phx     !* Slope Film Thickness IC .....
x(i) = 0.D0     !* Starting point of integration .....
xout(i) = 0.D0
185  hxx(i) = 0.D0 !* 2nd Deriv. Film Thickness IC .....

```

```

hxxx(i) = 0.D0          !* 3rd Deriv. Film Thickness IC .....
mdot(i) = 0.D0          !* Evaporation rate (kg/(s-m^2)) .....
dpdx(i) = 0.D0          !* Initial Pressure Gradient (Pa/m) ...
dpx      = dpdx(i)      !* FEX Common Var .....
190 dpidx(i) = 0.D0       !* Initial Disjoining Pres Grad (Pa/m)
dpix      = dpidx(i)     !* FEX Common Var .....
dTdx(i) = 0.D0          !* Temperature Gradient (K/m) .....
dtx       = dTdx(i)      !* FEX Common Var .....
dsdx      = 0.D0         !* Surface Tension Gradient (N/m^2)...
195 lamda   = 0.D0

!*****!
!*                                           *!
!*      Calculated fluid and substrate constants      *!
200 !*                                           *!
!*****!

stp      = dom/DBLE(res)      !* Step size (nm) .....
Tv       = Tw - DT0          !* Wall temp (K) .....
205 Ti(i) = Tw                !* Interface temp (K) .....
Rg       = R/M               !* Gas Constant (J/(kgK)) ...
rho1     = rho1 * Ti(i)**2 + rho2 * Ti(i) + rho3 !* Liquid Density (kg/m^3)..
Vl       = M/rho1            !* Molar Volume (kmol/m^3)..
sig(i)   = sig1 + Ti(i)*gam   !* Surface Tension (N/m) ....
210 ds     = sig(i)          !* Common Var .....
Pc       = 2.D0*ds*DCOS(th)/R0 !* Capillary Pressure (Pa) ..
Psv      = Psv1*DEXP(Psv2*Ti(i)) !* Sat Vapor Press (Pa) .....
mul      = mu1*DEXP(mu2*Ti(i)) + & !* Liquid D Visc. (Pa-s) ....
          mu3*DEXP(mu4*Ti(i))
215 nul    = mul/rho1         !* Liquid K Visc. (m^2/s) ...

CALL NRH(R0,Tw,kl,hfg,Tv,rho1,alp,bet,hold,ds,acc,M,R,Psv, &
          Vl,Rg)

220 h(i)   = hfin
Pv       = Psv*alp*h(i)**bet
K(i)     = (1.D0/(R0-h(i)))*(1.D0+hx(i)**2.D0)**(-0.5D0)+hxx(i)* &
          (1.D0+hx(i)**2.D0)**(-1.5D0)

225 DP(i)  = (3.11D-21/(h(i)**3))*(th**4-hx(i)**4+2.D0*h(i)* &
          hx(i)**2*hxx(i))

Pl(i)    = Psv-ds*K(i)-DP(i)   !* Liquid Pressure (Pa) .....
!*****!
230 !*                                           *!
!*      Forward steps in the spatial domain      *!
!*                                           *!
!*****!

235 DO i=2,res
  IF ( iflag .EQ. 2) THEN

```

```

        iflag = -1
ELSE IF ( iflag .EQ. 5) THEN
EXIT
END IF
240

F1      = (R0-h(i-1))*hfg*DLOG(R0/(R0-h(i-1)))
a       = acc*DSQRT(M/(2.D0*pi*R*T(i-1)))* &
        (Psv*M*hfg/(R*Tv*T(i-1)))
245 b     = acc*DSQRT(M/(2.D0*pi*R*T(i-1)))* &
        (Vl*Psv/(R*T(i-1)))
x(i)    = x(i-1) + stp
xold    = x(i-1)
xnew    = x(i)
250 mdot(i) = a*(Ti(i-1)-Tv)+b*(Pl(i-1)-Psv) !* Evaporation Rate (kg/s)
Ti(i)   = ((( Tw*kl/F1)+a*Tv+b*ds*K(i-1))/(kl/F1+a+b*rhol* &
        Rg*DLOG(alp*h(i-1)**bet)))
mdot(i) = a*(Ti(i-1)-Tv)+b*(Pl(i-1)-Psv) !* Evaporation Rate (kg/s)
dTdx(i) = (Ti(i)-Ti(i-1))/stp             !* Temperature Grad.(T/m).
255 dTx   = dTdx(i)                       !* Common Var .....
rhol    = rho1*T(i)**2+rho2*T(i)+rho3 !* Liquid Density (kg/m^3)
Vl      = M/rhol                         !* Molar Volume (kmol/m^3)
sig(i)  = sig1+Ti(i)*gam                 !* Surface Tension (N/m)..
ds      = sig(i)                         !* Common Var .....
260 dsdx  = (sig(i)-sig(i-1))/stp          !* SIGMA Gradient (N/m^2).
Pc      = 2.D0*ds*DCOS(th)/R0            !* Capillary Pressure (Pa)
Psv     = Psv1*DEXP(Psv2*T(i))           !* Sat Vapor Press (Pa) ...
Pv      = Psv*alp*h(i-1)**bet
mul     = mu1*DEXP(mu2*T(i))+ &         !* Liquid D Visc. (Pa-s)..
265      mu3*DEXP(mu4*T(i))
nul     = mul/rhol                       !* Liquid K Visc. (m^2/s).

!*****!
270 !*                                     *!
!*      Runge-Kutta-Fehlberg Solver:      *!
!*      -Setting input variables for solver *!
!*      -Calling RKF45 Solver              *!
!*      -Storing solver output to appropriate variables *!
275 !*                                     *!
!*****!

y(1)    = h(i-1)
y(2)    = hx(i-1)
280 y(3)  = hxx(i-1)

CALL DRKF45(FEX, neqn, y, xold, xnew, rerr, aerr, iflag, work, &
            iwork, ds, gam, dTx, dpx, dpix, R0)

285 h(i)   = y(1)
hx(i)    = y(2)
hxx(i)   = y(3)

```

```

xout(i) = xnew

290 K(i) = (1.D0/(R0-h(i)))*(1.D0+hx(i)**2.D0)**(-0.5D0)+hxx(i)* &
      (1.D0+hx(i)**2.D0)**(-1.5D0)
DP(i) = -rhol*Rg*Ti(i)*DLOG(alp* & !* Disjoining Pressure (Pa).
      h(i)**bet)

295 dpidx(i) = (DP(i)-DP(i-1))/stp      !* DJPress Gradient .....
dpix      = dpidx(i)                  !* Common Var .....

c3      = (1.D0/(2.D0*mul))*((R0-h(i))**2*DLOG(R0)-0.5D0*R0**2)
c4      = (1.D0/mul)*(R0-h(i))*DLOG(R0)
300 c5      = R0**2*(DLOG(R0)-0.5D0)-(R0-h(i))**2*(DLOG(R0-h(i))-0.5D0)
c6      = (pi/(8.D0*nul))*((R0**4-(R0-h(i))**4)-4.D0*(R0-h(i))**2* &
      c5)+pi*rhol*(2.D0*R0*h(i)-h(i)**2)*c3
c7      = -(pi/nul)*(R0-h(i))*c5+pi*rhol*(2.D0*R0*h(i)-h(i)**2)*c4

305 lamda = lamda-mdot(i)*stp
dpdx(i) = -(c7/c6)*dsdx-(2.D0*pi*kl/(hfg*c6))*lamda
dpix = dpdx(i)
Pl(i) = (Psv-ds*K(i)-DP(i))

310 END DO

OPEN(UNIT=12,FILE="OUTPUT.dat")
DO j=1,i-1
  WRITE(12,*) K(j),h(j), mdot(j), Pl(j), xout(j), Ti(j), DP(j), &
315      hx(j), hxx(j), dpdx(j)
END DO
CLOSE(12)

RETURN
20 20 FORMAT(3D20.20)
END SUBROUTINE PORE_EVAP

SUBROUTINE NRH(R0,Tw,kl,hfg,Tv,rhol,alp,bet,hold,sig,acc,M,R,Pv, &
      Vl,Rg)
325 !*****!
!*                                     *!
!*      Newton's Method to solve for Adsorbed Film thickness *!
!*      for a polar fluid . *!
!******!

330 IMPLICIT NONE
DOUBLE PRECISION :: a, b, acc, R, Tw, Tv, Pv, M, hfg, kl, R0, &
      rhol, alp, bet, hold, sig, Vl, hnew, dh, h1, &
      h2, hfin, db, Rg, dTx, dpix, gam

COMMON hfin
335 DOUBLE PRECISION, &
PARAMETER :: pi=4.D0*DATAN(1.D0)

a = acc*DSQRT(M/(2.D0*pi*R*Tw))*(Pv*M*hfg/(R*Tv*Tw))

```

```

340      b = acc*DSQRT(M/(2.D0*pi*R*Tw))*(V1*Pv/(R*Tw))

      db = 1.D0

      DO WHILE (db .GT. DABS(1.D-16))

345      h1 = ((( Tw*kl)/(( R0-hold)*hfg*DLOG(R0/(R0-hold)))+a*Tw+b*sig*( &
          1.D0/(R0-hold)))/(( kl /(( R0-hold)*hfg*DLOG(R0/(R0-hold)))+a &
          +b*rhol*Rg*DLOG(alp*hold**bet)))-Tw

      h2 = ((b*sig)/(R0-hold)**2+(Tw*kl)/(hfg*DLOG(R0/(R0-hold)) &
          *(R0-hold)**2)-(Tw*kl)/(hfg*DLOG(R0/(R0-hold))**2*(R0- &
          hold)**2))/(a+kl/(hfg*DLOG(R0/(R0-hold))*(R0-hold))+ &
          Rg*b*rhol*DLOG(alp*hold**bet))-((Tv*a+(b*sig)/(R0-hold)+ &
          (Tw*kl)/(hfg*DLOG(R0/(R0-hold))*(R0-hold)))*(kl/(hfg*DLOG( &
          R0/(R0-hold))*(R0-hold)**2)-kl/(hfg*DLOG(R0/(R0-hold)) &
355      **2*(R0-hold)**2)+(Rg*b*bet*hold**bet-1.D0)*rhol)/ &
          hold**bet))/(a+kl/(hfg*DLOG(R0/(R0-hold))*(R0-hold))+ &
          Rg*b*rhol*DLOG(alp*hold**bet))**2

      dh = h1/h2
360      db = DABS(dh)

      hnew = hold - dh
      hold = hnew

365      END DO
      hfin = hold
      RETURN
      END SUBROUTINE NRH

370      SUBROUTINE FEX(x,y,yp,sig,gam,dTx,dpx,dpix,R0)
      !*****!
      !*                                     *!
      !*      Subroutine to evaluate the derivatives of h      *!
      !*                                     *!
375      !*****!
      IMPLICIT NONE

      DOUBLE PRECISION :: x, dTx, dpx, dpix, gam, R0, sig
      DOUBLE PRECISION :: yp(3), y(3)
380      INTEGER          :: res

      yp(1) = y(2)
      yp(2) = y(3)
      yp(3) = 3.D0*y(3)**2*y(2)*(1.D0+y(2)**2)**(-1.D0)+y(3)*y(2)*(R0- &
          y(1))**(-1.D0)-y(2)*(1.D0+y(2)**2)*(R0-y(1))**(-2.D0)- &
385      (gam/sig)*((1.D0+y(2)**2)*(R0-y(1))**(-1.D0)+y(3))* &
          dTx-(1.D0/sig)*(1.D0+y(2)**2)**1.5D0*(dpx+dpix)

      END SUBROUTINE FEX

```